Rocket Science

Mahdi H. Gholi Nejad

Professor Mofid Gorji-Bandpy

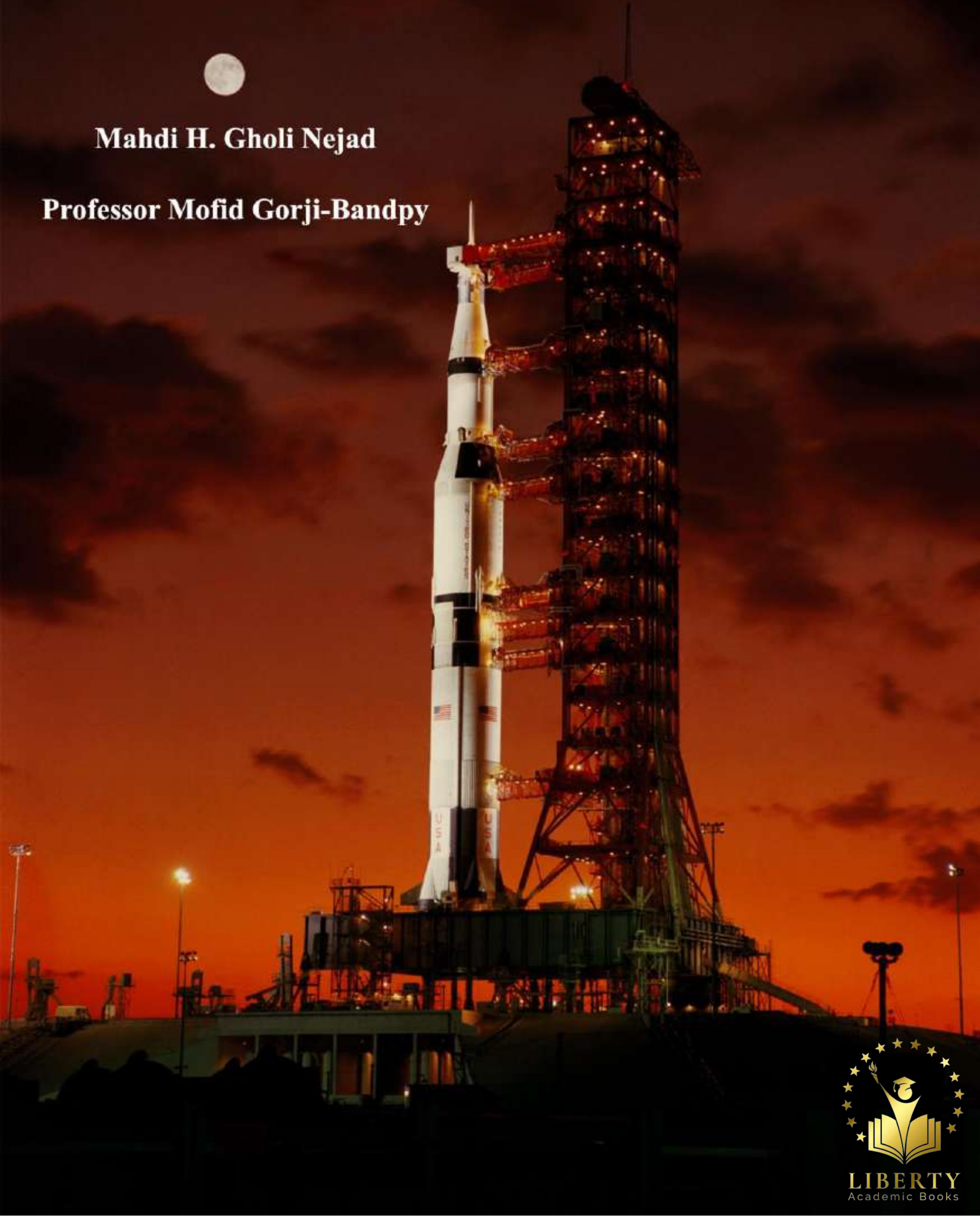

LIBERTY
Academic Books

26.09.2022
by Liberty Academic Publishers
New York, USA

For citation purposes, cite as indicated below:
M. H. G. Nejad & M. Gorji-Bandpy , Rocket Science; Liberty Academic Publishers : New York, USA, 2022.

Liberty Academic Publishers works to counter discrimination on grounds of gender, race, disability, age and sexuality.

Cover design by Andrew Singh

ISBN: 978-1-955094-29-0

ISBN 978-195509429-0
9 781955 094290

Prepared For National Aeronautics and Space Administration, George C. Marshall Space Flight Center

Rocket Science

Mahdi H. Gholi Nejad[1]

Professor Mofid Gorji-Bandpy

LIBERTY
Academic Books

[1] Contact info.:
Mahdi.hgn1998@gmail.com
Gorji@nit.ac.ir

"For forty-nine months between 1968 and 1972, two dozen Americans had the great good fortune to briefly visit the Moon. Half of us became the first emissaries from Earth to tread its dusty surface. We who did so were privileged to represent the hopes and dreams of all humanity. For mankind, it was a giant leap for a species that evolved from the Stone Age to create sophisticated rockets and spacecraft that made a Moon landing possible. For one crowning moment, we were creatures of the cosmic ocean, an epoch that a thousand years hence may be seen as the signature of our century."

Buzz Aldrin

PREFACE

Today, with the dramatic advancement of space science, the attempt to conquer space and discover the many unknowns in it, such as human travel to other planets or launching and placing satellites in Earth orbits for various applications, all depend on the design of a suitable rocket containing cargo, (Astronauts, satellites, food, etc.). In this book, we have tried to express the contents related to different components of the rocket, their functionality, and their design in a very fluent way and in the simplest way. The existing material that derives from the basic laws of fluid mechanics, dynamics, physics, and thermodynamics is fully and eloquently stated. Also, due to limited resources, this book is taken from more than 400 technical and memorandum reports from NASA, which makes it easier for those interested in this basin to access this volume of less accessible resources. Due to its eloquence and simplicity of expression, this book is a unique book for all undergraduate, post-graduate, and graduated students and also enthusiasts of space rocket design science. On the other hand, the redesign and colorful pictures and tables are the motivating factors for the readers of this book. Due to the comprehensiveness of the subject, this book will be further developed (e.g., Turbo pumps, ramjet, rocket advanced navigation, and many more interesting subjects) in future editions, but now many matters and concepts have been explicitly clarified.

CONTENTS

Preface ... 3
Introduction ... 21
Thrust ... 23
Chemical Rocket ... 28
Orbital mechanics ... 31
  Circular Orbits ... 42
  Elliptical orbits ... 48
  parabolic trajectories ... 50
  hyperbolic trajectories ... 51
Burning rate determination ... 53
    Erosive burning ... 54
    Grain design ... 62
Propellant and propulsion ... 73
  Solid propellant ... 74
  liquid propellant ... 77
  Hybrid propellant ... 86
Lift-off engines ... 89
  Gas generator ... 96
Reaction control systems (RCS) ... 99
Orbital Maneuvering Systems (OMS) ... 100
New Parameters in Rocket Propulsion ... 106
  Specific Impulse ... 111
  Thrust Coefficient ... 116
  Flight Performance ... 120

Total, Propulsive and Thermal Efficiency 123
Multistage Rockets 125
Chemical Rocket Combustion Chamber 130
Injector 131
Unlike impinging 134
Like impinging 136
Non-impinging Elements 137
Hybrid elements 138
Impinging Angle 141
Combustion Chamber Instability 146
Solid propellant combustion chamber 150
Hybrid propulsion heat transfer 154
Combustion Chamber Cooling 168
Cooling in the combustion chamber with liquid propellants 168
Cooling in the combustion chamber with solid propellants 179
Combustor Volume and Shape 182
Combustor Shape 182
Combustor Volume 185
Rocket nozzle with liquid propulsion 189
Nozzle configuration 195
Geometry 196
Expansion Geometry 198
Multiphase Flow in Rocket Nozzle 206
Flow Expansion in Rocket Nozzle 214

Thrust Vectoring Nozzle 214
Bell Nozzles 215
Non-Optimum Contour 217
Over-Expanded Nozzle 221
Nozzle Extensions 222
Small Nozzle 223
Plug Nozzle 223
Expansion-deflection nozzle 231
Nozzle Expansion Area Ratio 232
Conical nozzle 232
Method of Characteristics 235
Characteristic Method Procedure 237
Parabolic Approximation of Bell Nozzle 246
Annular Nozzle 248
Thrust Chamber Cooling 253
Regenerative cooling: 258
Design of cooling passages 274
Dump Cooling: 284
Film cooling: 284
Transpiration Cooling: 293
Nuclear Propulsions 307
Electric propulsions 308
Electrothermal propulsions 310
Electromagnetic Propulsions 311
Electrostatics Propulsion 312

REFERENCES 315

TABLE OF FIGURES

Figure 1- Rockets classification..23

Figure 2- Mass and Energy Balances 24

Figure 3- Dependence of specific impulse and Mach number in different types of propulsion. Adopted from AIAA 2017-2343................................26

Figure 4- Elements of Solid and Liquid Rocket Propulsion-Ahmed F.EL29

Figure 5- simple chemical rocket thrust chamber and T-S diagram (from Mechanics and Thermodynamics of Propulsions) 30

Figure 6- Cartesian coordinate system for a rigid moving object..............32

Figure 7- Free-body diagram of two masses located in an inertial frame. (Adopted from Orbital Mechanics for Students)...33

Figure 8- The path of $\boldsymbol{m2}$ around $\boldsymbol{m1}$ with its characteristics 35

Figure 9- (A) Velocity components from top plane. (B) Differential area swept out by the relative position vector during time interval dt................36

Figure 10- Periapsis, Flight path angle, and the true anomaly (polar angle) concepts 40

Figure 11- Illustration of chord line, latus, and semi latus rectums concepts 41

Figure 12- Stellar day and mean solar day concepts...................................44

Figure 13- Ecliptic plane position at celestial sphere and equinox concept 45

Figure 14- Equator and Ecliptic precessions concepts 46

Figure 15- GEO's, Polar orbits with respect to the equator, and low, medium, and high earth orbits altitude ranges 46

Figure 16- The exposed area of the earth by the satellite (Footprint). 47

Figure 17- Elliptical orbits schematic drawing. 48

Figure 18- Orbit shape variation as eccentricity changes. (Adopted from Orbital Mechanics for Students)..52

Figure 19- Pressure-time variation in erosive burning. 56

Figure 20- Schematic drawing of Actual and Ideal Grains Burn-Back.....56

Figure 21- (a) Erosive burning regimes. (b) Variation of ballistic burn rate with Mach number ratio exponent (x) at different static pressures. 57

Figure 22- Typical effect of combustion gas velocity on burning-rate augmentation. (Adopted from NASA-SP-8039)...58

Figure 23- Typical effect of mass flux on burning-rate augmentation. (Adopted from NASA-SP-8039)...59

Figure 24- Burning rate variation with acceleration direction; and effect of grain size (i.e., Aluminum) on burning rate. Adopted from Effects of Acceleration upon Solid-Rocket Performance by G. B. Northam and M. H. Lucy...60

Figure 25- Acceleration effect on four types of propellants burning rate. Adopted from Effects of Acceleration upon Solid-Rocket Performance by G. B. Northam and M. H. Lucy 61

Figure 26- Typs of Thrust-time diagrams and Cylindrical and Tubular Grains ahcematic drawings...63

Figure 27- Burning effect on different solid propellant Cusp's 63

Figure 28- Common tubular grain perforations 64

Figure 29- Burning profile as a function of $\boldsymbol{d/D}$ and $\boldsymbol{L/D}$ ratios...............64

Figure 30- Boost-Sustain performance thrust-time diagram.......................66

Figure 31- Grains star configuration and its burning profiles at different web burning heights. 67

Figure 32-Solid grains different configurations....69

Figure 33- Internal-burning charge design with their thrust-time program, (from courtesy shafer). 70

Figure 34- Typical thrust-time plots for space engine missions. From NAS-7-103 72

Figure 35- Experimental Study of the Swirling Oxidizer Flow in. Adopted from Experimental Demonstration of the Vacuum Specific Impulse of a Hybrid Rocket Engine. 73

Figure 36- Hybrid rocket combustion schematic....73

Figure 37- Vapor pressure for liquid oxidizers at top and liquid fuels at the bottom. Adopted from Liquid Rocket Propellants....84

Figure 38- liquid cryogenic propellant densification ground facility (Adopted from US005644920A)....85

Figure 39- Specific gravity for several liquid propellants- Adopted from Liquid Rocket Propellants....86

Figure 40- SSME throttling profile 91

Figure 41- Propellant feed-system schematic 92

Figure 42- Closed cycle engine types....94

Figure 43- Types of open cycle engine 95

Figure 44- Space shuttle aft fuselage OMS/RCS concepts....101

Figure 45- Space shuttle RCS. Adapted and modified from Space Shuttle System and Flight Mechanics Ulrich Walter Institute of Astronautics, Technical University, Munich, Germany....102

Figure 46- (A) ACA manipulations, (B) Throttle jets select lever. From LMA-790-3-LM 10 103

Figure 47- Typical thrust time histories (adopted from Fundamental of Aircraft and Rocket Propulsion) 106

Figure 48- The momentum of the rocket and the mass exhausted of it. ..108

Figure 49- Tsiolkovsky rocket equation. 109

Figure 50- Maximum vhicle velocity changes about (a) specific impulse and mass ratio. (b) Average effective exhaust velocity, specific impulses, and propellant mass fraction. `Adopted from Rocket Propulsion Elements 110

Figure 51- Variation of optimum thrust coefficient for different nozzle pressure and area ratios at the various gas ratios of specific heat. Adopted from Rocket Propulsion Elements 120

Figure 52- Definition sketch of flight path line. 121

Figure 53- Variation of Drag and Lift coefficient of V-2 engine for different Mach numbers as a function of angle of attack. Adopted from Rocket Propulsion Elements. 121

Figure 54- definition sketch of rocket staging 129

Figure 55- Types of injector plate design 131

Figure 56- Relation of injector components to total injector flow system. From SP8089 132

Figure 57- Injection Element Spray Pattern Schematics, Adopted from NASA-TM-110632 133

Figure 58- Design variables for like impinging doublet. From SP 8089.136

Figure 59- Three configurations for concentric tube element. From NASA SP 8089 138

Figure 60- illustration of pintle element showing inner slots and outer annulus. from SP 8089. 139

Figure 61- Two-dimensional flow field for a typical unlike impinging element. From SP 8089. 141

Figure 62- illustration of inner-post chamfer angle in a concentric tube element. From SP 8089. 142

Figure 63- Schematic of Pintle deflector angle. From SP 8089. 142

Figure 64- Illustration of splash-plate angle. From SP 8089 143

Figure 65- Thermochemical calculation for Oxygen- 〖RP〗_1 combustion. Adopted and redesign From Aircraft Propulsion 2009........145

Figure 66- Discharge coefficient for typical injector orifice geometries, based on water test. (From Sutton and Biblarz 2001)...............................145

Figure 67- Schematic drawing of possible propellant injection pattern in the combustion chamber. Adopted and redesign from Aircraft Propulsion 2009 146

Figure 68- Definition sketch of two impinging jets. Adopted and redesign from Aircraft Propulsion 2009...146

Figure 69- SSME_Presentation_2...147

Figure 70- F1 engine by Davidson Center for Space Exploration...........148

Figure 71 -Baffle concept and main chamber instabilities. Adopted from NASA TN D-4730- NASA SP 8113 and Designing Liquid Rocket Engine Injectors for Performance, Stability, and Cost, respectively. 149

Figure 72- Blocking parameter versus the blowing term. The simple expression $\boldsymbol{CfCfo = B - 0.68}$ shows an excellent fit in the range of $\boldsymbol{5 < B < 20}$ for most hybrid fuels. 157

Figure 73-Hybrid Propulsion Boundary Layer 159

Figure 74- Pressure sensitivity versus regression rate. Adopted from Hybrid Rocket Propulsion 159

Figure 75- O/F shifting versus port diameter ratio at different n values. Adopted from Rocket Motor, Hybrid 166

Figure 76-Definition Sketch of a Regenerative Cooling and Components of the Arian 5G Rocket, and physics of the regeneratively cooled C.C. (Top left image is a redesigned version from Thermomechanical Analysis and Optimization of Cryogenic Liquid Rocket Engines and Top right image adopted from ESA-D. Ducros, the bottom image is edited version from Additively Manufactured Rocket Engine Combustion Chamber Structural Analysis) 170

Figure 77- Wall configuration-from Modern Eng. 174

Figure 78- Figure A. The Reusable Solid Rocket Motor (RSRM) is a primary booster for NASA's Space Transportation System (STS). Section A-A shows 11-point slot and fin star grain structure in the RSRM'3s forward segment. Propellant in forward-center and aft-center segments form straight walled cylinders; aft-segment propellant tapers outward to submerged nozzle. Inhibitors between segments are asbestos-filled carboxyl terminated polybutadiene used to tailor burning surface to meet the motor's thrust requirements. (Adopted from Virtual prototyping of solid propellant rockets)..180

Figure 79- Typical solid rocket motor case. (Redesigned and adopted from NASA SP- 8025)...181

Figure 80- Elements of basic cylindrical combustion chamber (modified and adopted from Design of Liquid Propellant Rocket Engines) 182

Figure 81- Variation of contraction ratio and chamber length diameter with different throat diameters on several tests (from Modern Eng.) 183

Figure 82- Effect of L* on c* value of experimental thrust chamber. from Design of Liquid Propellant Rocket Engines 184

Figure 83-Solid-Wall-Segment Contours. Adopted from confidential NASA 383164 187

Figure 84- The shape of nozzle types from NASA-Confidential.............190

Figure 85- Sketch illustrating basic nozzle configuration and nomenclature 195

Figure 86- Variation of A t/A t with Ru/R t. from SP8120 197

Figure 87-from Carbon/Carbon Extendible Nozzles† M. Lacoste‡, A. Lacombe And P. Joyez Soci5et5e Europ5eenne De Propulsion, Bp 37, 33165 Saint Medard En Jalles, Cedex, France And R. A. Ellis, J. C. Lee And F. M. Payne Pratt & Whitney, Csd, San Jose, Ca, Usa & Aiaa........201

Figure 88- Working sketch used to derive flow angularity loss (or divergence correction factor) for a conical nozzle of half angle in attached exit flow- AIRCRAFT PROPULSION 2009 202

Figure 89- Flow pattern and pressure distribution in a linear aerospike nozzle. from AIRCRAFT PROPULSION 2009...205

Figure 90- (a), (b) From Air Propulsion System & Carbon/Carbon Extendible Nozzles† M. Lacoste‡, A. Lacombe And P. Joyez Soci5et5e Europ5eenne De Propulsion, Bp 37, 33165 Saint Medard En Jalles, Cedex, France And R. A. Ellis, J. C. Lee And F. M. Payne Pratt & Whitny, Csd, San Jose, Ca, Usa 206

Figure 91- Definition sketch of a slab in a two-phase flow in a nozzle...208

Figure 92- Variation of specific impulse with solid flow fraction in the gaseous exhaust nozzle..212

Figure 93-variation of Nozzle thrust coefficient with pressure ratio. from AIRCRADT PROPULSION 2009..215

Figure 94- Computed performance loss due to viscous-drag effects in bell nozzles (storable propellants). From SP8120..217

Figure 95- Canted-parabola contour as an approximation of optimum bell contour. From SP8120..219

Figure 96-Graphic display of region over which the mathematical-optimum method for contour design can be used. From SP 8120 220

Figure 97-Variation of theoretical nozzle divergence efficiency with area ratio and divergence half-angle. From SP 8120 221

Figure 98- Nozzle discharge coefficient as a function of Reynolds number at throat for various values of Ru/R t. from SP8120 223

Figure 99- Internal and External Expansion Process for Plug Nozzle. 225

Figure 100- Plug Nozzle Clustered Configuration 227

Figure 101- Modules Configuration in Terms of Chamber Pressure, Number of Modules, and Specific Impulse With Respect To The Vehicle Diameter. 228

Figure 102-Thrust Coefficient Variation with Plug Length and The Gap Distance 229

Figure 103- Plug Nozzle Phenomena at different Pressure Ratios, from Advanced Rocket Nozzles 230

Figure 104- Expansion-Deflection nozzle phenomena at different pressure ratios 232

Figure 105- Conical nozzle contour. From Design of Liquid Propellant Rocket Engines 233

Figure 106- The Effect of The Coefficient Factor on Efficiency for Certain $\boldsymbol{LRt}$ and Half-angle. 234

Figure 107- Thrust efficiency versus bell nozzle length. (Shown for comparison: effect of shortening conical nozzle, increasing half-angle. From Design of Liquid Propellant Rocket Engines. 235

Figure 108- Bell nozzle contour. from Design of Liquid Propellant Rocket Engines 236

Figure 109- (a)Grid points, (b) the concept of the characteristic line and the Mach line 240

Figure 110- Left, and right-running characteristics lines from point A...241

Figure 111- Continuity condition of the axial velocity 241

Figure 112- Two Common Types of Nozzle Contour Design 243

Figure 113- Designing of supersonic nozzles by characteristic s' method. (a) refers to the Gradually expanded nozzle and (b) to the minimum length nozzle. 246

Figure 114- Parabolic approximation of bell nozzle contour. From Design of Liquid Propellant Rocket Engines 247

Figure 115- θn and θe as function of expansion area ratio ϵ. From Design of Liquid Propellant Rocket Engines 248

Figure 116- Comparison of bell nozzle. From Design of Liquid Propellant Rocket Engines 249

Figure 117- E-D nozzle at low and high-altitude operation. From Design of Liquid Propellant Rocket Engines. 250

Figure 118- The Plume Physics Behind Aerospike Nozzle Altitude Compensation And Slipstream Effect By J.H.Ruf And P.K. Mcconnaughey. 251

Figure 119- Flow phenomena of a truncated conical aerospike nozzle: a) overexpansion, b) optimal expansion, and c) underexpansion. Study of Conical Aerospike Nozzles with Base-Bleed and Freestream Effects Prasanth P. Nair and Abhilash Suryan and Heuy Dong Kim. 252

Figure 120- from rocket heat transfer...254

Figure 121- wall cooling channels configuration. From rocket heat transfer 259

Figure 122- Heat transfer modes, adopted from Thermal Protection Materials: Development, Characterization and Evaluation. 262

Figure 123- Distribution of heat transfer coefficient for nozzle of Fig. 2, Ref. 2. From D.R. BARTZ 263

Figure 124- Values of the property's variation parameter $\boldsymbol{\sigma}$. From D. R. BARTZ 264

Figure 125- Thermal resistance of carbon deposit on chamber walls LO2/RP-1, mixture ratio = 2.35, (pc)ns - 1.000 psia. From Design of Liquid Propellant Rocket Engines....265

Figure 126- Regimes in transferring heat from a hot wall to a flowing liquid. From Rocket Propulsion Elements....268

Figure 127-Selected pictures of a single bubble during a growth-departure cycle inception of nucleation. Nucleate Boiling Heat Transfer Studied Under Reduced-Gravity Conditions by Dr. David F. Chao and Dr. Mohammad M. Hasan. Glenn center....271

Figure 128- Moody diagram. Tom Davis (2021). Moody Diagram (https://www.mathworks.com/matlabcentral/fileexchange/7747-moody-diagram), MATLAB Central File Exchange. Retrieved September 13, 2021....272

Figure 129- Coaxial shell thrust chamber cutaway. Note overheated and burnt-through spot on clamber wall. 274

Figure 130- (a) - (b) milled cooling channel 275

Figure 131- 5 Elongated and circular tube wall of regeneratively cooled thrust chamber. From Design of Liquid Propellant Rocket Engines....277

Figure 132- Relative position of pipes, Adopted from US5477613....279

Figure 133- Bounding fixture of pipes, Adopted from US5477613....280

Figure 134- Construction Schematic of the Pipes and Fixture, Adopted from US5477613....281

Figure 135- an overview of the construction model, Adopted from WO1995029785A1....282

Figure 136- Typical regeneratively cooled tube wall thrust chamber. From Design of Liquid Propellant Rocket Engines 283

Figure 137- Typical dump-cooled chamber fabrication methods. From Design of Liquid Propellant Rocket Engines 283

Figure 138- (a) Film cooling model, (b) Film cooling slot shapes. From N66 38728 & Large Eddy Simulation of the Film Cooling Flow System of Turbine Blades: Public Shaped Holes by SIMIRIOTIS Nikolaos............288

Figure 139- Experimental hydrogen/oxygen, film-cooled thrust chamber. From Design of Liquid Propellant Rocket Engines. 289

Figure 140- Agreement Between Equation (44) and the Data of Various References. From N6638728...291

Figure 141- (a) Multi-slot, Filmed cooled pyrolytic graphite nozzle, (b) Gaseous film cooling for standard nozzle with multi-slot cooling. From N6638728 293

Figure 142- Comparison of Cooling Techniques for Nozzles $\boldsymbol{O2H2}$ Fuel and $\boldsymbol{H2}$Coolant. From N6638728...294

Figure 143- evaporative-transpiration cooling. 295

Figure 144- Sketch of element of wall used in setting up Heat balance for transpiration cooling. Adopted from N6638728. 302

Figure 145- Comparison of transpiration cooling with convection cooling. From N6638728 304

Figure 146- (a): Model after the liquid/vapor interface has formed, (b): Flow of hot gas through a rocket nozzle with a linear at the throat. From N6638728 305

Figure 147- Nuclear Thermal Rocket Schematic. (Adopted from Moon/Mars Prospects May Hinge on Nuclear Propulsion) 308

Figure 148- Electric Propulsion Schematic Draft.......................................308

Figure 149- Electric Propulsion Systems 310

Figure 150- Schematic of Electrothermal Rocket. (Adopted from Moon/Mars Prospects May Hinge on Nuclear Propulsion) 312

Figure 151- Schematic of Ion Rocket. (Adopted from Moon/Mars Prospects May Hinge on Nuclear Propulsion) 313

Figure 152- Hall Thruster Schematic Drawing 313

Figure 153- Thrust Ranges Versus Specific Impulse in All Types of Rocket Propulsions. 314

TABLES

Table 1- Some solid propellants and binders are used in spacecraft..........77

Table 2- Physical properties of liquid oxidizers- Adopted from Liquid Rocket Propellants. 82

Table 3- Physical properties of liquid fuels- Adopted from Liquid Rocket Propellants..83

Table 4-Typical Propellant Feed Systems 93

Table 5- Experimentally mixing factors...135

Table 6- Burning rate of typical solid rocket propellants dependence on chamber pressure and initial grain temperature. Adopted from Aircraft propulsion 2009..152

Table 7- Characteristics of some solid propellants....................................153

Table 8- Summery of ballistic parameters. Adopted from Rocket Motors, Hybrid 167

Table 9- Theoretical performance of liquid rocket propellant combinations. Notes: combustion chamber pressure- 1000 psia (6895 $\boldsymbol{kNm2}$): nozzle exit pressure -14.7 psia (1 atm): optimum expansion. Adiabatic combustion and isentropic expansion of ideal gas. Specific gravity at the boiling point was used for those oxidizers or fuels that boil below 20°C at 1 atm pressure. Mixture ratios are for approximate maximum value of $\boldsymbol{Is}$...171

Table 10- General data of some storeable liquid rocket propellants (continues)..172

Table 11- General data of some storeable liquid rocket propellants 173

Table 12- General data of some cryogenic liquid rocket propellants.......174

Table 13- Physical properties of some liquid propellants. From AIRCRAFT PROPULSION 2009 177

Table 14- Heat transfer of some liquid propellants (from Aircraft Propulsion 2009) 178

Table 15- Recommended Combustion Chamber Characteristic Length (L*) for Various Propellant Combinations. from Design of Liquid Propellant Rocket Engines...185

Table 16- (continued)..191

Table 17- The Main Characteristics of the Nozzles Used in Most Liquid Rocket Engines..194

Table 18-Rocket nozzle configuration and their altitude performance. from AIRCRAFT PROPULSION 2009 204

Table 19- Wall close out coating coolants slide 12 rocket heat transfer NY slide 14. 259

Table 20- Common coolants and their properties. Adopted from thermal protection by Polezhayev Yu V & Yurevich F B. 289

Table 21- Advantages and disadvantages of various wall materials. From N66 38728..298

Table 22-Properties of some refractory materials 299

Table 23- Summary of propulsion technologies surveyed. (Adopted from NASA) 314

** The Picture of The Book Cover Refers to Apollo 4 Launches – Nov. 9, 1967:
This week in 1967, Apollo 4 launched from NASA's Kennedy Space Center. The uncrewed mission was the first "all-up" test of the three stages of the Saturn V rocket and was designed to test all aspects of the launch vehicle. Rather than traditional methods of testing rockets, "all-up" called for a rocket comprised entirely of live stages from the very first launch. NASA's Marshall Space Flight Center designed, developed, and managed the production of the Saturn V rocket that took astronauts to the Moon. Today, Marshall is developing NASA's Space Launch System, the most powerful rocket ever built, capable of sending astronauts to Mars and deeper into space than ever before. The NASA History Program is responsible for generating, disseminating, and preserving NASA's remarkable history and providing a comprehensive understanding of the institutional, cultural, social, political, economic, technological, and scientific aspects of NASA's activities in aeronautics and space. For more pictures like this one and to connect to NASA's history, visit the Marshall History Program's webpage. (Adopted from NASA[2])

** The Last Picture on the Book Cover Refers to: 04-14-2021, The Pencil Nebula Supernova Shock Wave
This supernova shock wave plows through interstellar space at over 500,000 kilometers per hour. Near the middle and moving up in this sharply detailed color composite, thin, bright, braided filaments are actually long ripples in a cosmic sheet of glowing gas seen almost edge-on. Cataloged as NGC 2736, its elongated appearance suggests its popular name, the Pencil Nebula. The Pencil Nebula is about 5 light-years long and 800 light-years away, but represents only a small part of the Vela supernova remnant. The Vela remnant itself is around 100 light-years in diameter, the expanding debris cloud of a star that was seen to explode about 11,000 years ago. Initially, the shock wave was moving at millions of kilometers per hour but has slowed considerably, sweeping up surrounding interstellar material. In the featured narrow-band, wide field image, red and blue colors track, primarily, the characteristic glows of ionized hydrogen and oxygen atoms, respectively. (Adopted from NASA[3], Image Credit & Copyright: Greg Turgeon & Utkarsh Mishra)

[2,3] Source: www.nasa.gov/multimedia/imagegallery/

ROCKETS AND SUPERSONIC PROPULSION

INTRODUCTION

Chemical rockets are a redundant type of turbine engine of ambient air that carry the fuel and oxidant needed in the combustion chamber. Compared to jet engines, which are air-breathing and require a separate air intake as the first part of the engine, Chemical rockets do not have a separate air intake and are therefore also referred to as non-air breathing systems. As a result, these systems are said to be better candidates for space propulsion in terms of production cost and efficiency. These rockets, in which the primary energy source is embedded and have minimal dependence on the environment, are a type of reaction engine. Reaction engines are a group of engines that use both the fuel embedded in the flying object body and the environment to supply its energy. So that the output flow from the engine output is called the jet flow and the resulting force is called its propulsive force. It should be noted that the mode of operation is such that the fuel and oxidizer, each of which can be embedded in different phases inside the rocket, undergo phase change as they enter the combustion chamber and after performing complex chemical reactions that take place inside the combustion chamber, hot gases will be released through the exhaust nozzle in the form of a jet at a very high speed, which will produce a thrust force. The role of the nozzle in this type of system is to direct the flow and convert chemical energy from combustion into kinetic energy that will lead to the production of thrust.

All these phenomena stem from Newton's third law of motion, which states that for every action, there is an equal reaction in the opposite direction. This is the basis of the work of missiles, i.e., the production thrust, is the reaction of the forces applied to the body of the engine chamber (which is the result of the pressure difference inside the chamber) in the direction of the exhaust gases. To clarify this, we can refer to the force exerted by the flow of water inside the hose or gun recoil when firing.

Chemical rockets can be divided into several categories based on the states of fuel and oxidant used in it, so that the propellant (propellant refers to the set of fuel and oxidizer in the engine) to liquid propellants, solid propellants and gas propellants will be categorized and if the fuel is in solid and oxidizing state is also in liquid state, it will be hybrid propulsion. Engines whose primary energy is derived from electrical, beamed, solar, cold gas, or nuclear energy fall into the category of thermal non-chemical engines. For example, the space shuttle consists of two solid boosters called Solid Rocket Booster (SRB's) for the moment it takes off from the ground and accelerates to orbit, and three rocket engines with liquid propellant in its orbiter, which are called the space shuttle main engines (SSME). In liquid propellant rockets, the fuel and oxidizer are stored in separate tanks in the liquid state, while solid propellant rockets contain a combination of solid fuel and oxidizer. In contrast to chemical rockets, which consume a lot of fuel to generate thrust, which in turn entails high costs, there are systems with electric propulsion. As the name implies, these systems use solar cells or nuclear reactors to generate propulsion, which reduces and eliminates many of the limitations posed by propellants transport. These energies are used to ionize neutral gases (noble gases) such as xenon and krypton, and as a result these ions are accelerated by an electromagnetic field (Hall effect thruster) or electrostatic field (Gridded ion) and thrown out which in turn provides high speed for the spacecraft. Typically, electric rockets can be categorized into six divisions concerning their method of generating thrust: 1- Hall effects Electrostatic Thrusters, 2- Ion Electrostatic Thruster, 3-Arc-Jet Electrothermal Thrusters, 4- Resistojet Electrothermal Thrusters, 5-Magneto-Plasma Dynamic (MPD) Electromagnetic Thrusters, and 6- Cold Gas Expansion Thrusters. In these electric rockets, unlike chemical rockets, which have a fire tail at their output, in the electric type, a bright green-blue tail will be created behind the rocket. However, for atmospheric applications that include very strict pollution standards, only the use of chemical rockets with solid and liquid propellants is appropriate and permitted. Solar rockets are categorized into solar sail and solar-heated rocket types. On the other hand, nuclear rockets also can be divided into nuclear fission, nuclear fusion, and photon rockets types. It should be noted that air-breathing systems like ramjets, scramjets, and turbojet engines also can be used in some cases combined with chemical rocket engines. Utilizing scramjet engines in solid rocket boosters is the biggest application of air-breathing engines in the rocketry approach.

Liquid propellant rockets may be classified as monopropellant, bipropellant, or tripropellant which the third one is not used yet due to the presenting of many developmental problems. In a monopropellant rocket, a propellant (e.g., hydrazine) is passed through a catalyst to promote a decomposition reaction to generate favorable thrust. On the other hand, a bipropellant rocket burns propellants after both fuel and oxidizer are injected through the injector plate. In a tripropellant rocket, three different species, such as hydrogen, oxygen, and beryllium, are mixed in the combustion chamber and are burned together.

As mentioned earlier, rockets can be classified based on their propulsion system. The tree table below provides an overview of the rocket category.

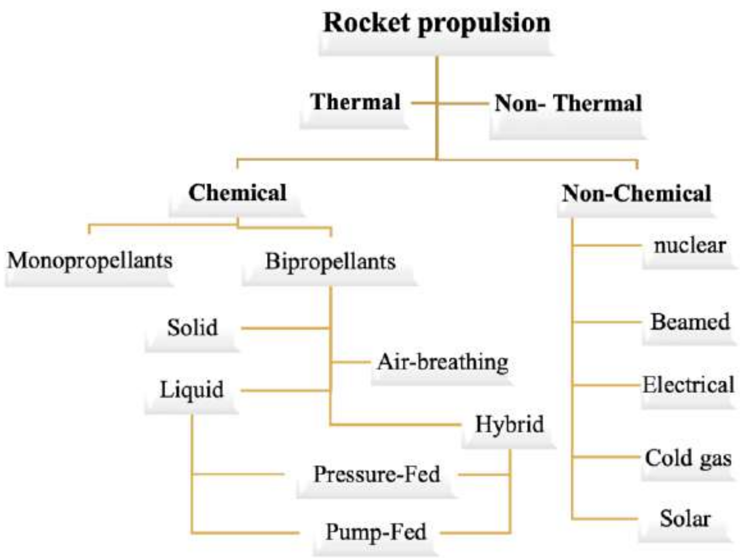

Figure 1- Rockets classification

THRUST

Thrust is generally defined as the force that moves a flying object and is measured in Newtons, pounds, or kilograms. This force is physically the result of a pressure difference in the combustion chamber wall. The pressure inside the combustion chamber is distributed asymmetrically so that it changes slightly in the vicinity of the nozzle. High temperatures and pressures in the combustion chamber are possible as a result of the use of very high energy and low molecular weight fuels. Also, as we will see in the thrust relation, the maximum thrust will be obtained when the nozzle outlet pressure equals its ambient pressure (atmospheric pressure). And the solution to achieve this is to adjust the ratio of sections or expansion in the nozzle, which is defined as the ratio of the output cross-section of the nozzle to the cross-sectional area of its throat.
The thrust relation can be obtained by combining the two laws of conservation of mass and momentum. A linear momentum is a product of its velocity and mass:

$$P = mv \tag{1}$$

According to Newton's second law, the effect of a force applied to any particle will be seen as a change in the linear momentum of that particle. that's mean:

$$F = ma = \frac{dP}{dt} \tag{2}$$

If the particle is not affected by an external force, then its linear momentum changes will also be zero, which is called the linear momentum conservation law.

This law applies to a rocket moving in a vacuum without being influenced by any external force. Consider a rocket at two moments t and $t + \Delta t$. Initially, the mass of the rocket is M, which is moving at a speed v relative to the stationary observer, and at the next Δt second, the mass ΔM is observed at a speed u in the direction of the rocket moving by the stationary observer and at this time, the rocket with mass $M - \Delta M$ is moving at a speed of $v + \Delta v$. The linear momentum conservation equation for a rocket with the above conditions is written as follows:

$$F = \frac{\Delta P}{\Delta t} = \frac{P_2 - P_1}{(t+\Delta t) - t} = \frac{[(n-\Delta M)(v+\Delta v) + \Delta M u] - Mv}{\Delta t} = 0 \tag{3}$$

By simplifying and limiting the above relation, when Δt tends to zero:

$$M\frac{dv}{dt} = \left(u - (v + \Delta v)\right)\left(\frac{dM}{dt}\right) = v_{rel}\left(\frac{dM}{dt}\right) \tag{4}$$

The right term is related to the characteristics of the rocket, and the left term, due to its unit, is made of force, which is called thrust which states that scientists and designers can maximize the thrust force by changing and enlarging the output mass flow rate $\left(\frac{dM}{dt}\right)$ and the maximum relative velocity.

The thrust force of a turbojet operating in atmospheric condition will be as follows:

$$F = (\dot{m}_a + \dot{m}_f)v_e - \dot{m}_a v_i + (P_e - P_a)A_e \tag{5}$$

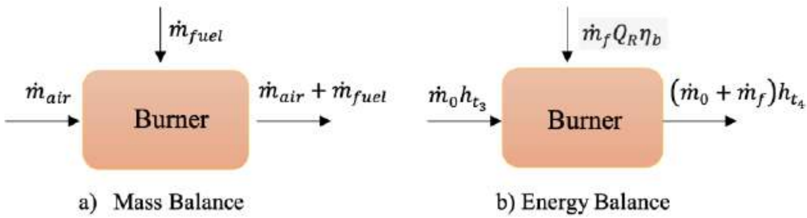

Figure 2- Mass and Energy Balances

Since there is no Ram drag due to air intake in chemical rockets, the thrust equation is written as follows:

$$F = (\dot{m}_a + \dot{m}_f)v_e + (P_e - P_a)A_e \tag{6}$$

$$q = \dot{m}_a + \dot{m}_f \tag{7}$$

$$F = qv_e + (p_e - p_a)A_e \tag{8}$$

Where q is the mass flow rate of the passing fluid, v_e is the exhaust gas velocity, p_e and p_a are the gas pressure at the nozzle outlet and the atmospheric pressure of the outside air respectively, and A_e is the nozzle outlet area.

The term qv_e that we previously represented with $v_{rel}\frac{dM}{dt}$ is the same as thrust or momentum and the force expression $(p_e - p_a)A_e$ that results from the pressure difference is called the **compressive thrust** which states that the closer the outlet pressure in the nozzle is to the ambient pressure, the more thrust is generated.

The resulting thrust relation can be simplified by defining a new parameter as follows:

$$C = v_e + \frac{(p_e - p_a)}{q}A_e \tag{9}$$

C in this equation is Effective exhaust gas velocity, which depends more than anything on the type of propulsion. Therefore:

$$F = qC \tag{10}$$

One of the performance disadvantages of rocket engines compared to turbojets in atmospheric conditions is the very high fuel consumption per produced thrust. A parameter called **Specific impulse** is defined to compare the performance and merits of rockets compared to turbojets.

Since the production of thrust with the lowest amount of fuel consumption is a parameter for evaluating engine efficiency, for an air-breathing engine, the ratio of fuel flow rate to the production of thrust is called **thrust specific fuel consumption (TSFC)**. Accordingly, the lower the thrust specific fuel consumption, the greater the efficiency of the system. In the case of rockets, contrary to what exists in air breathing, oxidizer and fuel will be used together to generate thrust in the engine, and it is common for the design parameter in rockets to be defined as a ratio of generated thrust to propulsion weight. that's mean:

$$I_s = \frac{F}{\dot{m}_p g_0} \qquad \text{(For Rockets).} \tag{11}$$

$$\dot{m}_p = \dot{m}_f + \dot{m}_{ox} \tag{12}$$

$$I_s = \frac{F}{\dot{m}_f g_0} \quad \text{(For Air breathing engines).} \tag{13}$$

When the thrust and mass flow rate remain constant during propellant combustion the specific impulse indicates that the thrust produced by the rocket engine is equal to the weight of the propellant consumed.

The denominator of the fraction in equations (11) and (13) is different for rockets and air-breathing systems, but due to their units, which are the same in both SI (i.e., $[N/(kg/s)] or [m/s]$) and US (i.e., $[Pound\,(force)/Pound\ per\ second]\, or\ [s]$) units, it is a suitable criterion for comparing the generated thrusts by both of systems. It should be noted that using higher energy fuels such as hydrogen than hydrocarbons cause fuel consumption to be reduced by approximately 2.5 times to reach the same temperatures in the combustion chamber. Since we do not have a Ram drag in the thrust equation for rockets, so the air inlet velocity is zero. Therefore, the thrust is not dependent on Mach number. If the ratio of the specific impulse to Mach number for rockets and air-breathing engines are plotted for hydrogen and hydrocarbon fuel, then it is observed that rockets have a much lower specific impulse than air-breathing systems and are also independent of Mach number.

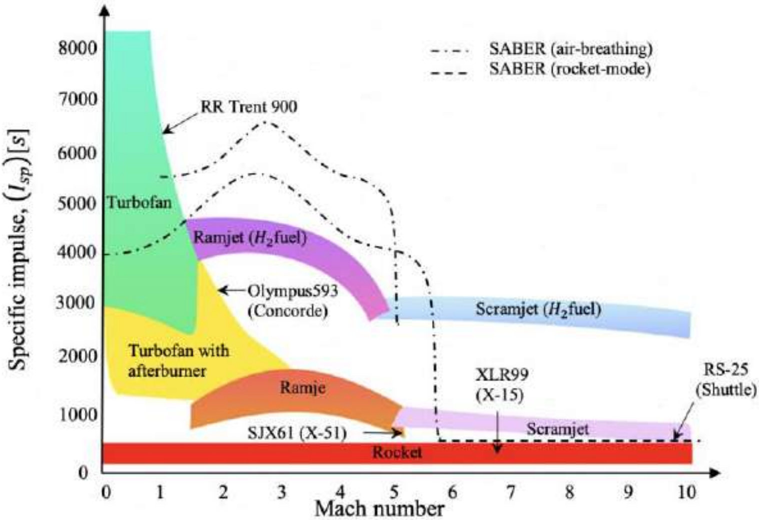

Figure 3- Dependence of specific impulse and Mach number in different types of propulsion. Adopted from AIAA 2017-2343

The specific impulse equation also demonstrates that in a vacuum, as more thrust is generated, the amount of specific impulse will increase, i.e., as the ambient pressure increases, its magnitude decreases in proportion to the pressure.
For example, the Russian Energia missile, which has four combustion chambers (RD-170 engine) that use hydrocarbon (RP-1) as a fuel with the liquid oxygen (LOX) as its oxidizer. The generated thrust of this engine is 29 meganewtons at sea level and 32 meganewtons at vacuum, which makes this engine one of the most powerful engines. Also, the specific impact of this engine at sea level and vacuum is 309 and 337 seconds, respectively. Another example of such a powerful Russian engine is the RD-180 engine, which is used in the Atlas V rocket and has almost a specific impulse and generated thrust equal to the previous engine.
As another example, the space shuttle originally mentioned consists of two rockets(boosters) with solid propellants (combined propellants of ammonium perchlorate as oxidizer and aluminum as fuel) (APCP) and a tank carrying liquid propellants (with liquid hydrogen fuel and oxygen as its oxidizer) which is responsible for refueling three RS-25 engines (SSME) and also maneuvering motors on the orbiter. At the time of lifting off, two solid-propelled rockets (SRB's) start with three orbital engines. Solid rocket boosters were detached from the rocket before it reached orbit, and the liquid propellant tank was disconnected jettisoned from the body of the orbiter with maneuvering when it's reached orbit. At the end of the mission, the orbiter war used the built-in fuel to return to the Earth or even to continue the mission for longer distances. Each of the space shuttle engines (RS-25) has a thrust capacity of 1.86 MN and 2.279 MN (at sea level and vacuum, respectively), which is smaller than RD-180 but also has a higher specific impact (366 and 452.3 seconds at sea level and vacuum, respectively) compared to the Russian engines. In the following sections, the space shuttle performance will be further explained.
To reach the low earth orbit (LEO), the Mach number must be approximately equal to or greater than 24 because a centrifugal force is applied to each particle. For as much as the radius of the earth is about 6371 km and by assuming that the lowest orbit of the earth is at an altitude of 100 km above the earth, it is easily proved that the speed required to maintain balance in rotation around the earth is about 24 times the speed of sound at that height. That is:

$$m\frac{v^2}{r} = mg_0 \tag{14}$$

Therefore:

$$v = \sqrt{rg_0} = \sqrt{6371 \times 9.8} = 7901.6\,\frac{m}{s}$$

Of course, it should be noted that in these calculations, several simplifying assumptions have been used, such as approximation of the average radius of the earth, ignoring atmospheric drag and, the reduction of gravity acceleration at an altitude of 100 km. According to the minimum Mach number obtained and the data in figure 3, if we want to use air-breathing engines in the atmospheric range instead of chemical rockets for space applications, we must first use a turbofan with a bypass coefficient variable by Mach number, qua by reaching $Mach$ 3, the bypass factor is reduced to such an extent until it acts like a turbojet engine. Then we should be able to turn off all the gas generators and activate the RAM jet until the Mach number reaches a little more than 6. At this point we must use the scram jet to reach $Mach$ 9 to 17 depending on whether hydrogen or hydrocarbons are used as fuel. However, we are still a long way from the minimum Mach number required to reach LEO. Therefore, chemical rockets should be turned on as the last step to reach $Mach$ 24 and LEO. The complexity of placing these air breathing systems in a set and changing the type of engine at each step has made these systems inefficient for space applications.

CHEMICAL ROCKET

Chemical rockets are known as rockets that provide all the required energy to accelerate and generate thrust from their propulsion (i.e., the combustion of a fuel-oxidizer combination). This type of rockets categorized into three main models, namely Liquid propellant rocket, Solid propellant rocket, and Hybrid propellant rocket. The fuel and oxidizer in liquid rockets are stored in separate thin-walled tanks at low pressure and sprayed into the chamber by injectors through turbine-driven pumps to result in high-pressure combustion. In solid propellant rockets, grains, which are pre-mixed fuel and oxidizer compounds, are embedded in the combustion chamber and start burning as soon as sufficiently heated. It should be noted that the combustion process, in this case, depends on several factors such as pressure and temperature inside the combustion chamber, and the geometry of the burning surface. All of these will be explained further in detail below. Chemical rockets are made up of different parts, which are shown schematically in the following figure:

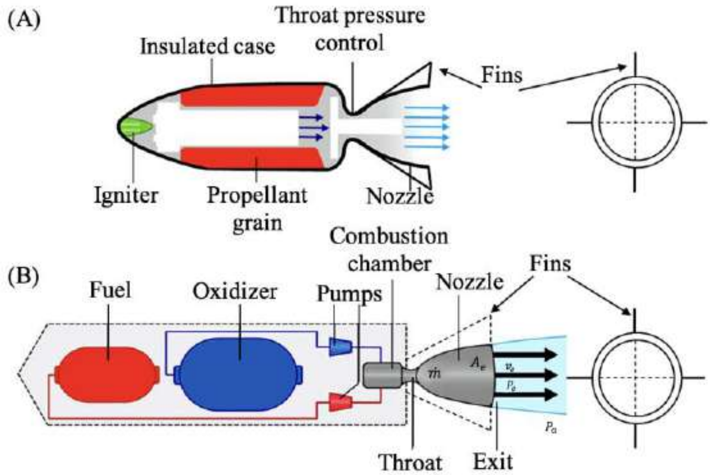

Figure 4- Elements of Solid and Liquid Rocket Propulsion-Ahmed F.EL

As shown in Figure 4-b, in a chemical rocket with liquid propellants, fuel and oxidizer are stored in separate tanks. The fuel and oxidizer enter the injector plate by two separate pumps and then are injected into the combustion chamber through the injectors that combustion takes place there. The combustion chamber pressure is about 20% less than the pressure of the injectors to prevent chugging. The reaction of fuel and oxidizer increases the temperature and pressure of the combustion chamber and then the combustion products are accelerated by the outlet nozzle. Fuel and oxidizer pumps can be used to control the output thrust. The guidance, navigation, and control system in front of the rocket is shown in the figure. The fins play a role in controlling the aerodynamics and stability of the rocket. The guidance, navigation and control systems are located at the tip of the rocket, although some of these systems can be used in other locations. The fins that play the role of aerodynamic control and rocket stability are also part of these systems are shown in the figure 4 (although in some cases the fins are also used in the middle parts of the rocket).
The solid rocket engine is shown in section (a) in figure 4. Solid propellants, which are a combination of solid fuel and oxidant, are embedded in a rocket chamber, also called a grain or charge. The way of housing this propellant is that inside the rocket chamber, which is full of grains, there is a hollow cylindrical space with the center of igniter that is placed at the top of this hypothetical cylinder. When ignition starts, the grains start to burn and accelerate through the nozzle, which will eventually generate thrust. The way of housing of grains is effective on the generated thrust over the time. The

effect of grain design on the trust-time curve is shown in the figure below. It should be noted that in this type of rocket it is not possible to control the output trust and the reason is due to its structure and the lack of pumps to control the flow of propulsion. The only action that can be taken is to extinguish the igniter and separate the rockets from the main body of the rocket, which is done with a few maneuvers.
Chemical rockets, apart from their consuming propellant type, always have complexities such as propulsion supply and feed system, a combustion chamber, and an exhaust nozzle. Some of the simplifying assumptions used in analyzing the combustion chamber and nozzle are as follows: (from Mechanics and thermodynamics of propulsion)

1. The working fluid is perfect gas of constant composition.
2. The chemical reaction is equivalent to a constant pressure heating process.
3. Expansion process is a steady, one dimensional, and isentropic.

Thrust chamber T-S diagram can be plotted according to this assumption as in figure 5. Propellants enter the thrust chamber at state (1), and there the heat (Q_R) which is the heat value of the propellant combination per unit mass will be added where the combustion initiated (state (2)). Combustion products pass through the throat where isentropic expansion happening at the unity Mach, and thereafter these gases are exhausted at velocity V_e through the nozzle.

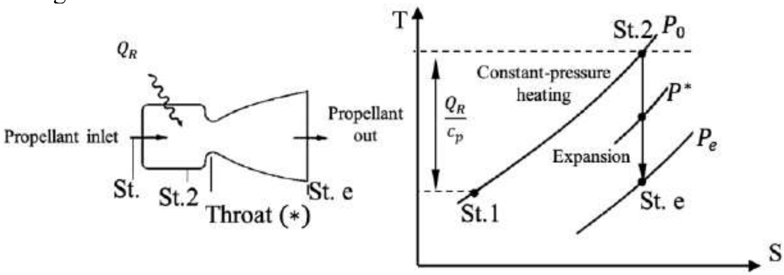

Figure 5- simple chemical rocket thrust chamber and T-S diagram (from Mechanics and Thermodynamics of Propulsions)

ORBITAL MECHANICS

One of the influential factors on the engine performance is the path of the vehicle in the space expedition. In this section, we will give a straightforward explanation of the mechanics of orbitals and the circumstances required to get out of the earth's gravity and orbital maneuvering. In general, two basic forces are effectively applied to the fuselage of the moving rocket, which the design of the rocket is highly dependent on there's magnitude and control:

1. Drag Force
2. Gravitational Force

The focus of this section is on gravitational force and how it affects the rocket.

To further simplify, consider the solar system, where each planet swivels in separate orbits at different speeds by the gravitational attraction of the sun. To further simplify, consider the solar system, where each planet swivels in separate orbits at different speeds by the gravitational attraction of the sun: The force exerted on a rocket or satellite during this orbital displacement is due only to the reaction between the earth's gravity and the vehicle, whereas this is the process of transferring the interaction between the sun and the vehicle. It should be noted that the extinguished vehicle is located on an aircraft to which gravity is applied. Figure 6 present the Cartesian coordinate system for such a case; Which includes a rigid inertial frame of reference at the center of the planet (Earth) and a moving frame of reference (xyz) which is rigidly attached to the airplane. According to Newton's law of gravitation, the attraction force on a body of mass m located at a distance r from the mass m' is given by the following equation, where a negative sign denotes that a force pertains to the body m in the opposite direction r :

$$F_r = -G\frac{m.m\prime}{r^2} \quad (15)$$

Where the term G is the universal constant of gravity $(6.670 \times 10^{-11}\, N.M^2/Kg)$.

The force impulse, which is a set of forces applied in the time period t_1 to t_2, is defined as follows:

$$I = \int_{t_1}^{t_2} F dt \quad (16)$$

Expressing force as a time derivative, the above definition for a constant mass is:

$$I = \int_{t_1}^{t_2} \frac{m\, dv}{dt} dt = mv_2 - mv_1 = m\,\Delta v \quad (17)$$

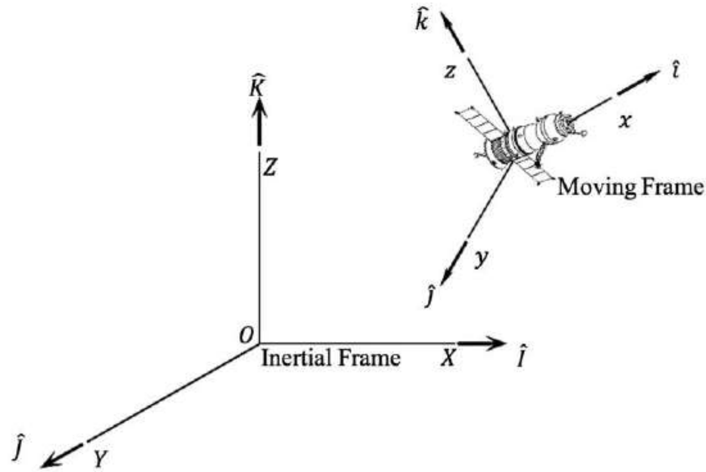

Figure 6- Cartesian coordinate system for a rigid moving object

Where the obtained term is called linear momentum. Assuming the force in Equation 16 to be constant, Equation 17 is rewritten as follows:

$$\Delta v = \frac{F_{net}}{m}\Delta t \tag{18}$$

Another important concept to recall is the angular momentum, the value of which, for a constant force about a fixed origin, is:

$$M_{O_{net}} = r \times F_{net} \tag{19}$$

By simplifying the above equation:

$$M_{O_{net}} = r \times F_{net} = r \times m\frac{dv}{dt} = \frac{d}{dt}(r \times mv) - \left(\frac{dr}{dt} \times mv\right) =$$

$$\frac{d}{dt}(r \times mv) - (v \times mv) \xrightarrow{v\times mv = m(v\times v) = 0} M_{O_{net}} = \frac{d}{dt}(r \times mv)$$

(20)

Therefore, the angular momentum can be obtained by

$$H_O = r \times mv \tag{21}$$

For the relative case, the angular momentum of the object m_2 with respect to m_1 is the same as that of the object m_2 relative to the linear momentum m_2, i.e.:

$$H_{2/1} = r \times m_2\dot{r} \tag{22}$$

Where $v = \dot{r}$ is the velocity of the m_2 body in respect to the m_1. Defining the specific angular momentum per the mass, results in:

$$h = r \times \dot{r} \qquad [km^2 s^{-1}] \tag{23}$$

To examine the temporal variations of h, we take the time derivative of the above expression:

$$\frac{dh}{dt} = \dot{r} \times \dot{r} + r \times \ddot{r} \tag{24}$$

Consider two bodies m_1 and m_2 that do not apply gravitational force to each other in the non-rotational inertial frame. The position vector of the center of mass of system G as well as its absolute velocity and acceleration relative to the inertial frame reference can be calculated from the following equation:

$$R_G = \frac{m_1 R_1 + m_2 R_2}{m_1 + m_2} \tag{25}$$

$$V_G = \ddot{R}_G = \frac{m_1 \dot{R}_1 + m_2 \dot{R}_2}{m_1 + m_2} \tag{26}$$

$$a_G = \ddot{R}_G = \frac{m_1 \ddot{R}_1 + m_2 \ddot{R}_2}{m_1 + m_2} \tag{27}$$

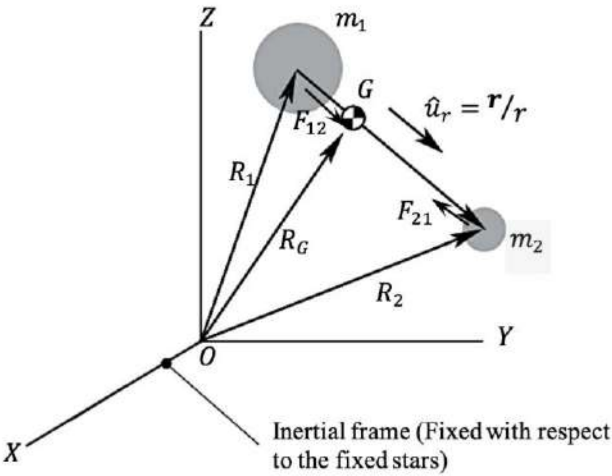

Figure 7- Free-body diagram of two masses located in an inertial frame. (Adopted from Orbital Mechanics for Students)

Consider the position vector m_2 relative to m_1 as follows:

$$\boldsymbol{r} = R_2 - R_1 \tag{28}$$

By defining a unit vector pointing from m_1 toward m_2,i.e.,

$$\hat{u}_r = \frac{\boldsymbol{r}}{r} = \frac{\boldsymbol{r}}{\|\boldsymbol{r}\|} \tag{29}$$

Given to Newtons gravitational law, the force exerted on m_2 by m_1 in term of the unit vector which is implying that the attractions act along the line connecting the center of two bodies, can be calculated by:

$$F_{21} = \frac{Gm_1m_2}{r^2}(-\hat{u}_r) = -\frac{Gm_1m_2}{r^2}\hat{u}_r \tag{30}$$

Given to the Newton's second law and by the same procedure as m_2, for the m_1:

$$-\frac{Gm_1m_2}{r^2}\hat{u}_r = m_2\ddot{R}_2 \tag{31}$$

$$-\frac{Gm_1m_2}{r^2}\hat{u}_r = m_1\ddot{R}_1 \tag{32}$$

Summiting each side of above equations, and then considering the equation 27, it concluded that the acceleration of the center of the mass G of the system of two bodies m_1 and m_2 is zero. In other words, the center of the mass moves along the straight line with a constant velocity of v_G. The position vector about to the inertial frame of reference (XYZ) is as follows, where R_{G0} is the position of the center of the mass at $t = 0$.

$$R_G = R_{G0} + v_G t \tag{33}$$

Given that the gradient of the potential energy is mean to it force, namely

$$F = -\nabla V \tag{34}$$

Where,

$$\nabla = \frac{\partial}{\partial x}\hat{\imath} + \frac{\partial}{\partial y}\hat{\jmath} + \frac{\partial}{\partial z}\hat{k} \tag{35}$$

Therefore, the potential energy due to the gravitational attraction between bodies of m_1 and m_2 is

$$V = -\frac{Gm_1m_2}{\boldsymbol{r}} \tag{36}$$

Multiplying the equation 31 by m_1 and equation 32 by m_2, result in:

$$-\frac{G{m_1}^2m_2}{r^2}\hat{u}_r = m_1m_2\ddot{R}_2 \tag{37}$$

$$-\frac{Gm_1m_2{}^2}{r^2}\hat{u}_r = m_1m_2\ddot{R}_1 \tag{38}$$

By subtracting the equations from each other and simplifying, as well as according to Equations 28 and 29, the result is:

$$\ddot{r} = -\frac{G(m_1+m_2)}{r^2}\hat{u}_r = -\frac{G(m_1+m_2)}{r^3}\boldsymbol{r} \tag{39}$$

By defining the gravitational parameter μ, the above relation is rewritten as:

$$\ddot{r} = -\frac{\mu}{r^3}\boldsymbol{r} \tag{40}$$

Where,

$$\mu = G(m_1 + m_2) \tag{41}$$

This second-order differential equation (Eq. 40) examines the motion of the object m_2 relative to m_1.
Now back to Equation 24 and start simplifying it. Given that the cross product of a vector on itself is zero, that is:

$$\frac{dh}{dt} = \dot{r} \times \dot{r} + r \times \ddot{r} = r \times \ddot{r} \tag{42}$$

According to Equation 40, the final value of the angular momentum changes is obtained:

$$\frac{dh}{dt} = \boldsymbol{r} \times -\frac{\mu}{r^3}\boldsymbol{r} = -\frac{\mu}{r^3}(\boldsymbol{r} \times \boldsymbol{r}) = 0 \tag{43}$$

The result shows that at any given time the position and velocity vectors are on the same plane and their cross product is a unit vector perpendicular to that plane, i.e.,

$$\hat{h} = \frac{\boldsymbol{h}}{\|h\|} = \boldsymbol{r} \times \dot{\boldsymbol{r}} \tag{44}$$

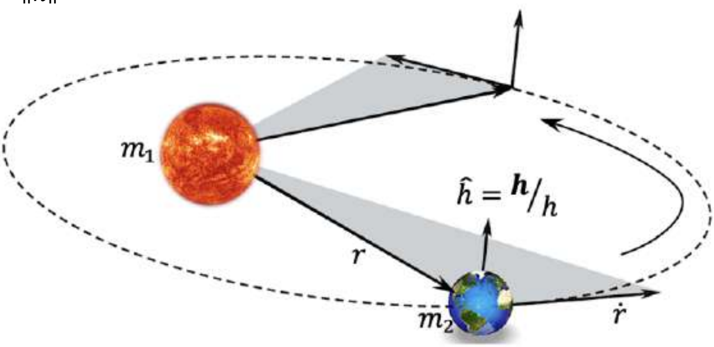

Figure 8- The path of m_2 around m_1 with its characteristics

Consider the orbit on which the object m_2 is located (Figure 8). Decomposing the relative velocity component in the direction and perpendicular to the r direction, turns it to the radial and azimuthal velocity vector units, respectively. Again, by establishing equation 23 in terms of decomposed relative velocities:

$$\boldsymbol{h} = r\hat{u}_r \times (v_r\hat{u}_r + v_\perp\hat{u}_\perp) = rv_\perp\widehat{\boldsymbol{h}} \tag{45}$$

Which means

$$h = rv_\perp \tag{46}$$

It is clear that angular momentum depends only on the vertical component (Azimuthal) of relative velocity.

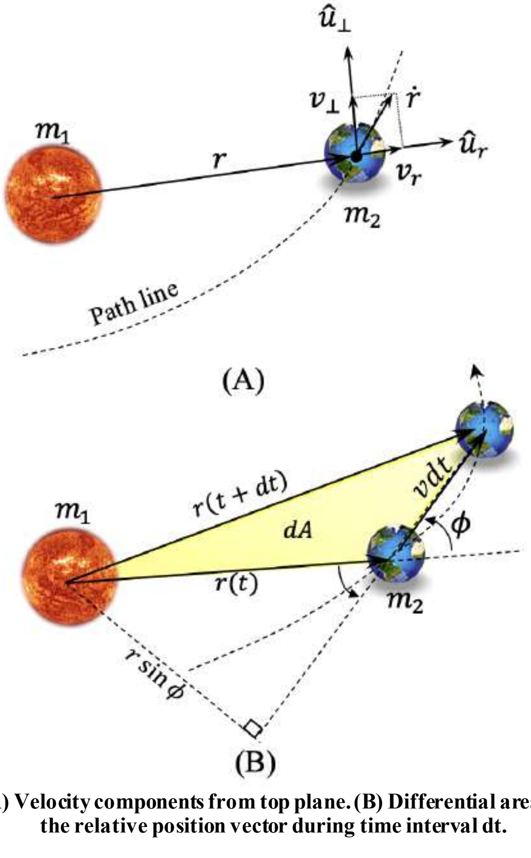

Figure 9- (A) Velocity components from top plane. (B) Differential area swept out by the relative position vector during time interval dt.

During the time interval dt, the position vector r sweeps the area dA (Fig. 9- B), which this triangular swept area can be attained by:

$$dA = \frac{1}{2} \times r \sin\phi \times vdt = \frac{1}{2} \times r(v \sin\phi)dt = \frac{1}{2} r v_{\perp} dt \qquad (47)$$

Combining Equations 46 and 47, resulting in:

$$\frac{dA}{dt} = \frac{h}{2} \qquad (48)$$

where the left term of this equation is called the areal velocity. This equation, which represents Kepler's (1571-1630) second law, states that at equal times, equal areas are swept out.

Let's take the cross product from each side of equation 40 with the specific angular momentum (**h**):

$$\ddot{\boldsymbol{r}} \times \boldsymbol{h} = -\frac{\mu}{r^3} \boldsymbol{r} \times \boldsymbol{h} \qquad (49)$$

Given that:

$$\frac{d}{dt}(\dot{\boldsymbol{r}} \times \boldsymbol{h}) = \ddot{\boldsymbol{r}} \times \boldsymbol{h} + \dot{\boldsymbol{r}} \times \dot{\boldsymbol{h}} \qquad (50)$$

So, by knowing that the variation of the specific angular momentum is zero (i.e., $\frac{d}{dt}\boldsymbol{h} = \dot{\boldsymbol{h}} = 0$), hence:

$$\frac{d}{dt}(\dot{\boldsymbol{r}} \times \boldsymbol{h}) = \ddot{\boldsymbol{r}} \times \boldsymbol{h} \qquad (51)$$

For the right-hand side of Equation 49 with respect to Equation 23 ‹the solving procedure is as follows:

$$\frac{1}{r^3} \boldsymbol{r} \times \boldsymbol{h} = \frac{1}{r^3} [\boldsymbol{r} \times (\boldsymbol{r} \times \dot{\boldsymbol{r}})] = \frac{1}{r^3} [\boldsymbol{r}(\boldsymbol{r}.\dot{\boldsymbol{r}}) - \dot{\boldsymbol{r}}(\boldsymbol{r}.\boldsymbol{r})] =$$

$$\frac{1}{r^3} [\boldsymbol{r}(r\dot{r}) - \dot{\boldsymbol{r}} r^2] = \frac{\boldsymbol{r}\dot{r} - \dot{\boldsymbol{r}} r}{r^2} \qquad (52)$$

On the other hand:

$$\frac{d}{dt}\left(\frac{\boldsymbol{r}}{r}\right) = \frac{r\dot{\boldsymbol{r}} - \boldsymbol{r}\dot{r}}{r^2} = -\frac{\boldsymbol{r}\dot{r} - r\dot{\boldsymbol{r}}}{r^2} \qquad (53)$$

Therefore

$$\frac{1}{r^3} \boldsymbol{r} \times \boldsymbol{h} = -\frac{d}{dt}\left(\frac{\boldsymbol{r}}{r}\right) \qquad (54)$$

Substituting equations 51 and 54 in 49, result in:

$$\frac{d}{dt}(\dot{\boldsymbol{r}} \times \boldsymbol{h}) = \frac{d}{dt}\left(\frac{\mu \boldsymbol{r}}{r}\right) \qquad (55\text{-}1)$$

Or

$$\frac{d}{dt}\left(\dot{\boldsymbol{r}} \times \boldsymbol{h} - \frac{\mu r}{r}\right) = 0 \tag{55-2}$$

From the above relation, it can be concluded that the expression in parentheses is a constant value, i.e.,

$$\dot{\boldsymbol{r}} \times \boldsymbol{h} - \frac{\mu \boldsymbol{r}}{r} = C \tag{56}$$

Where C is a constant value in units of μ.

Taking dot product from both sides of the above equation with the specific angular momentum:

$$(\dot{\boldsymbol{r}} \times \boldsymbol{h}).\boldsymbol{h} - \mu\frac{\boldsymbol{r}.\boldsymbol{h}}{r} = C.\boldsymbol{h} \tag{57}$$

Since the product of $(\dot{\boldsymbol{r}} \times \boldsymbol{h})$ is a vector perpendicular to both $\dot{\boldsymbol{r}}$ and h, according to the rules of interior product, the product of the first term on the left-hand side is zero. Given the definition of the specific angular momentum ($h = r \times \dot{r}$), the product of $\boldsymbol{r}.\boldsymbol{h}$ is also perpendicular to $\boldsymbol{r}$ and will be zero, which means that C and $\boldsymbol{h}$ are orthogonal. Therefore, since according to Equation 44, $\boldsymbol{h}$ is perpendicular to the orbital plane, C must be on the orbital plane.

Dividing the sides of Equation 56 by μ:

$$\frac{\boldsymbol{r}}{r} + e = \frac{\dot{\boldsymbol{r}} \times \boldsymbol{h}}{\mu} \tag{58}$$

Where,

$$e = \frac{C}{\mu} \tag{59}$$

e is a dimensionless vector, which is called the eccentric vector, and the line that defines this vector is called the apse line. To obtain the scalar form of Equation 58, taking the dot product of both sides of it with $\boldsymbol{r}$.

$$\frac{\boldsymbol{r}.\boldsymbol{r}}{r} + \boldsymbol{r}.e = \frac{\boldsymbol{r}.(\dot{\boldsymbol{r}} \times \boldsymbol{h})}{\mu}$$

$$\xRightarrow{intercheng\ of\ the\ dot\ and\ cross\ rule} = \frac{(\boldsymbol{r} \times \dot{\boldsymbol{r}}).\boldsymbol{h})}{\mu} = \frac{\boldsymbol{h}.\boldsymbol{h}}{\mu} \tag{60}$$

Therefore

$$r + \boldsymbol{r}.e = \frac{h^2}{\mu} \tag{61}$$

The result demonstrate that track of the variable time has been lost from the equation because h is constant. From the definition of dot product for the left-hand side phrase:

$$r + re\cos\theta = \frac{h^2}{\mu} \Longrightarrow r = \frac{h^2}{\mu}\frac{1}{1+ e\cos\theta} \tag{62}$$

Where, e, μ ,and h are all constants. This expression is the orbit equation and presents the path of the object m_2 around m_1 and relative to it. The form of the equation represents the orbital equation of conic sections. For $e \geq 0$, this expression refers to Kepler's first law, which declares that planets revolve in elliptical orbits around the sun.
Radial and vertical velocities can also be calculated. To determine the azimuth velocity, which is expressed as angular velocity, Equation 46 and the definition of angular velocity are used:

$$\begin{cases} v_\perp = r\dot{\theta} \\ h = rv_\perp \end{cases} \longrightarrow h = r^2\dot{\theta} \tag{63}$$

According to Equations 46 and 62, the value of $v_\perp$ is obtained:

$$v_\perp = \frac{h}{r} = \frac{\mu}{h}(1 + e\cos\theta) \tag{64}$$

According to the definition of radial velocity, by taking the derivative of Equation 62, the result is:

$$v_r = \frac{dr}{dt} = \frac{h^2}{\mu}\left[-\frac{e(-\dot{\theta}\sin\theta)}{(1+e\cos\theta)^2}\right] = \frac{h^2}{\mu}\frac{e\sin\theta}{(1+e\cos\theta)^2}\frac{h}{r^2} \tag{65}$$

Where,

$$\dot{\theta} = \frac{h}{r^2} \tag{66}$$

By simplifying the above relation (Eq. 65) by Equation 63:

$$v_r = \frac{\mu}{h}e\sin\theta \tag{67}$$

Figure 10 shows that as θ decreases, the distance r will also decrease (unless $e = 0$, in which case the distance m_1 and m_2 will be constant). The point where the two objects are closest to each other corresponds to the apse line and is called periapsis (perigee for the earth).

The periapsis distance could be obtained by

$$r_P = \frac{h^2}{\mu}\frac{1}{1+e} \tag{68}$$

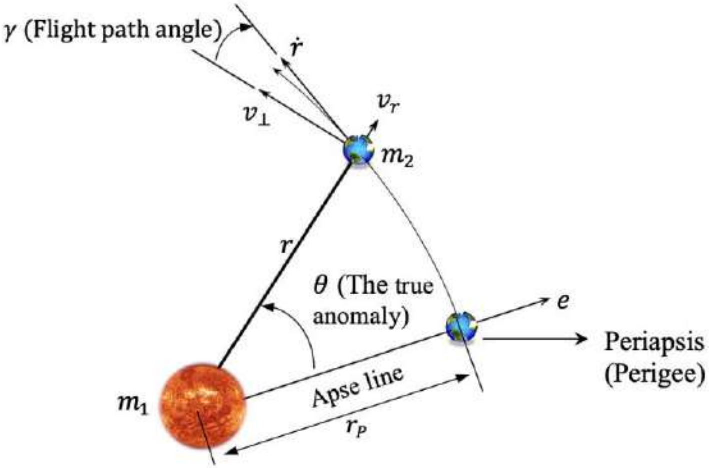

Figure 10- Periapsis, Flight path angle, and the true anomaly (polar angle) concepts

According to Equations 62 and 68 and considering the properties of cosines (i.e., $\cos(-\theta) = \cos\theta$), it is clear that the path of the orbit is symmetric with respect to the apse line. The flight path angle, which is the angle between the velocity vector and the perpendicular to the position vector (in the direction of the normal azimuth velocity called the local horizon), can be calculated as follows:

$$\gamma = \tan^{-1}\left(\frac{v_\perp}{v_r}\right) \tag{69}$$

Implying relations 64 and 67, in the above equation, result in:

$$\gamma = \tan^{-1}\left(\frac{e\ \sin\theta}{1+e\cos\theta}\right) \tag{70}$$

The chord line is the line connecting every two points of the orbit. Whenever the chord line passes through the center of gravity where is perpendicular to the apse line, it is called latus rectum; meanwhile, given the axial symmetry of the orbit about the apse line, the latus rectum will be intersected in two semi latus rectums with length p, which could be calculated by: (All These concepts are depicted in Figure 11).

$$p = \frac{h^2}{\mu} \tag{71}$$

So far, the orbit equation has been obtained by taking the cross-product of both sides of equation 49 with the specific angular momentum. So now, taking the dot product of this equation with the linear momentum per unit mass.

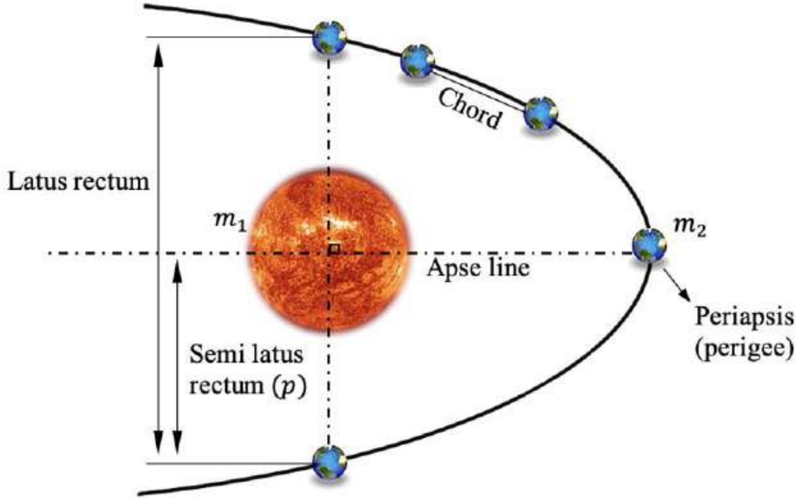

Figure 11- Illustration of chord line, latus, and semi latus rectums concepts

The linear momentum per unit mass is the same as the relative velocity, namely

$$\frac{m_2 \dot{r}}{m_2} = \dot{r} = v \tag{72}$$

Therefore

$$\ddot{\boldsymbol{r}}.\dot{\boldsymbol{r}} = -\frac{\mu}{r^3}\boldsymbol{r}.\dot{\boldsymbol{r}} \tag{73}$$

Given the rules of the scalar product, the left-hand side of the above equation simplifies as follows:

$$\ddot{\boldsymbol{r}}.\dot{\boldsymbol{r}} = \frac{1}{2}\frac{d}{dt}(\dot{\boldsymbol{r}}.\dot{\boldsymbol{r}}) = \frac{1}{2}\frac{d}{dt}(v.v) = \frac{d}{dt}\left(\frac{v^2}{2}\right) \tag{74}$$

On the other hand,

$$\frac{d}{dt}\left(\frac{1}{r}\right) = \left(-\frac{1}{r^2}\right)\frac{dr}{dt} \tag{75}$$

Hence,

$$\frac{\mu}{r^3}\boldsymbol{r}.\dot{\boldsymbol{r}} = \mu\frac{r\dot{r}}{r^3} = \mu\frac{\dot{r}}{r^2} = -\frac{d}{dt}\left(\frac{\mu}{r}\right) \tag{76}$$

Substituting the relations 76 and 74 in to 73, result in:

$$\frac{d}{dt}\left(\frac{v^2}{2} - \frac{\mu}{r}\right) = 0 \tag{77}$$

According to the result, the value in parentheses has a constant value:

$$\frac{v^2}{2} - \frac{\mu}{r} = \varepsilon \text{ (constant)} \tag{78}$$

The terms $(\frac{v^2}{2})$ and $(-\frac{\mu}{r})$ represent the amount of kinetic energy per unit mass and potential energy per unit mass of the body m_2 in the gravitational field of m_1, respectively. Mechanical energy per unit mass, which is the sum of potential and kinetic energy, is also represented by ε. (Thus, it declares the conservation of energy).
Using Equations 64 and 68 for the case $\theta = 0$ (i.e., periapsis), this amount of energy will be:

$$\varepsilon_P = -\frac{1}{2}\frac{\mu^2}{h^2}(1 - e^2) \tag{79}$$

As mentioned earlier, Equation 62 determines the shape of the orbit because of the presence of eccentricity (e). For further investigation, eccentricity will be considered at $e = 0$, $0 < e < 1$ and $e > 1$.

CIRCULAR ORBITS

By placing $e = 0$ in Equation 62, the orbit equation is simplified as follows:

$$r = \frac{h^2}{\mu} \tag{80}$$

Due to the fact that the quantities h and μ are constant, the value of r (radius of the orbit) remains constant, which indicates that the orbit is circular. The velocity in this orbit due to the constant r appears only in the vertical component (namely, $v_r = \dot{r} = 0, v_\perp = v$). Therefore, considering the linear momentum relation (Equation 46), the orbital equation (Eq. 80) is rewritten as follows:

$$v_{circular} = \sqrt{\frac{\mu}{r}} \tag{81}$$

As the velocity attained, knowing that the amount of distance traveled by m_2 around m_1 in a circular orbit is the perimeter of that circular orbit, the period of rotation (T) can be calculated:

$$T = \frac{2\pi r}{v_{circular}} = \frac{2\pi r}{\sqrt{\mu/r}} = \frac{2\pi}{\sqrt{\mu}} r^{3/2} \tag{82}$$

The amount of energy for the case $e = 0$ is

$$\varepsilon = -\frac{1}{2}\frac{\mu^2}{h^2} \xrightarrow{r=\frac{h^2}{\mu}} \varepsilon_{circular} = -\frac{\mu}{2r} \quad (83)$$

The above equation emphasizes the negative energy of the orbit and that the larger the radius of the orbit (the smaller the negative value), the more energy it has.
Most manned and unmanned remote sensing spacecraft, navigation, and imaging satellites are in low-Earth orbit. The low earth orbit lies at an altitude about of 160 km to 2000 km (100 to 1200 $miles$) covering many circular (almost up to 1000 km) and elliptical orbits, approximately 80 km (50 $miles$) above the drag-producing atmosphere and well below the hazardous Van Allen radiation belts, the innermost of which is at an altitude of 2400 km (1500 $miles$). The orbital period ranges between about 88 to 127 minutes with an orbital velocity of about 7.8 km/s to maintain a stable low earth orbit. However, this mid-velocity will be reducing as the orbital altitude increases (almost about 7.79 km/s at 200 km to 7.12 km/s at 1500 km). The required (Δv) to achieve a normal low Earth orbit starts from 9.4 km/s, whereas the atmospheric drag and gravitational effect associated with the launch typically detract 1.3 km/s $-$ 1.8 km/s of the launch vehicle (Δv). Objects are also encountered atmospheric drag is due to the gases on the thermosphere (about 80 to 500 km) or exosphere (500 km and up), depending on their orbital height. As the altitude decreases, the orbital velocities of the satellites will increase ($v \geq$ 6.944 km/s), which means that they will make 12 to 16 turns per 24 hours meanwhile for a satellite above the local horizon the time duration is about 20 min for an observer on earth.
A stellar day is a time when the earth rotates one full turn relative to inertial space or International Celestial Reference Frame (ICRF) with axes with respect to fixed stars (almost $23h\ 56m\ 4.098903691s$). Further rotation causes the sun overhead again, which is called a mean solar day (24 h), or in other word, it means the complete rotation in relation to distant stars (synodic day). In fact, the difference between stellar and mean solar days concepts stems from the rotation of the earth (spinning around its axis) during its revolution motion (revolving around the sun).
It should be noted that the plane of the earth and the celestial sphere equators make an angle about $23.23'$ with respect to the ecliptic plane, which is known as the obliquity of the ecliptic. As time passes and the earth rotates around its axis, the axis will progress with spinning, which is the same as the precession of a spinning top, designed to be spun on its vertical axis, balancing on apices due to the gyroscopic effect. In the case of the earth, this special kind of spinning, along with the precession, causes the rotating

body due to the centrifugal forces exerted on the rotation axis tends to form an oblate spheroid instead of the sphere. This tendency to deform causes the equatorial radius to be larger than the polar radius, which is known as the equatorial bulge.

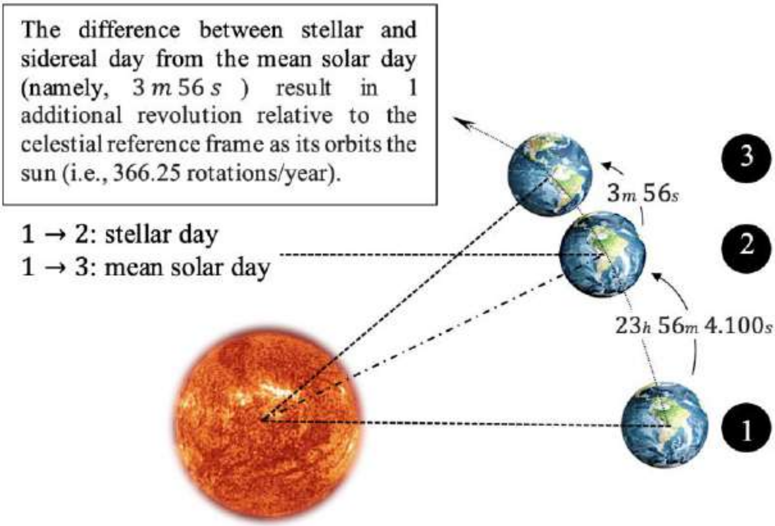

Figure 12- Stellar day and mean solar day concepts

In general, this general precession includes two categories of precessions:

1. Precession of the equator (Lunisolar precession)
2. Precession of the ecliptic (Planetary precession)

The Lunisolar precession is due to the gravitational forces of the moon, sun, and other planets on the equatorial bulge, which causes the earth's axis to move with respect to the inertial space or (ICRF). Also, due to the obliquity of the ecliptic, and exerting other planet gravitational attractions on it, the ecliptic leads to moving slightly with respect to the inertial frame. This general precession was known as the precession of the equinoxes earlier in 2nd-century BD by Hipparchus, as follows: The equinoxes are moved westward along the ecliptic relative to the fixed stars. The point is, this precession takes place over a period of 26,000 years. However, the lunisolar precession is about 500 greater than the planetary precession.

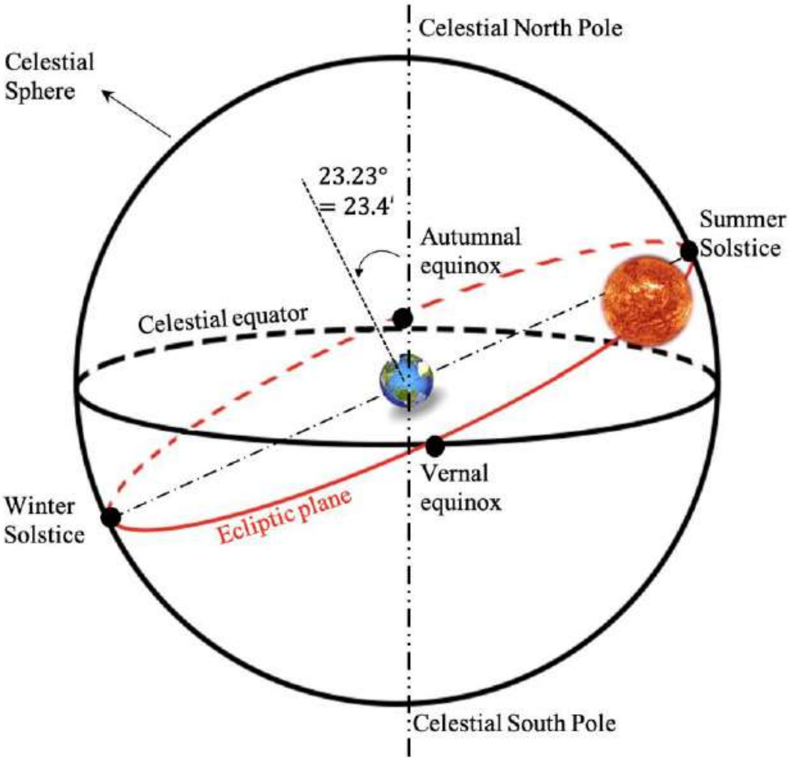

Figure 13- Ecliptic plane position at celestial sphere and equinox concept

The subsolar points appear to leave the Southern Hemisphere, heading northward in the earth that is called vernal equinox at the Northern Hemisphere and as the autumnal equinox at the Southern Hemisphere. As the definition of stellar day, the sidereal day is the period of time relative to the precessing mean vernal equinox. (it's about $23h\ 56m\ 4.09053083288s$).

In fact, given the concept of the solar day, the earth precesses as much as $(\frac{2\pi}{365.26})$ radians per day (solar day) in its solar orbit (in addition to the rotation of (2π) radians around itself on a sidereal day). As a result, the inertial angular velocity of the Earth during a solar day would be:

$$\omega_E = \frac{(2\pi + (2\pi/365.26))}{24} = 72.9217 \times 10^{-6}\, {rad}/{s} \tag{84}$$

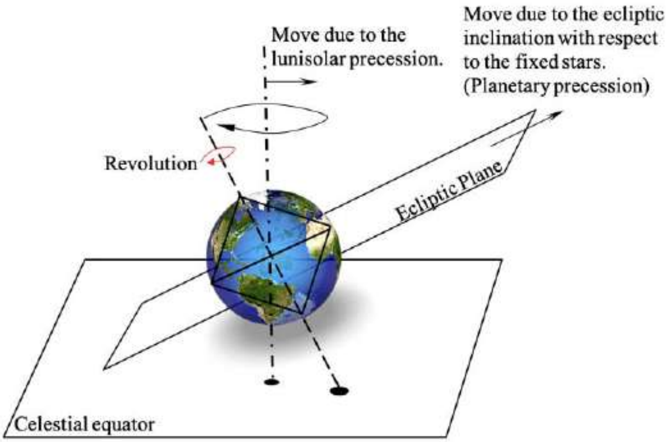

Figure 14- Equator and Ecliptic precessions concepts

The three orbital phases Geostationary, Geosynchronous, and polar are shown in the figure below.

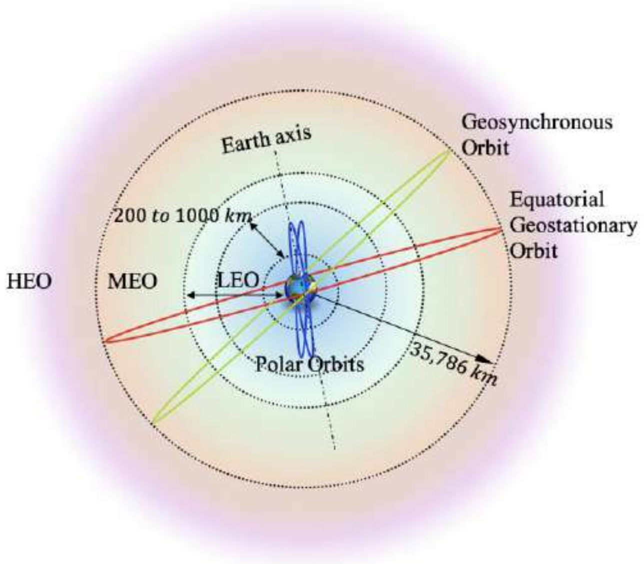

Figure 15- GEO's, Polar orbits with respect to the equator, and low, medium, and high earth orbits altitude ranges

A geostationary as an equatorial orbit is at an altitude, in which the angular velocity of objects in that orbit is the same as the angular velocity of the earth (i.e., the angular velocity during the sidereal day). Hence, satellites that are located on a geostationary orbit which is appearing motionless, are not trackable by the ground stations. The velocity in a circular orbit can be calculated from Equation 81, so for the Geostationary orbit:

$$v_{Geo} = \sqrt{\frac{\mu}{r_{Geo}}} \tag{85}$$

On the other hand, according to Kinematics:

$$v_{Geo} = \omega_E r_{Geo} \tag{86}$$

Equating the above equations, the radius of the geostationary orbit, resulting in:

$$r_{Geo} = \sqrt{\frac{\mu}{{\omega_{Geo}}^2}} \tag{87}$$

By setting the earth characteristics and considering the mass of the satellite is neglected compared to the earth, the orbital radius of $42146\ km$ will be obtained. Subtracting this value from the earth's radius, the distance from the orbit to the earth's surface becomes $35{,}786\ km$.
To see how much of the earth's surface is exposed to satellite view, consider the following figure, where the maximum visible latitude is φ.

$$\varphi = \cos^{-1}\frac{R_e}{r} \tag{88}$$

The visible zone in this latitude, shown as the shaded region in figure 16, will have an area S:

$$S = 2\pi {R_E}^2(1 - \cos\varphi) \tag{89}$$

The amount of exposed area is usually expressed as a percentage of the total area ($2\pi {R_E}^2$), which will eventually be 89.4%.

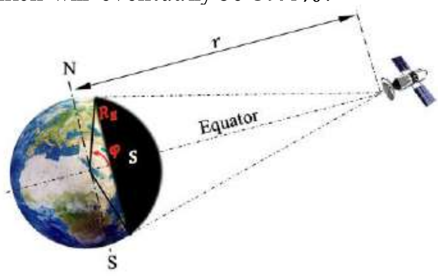

Figure 16- The exposed area of the earth by the satellite (Footprint).

Geosynchronous orbits are similar to geostationary orbits, except that they have some deviation from the equator. A Polar Orbit is an orbit in which a satellite passes roughly Earth's North and South poles on each revolution in an altitude range of 200 km to 1000 km. It might have an inclination of (or very close to) 90 degrees to the equator, but also a deviation within 20 to 30 degrees with respect to the earth's axis is classified as a polar orbit.

ELLIPTICAL ORBITS

For the orbit that $0 < e < 1$, consider Equation 62, which, given the range of variations θ, will still have a positive value. For $\theta = 0$, the position vector will have the lowest value, called periapsis. Also, when the denominator of the fraction has the smallest value (namely, $\theta = 180°$), the position vector will have the longest length, in which case it is called apoapsis, and is equal to:

$$r_A = \frac{h^2}{\mu}\frac{1}{1-e} \tag{90}$$

Due to the constraint of the position vector, the shape of the resulting orbit draws an ellipse. Thus, the major diameter of this elliptical orbit is considered as the sum of the lengths of apoapsis and periapsis, i.e.

$$2a = r_A + r_P \tag{91}$$

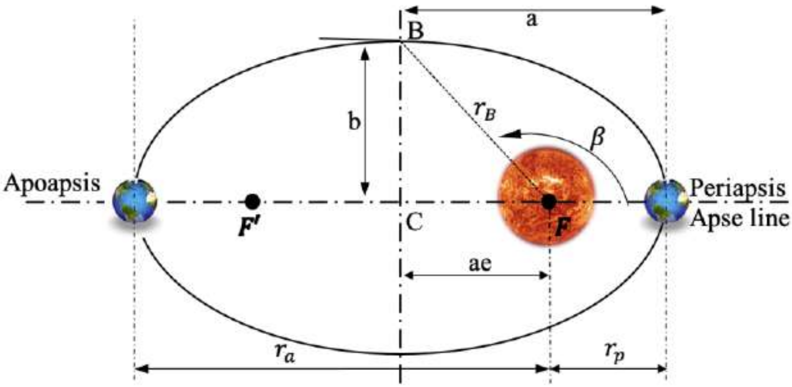

Figure 17- Elliptical orbits schematic drawing.

By substituting equations 68 and 90 in the above relation, the value of a, which is the semi-major axis of the ellipse, will be obtained:

$$a = \frac{h^2}{\mu}\frac{1}{1-e^2} \tag{92}$$

Placing the obtained relation in the original equation of the position vector

of the orbit, the orbit equation is rewritten as follows:

$$r = a\frac{1-e^2}{1+e\cos\theta} \tag{93}$$

Which could be attained for the periapsis ($\theta = 0$):

$$r_P = a(1-e) \tag{94}$$

According to Figure 17, CF will be calculated:

$$CF = a - r_P = a - a(1-e) = ae \tag{95}$$

For point B at a distance b from the center of the ellipse (i.e., the semi-minor axis) with anomaly β, according to Equation 93, results:

$$r_B = a\frac{1-e^2}{1+e\cos\beta} \tag{96}$$

Given that the r_B projection on the apse line is the same as ae:

$$ae = r_B\cos(180-\beta) = -\left(a\frac{1-e^2}{1+e\cos\beta}\right)\cos\beta \tag{97}$$

Therefore:

$$e = -\cos\beta \tag{98}$$

By inserting the value obtained in Equation 96, the value of r_B (semi-minor axis) is obtained:

$$r_B = a \tag{99}$$

Once again, by considering the above ellipse in Cartesian coordinates and converting the position (r,θ) for a selected point on the orbit, the elliptic equation will be obtained:

$$\begin{cases} x = ae + r\cos\theta \\ y = r\sin\theta \end{cases} \Rightarrow \begin{cases} \dfrac{x}{a} = \dfrac{e+\cos\theta}{1+e\cos\theta} \\ \dfrac{y}{b} = \dfrac{\sqrt{1-e^2}}{1+e\cos\theta}\sin\theta \end{cases} \tag{100}$$

According to the elliptic equation (i.e., $\frac{x^2}{a^2} + \frac{y^2}{a^2} = 1$) and setting above expressions on its left-hand side, the hypothesis that the orbit is elliptical is confirmed.
The mechanical energy equation of the orbit (Equation 79) in periapsis, employing Equation 92, result in:

$$\begin{cases} \varepsilon_P = -\frac{1}{2}\frac{\mu^2}{h^2}(1-e^2) \\ a = \frac{h^2}{\mu}\frac{1}{1-e^2} \end{cases} \Rightarrow \varepsilon_P = -\frac{\mu}{2a} \tag{101}$$

The above relation refers to the independence of energy from eccentricity and its affiliation to the semi-major axis. Thus, orbits that have the same semi-major axis also have identical periods and energies.
Using Kepler's second law, the value of the rotation period T for this ellipse is:

$$\begin{cases} A = \pi ab \\ \Delta A = \frac{h}{2}\Delta t \end{cases} \Rightarrow T = \frac{2\pi ab}{h} \tag{102}$$

Therefore, using equation 92 and applying the Pythagorean theorem in the BCF triangle, the period of rotation results:

$$T = \frac{2\pi}{\sqrt{\mu}} a^{3/2} \tag{103}$$

This relationship represents Kepler's third law: the period of the planet's rotation is proportional to the power of $(3/2)$ of the semi-major axis.

PARABOLIC TRAJECTORIES

For the case where the eccentricity is 1, Equation 62 states that at $\theta = 180°$ the path of the orbit tends to infinity. Also, from the energy equation, it can be concluded that the amount of energy is zero, i.e.

$$\varepsilon = \frac{v^2}{2} + \frac{\mu}{r} = 0 \tag{104}$$

Hence

$$v = \sqrt{\frac{2\mu}{r}} = v_{esc} \tag{105}$$

The above equation indicates the velocity required for the body m_2 to escape the gravitational orbit of the m_1 body. Therefore, for a satellite of mass m in a circular orbit with radius r from the center of the earth at velocity v_0 (equation 81), the escape velocity is:

$$v_{esc} = \sqrt{2v_0} \tag{106}$$

The flight path angle for parabolic trajectories will be equal to:

$$\gamma = \frac{\theta}{2} \tag{107}$$

The equation of parabolic paths whose origin acts as a focal point is as follows:

$$x = \frac{p}{2} - \frac{y^2}{2p} \quad (108)$$

Where p is obtained from Equation 71.

HYPERBOLIC TRAJECTORIES

Equation 62 becomes a hyperbola when $e > 1$. In this case, the denominator of Equation 62 could be zero, which means that the orbit tends to infinity:

$$\cos\theta = -\frac{1}{e} \quad (109)$$

θ is known as asymptomatic anomaly and has a value between 90° and 180°. Periapsis is located on the apse line on the physical side of the hyperbolic, while apoapsis is located on the apse line in the vacant orbit, which is not physically possible due to the need for repulsive gravitational force. The values of a, r, r_P, r_A and b can also be calculated by:

$$a = \frac{h^2}{\mu}\frac{1}{e^2 - 1} \quad (110)$$

$$r = a\frac{e^2 - 1}{1 + e\cos\theta} \quad (111)$$

$$r_P = a(e - 1) \quad (112)$$

$$r_A = -a(e + 1) \quad (113)$$

$$b = a\sqrt{e^2 - 1} \quad (114)$$

Considering the hyperbola (i.e., $\frac{x^2}{a^2} - \frac{y^2}{a^2} = 1$) in the Cartesian coordinates, the values x and y for a point are:

$$\begin{cases} \frac{x}{a} = -\frac{e + \cos\theta}{1 + e\cos\theta} \\ \frac{y}{b} = \frac{\sqrt{1 - e^2}}{1 + e\cos\theta}\sin\theta \end{cases} \quad (115)$$

Using equations 79 and 115, the energy equation becomes:

$$\varepsilon = \frac{\mu}{2a} \quad (116)$$

Unlike the previous cases, it is observed that the orbital energy has a positive value and is independent of eccentricity. Therefore:

$$\frac{v^2}{2} - \frac{\mu}{r} = \frac{\mu}{2a} \tag{117}$$

When the object reaches infinity, i.e., its potential energy is zero, a value of v_∞, called hyperbolic excess speed, will be obtained from the following equation; And indicates the amount of energy required in addition to the v_{esc} to exit the center of gravity.

$$v_\infty = \sqrt{\frac{\mu}{a}} \tag{118}$$

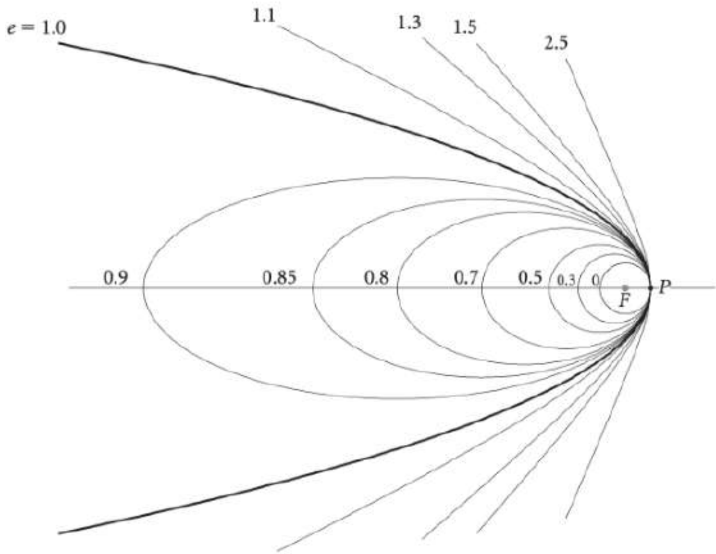

Figure 18- Orbit shape variation as eccentricity changes. (Adopted from Orbital Mechanics for Students)

BURNING RATE DETERMINATION

As we found the thrust-pressure dependence in the equations of thrust and thrust coefficient, as the pressure inside the chamber is determined, the engine thrust can be determined. Since the pressure inside the chamber is emanated by the burning of propellant grains, we first scrutinize the combustion of the propellant as the parameter that plays a vital role among the parameters controlling the operation of solid rocket motors. Let us first recall the burning rate, which is expressed as the speed at which solid propellant is consumed during the process, perpendicular to the propellant surface in inches per second (ips). For instants, consider a solid propellant in a cigarette fashion with a burning rate of 1.7 ips, the burned length of this propellant is 69 inches almost in 40 seconds. However, for some certain propellants that have a low gas velocity or mass flux in the propellant cavity, the burning rate augmentation (r_b) is calculated in terms of chamber pressure (P_c) according to the following empirical relation (St. Robert's or Vieille's law when pressure exponent be constant with pressure), assuming that other factors are small compared to the initial grains temperature and chamber pressure, (Temperature dependence is shown as constant a). The four most commonly used coefficients to describe both temperature and pressure influences are as equations 120 to 123.

$$r_b = a \times {P_c}^n \tag{119}$$

$$\pi_K = [\frac{\partial \ln P}{\partial T_0}]_{K_n} \tag{120}$$

$$\sigma_P = [\frac{\partial \ln r}{\partial T_0}]_P \tag{121}$$

$$\sigma_K = [\frac{\partial \ln r}{\partial T_0}]_{K_n} \tag{122}$$

$$\pi_{P/r} = [\frac{\partial \ln P}{\partial T_0}]_{P/r} \tag{123}$$

T_0 and K_n are conditioning temperature of the propellant in °F, and ratio of propellant burning rate to nozzle throat area, respectively.

For most restricted burning propellants, constants a and n have values between 0.05 and 0.002 and 0.4 to 0.85, respectively. It should be noted that the above equation is true only in a certain range of temperature and pressure because, at pressures below a certain value, combustion becomes unstable and possibly stops completely. For some propellants whose combustion behavior is in such a way that for a given temperature, the burning rate is constant in a certain range of pressures. The above equation will be written in the form of polynomial equations at those pressures. Generally, burning rate is affected such parameters likes chamber pressure, grain initial temperature, propellant composition, oxidizer ingredients size, and erosive burning. Generally, the burning rate affecting by such parameters likes chamber pressure, grain initial temperature, propellant composition, oxidizer ingredients size, and erosive burning. In addition to the above factors, the inclusion of metal wire strands in the propellant can be mentioned as an external factor affecting the increase of burning rate without modifying the chemical composition. As another way, adding burn rate modifiers, such as $CuCr_2O_3$, Fe_2O_3, Cr_2O_3, and CuO that enhances the burning rate by lowering the decomposition temperature of ammonium perchlorate, can be mentioned. Also, decreasing the particle size of ammonium perchlorate (oxidizer) will boost the burning rate.

EROSIVE BURNING

The study of erosive burning date back to 1889 in Germany, Japan, Britain, and the Soviet Union. Mansel is the first who observed the dramatic increases in the engine pressure and its dependence on the propellant grain size in an experiment on a modified double-base propellant (cordite). The effects of this phenomenon were later explicitly stated by Muraour. The first systematic study of erosive burning was also initiated by Britain and the United States.

As the solid propellant starts to burn, the combustion gases begin to accelerate. This rapid flow of gases parallel to the propellant surface increases its burning rate, which seriously affects the performance of the solid rocket engine. The severe pressure gradient created (i.e., a pressure difference of downstream (flame zone), which is almost constant, with the upstream pressure, which is transient and fluctuated) after the ignition cause to gases acceleration from the aft end to the front end, and then it leads to erosive burning. It should be noted that erosive burning is more severe in the smaller area ratios due to the higher velocity. There are two scenarios associated with erosive burning: 1) The rapid gas flow over the solid propellant increases the transport coefficient and turbulence-enhance mixing, which in turn increases the gas-to-solid heat feedback, thus increasing the burning reaction rate. 2) The reaction of oxidizer and fuel-rich pyrolysis gases from composite propellants. The flame zone causes the propellant to pyrolyze, and the pyrolyzed gases start to react near the propellant surface.

For example, the engine case was designed to keep the pressure constant, but it was observed that the actual pressure during the test has a peak at beginning of firing that tends rapidly towards the design pressure. The point

is, when the port is larger, this peak gets higher in dimension and burn. To increase the burning rate in this experiment, the grains were finely chopped so that the pressure regains roughly to the design pressure (represented by the dotted line in figure 19). This pressure tail-off, which accelerated the regression rate of the propellant, changed the burn-back pattern, causing the burnout of the aft end to occur earlier than expected (well before the head end).
It should be noted that erosive burn merely occurs at a velocity higher than the critical gas velocity (approximately 76.2-91.44), which means that erosive burning is associated with a threshold effect. Erosive burning can be interpreted in three regimes, the non-erosive, transition, and full erosive regimes, which are asserted by the local Mach number for a given static pressure. Saderholm presented an experimental relation (equation 124) to erosive burning that is used in many ballistic applications:

$$r_b = a \times {P_c}^n \times (\frac{M}{M_C})^x \qquad \text{for} \qquad M < M_C \tag{124}$$

Where M_C represent the threshold Mach number and is typically employed in 0.7 with $x = 0.5$. The exponent (x) is a function of the local static pressure and ballistic burn rate of the certain propellant (i.e., polybutadiene acrylic acid (PBAA) in Saderholm's research); Also he found that erosive burning is related to the parameters of the fluid flow, regulating the heat transfer to the propellant by forced convection.
Burn rate in high subsonic Mach numbers (greater than 0.5) refer to fully-erosive region and obtain independently of equation 119 as follows: (M and P are local Mach number, and local static pressure in Pa, respectively).

$$r = 4.44599 \times 10^{-7}(MP)^{0.71} \tag{125}$$

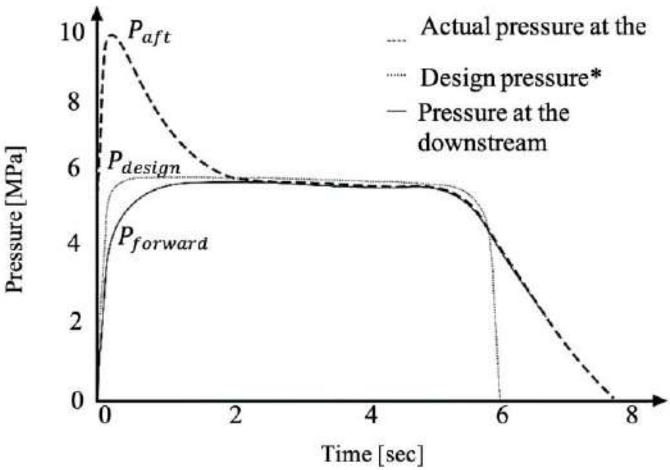

Figure 19- Pressure-time variation in erosive burning.

Burning rates in Mach number less than 0.06 are not affected by the gas flow and are in the non-erosive zone. The burning rate in this area can be calculated from equation 119; In this case, the burn rate known as ballistic burn rate. The transition zone is related to the Mach numbers between 0.06 and 0.5, and its burning rate is obtained by equation 124. Figure (21-a) shows all these regions and the burn rate variation with different Mach numbers. The effect of static pressure on the variation of ballistic burn rate in different Mach number ratio exponent (x) for PBAA propellant is shown in Figure (21-b).

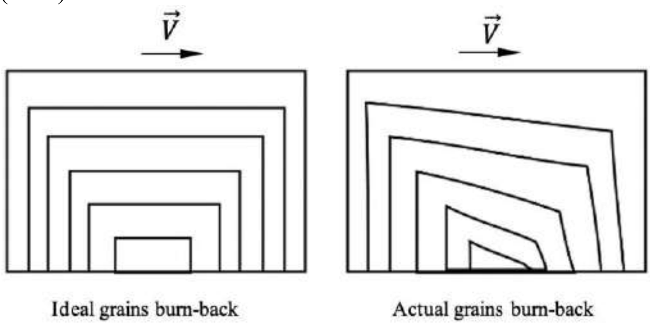

Figure 20- Schematic drawing of Actual and Ideal Grains Burn-Back

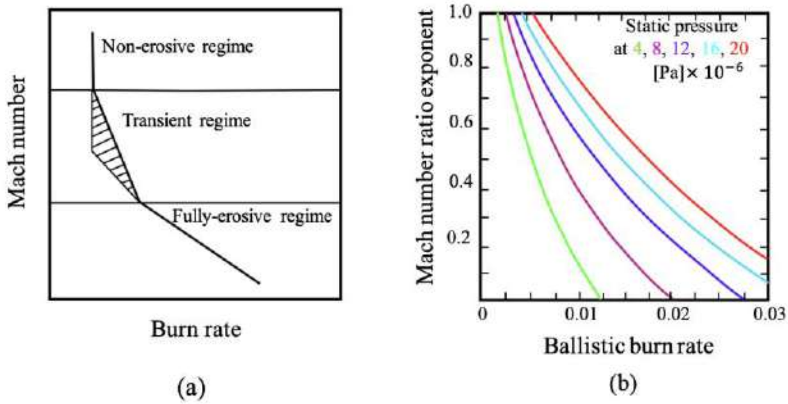

Figure 21- (a) Erosive burning regimes. (b) Variation of ballistic burn rate with Mach number ratio exponent (x) at different static pressures.

Figures 22 and 23 illustrate typical characteristics of this progression as affected by gas velocity and mass flux, respectively. The velocity and mass flux at the beginning of each augmentation, referred to as the threshold value, are usually interpreted by quasi-experimental expressions associated with operating pressure. Examples of these expressions for velocity (u_{tv}) and mass flux (G_{tv}) thresholds are as follows:

$$u_{tv} = k_1 + k_2 P^{k_3} + k_4 P^{k_5} \qquad [{}^{ft}/_{sec}] \tag{126}$$

$$G_{tv} = k_6 + k_7 P^{k_8} + k_9 P^{k_{10}} \qquad [{}^{lb}/_{sec.\,in^2}] \tag{127}$$

Where, $k_{1,2,..}$ are the experimental determine coefficients and exponents. But experience has shown that these linear equations cannot be successfully applied in engines with high mass flux values. Thus, another appropriate semi-experimental expression was presented that was more compatible with the high-velocity condition. In the following expression, δ is a parameter estimating the local burning rate, which contains the characteristics of the internal flow field and the geometry of the grains. Also, it will be evaluated by the experimental data for erosive burning.

$$r_b = a \times P_c{}^n (1 + \delta_{augmentation}) \tag{128}$$

Burning rate increases with engine acceleration. Since most rocket propellants contain finely ground particles such as aluminum as fuel, they begin to melt when the flame strikes these particles and are swept to the gas stream, where they continue to burn or oxidize. The rocket engine is always affected by force in different directions. Forces at an angle of approximately

60 to 90 degrees to the longitudinal axis are prone to increased burning speeds because most combustion surfaces in most grain configurations are perpendicular to the engine axis. As a result, when the engine spins about its axis (for flight stability), centrifugal forces cause the molten particles to adhere to the grain surface, increasing heat transfer and burning rate. In other words, the spinning decreases the mass flux in the throat, which has the same effect as reducing the throat area, and therefore the pressure inside the chamber and the consequent burning rate increase. Other influential factors include increased turbulence. Symptoms of the spinning effect include increased engine pressure, decrease burn time, an extended tail-off, and envelope overheating. The axial velocity of the combustion gases, considering the rotational flow, at the throat section is obtained from the following equation:

$$u_t^2 = 2\frac{g\gamma RT_0}{\gamma+1} - \omega^2\left(\frac{R_0}{R_t}\right)^2[2\left(\frac{R_0}{R_t}\right)^2 - 1]r^2 \qquad (130)$$

g = gravitational constant, γ = Specific heat ratio of propellant gases,
R = Gas constant
T_0 = Stagnation temperature, R_0= Combustion chamber radius,
R_t = Nozzle throat radius, ω = Spin rate, r = radial position.

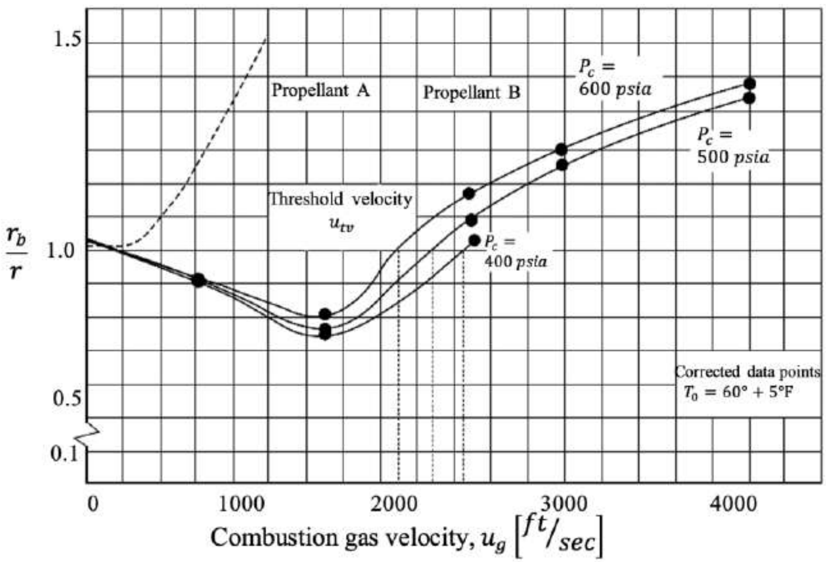

Figure 22- Typical effect of combustion gas velocity on burning-rate augmentation. (Adopted from NASA-SP-8039)

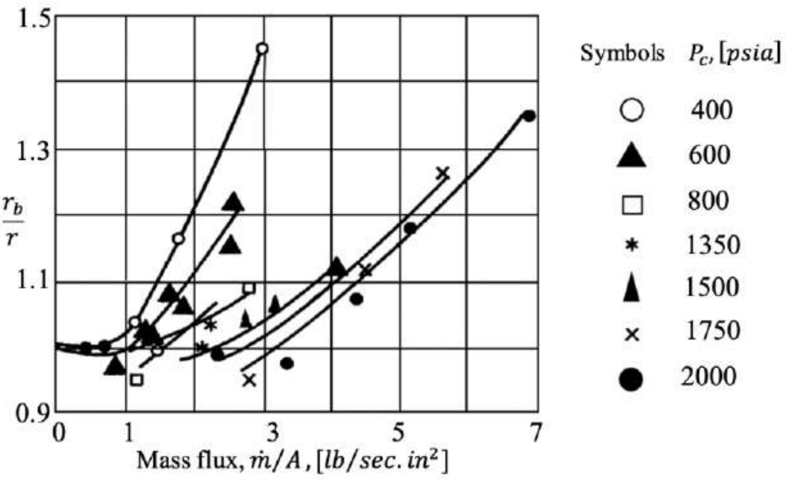

Figure 23- Typical effect of mass flux on burning-rate augmentation. (Adopted from NASA-SP-8039)

The point is that the effects of angular acceleration are not limited to burning rate augmentation. For instance, centrifugal accelerations of less than $10g$ perpendiculars to the metalized propellant surface have the following consequences:

- Burning time regression.
- Ignition delay time and motor operating pressure increments.
- Extending the tail off burning period.
- Motor thermal and burnout mass protection requirements.

The most influential factors that affect the engine performance in the spin environment are the acceleration level, the orientation of the burning surface to the acceleration vector, the metal content, and the grain size. The three most common methods for experimentally measuring the combustion rate of a solid propellant are the closed bomb, the small BEM, and the strand burner. As the name of the first method implies, the experiment is performed at a constant volume with variable pressure. This method is generally restricted to preliminary screening or propellant research. The other two methods are used to estimate the burning rate more accurately; With ballistic evaluating motors (BEM) being used specifically to measure propellant burning rates in the design of particular engines. The third technique also involves the use of a strand burner, which is dedicated to propellant screening and quality control testing.

Both diagrams are plotted for PBAA 16% A1 propellant

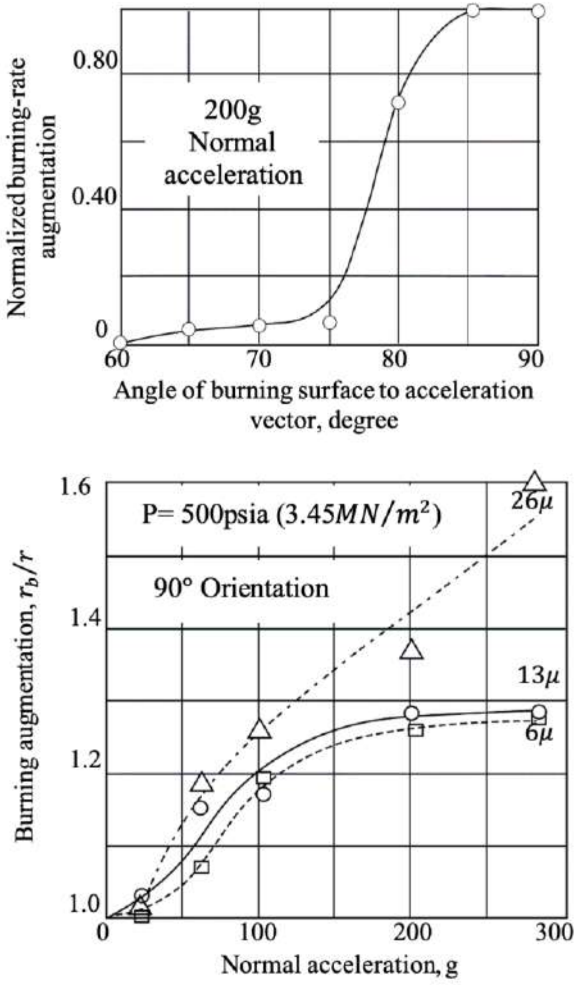

Figure 24- Burning rate variation with acceleration direction; and effect of grain size (i.e., Aluminum) on burning rate. Adopted from Effects of Acceleration upon Solid-Rocket Performance by G. B. Northam and M. H. Lucy

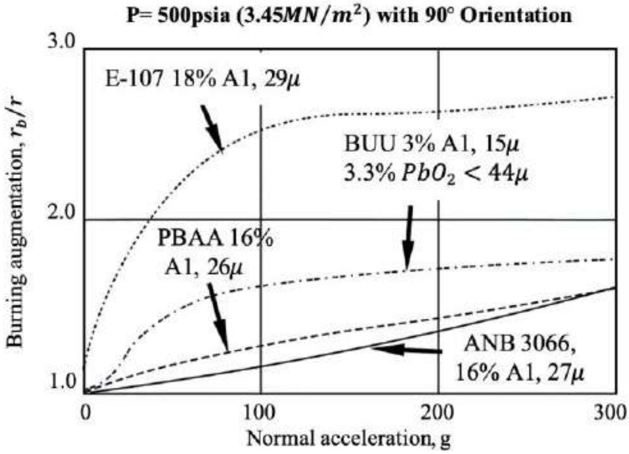

ure Ac- ation on types pro- lants ing

Fig- 25- celer- effect four of pel- burn- rate.

Adopted from Effects of Acceleration upon Solid-Rocket Performance by G. B. Northam and M. H. Lucy

As mentioned earlier, there are many methods for measuring the burning rate of a solid propellant experimentally. In one of the oldest and most common methods (i.e., strand burner or Crawford techniques) the test can be fairly time-consuming because to draw a burning rate-pressure diagram, this test had to be done at least 4-5 times at different pressures. The operation and measurement are that in a constant pressure tube there is a propellant strand so that two wires are buried in the propeller at a distance of L from each other. When combustion starts, the propellant starts to burn from the end (in cigarette fashion). By melting each of those wires, the chronometer connected to them starts and stops, respectively. Therefore, at constant pressure, having the burning time and the predetermined value of the burned propellant (cylinder with length L and radius r), the value of the burning rate is obtained. By repeating this experiment at various pressures, a graph of pressure burn rate changes is obtained.

In contrast to this method, there is the slab burner, which is relatively simpler, cheaper, and more accurate. In this method, a brick of propellant with exact dimensions is placed inside the rocket engine. As the combustion starts, the propellant brick begins regression on all surface sides. Since the pressure changes transiently with the surface area, the burning rate at each time step can be calculated using a computer program. As a result, by plotting these burning rates at each time-step in terms of pressure, a recessional graph of burning rate and pressure-time is plotted.

GRAIN DESIGN

Consider the following time-thrust diagram (Figure 26-A), all four paths have equal impact (area under the curve) of equality. However, in all these cases, the engine performance is different. The reason for this could be that the way the propulsion is configured in the engine is different in each case. In other words, we know that the thrust is directly related to the chamber pressure, which is proportional to the exposed surface of the propellant; Therefore, it is crucial to design and configure the propellant in such a way that the changes in the exposed surface conform to the desired thrust. For instance, in an engine whose thrust is continuously increasing, the propellant is packaged in such a way that the burning surface progress as the propellant consumes.

Most solid propellants today are designed as hollow cylindrical cylinders to protect the chamber wall against hot combustion products. The burning surface area in such cylindrical grains (figure 26-B) is obtained from the following equation.

$$A_s = L \times \ell \tag{131}$$

The surface exposed to propellant burning (i.e., the head end) could be in different shapes. For propellant grains in convex or concave cusps modes, the process of deformation (namely progressive, regressive, or neutral) following combustion is interpreted as follows: when convex is towards gases, convexity remains the same and only recesses, but when concave cusp to the gases, the concavity is a radius of a circle or sphere to the center of the initial concavity. These concepts are shown in the figure 27.

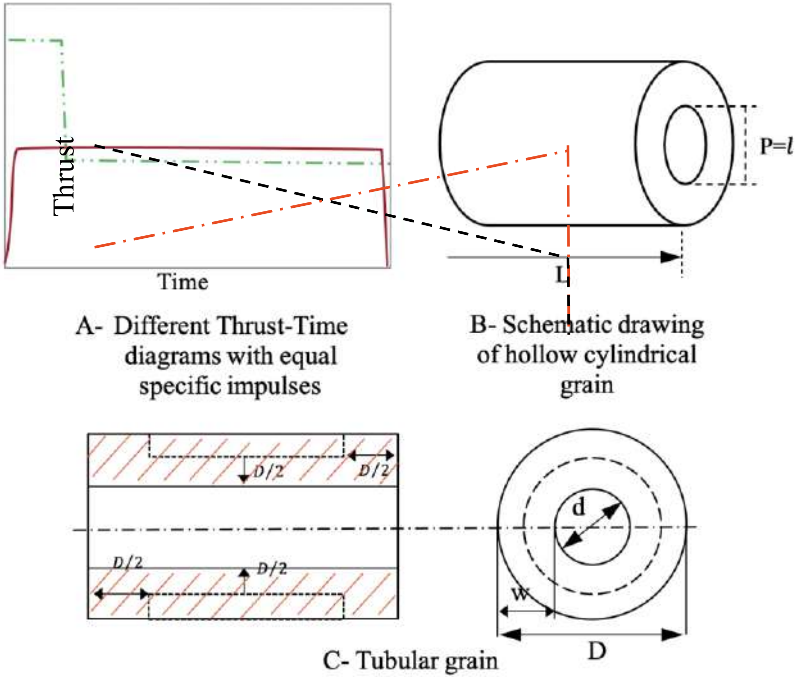

Figure 26- Typs of Thrust-time diagrams and Cylindrical and Tubular Grains ahcematic drawings

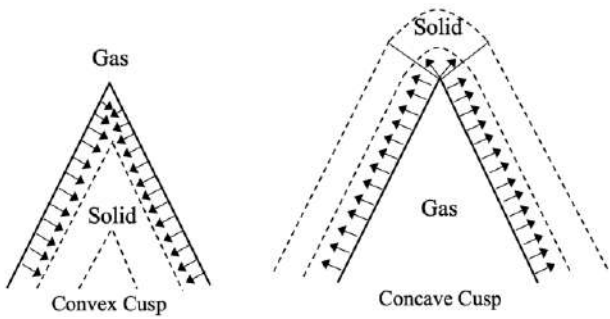

Figure 27- Burning effect on different solid propellant Cusp's

In some designs, a sudden decrease in the burning surface may occur. In these cases, the chamber pressure is reduced to such an extent that even combustion is stopped, or no effective thrust is achieved. Therefore, the exhausted propellant does not participate in propulsion and is considered dead weight, which is known as a **sliver**.

A simple example of cylindrical grains is end-burning grain or cigarette fashion. As the grains burn from the head end, so the burned surface is equal to the cross-section. The small burnt surface of these grains limits the mass flow and thrust production, making it suitable only for very specific applications (low thrust, low performance with higher combustion). There is another class of end-burning grain in that a hole surrounds it in the center. In this case, burning can occur in all three forms of progressive, regressive, and neutral. The configuration of this type of grains is usually done in the form of rod & shell or ID-OD (which are depicted in figure 28); So that in the first category, the engine compartment will not be exposed to the high heat of the combustion gases and is protected by its propellant, but the second category requires the use of insulation and inhibitors as a heat shield. The burning state of these grains depends on the burning conditions of both ends. When the outer surface is not exposed to burning, it can protect the chamber wall as insulation, in which case the burning is progressive due to the increasing burning perimeter (from the inside out). The diagram of the burning surface in terms of burnt distance at different L/D and d/D with both ends unrestricted is shown in the figure below.

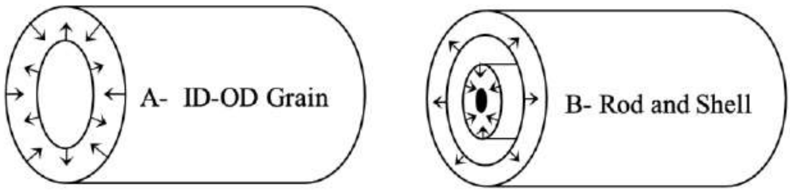

Figure 28- Common tubular grain perforations

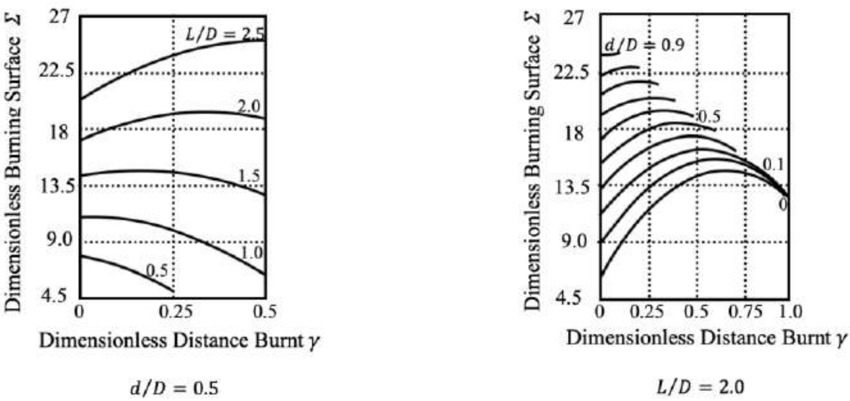

Figure 29- Burning profile as a function of d/D and L/D ratios.

As depicted in figure 29, in a constant d/D, by increasing L/D to the value of 2, we achieve almost neutral burning, more than this amount, the combustion continues as progressive. To illustrate the effect of d/D, diagram 29-B is plotted, which shows the effect of different d/D on the burning surface in terms of burnt distance at a constant L/D. As shown in the figure, by increasing the d/D value from 0 to 1, the natural burning increases. It should be noted that $\frac{d}{D} = 0$ is a hypothetical case in which the propellant starts burning from its axis and both ends.

In contrast to circular grains, there are other types of grains that have more flexibility, complexity, and slivers. Here are three of the most commonly used of these configurations: Star, Wagon wheel, and Finocyl. The first type of non-circular perforation is the star configuration, which burns in a radial direction. The geometry of this configuration consists of 6 basic parameters N, r, R, ω, ξ, and η, which reveal its combustion model. In general, the burning of this geometry is examined in 4 sections according to its basic parameters. Figure 30 illustrates a schematic drawing of the geometry of this configuration along with its zoning. The burning in the first and second zones can be done in one of these three states of progressive, regressive, and neutral according to the two parameters r and w, but zone three generally has progressive burning. Zone four, which is considered as the sliver, will also suffer from regressive burning. Another widely used configuration is the wagon wheel perforation. As the name implies, its geometry includes spokes whose presence has added two parameters, β, and L, to the parameters of the previous pattern, (Which this concept is depicted in figure 32-a). Most usages of this configuration are applications with web fraction requirements. In addition to the conventional model of this configuration, there are other models such as dendrite or forked wagon wheel with the same specifications, which have a higher volumetric loading fraction (depicted in figures 32-b, 32-c). Since the wagon wheel configuration hires two more parameters than the star perforation ones, it could be constructed in more shapes. Other uses for wagon wheels include boost-sustain grain due to the discontinuous regression in the combustion perimeter after all spokes have burned. In systems with a low L / D ratio or high burn time, another class of grains called finocyl or fin in the cylinder is used. This configuration includes axial ports which, by decreasing burning on these ports (i.e., regressive burning), compensate for increasing the burning of the cylindrical part (i.e., progressive burning) and increasing burning time. This perforation requires the use of inhibitors and insulation because the chamber wall will be exposed to hot combustion gases then after the propellants under the ports are burned. It is important to note that this is a sliverless propellant configuration. Each short-term, high-thrust performance period continues with a longer, lower-thrust performance period, in which the whole thrust durations are called boost-sustain performance. This performance can be achieved depending on the ratio of the thrust of the boost to sustain of single-fuel or even two different fuels. The selection of the appropriate configuration from the designer's point of view, which ends in the final web fraction, is based on the following indicators:

- Favorable thrust history.
- Volumetric forces required.
- Burnt time (Propellant burning rate).

Several thrust-time diagrams of various common grain configurations for internal burning are plotted in figure 33. Figure 34 is also demonstrating the variety of burning profiles during a space engine mission.

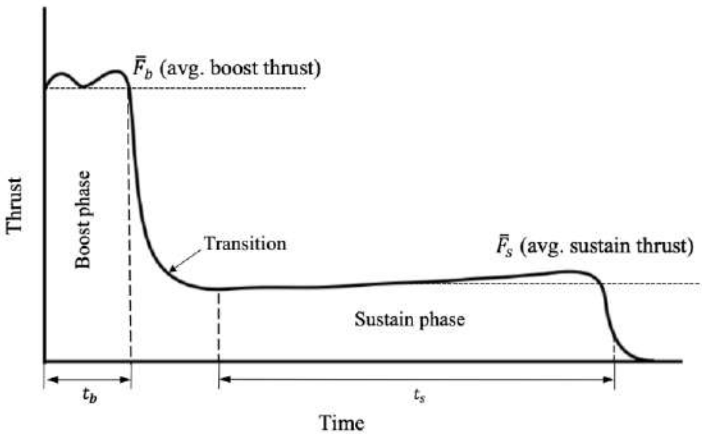

Figure 30- Boost-Sustain performance thrust-time diagram.

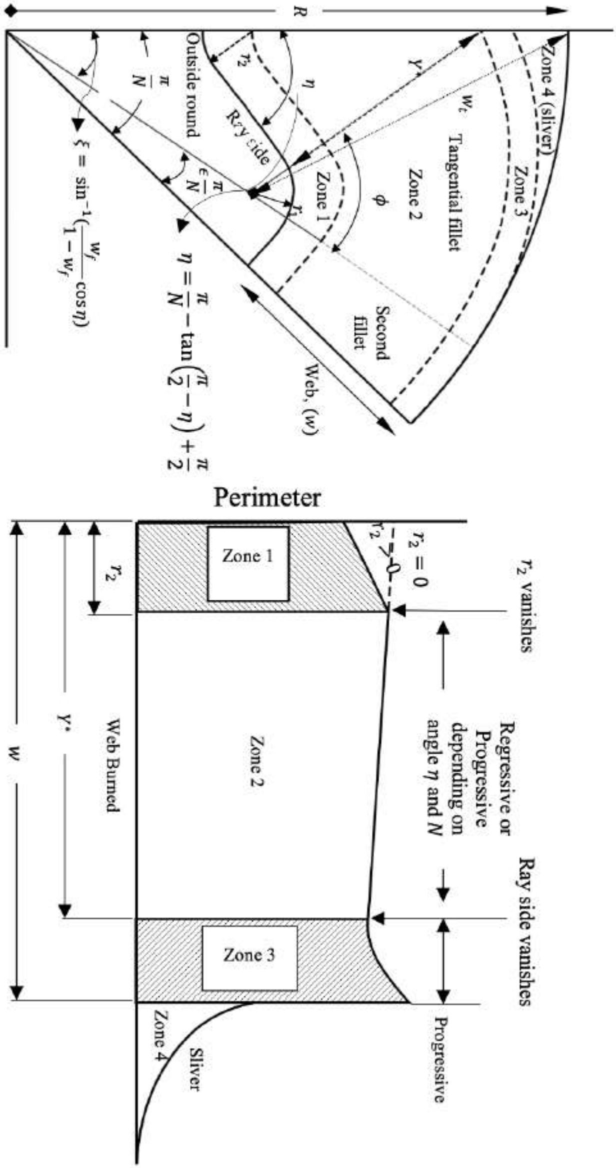

Figure 31- Grains star configuration and its burning profiles at different web burning heights.

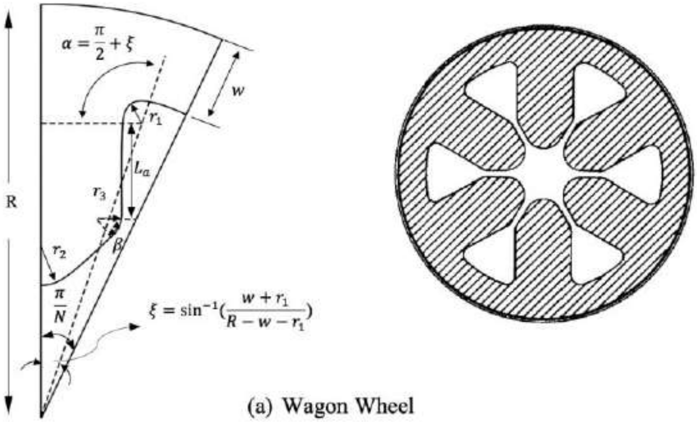

(a) Wagon Wheel

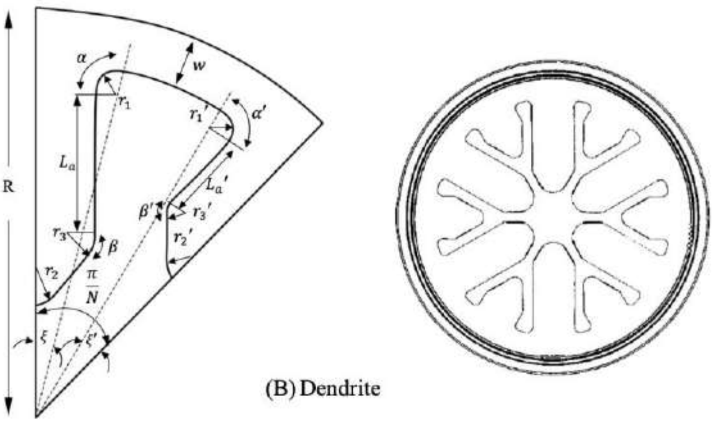

(B) Dendrite

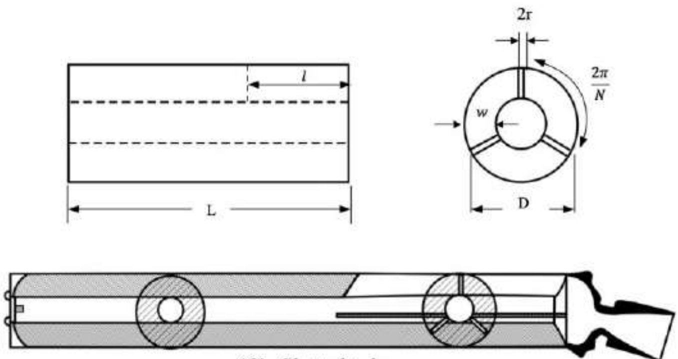

(C) Slotted-tube

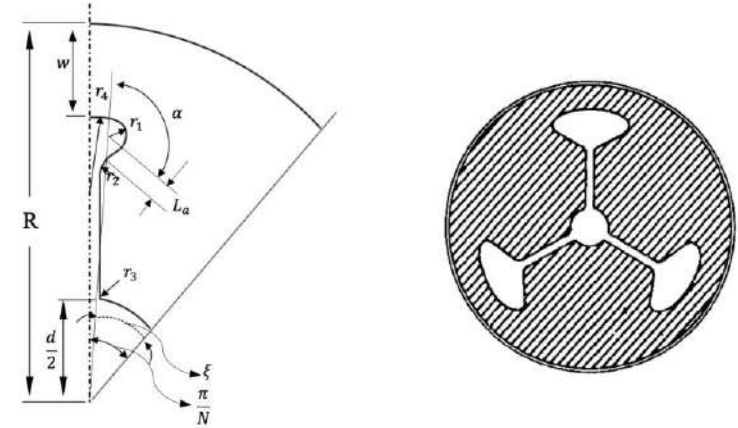

(D) Dogbone

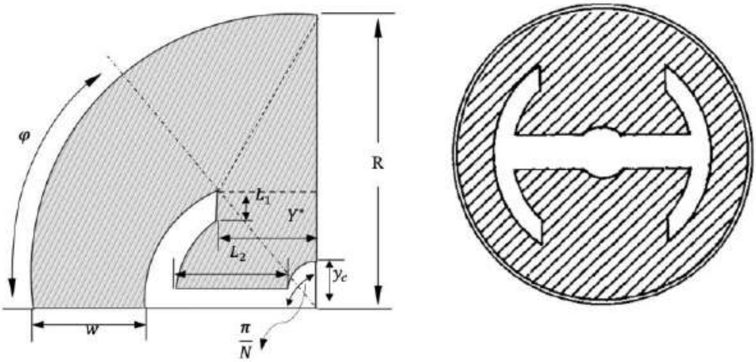

(E) Anchor

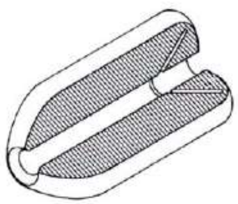

(F) Conocyl

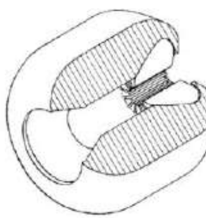

(G) Finocyl

Figure 32-Solid grains different configurations

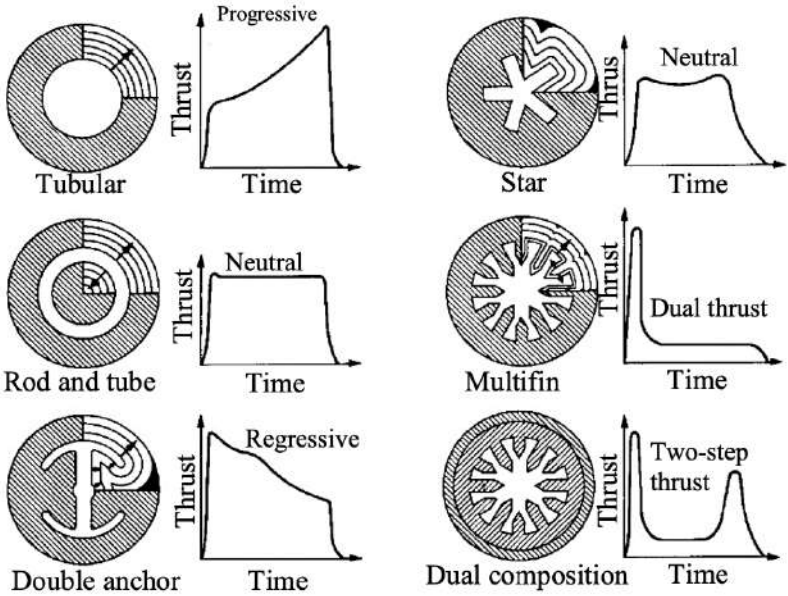

Figure 33- Internal-burning charge design with their thrust-time program, (from courtesy shafer).

In the grain design, the available volume fraction required in the engine compartment to embed the propellant is called volumetric loading fraction (V_l) , which is expressed as follows. Neutral combustion limits the application of each grain configuration to a certain range of (V_l), so volumetric loading fraction is one of the most important factors in choosing the suitable grain configuration. some of these parameters will be explained in the following sections.

$$V_l = \frac{V_p}{V_a} = \frac{I_{tot}}{I_{spd}\ \rho_p\, V_a} \tag{132}$$

V_l: Volumetric loading fraction

V_p: Propellant volume $\left(\frac{W_p}{\rho_p}\right)$, $in.^3$ (m^3)

V_a: Chamber volume available for propellant, $in.^3$, (m^3)

I_{tot}: Total impulse $(W_p . I_{spd})$, lbf. sec, (N. sec)

W_p: Propellant weight lbm (kg)

ρ_p : Propellant mass density $lbm/in.^3$, (kg/m^3)

Another influential factor in the selection of the appropriate grain configuration is the web fraction so that the range of the applicable web fractions depends on the range of available propellant burning rates. For internal burning, the following relation provides the required web fraction in terms of burning duration (t_b). D, d are the outside and inside diameter of grain, and w_f is the ratio of the web to grain outer radius, which is frequently written as $(D - d)/D$ after d has been determined.

$$W_f = \frac{2rt_b}{D} \tag{133}$$

The values of volumetric loading fraction for Internal-External burning tube (ID-OD), Internal burning tube (Shell), and Rod and Shell-type configuration are obtained from the following expression, respectively:

$$V_l = W_f(1 - W_f)\frac{\pi D^2 L}{V_a} \tag{134-1}$$

$$V_l = W_f(2 - W_f) \tag{134-2}$$

$$V_l = 2W_f \tag{134-3}$$

The controllable type of solid fuel rockets includes hybrid rockets, which include solid fuel and liquid oxidizer. The process is that the fuel and oxidizer are placed in two separate tanks in the rocket and the liquid oxidizer, which is inside a pressure regulating tank, is connected to the solid fuel tank by a valve and injected into it. And after combustion, the hot exhaust gases that cause the production of thrust are released from the exhaust. Typically, the fuel is a solid polymeric hydrocarbon such as hydroxyl-terminated polybutadiene (HTPB), an oxidizer can be any of the oxidizers used with liquid-bipropellant engines (e.g., hydrogen peroxide). Since HTPB has a low burning rate, it might cause the structural failure of the combustion chamber due to containing many holes in solid fuel that are exposed to high heat for burning. The concept and schematic of this type of rocket have shown in figures 35 and 36.

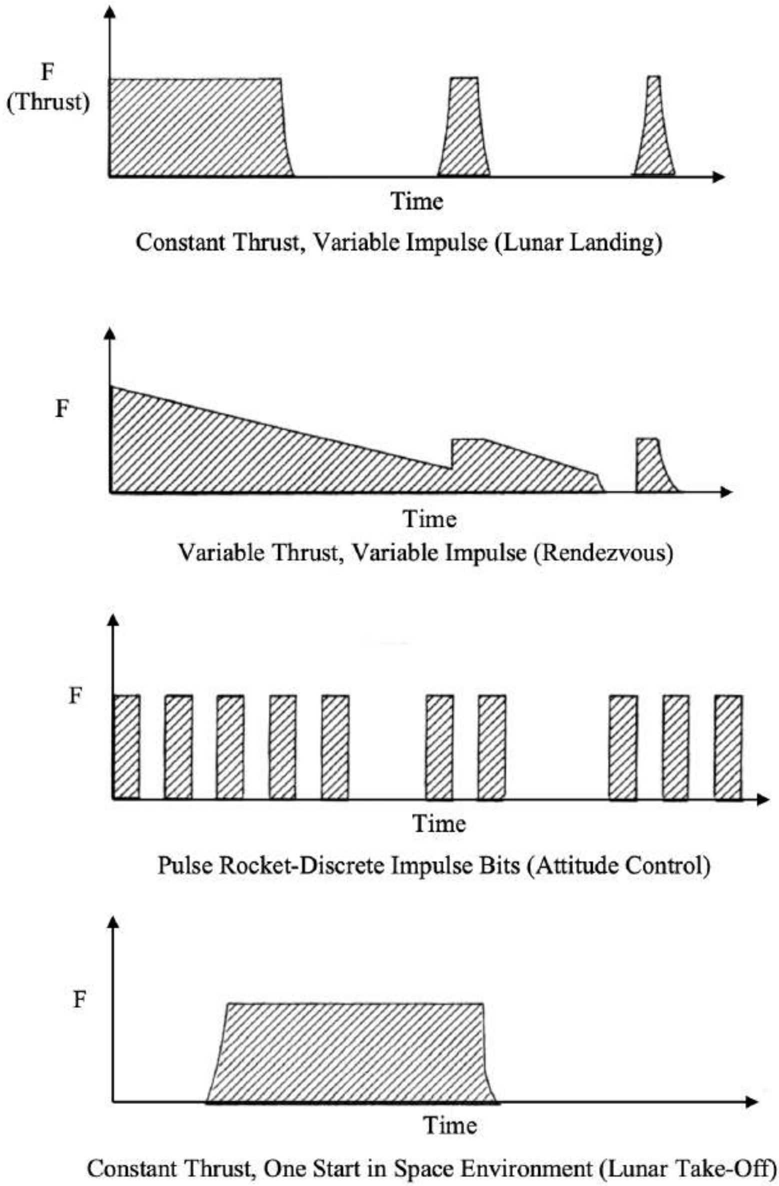

Figure 34- Typical thrust-time plots for space engine missions. From NAS-7-103

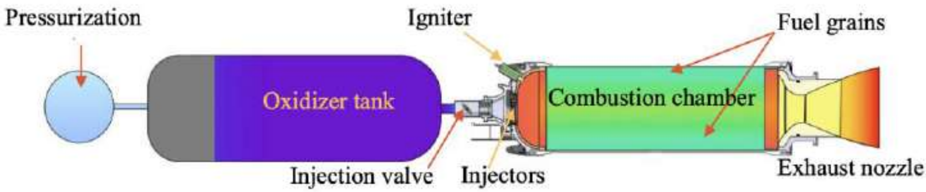

Figure 35- Experimental Study of the Swirling Oxidizer Flow in. Adopted from Experimental Demonstration of the Vacuum Specific Impulse of a Hybrid Rocket Engine.

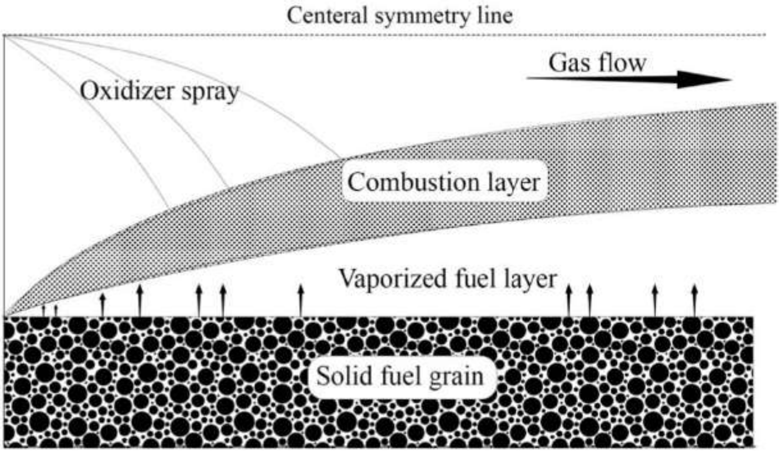

Figure 36- Hybrid rocket combustion schematic

PROPELLANT AND PROPULSION

In retrospect, it may seem surprising that until World War I, missiles were neither comparable in range nor accuracy with rifles. Before World War I, the only propellant used in rockets was a kind of black powder (consist of a mixture of charcoal, sulfur, and potassium nitrate (saltpeter)). Rocket propellant technology did not advance until the time smokeless powder had been developed. Goddard can be considered one of the pioneers of change in the missile and rocket industry. Developments by Dr. Goddard include the use of propellants such as gasoline and oxygen in liquid propulsion systems in 1909, as well as an ideology of using liquid hydrogen-liquid oxygen for interplanetary rockets (which are widely used today). The first experience of double-base solid propellant (nitrocellulose-niter, glycerin) is another of his honors. These developments in the propellant industry continued during World War II, with the introduction of fuels such as alcohol, gasoline, and aromatic amines, as well as oxidizers such as liquid oxygen, hydrogen peroxide, and fuming nitric acid for liquid propulsion systems. During the war, it was the belief that large rockets used only liquid propellant with an oxidizer; and solid propellants were used only for small short-range missiles (about a few miles) such as bazooka. But the growing importance of solid propellants has changed this point of view to such an extent that they can be used not only for long-range missiles but also in multi-stage rockets (including satellite-based rockets).

Propulsion is a chemical mixture of fuel and oxidizer that participates in a chemical reaction to produce thrust, which in turn produces extremely hot gases; These expanded gases exert pressure that propels the rocket forward while they're expelled in the form of a jet through the nozzle at the rear.

Selecting the adequate propellant for each engine is a vital criterion of designing the propulsion system that directly influences all sub-systems' performances. Generally, propellants are divided into four categories such as liquid, solids, and hybrid propellants. In terms of liquid rocket engines, propellants fall into monopropellants, bipropellants, cryogenic propellants, and storable liquid propellants. It should be noted that in some cases, additive materials (e.g., Inco625, Inco718, SS347, GRCop-84, etc.) might be required to be mixed with liquid propellant to improve some of its properties such as cooling characteristics, deducing freezing point and corrosive effects, facilitating ignition, and stabilizing combustion.

SOLID PROPELLANT

The earlier rockets used a type of black powder as a propellant. As mentioned, this black powder was a type of gunpowder that combines charcoal (15%) as a fuel and potassium nitrate (75%) as an oxidizer, and sulfur (referred to as brimstone) (10%), which lowers the ignition temperature required to start the reaction. But scientists have been trying to improve the performance of these rockets, and as a result, in the 1950s, they were able to achieve a high-energy propellant for solid rockets. It was a combination of fine aluminum powders as fuel and ammonium perchlorate and mineral salt as oxidizers held together by a polymeric binder, polybutadiene-acrylic acid- acrylonitrile terpolymer (PBAN), which is also consumed as fuel. The mixture, with the rubber like substance with the consistency of a hard rubber eraser, is then packed into a steel tank. This solid propellant storage tank, which is also the engine compartment, is made of steel, aluminum, or plastic-fiber composites. Aluminum is one of the most suitable options as a solid fuel due to the abundance in the earth and also its high reactivity. Ammonium perchloride (i.e., the salt of perchloric and ammonia) is also a very strong oxidizer. Some ingredients used in this type of propellant include synthetic rubber, nitrocellulose plasticized with energetic liquids such as nitroglycerin. The combustion reaction of this solid propellant is as follows:

$$2.0\ NH_4ClO_4 + 3\,{}^{1}\!/_{3}\ Al \rightarrow 2.0\ HCl + 3.0\ (H_2O)_{(g)} + N_{2_{(g)}} + 1\,{}^{2}\!/_{3}\ Al_2O_3 + lots\ of\ energy$$

This heat of reaction raises the temperature inside the boosters to 5000 °F, which leads to the rapid expansion of gaseous nitrogen and water vapor. These expanded gases will pass through the funnel nozzle the thrust needed to lift the rocket from the launch pad will be provided.

In general, solid propellants can be classified into homogeneous and composite. The first category includes the simple base and double base propellants, which contain unstable chemical compounds. These homogeneous propellants do not contain any crystals but include sufficient chemically bonded oxidizer material to sustain combustion. Simple base propellant consists of a component (usually nitrocellulose) that has both oxidizing and reduction properties. In contrast, the double-base propellant is usually composed of nitrocellulose and nitroglycerin, to which a plasticizer is added. Homogeneous propellants under normal conditions usually have a specific impulse of less than 210 s. Since these engines do not produce traceable fume or visible exhaust plume, smaller size, and instantaneous readiness, they are mostly used in the defense industry. Use in side-steps, such as using at stages separating, space exploration instruments, astronauts escape system (e.g., Mercury with 2 engines and Apollo with 3 engines arranged in tandem), manned spacecraft injected as satellites by sounding rocket or lunar and planetary probs, tank pressurization, turbopump starters, attitude controls, and axillary power system are another application of this type of propellant. Because many of these propellants are based largely on a colloid of nitroglycerin and nitrocellulose, they are often referred to as double-base propellants (this differentiates them from many gun powders which traditionally have been based on one or the other), (adopted from ADA250424). The composite is another type of solid propellant, which also has two crucial ingredients (namely fuel and crystalline, finely ground oxidizers), neither of which would burn satisfactorily without the presence of the other. Modern composite propellants are heterogeneous powders (mixtures) consisting of mineral salts and sometimes ammonium perchlorate, which account for 60% to 90% of the propellant mass, and aluminum powder as the fuel. It should be noted, however, that the release of perchlorate into the environment will result in an unsuccessful launch. Composite propellants often are identified by the type of binder used. Two of the most famous binders are polybutadiene acrylonitrile (PBAN) and hydroxy-terminator polybutadiene (HTPB). This combination is used in major U.S. space boosters' application. Higher performance is obtained by using more energetic oxidizers such as cyclotetramethylene tetranitramine (HMX) and by energetic plasticizers in the binders or by energetic binders (e.g., nitrocellolous-nitrogelycerin system). As another great combination to improve specific impulse, lithium ozonide as oxidizer, nitropolymers and acetylenic polymers as fuel-binders or light metal hybrids as pure fuel can be mentioned. Freezing a mixture of oxygen and hydrogen or a light metal hybrid is another way to use more effectively solid propellant, which are known as an ultra -energetic solid propellant. The advantage of using some cold solid propellants (e.g., BeH_2 and frozen hydrogen peroxide) is the generation of a theoretical specific impulse of about 500_{sec}. Compared to HTPB, PBANs have a higher specific impulse, density, and higher burning rate, but in addition to their advantages, it is more difficult to mix and process and requires a higher burning temperature. In contrast, HTPBs are more robust and more flexible. Solid propellant engines have many applications. Small motors, for example, are often used in the final stages of a launch vehicle or attached to payloads to take them to higher orbits. Intermediate engines such as the Payload Assist Module (PAM) and the Inertial Upper Stage (IUS) provide even more power to place satellites in geosynchronous orbit or planetary trajectories. Stage zero on Titan (III-C), Delta, and Space shuttle are examples of the bigger solid engine (10 to 13 ft in diameter) application which fire on as boosters to provide lift-off for the entire rocket. In each space shuttle booster (stage-zero), almost half a million kilograms of propellants will be consumed on the production of thrust in about 2 minutes.

One of the characteristics of well-designed propellant charges is that during ignition, the grains (i.e., a physical mass or body of the propellant) burn smoothly without severe surges or detonations. Propellant mass flow, operating pressure, thrust, and durations are among the factors that are calculated according to combustion characteristics. The shape, size, exposed burning surface, and geometric form of the grains also affect the combustion chambers. Generally, any solid propellant usually contains the following components: (adopted from ADA250424)

- Oxidizer (nitrates or perchlorates).
- Fuel (organic resins or plastics).

- Chemical compounds combining fuel and oxidizer qualities (nitro-cellulose or nitroglycerin).
- Additives (to control fabrication, process, burning rate, etc.).
- Inhibitors (bonded, taped, or dip-dried onto propellant) to restrict burning surfaces.

The main purposes of using additives in solid propellants are as follows: (adopted from ADA250424)

- Use as a catalyst (accelerate or decelerate burning rate).
- Increase chemical stability to avoid deterioration during storage.
- Control various processing properties of propellant during fabrication (curing time, fluidity for casting, wetting agent, etc.).
- Control heat absorption properties of burning propellant.
- Increase physical strength and decrease elastic deformation.
- Minimize temperature sensitivity.

Table 1 shows some of the solid propellants and binders which are used for spacecraft or space vehicles.
Factors that make solid propellant a candidate for continued use in the future rocketry industry include inherent simplicity and high reliability in dynamic and weightless conditions.

Solid propellant	Binder
Poly-urethane	Crystalline oxidizer with/without aluminum/beryllium powder
Poly butadiene-acrylic acid	
Poly butadiene-acrylic acid-acryloni	
Carboxyl-terminated poly butadiene	
Thermoplastic polymers	

Table 1- Some solid propellants and binders are used in spacecraft.

LIQUID PROPELLANT

Liquid propellants are considered to be the main propellants of chemical rockets that estimate the required kinetic energy due to their ability to release high chemical energy within combustion. The high thermal energy generated leads to the expansion of the working fluid, which eventually leads to the production of thrust. In addition to generating thrust, these propellants will also be used in gas generators to provide the power needed to drive other engine components such as turbocharged pumps, hydraulic pumps, and alternators. The term liquid propellant includes both oxidizer and fuel in bi-propellants and fuel in mono-propellant systems. The combinations of the tripropellant also include a surplus solid component. Hybrids are like bipropellant systems in that they have an extra liquid component, whereas a mixture of fuel and oxidizer is in the form of solid grains. The tri-propellant are used in two ways according to their combinations. The first case is related to simultaneous burning, i.e., three propellant streams start to burn simultaneously. This propulsion system includes high energy density metal additives such as beryllium and lithium so that the energy from the reaction of solid and liquid propellants provides the activation energy needed for the reaction of metal particles and oxidants. The second case is that the propulsion system consists of two fuels and an oxidizer so that the engine can have the advantage of rocket staging, i.e., the engine has the ability to change the fuel during flight. The ability to combine high thrust of condensed fuel early in flight with the high special impulse of the lighter fuel later in the flight. Hybrid systems where the fuel is in a liquid state and the oxidizer is in the form of solid grains are known as inverse hybrids. Heterogeneous propellants are a group of energetic powders suspended in a thick liquid medium.

Choosing the right propellant type can be very broad-based on the importance of the project and the type of mission. Performance, storability, physical characteristics, transportation, safety, cost, and ease of access are among the parameters that must be considered in choosing the right type of propellant. One of the best methods that can be used to select the right propellant for a particular project is a synthesis program, which mixes the propellants to obtain new compounds that are theoretically desirable properties and meet many specific needs. Therefore, with a right understanding of the physical and chemical properties, proper selection of materials, components, and use of appropriate methods and equipment, the choice of liquid propellant is done effectively and safely.

One of the most important considerations in propellant selection is the high performance and lightweight of the system. In military applications, the need for immediate readiness by the military, which leads to long-term storage and ease of transportation, is another key consideration in choosing the type of propellant. Other fundamental factors that include the chemical and physical properties of the propellants can be mentioned as follows:

- Chemical energy: Since the products of the combustion process are released as hot gases from the exhaust, the higher the volume of exhaust gas per consumed propellant (i.e., the molecular weight of the propellant) and the higher the temperature of the exhaust gas (i.e., flame temperature), the combustion performance leads to be higher value.

- Liquid range: As mentioned, one of the most basic and rudimentary regards that will be considered in selecting the right propellant is the lightweight of the system. It should be noted that the operating environment of the rocket or spacecraft determines the freezing conditions and boiling point of the propellant. Propellants with low-boiling temperatures require heavy-duty tanks or equipment's to keep the propellant cold. The high vapor pressure of the propellant results in the intricate design of the pumps and the regeneratively cooled thrust chamber. In other words, servicing the cryogenic systems requires special handling procedures and equipment. The vapor pressures, freezing, and boiling points of some oxidants with selected propellants are shown in Tables 2 and 3 and figures 38.

- Stability: One of the features of propellant that is highly regarded in military applications is the ability to be prepared immediately, or its readiness, which in other words is the long-term storage of propellant in the fuel tank. The fact that the propellants can be stored in the tank for the required time without decomposing and forming new gas species or reacting with the tank wall is always one of the key points in choosing the right propellant. Because the appearance of any new chemical like metallic ingredients at high temperatures will have negative consequences on the whole system and especially on regenerative cooling. Factors such as resistance to mechanical and hydrodynamic shocks and adiabatic compression are the other important that should be considered.

- Reactivity: According to what was mentioned in the stability section, the reaction of the propellants with the tank wall and the occurrence of corrosion in the tanks and its components can lead to contamination of the propellant and clogging of filters and small passages. Also, reactivity with air and moisture is one of the cases that require unique transfer techniques.

- Density: The high density of the propellant allows the use of smaller tanks. Thus, the overall inert weight of the vehicle is minimized. On the other hand, by reducing the expansion coefficient of propellant, rockets or spacecraft are used in a wider temperature range without loss of performance. The specific gravities for common propellants are provided in tables 2 and 3, and their variations with temperature changes are depicted in figure 40.

- Viscosity: As the basics of fluid dynamics, we know that there is an important factor against fluid motion, which is called viscosity. When a lower viscosity propellant is utilized, there is less pressure drop in the combustion chamber feed systems and injectors, which minimizes the need for large pumps with heavy pressure feed systems.

- Ignition: In some cases, the use of multi-stage rocket systems reduces reliability because there may be a problem in starting the combustion of each stage (e.g., low reliability of secondary ignition in space) or the end of the previous stage (i.e., separation). While using hypergolic fuel, the weight of the separation systems and the weight of the extra ignition system are removed from the system.

- Logistics: The cost of producing propellant is another part of choosing the right propellant for a particular application. In addition to the cost of its production, which itself can depend on several factors, the costs of maintenance, storage, handling, and transportation are also influencing factors that are considered as the cost of propellant production.

The best oxidizers are O and F, while their molecular form is O_2 and F_2 are cryogenic. Cl and Br can also be mentioned as elements that strengthen the physical properties of oxidants but will enhance molecular weight. Nitrogen is used as a backbone in the transport of O and F and several oxidants while producing a slight increase in performance. Hydrogen is also a good choice as a working fluid and oxidizer due to its low molecular weight. O_3, F_2, OF_2, NF_3, O_2, N_2F_4, ClF_5, ClO_3F, ClF_3O, ClF_3, N_2O_4, H_2O_2, and HNO_3 are some of the best oxidants that have the highest performance, respectively, where the first five are cryogenic. The number of the elements considered as fuel or its ingredient is limited. Depending on the heat of combustion, any of the elements such as Al, H, Li, Be, B, C, and Mg can be employed. Nitrogen, as in oxidizers, contributes little to the heating of combustion but is used as a good building block for the transport of hydrogen and the production of amine groups. Carbon can also be used to carry hydrogen, which leads to hydrocarbons. The disadvantages of using metals can be pointed out that when oxygen is used as an oxidizer, they form solid oxide products that are not expandable and even lead to a specific impulse penalty. Usable fuels include hydrogen, ammonia and derivatives (amines, hydrazines), hydrocarbons, Borohydrides, and alcohols. As mentioned earlier, the desirable conditions arise from higher-density propellants. The method used to take advantage of this is super-cooling of the liquid cryogenic propellant because it makes the propellant denser, resulting in more fuel being transported in a tank of the same volume. Reducing the vapor pressure and thus reducing the working pressure of the tank, which is done as a result of this compression, decreases the stresses of the tank wall and, as a result, makes its wall thinner. The smaller tank volume and thinner wall thickness decrease the size and weight of the vehicle as well as increase the payload capacity. The cryogenic propellant is transferred from the fuel tank to a ground cooling unit, which is a combination of a heat exchanger and compressor and is cooled to a temperature much lower than the normal boiling point. The compressor reduces the coolant bath pressure, resulting in a low-temperature boiling fluid being used to cool the recirculating fluid. This cooled propellant is then returned to the vehicle's fuel tank. A schematic of the ground facilities for cryogenic propellant densification is depicted in figure 39.

oxidizer	Molecular weight	Freezing point		Normal boiling point[a]		Specific gravity
		°F	K	°F	K	
Bromine pentafluoride (B_rF_5)	174.9	-78.3	211.8	104.9	313.6	2.47 @ 298 K
Chlorine pentafluoride (ClF_5)	130.4	-153.4	170.2	7.3	259.4	1.78 @ 298 K
Chlorine trifluoride (ClF_3)	92.4	-107.1	195.9	53.2	284.9	1.81@ 298 K
Florox (ClF_3O)	108.4	-86.8	207.1	84.7	302.6	1.85 @ 298 K
Fluorine (F_2)	38.0	-362.3	54.1	-306.6	85.0	1.50 @ NPB
Fluorine/Oxygen (Flox) (70% F_2/30% O_2)	36.2	-	-	-304	86.5	1.24 @ NPB
Hydrogen peroxide (90 % H_2O_2/ (10% H_2O)	32.4	11.3	261.6	286.1	414.3	1.39 @ 293 K
Hydrogen peroxide (98% H_2O_2)	34.0	31.2	272.2	302.4	423.4	1.45 @ 293 K
MON-10 (10% NO/90% N_2O_4)	85.8	-9	250.4	50.8	283.6	1.47 @ 273 K
Nitric acid-type IIIA[c]	59.4	-56	224.3	140	333[b]	1.55 @ 298 K
Nitric acid-type IV[c]	55.0	-35	235.9	76.5	297.9[b]	1.62 @ 298 K
Nitrogen tetroxide (N_2O_4)	92.0	11.8	261.9	70.1	294.3	1.43 @ 293 K
Nitrogen trifluoride (NF_3)	71.0	-341	65.9	-201	143.7	1.54 @ NPB
Oxygen (O_2)	32.0	-361.1	54.7	-297.3	90.2	1.15 @ NPB
Oxygen difluoride (OF_2)	54.0	-371	49.3	-228.6	128.4	1.52 @ NPB
Ozone (O_3)	48.0	-316	79.8	-170	160.9	1.61 @ 78 K
Perchloryl fluoride (ClO_3F)	102.4	-231	127	-52.3	226.3	1.39 @ 298 K
Tetra fluoro hydrazine (N_2F_4)	104.0	-261.4	110.2	-99.4	200.2	1.56 @ 173 K

a: NPB is normal boiling point at 1 atm.
b: Bubble point, where liquid appears to boil.

Table 2- Physical properties of liquid oxidizers- Adopted from Liquid Rocket Propellants.

Fuel	Molecular weight	Freezing point		Normal boiling point[a]		Specific gravity
		°F	K	°F	K	
Aerozine-50 (50% Hydrazine/50% UDMH[a])	41.8	22	267.6	158	343.15	0.899 @ 298 K
Ammonia (NH_3)	17.0	-107.9	195.4	-28.05	239.8	0.682 @ NBP
Aniline ($C_6H_5-NH_2$)	93.12	-207.4	266.8	363.9	457.5	0.999 @ 293 K
Diborane (B_2H_6)	27.69	-264.8	108.3	-134.5	180.6	0.438 @ NBP
Diethylcyclohexane [$(C_2H_5)_2C_6H_{10}$]	140.3	-110.2	194.2	345	447.2	0.804 @ 293 K
Diethylenetriamine (DETA) [$(NH_2C_2H_4)_2NH$]	103.2	-38.2	234	405	480	0.953 @ 298 K
u-Dimethyl hydrazine (UDMH) [$(CH_3)_2N_2H_2$]	60.1	-70.9	216.0	144.2	335.5	0.791 @ 298 K
Ethane (C_2H_6)	30.07	-297.9	89.95	-127.6	184.48	0.548 @ NBP
Ethanol (C_2H_5OH)	46.1	-174	158.7	172.9	351.4	0.789 @ 293 K
Ethene (C_2H_4)	28.054	-273.1	103.6	154.66	169.4	0.567 @ NBP
Ethylene dihydrazine ($C_2H_{10}N_4$)	90.1	55.4	285.95	> 491.[b]	> 528.[b]	1.096 @ 298 K
Ethylene oxide (C_2H_4O)	44.01	-168	162	50.9	283.6	0.887 @ NBP
Furfuryl alcohol (C_5H_5OOH)	98.1	-26	240	340	444	1.13 @ 293 K
Hybaline A-5	109.2	-58	223.2	505	536	0.736 @ 293 K
Hydrazine (N_2H_4)	32.04	34.75	274.7	236.3	386.6	1.008 @ 293 K
Hydrogen (H_2)	2.016	-434.8	13.8	-423.3	20.21	0.0709 @ NBP
JP-X (40% UDMH/60% JP-4)[a]	89.3	< -71	216	211	373	0.80 @ 293 K
Kerosine (RP-1) (H/C = 2.0)	172	< -50	228	350-525 450-547	450-547	0.80-0.81 @ 293 K
Methane (CH_4)	16.04	-296.5	90.6	-258.7	111.6	0.451 @ NBP
Methanol (CH_3OH)	32.04	-144	175.4	147	337	0.791 @ 293 K
MAF-1	100.0	-148	173	170	350	0.87 @ 298K
MAF-3	90.2	< -65	219	-	-	0.917 @ 298K
MHF-3 (86% MMH/14% N_2H_4)[a]	43.41	< -65	219	193.4	362.8	0.889 @ 298K
MHF-5	45.35	-43.6	231.2	205.8	369.7	1.011 @ 298 K
Monomethyl hydrazine ($CH_3H_2H_3$)	46.07	-62.3	220.8	189.8	360.8	0.879 @ 293 K
Nitromethane (CH_3NO_2)	61.04	-20.2	244.1	214	374.3	1.135 @ 298 K
Pentaborane (B_5H_9)	63.17	-52.2	226.4	140.1	333.2	0.623 @ 298 K
n-Propyl nitrate ($C_3H_7NO_3$)	105.1	< -150	172	230.9	383.6	1.058 @ 298 K
Otto Fuel II	186.52	-18.4	245.2	decomposes		1.232 @ 298 K
Propane (C_3H_8)	44.11	-305.84	85.5	-43.7	231.1	0.5853 @ NBP
Quadricyclane (C_7H_8)	92.14	-	-	226.4	381	0.982
Shelldyne-H	186.7	-101	200	460	511	1.11@293K
U-DETA (MAF-4, Hydyne) (60% UDMH/40% DETA)[a]	72.15	< -120	188.7	161	345	0.858 @ 289 K

a: Weight percent.
b: Estimated values courtesy of GenCorp Aerojet Tech Systems.

Table 3- Physical properties of liquid fuels- Adopted from Liquid Rocket Propellants

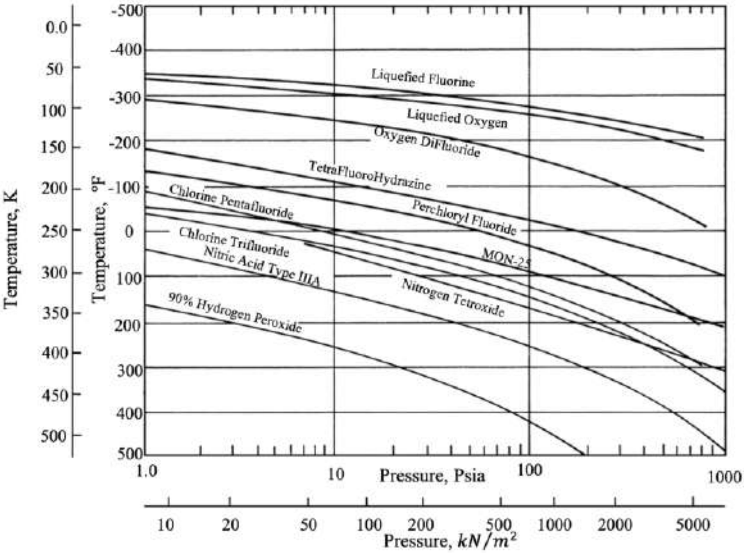

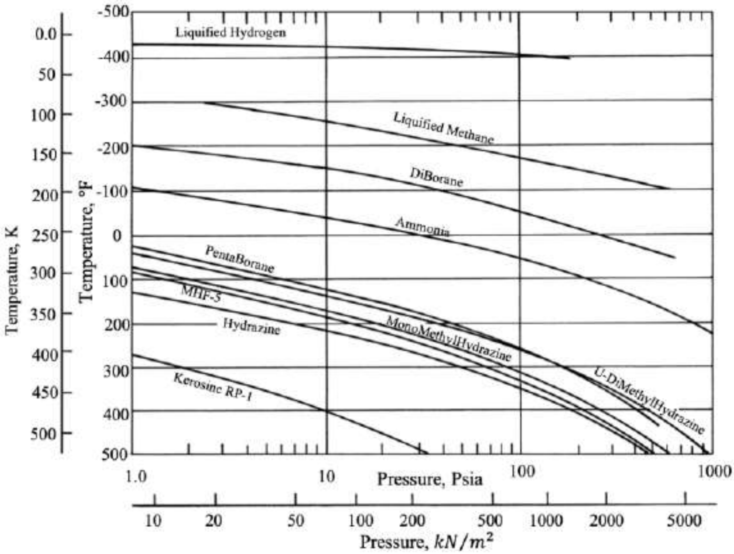

Figure 37- Vapor pressure for liquid oxidizers at top and liquid fuels at the bottom. Adopted from Liquid Rocket Propellants

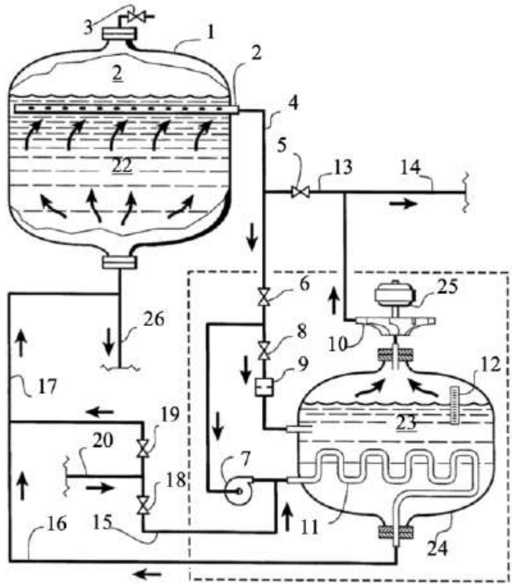

1) Vehicle tank
2) Recirculation manifold
3) Emergency relief valve (For In-flight pressure relief in case of a pressurization system failure during ascent of the vehicle).
4) Recirculation line
5) Ground vent valve
6) Pump isolation valve
7) Recirculation pump
8) Heat exchanger flow control valve
9) Metering orifice
10) Compressor
11) Heat exchanger coil
12) Liquid level sensor
13) Vent line
14) Vent line to an environmentally suitable capture device (not shown)
15) Feed line
16) Return line
17) Main feed line
18) Ground replenishment valve
19) Fill and drain valve
20) Main facility transfer line
21) Non-condensable gas such as helium
22) Cryogenic liquid propellant
23) Liquid bath

Figure 38- liquid cryogenic propellant densification ground facility (Adopted from US005644920A)

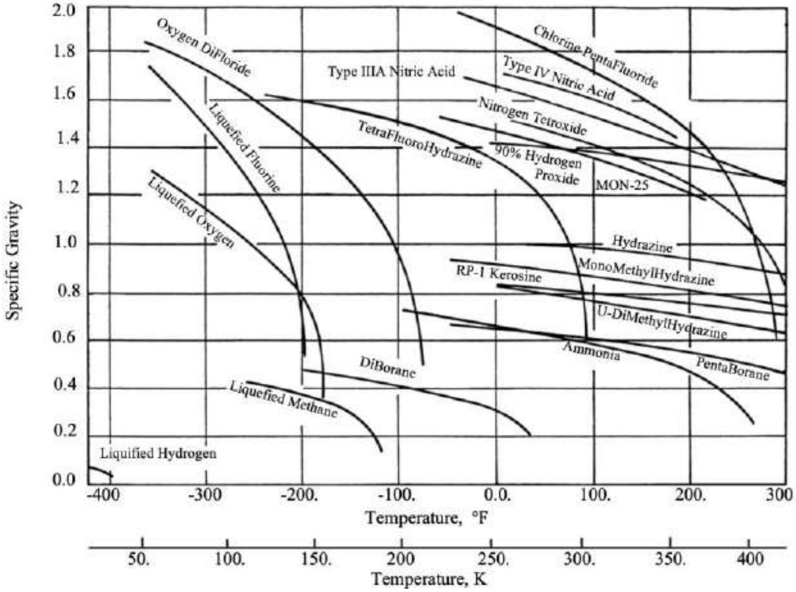

Figure 39- Specific gravity for several liquid propellants- Adopted from Liquid Rocket Propellants

HYBRID PROPELLANT

As the word hybrid implies, the propellants of this type of rocket are a combination of solid and liquid propellants. So that if it is solid fuel and a liquid oxidizer, it is called a normal hybrid, and if it is a liquid fuel and the oxidizer contains solid grains, it is called an inverse hybrid. Although many components of solid, liquid, and hybrid rockets are common, however hybrid rockets work differs from the other two categories. In solid rockets, the oxidizer and the fuel are mixed in two separate solid phases and begin to burn after the ignition temperature is reached at the exposed surface. In liquid rockets, the fuel and oxidizer near the injector form a combustible mixture. Combustion in both categories refers to the formation of a uniform mixture, while in hybrid rockets, the propellant is burned by a macroscopic diffusion flame whose oxygen-to-fuel ratio decreases steadily along with its chamber. These rockets look great because of the combination of the best features of liquid propulsion systems (such as high performance, clean exhaust, and safety) and solid propulsion (such as engine simplicity and low cost).

These systems are not explosive because an intimate mixture of oxidizer and fuel is not possible, so can be easily transported and manufactured. On the other hand, in hybrid rockets, unlike liquid ones, where both the fuel and oxidizer streams must be controlled, they control only one liquid flow rate (usually oxidizer) because the thrust can simply be stopped by cutting off the liquid flow. Therefore, these rockets have easier throttling and shut down. Unlike solid propellants in solid rockets, which are highly sensitive to cracking, hybrid propulsion has no sensitivity to cracking because solid fuel burns only when exposed to an oxidizing current. As mentioned in the section on liquid propellants, the number of compounds that can be used is very limited, while the wide range of propellants is applicable for hybrid propulsion. Furthermore, this variety of selection can be increased by adding metallic ingredients that also have higher energy levels without any restrictions. Hence, the density and as a result performance increase. Of course, in addition to these advantages, disadvantages such as lower regression rate and low bulk density, and lower flame temperature, resulting in lower specific impulse (although the generated specific impulse is still higher than ones produced by solid propulsion), reduced theoretical performance due to port opening presented during combustion, which changes the O/F ratio. It should also be noted that due to the low velocity of the transient current, its propulsion response to throttling is slow. However, to improve the increase in regression rate, multiple ports are used, which reduces the volume load of the fuel and moderates fuel sliver loss.

In these rockets, atomized liquid flows on the solid fuel near the port and reacts near it, causing the solid fuel to evaporate. Combustion is a turbulent flame that occurs in the flame region within the boundary layer at a distance y_b which is less than the momentum thickness of the boundary layer and at a velocity u_b which is less than the velocity of the outer edge of the boundary layer. The heat transfer from the combustion zone to the fuel surface causes its regression to feed the combustion layer, whereas for solid propellants, the theory of burning rate is cigarette burning and (r) represents the rate of burn. The rate of heat transfer to solid fuel and the heat of decomposition of solid fuel are the factors that control combustion. The mass flux of a liquid stream determines the amount of heat transfer and the amount of thrust.
The mass production rate in hybrid propulsion is written as follows:

$$\dot{m} = \dot{m}_{ox} + \rho_b A_b r_h \tag{135}$$

Where $\dot{m}_{ox}$, A_b, and r_h represent the oxidizer flow rate, burning area, and linear regression rate, respectively. The dependence of the burning rate (r_b) and the regression (r_h) on parameters such as pressure and mass flux are controlled by the mixing and chemical reaction processes. At first, the liquid oxidizer is sprayed onto the solid fuel by the injector, causing the fuel to start burning and evaporating, and then regressing. Initially, because diffusion is the predominant phenomenon, chemical kinetics and consequently pressure have less effect on regression. Marx man and Gilbert are the pioneers who have proposed a relation for the regression rate in 1963 based on boundary layer considerations. They showed how the local regression rate is a function of mass flux for a fuel slab submerged in an oxidizer stream:

$$\dot{r} = \frac{0.036G}{\rho_f}\left(\frac{Gx}{\mu}\right)^{-0.2}\left(\frac{u_e}{u_c}\frac{\Delta h}{h_v}\right)^{0.23} \tag{136}$$

$\dot{r}$: Instantaneous local fuel regression rate
G: Instantaneous mass flux
ρ_f: Fuel density
x: The distance along the port
μ: Absolute viscosity
$\frac{u_e}{u_c}$: The velocity ratio of the gas in the main stream to that at the flame
$\frac{\Delta h}{h_v}$: The ratio of the total enthalpy difference between the flame and fuel surface to the effective heat of vaporization of the fuel (Note that the coefficient 0.036 originally is derived for English units).

The simplified form of the above equation, which includes the mass flux of hot gases past the surface and the two constants a and n, is written as follows:

$$\dot{r}_h = aG^n \tag{137}$$

Usually, a is between 0.01 to 0.03, and n is considered 0.5 for laminar flows and 0.8 for turbulent flows. Due to the fact that the O/F ratio in hybrid engines is not constant, we can use the definition of the generated mass rate to express O/F in terms of the inner diameter of the fuel block that burns from the inside out as follows:

$$\frac{O}{F} \cong d^{2n-1}\left(\frac{m_{ox}}{\pi}\right)^{1-n} \bigg/ \rho_p a L \tag{138}$$

According to the above relation, in laminar flow, the O/F rate is constant, but in turbulent flows, when $n = 0.8$, the stream becomes oxidizer-rich, which will change the specific impulse. To solve this problem, two solutions have been proposed so that in the first method, the start of operations in the form of rich fuel is proposed. Over time, the flow reaches the equilibrium state, whereas it tends to the oxidizer-rich ones. The specific impulse in this method will change only about 1 to 2 percent. In the second method, which estimates a fixed O/F ratio, two injectors are used, one near the fore-end and the other at the head-end of the fuel block. At the first step of combustion, which is done in the head-end, the mixture is fuel-rich, and to optimize it, the final spraying is done, while in the next part, the combustion proceeds to the oxidant-rich, whereas the fore-end spraying rate continually decreases. Thus, The O/F ratio remains constant. Another feature of hybrid propulsion is that adding additives or even changing the entire propellant will have very little effect on the regression rate. The reason for this is the counterbalancing effect called the blowing effect. By elicitation of thermal equilibrium for the burning surface of the fuel:

$$\rho_b r_h = {q''}/{\Delta h_s} \tag{139}$$

Where Δh_s and q'' are the heat of phase change at the surface and heat flux toward the surface, respectively. It is observed that if r_h increases with decreasing Δh_s, as a result, the boundary layer becomes thicker and the surface heat flux and its gradient decrease. Therefore, the net regression rate will be increased. However, this amount of increase is less than what do we expect from a linear relationship. This non-linear correlation between the surface heat flux rate and the regression rate is such that with a 10% increase in the q'' leaves r_h virtually unaltered, and with a 35% increase, r_h will be increased only 10%.

LIFT-OFF ENGINES

The memorable Saturn V rocket, which made its first mission (Apollo 4) on November 9, 1967, and made its last flight on Skylab 1 on May 14, 1973, as well as its historic Apollo 11 mission on July 16, 1969. It was a three-stage rocket, the first stage of which was used for atmospheric conditions, and the next two stages of which were used outside the atmosphere (vacuum). The first stage of the Saturn V was powered by RP-1 as a hydrocarbon fuel, and consisted of five Rocketdyne F-1 engines capable of producing a thrust of $7{,}574{,}200\ lb$, while the total mass of the rocket was $6{,}348{,}659\ lb$.

The second and third stages of the rocket, which ran on liquid hydrogen, produced a thrust of $1{,}150{,}000\ lb$ and $207{,}000\ lb$, respectively. The oxidizer used in all stages was liquid oxygen. By calculating the ratio of the production thrust of the first stage to the total mass of the rocket, i.e., $\frac{7{,}547{,}200}{6{,}348{,}659} = 1.189$, it can be seen that this rocket produced about 19% more thrust than what was needed for the total mass. This created an acceleration of $(0.19\ g)$ as the initial acceleration for the whole set. The use time of each stage (**Burn time**) of this rocket was $168\ s$, $366\ s$ and $144\ s$, respectively. The reason for not using liquid hydrogen in the first stage of this rocket is also due to the low density of hydrogen because to produce such a high thrust, a large volume of this fuel was needed. Unlike the Saturn V, the space shuttle used three RS-25 engines as the main shuttle engine, each capable of creating a thrust of $376{,}000\ lb$ and $470{,}800\ lb$ in a vacuum. Of course, each solid propulsion engine generated a thrust of $3{,}300{,}000\ lb$, and it also uses two maneuvering motors that were installed on the orbiter to adjust the direction of the orbiter after entering the orbit, each of which has the ability to create a thrust of $6{,}000\ lb$. The main engines of the shuttles have the ability to change their production trust from $316{,}100\ lb$(i.e., 67% of the total trust) to $512{,}900\ lb$ (i.e., 109% of the total trust), In other words, the trust increases by approximately $4700\ lb$ per percentage change. These three values of trusts that are used in vacuum are called **rated power level**, **minimum power level** and **maximum power level**, respectively. These engines, as mentioned earlier, have a special impulse of $452\ s$ and the nominal thrust value for these engines is $491900\ lb$. The main engines of the space shuttle are the first reusable liquid-fuel rocket engines. Hence for such engines, another parameter is defined as **engine life: Total engine operating times that the value of other engine parameters can be maintained within the range of permissible changes**. According to the technical manual that Boeing has provided for the main engines of the space shuttle, these engines have a lifespan of $7.5\ hr$ ($832{,}500\ s$) or 2660 start (55), so that the time of each flight lasts about $520\ s$. The process of changing the thrust is such that about $20\ s$ with full power, combustion is done, and then with its rated power, it continues to move for about $10\ s$ and until the $40\ th$ second of flight, the thrust due to the sharp decrease in aerodynamic force on the rocket reaches its minimum value (65%). The thrust is held constant for up to 70 seconds and returns to its nominal value within $10\ s$, which is applied a $3g$ force to the astronauts in the orbiter.

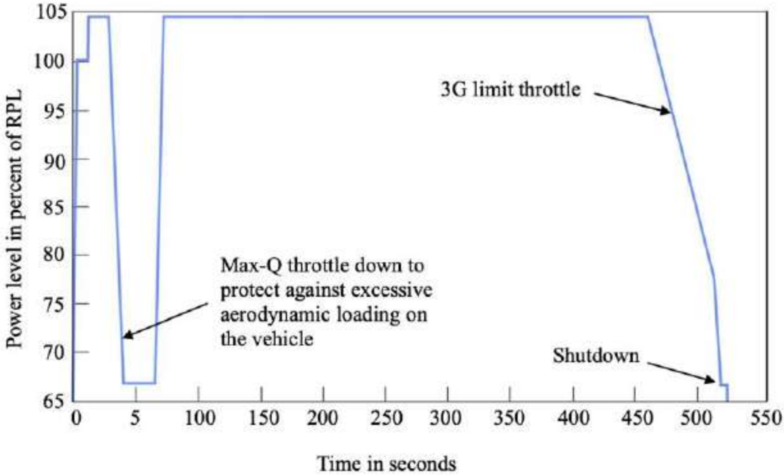

Figure 40- SSME throttling profile

This process continues until the $450th$ second, after which the thrust is reduced again in two steps, till to $510th$ second and reaches its minimum value, at which point the engine shuts down. The other category of motors used to precisely control the speed and direction of the orbiter in the circuit are the thrusters. The space shuttle consists of 38 primary thrusters and 6 vernier thrusters. These motors are of the pressure fed type, which uses the stored propellant to adjust the position of the orbiter. But these vernier thrusters have a limited life time due to the materials used in their chamber. A duration of operation of these thrusters (which known as pulses) is between milliseconds to a second. Engines can be classified based on initial energy and type of power supply system, type of propulsion and the possibility of controlling and changing the propulsion force and several other factors. The primary energy of motors can be chemical, nuclear energy, compressed gas energy, solar energy, or laser beam energy. Chemical rockets are also classified as liquid and solid fuel engines and hybrid engines, as mentioned earlier. Liquid fuel engines are also divided according to the type of power supply system and the type of propulsion consumed, which will be explained in detail below. Liquid fuel engines are divided into two parts based on the type of power supply system:

1. Turbo-pump feed system
2. Blowing feed system (without turbo pump).

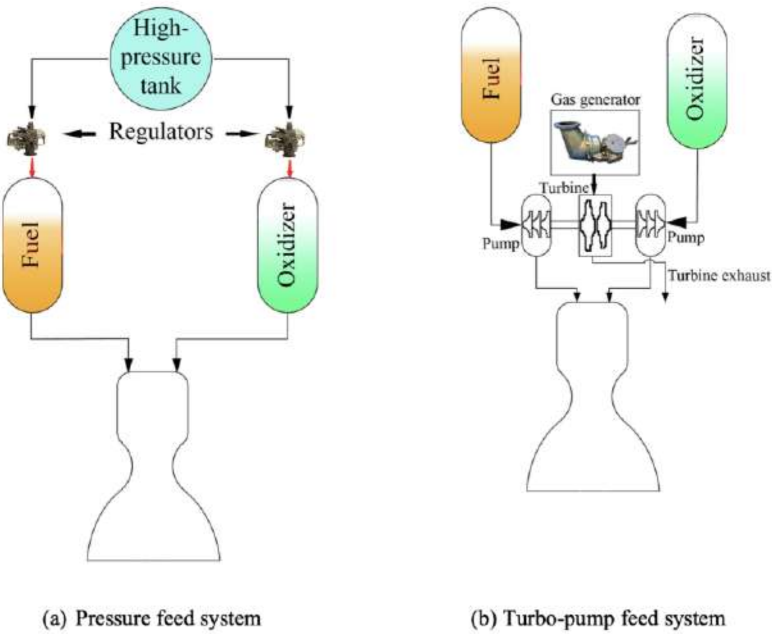

Figure 41- Propellant feed-system schematic

Propulsion System Engine Propellant Feed Technique	Advantages	Disadvantages
Tank Pressure Transfer	• Not complicated system due to lack of turbo pumps. • Simple to services. More reliable and maintainable.	• Low thrust and throttling limitation. • High strength tank due to high pressure. • Higher engine weight. • Considerable performance loss.
Turbopumps	• Fairly simple. • Wide thrust operating range. • Greatly increase thrust in a given envelope which reduces engine weight. • Higher area ratio in a given envelope, thus higher specific impulse. • Lower tank pressure, in turn, produces lower tank and feed system weight. • Flexibility in the choice of engine power cycle due to turbopumps.	• Low specific impulse and effective losses in performance • Gas-generator required • Complexity. • Turbopumps add cost. • Lower reliability than pressure feed due to more parts. • Turbopump safely On/Off. • Pump chill down required for cryogenic propellants. • Hazard control sub-system support (purge) requirement. • Drying and corrosion control throughout the ground processing cycle.
Reciprocating Pumps	• More operationally favorable pump drive solution, (e.g., electric vs. turbine).	• Limited applications (e.g., ACS/RCS), since only useable for high head, low flow applications. • Useable for non-continuous higher flowrate application if an accumulator used.
Electric Motor-Driven Pumps	• Simple. • Performance increases. • More efficient. • More reliability, dependability, safety. • Lower life cycle cost.	• Electrical generation and supply system requirement. • Higher engine and supply system weights for higher thrust. • Safety control concerns.

Table 4-Typical Propellant Feed Systems

In a blow-feed system, the fuel and oxidizer are sent through pipes directly into the combustion chamber due to the blowing that takes place inside their tanks. In the second category, the turbopump system, the fuel and oxidizer each have separate pumps to send them into the combustion chamber. Since this system requires a minimum pressure to prevent cavitation, thus itself includes a blow-fed system. Engines that use a turbopump feed system are divided into the open cycle and closed cycle engines categories. The main difference between the two systems is that in open cycle systems, the exhaust gas from the gas generator is released into the atmosphere after running the pump's turbine, but this does not happen in the closed cycle. In the closed cycle, the gases enter the combustion chamber and burn completely, thus producing useful thrust in the system. Combustion in the gas generator, if it occurs completely, will cause the temperature of the exhaust gases to rise, which may be beyond the durability of the turbine blades. And in an open cycle system, a lot of energy is lost when these high-energy gases are released into the environment. The gas generator used in the closed cycle can be of two types: The first type is (liquid-gas), which means that only one generator (which can be oxidizing or fuel) is used and the resulting gases enter the combustion chamber and then ignite. The second type is (gas-gas) which uses two gas generators and the resulting gases burn in the combustion chamber. There is another category of closed cycle so that the gas generator is no longer used in it, i.e., hydrogen, which has a high cooling capability, after cooling the chamber and even the nozzle, turns into a high temperature gas and makes run the pump's turbine, eventually enters the combustion chamber, where complete combustion takes place.

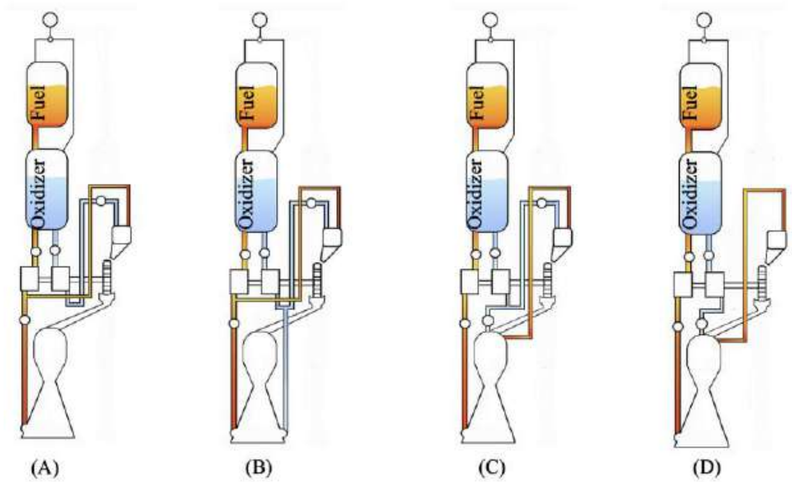

Figure 42- Closed cycle engine types

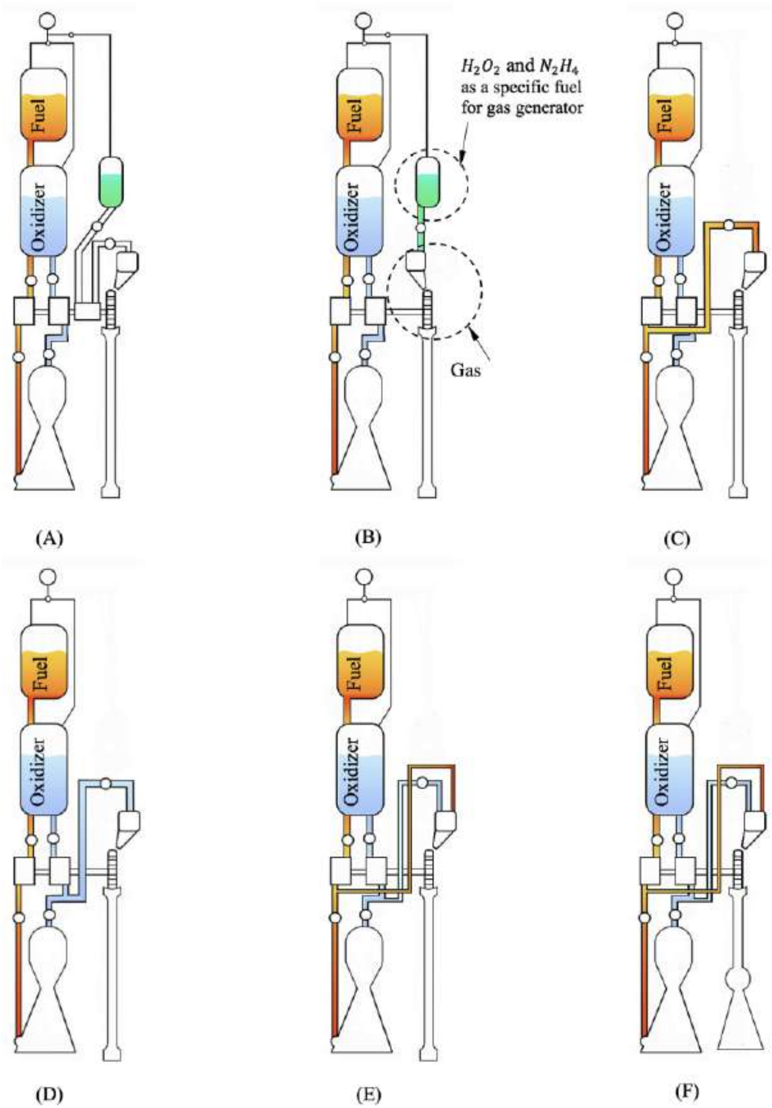

Figure 43- Types of open cycle engine

GAS GENERATOR

Rockets with liquid propellants are usually fed by high-pressure pumps, which are powered by hot gas turbines. These rotating turbines' hot gases can be obtained in two ways: thrust chamber bleed and gas generator. In addition to generating turbine hot gas, gas generators have other applications such as being used as auxiliary power drives, pressurization sources, and pre-burner for thrust chambers. In general, gas generators are divided into two subcategories based on the type of gas used: bipropellant (e.g., hydrogen proxied and hydrazine) and monopropellant, the first of which has a wider application, and its disadvantages include hot streak tendencies of design. The most serious problem in most monopropellant gas generators is catalyst problems. It should be noted that the turbine blades' durability is limited just in a predetermined temperature range, and the stratification of the gases even at reasonable overall mixture ratios can cause serious damage to the blades, duct, and manifold turbine, as well as the gas generator itself. On the other hand, most propellant compounds produce higher temperatures than the melting point of conventional metals, so mixing coolant propellant in the cold streams with near-wall combustion products can prevent its destruction and catastrophic phenomena. Although in the past the gas generator and the thrust chamber were designed in the same range of conditions and eventually led to hot spots and stratified flow, today's designing criteria of these two parts are not the same anymore. Because the gas generator, unlike other rocket components, requires a wider range of temperature, pressure, and flow rate, the gas generator must be designed in a relatively large operating range for both uniform combustion and controlled mixing.

As mentioned, initially the design of the thrust chamber and gas generator was the same and was done by the same engineers. This method called hot core injector means that an injector designed to operate with a higher temperature mixture ratio in the central area than in the outside surrounding area in which, some propellant was injected at the comparable to those used in the thrust chambers, and quenching propellant was added elsewhere. (From NASA SP-8081)

Following this design method, the hot-streak tendencies will cause severe burnout of the gas generator and turbine severe damage. Also, a lot of money was spent on improving the durability of this design, which was not the end of the problems, and after solving the main problem of durability, more small problems such as leaks, warping, and handling damage appeared. Durability improvements were generally made in two ways; First, the injector must be designed to minimize the area of hot zones, that is, to break these areas into a much larger number of smaller areas where mixing is easier to form. Practically, the basis of this method is to change the type of injector from hot-core to uniform mixture ratio (UMR) injector. The second technique to enhance durability is to use mixing baffles as well as reverse flow mixing chamber to expand the mixing range and maximize mixing, respectively. The reason for employing such components in a gas generator is that it is much more complicated to mix hot and cold gases in a gas generator than in a thrust chamber with higher turbulence. As mentioned earlier, hydrogen peroxide and hydrazine are among the most prominent propellants in the bipropellant category. For hydrogen peroxide, the silver screen catalyst showed the best results, while for the latter (hydrazine), the iridium catalyst appeared to perform better than the usual catalyst.

Gas generators generally consist of three parts: (from NASA SP-8081)

1. The manifold-valve assembly that controls the propellant entry to the injector and sequence of operation.
2. The injector that atomizes and distributes the propellants.
3. The body or combustion chamber where burning and mixing take place.

Experience has shown that for **normal** bipropellants (i.e., propellants whose thermal energy originates primarily from the oxidizer reaction and fuel, e.g., LOX-RP1 and LOX-LOH2), the design parameters for spraying, burning, and mixing are essentially autonomous from propellant characteristics (Density, storable or cryogenic, hypergolic or nonhypergolic, fuel-rich or oxidizer-rich). Also, almost all gas generators that have been used so far are fuel-rich based because:

- The damage potential of a hot streak is much lower in fuel-rich gases than with an oxidizer-rich gases.
- Turbine specific propellant consumption with fuel-rich gases is much better than oxidizer-rich, which usually has a higher molecular weight.

The finest atomization achieves when burning takes place in the smallest scattered locations, and mixing occurs more energetically with diluent. In the case of hydrocarbon gas generators, it should be noted that it is nearly impossible to describe fuel-rich combustion gases by conventional chemical kinetics techniques, as well as thermal cracks of hydrocarbons due to their high complexity. The mixing ratio for normal bipropellant gas generators is almost from 0.2 to 1.0, with hydrocarbons and hydrogen falling by approximately 0.3 at the lower limit and 0.98 to 1.0 at the upper limit, respectively. The mixing ratio for normal bipropellant gas generators is almost from 0.2 to 1.0, with hydrocarbons and hydrogen falling by approximately 0.3 at the lower limit and 0.98 to 1.0 at the upper limit, respectively. In gas generators, the rates of vaporization, and mixing are quite slow (several milliseconds), On the other hand, the oxidation rate will not matter due to the complete reaction in the chamber at full volume. All of this happened while the low level of mixing and vaporization did not match the experience of engineers in the design of the thrust chamber, meaning that the rates of comparable processes were much faster in the thrust chamber. Furthermore, this low mixing and vaporization rate will establish a wider range of combustion that requires minimum flow (secondary) atomization for fine stream injectors. And due to the presence of more additional fuel, the mixing ratio of (combustion products / excess fuel) will be longer compared to the thrust chamber, which emphasizes the use of gas generators in mechanical mixing devices. An extremely common point in the design of a gas generator with a thrust chamber is the extremely drastically unbalanced volumes in the manifold due to its heavily fuel-rich volume. As a larger common point, we can also refer to the assumptions of stream formation and placement. The concepts that improve the performance of the thrust chamber often improve mixing and suppress hot streaks on gas generators because the assumptions of gas generators' performance aren't serious. Two important principles of thrust chamber design were used in gas generators; First, the orifice rings were located at different points along the streamline of the chamber, creating a turbulent flow along the wall and preventing the central flow from mixing with the cooling layer near the wall. The second approach is an important part of the thrust chamber design, in which injected-partially mixed flow was forced to stagnate and then reverse direction.

There are other categories of propellants that contribute energy to the gas through Exothermic decomposition reactions Prior to the oxidation reactions, these propellants are known as **energetic** bipropellants. Aerozin-50 ($C_2H_{12}N_4$), UDMH (unsymmetrical dimethylhydrazine), and hydrazine are examples of this type of propulsion. In addition to the streaking problem, using this type of propellant causes reaction instability and even flameout in very low mixture ratios. Factors affecting stability in this type of bipropellant include exhaust temperature, injector design, chamber size, and chamber properties, although instability is usually due to marginal monopropellant decomposition reaction that alternately quenches and restarts. This temperature dependence is such that at temperatures below $1000°\text{F}$ $(811K)$, the reaction rate of the evaporated propellant is not fast enough to cause pressure pulses, and also at temperatures above

1400°F (1033K), since the propellants react quickly, there is sufficient time to form no accumulation and no pressure pulses.
The injectors used in this type of propulsion are usually hot-core injectors. In these systems, due to the low amount of oxidant that cannot be evenly distributed over the injector, the pilot light is formed for the reaction by the oxidizer injection system. The main goals of the injector designer are as follows: (from NASA SP-8081)

- Provide fine atomization of the large excess of fuel to enhance heat transfer to the fuel and at the same time prevent heavy drops from quenching the small heat sources.
- Provide void areas for enhanced recirculation of hot gases that are necessary to decompose the main part of the fuel flow.

REACTION CONTROL SYSTEMS (RCS)

The orbiter reaction control system is composed of forward RCS, which is located in the forward fuselage nose area, and aft RCS's that are located with the orbital maneuvering system on each side (right and left) of the orbiter in the OMS/RCS pods. The forward aft RCS unit is responsible for attitude (rotational) maneuvers (pitch, yaw, and roll) thrust, and small velocity changes along the orbiter axis during translation maneuvering. Each RCS consists of high-pressure gaseous helium storage tanks, pressure regulation and relief systems, a fuel and oxidizer tanks, a system that distributes propellant to its engine, and thermal control systems (electrical heaters), (from sts-rcs ksc science).

The fuel and oxidizer are supplied to the RCS engine by the gaseous helium pressure from helium tanks. In this system, monomethyl hydrazine, and nitrogen tetroxide are used as fuel and oxidizer, respectively. The propellants are earth-storable and hypergolic (they ignite upon contact with each other), (from sts-rcs ksc science). The propellants are supplied to the engines to generate thrust after atomization and ignition.
Space shuttle forward RCS comprises 14 primary and 2 vernier engines; the aft RCS has 12 primary RCS with 2 vernier engines in each pod. Each of the primary RCS engines can produce 870 pounds of vacuum thrust, whereas each vernier engine can only produce 24 pounds of vacuum thrust. The nominal chamber pressure of the primary and vernier engines are 150 and 110 $Psia$, respectively. The O-F (oxidizer-fuel) is 1.6 to 1 for each of these engines.

The primary engines are reusable for a minimum of 100 missions and are capable of sustaining 20000 start and 12800 second of cumulative firing. The primary engines are operable in a maximum steady-state thrusting mode of one to 150 seconds, with a maximum single mission contingency of 800 seconds for the aft RCS plus X engines and 300 seconds maximum for the forward RCS minus X engines as well as in a pulse mode with a minimum impulse thrusting time of 0.08 second above 125000 feet. The expansion ratio (exit area to throat area) of the primary engines' ranges from 22-to-1 to 30-to-1. The multiple primary thrusters provide redundancy. The vernier engines' reusability depends on chamber life. They are capable of sustaining 330000 starts and 125000 seconds of cumulative firings. The vernier engines are operable in a steady-state thrusting mode of one to 125 seconds maximum as well as in a pulse mode with a minimum impulse time of 0.08 second. The vernier engines are used for finite maneuvering and station keeping (ling-time attitude hold) and have an expansion ratio that ranges from 20-to-1 to 50-to-1. The vernier thruster are not redundant. (From sts-rcs ksc)

ORBITAL MANEUVERING SYSTEMS (OMS)

The orbital maneuvering system provides the thrust needed to orbit insertion, orbit circularization, orbit transfer, rendezvous, deorbit, and abroad the orbit. These systems are located in two separate pods, with aft control reaction systems on each side of the rear of the orbiter body. The OMS in each pod consist of a high-pressure gaseous helium storage tank, helium isolation valves, dual pressure regulation systems, vapor isolation valves for only the oxidizer regulated helium pressure path, quad check valves, a fuel tank, an oxidizer tank, a propellant distribution system consisting of tank isolation valves, cross feed valves, and an OMS engine. In fact, the hardware in these pod plays the role of performing speed maneuvers. The velocity required by the vehicle to adjust its orbit is approximately 2 $^{feet}/_{sec}$ for each nautical mile of changing altitude. There are five modes of attitude control consist of automatic, attitude hold, pulse, direct, and hardover (maneuverride). The automatic and attitude hold modes are selected with a Mode control: primary guidance and navigation system (PGNS) or lunar module or vehicle abort guidance system (AGS), which the pulse and direct modes with the Attitude control: roll, pitch, and yaw switches. After the main engine cutoff, the front RCS thrusters and aft RCS pods are responsible for providing the attitude hold until the external tank separation. Of course, it should be noted that RCSs are also active during the separation of the external tank to create a translation maneuver in the minus Z direction (approximately 4 $^{feet}/_{sec}$)

to keep the orbiter away from the external tank. This process continues until the pre-set OMS-1 maneuver time (before launch) arrives. It is also possible to modify and improve the OMS-1 thrusting performance period via the flight crew with the cathode ray tube keyboard; in this mode, astronaut command by displacing the attitude control assembly (ACA) hand controller, then this command is sent to the lunar model guidance computer (LGC). The LGC operates on these commands and provides signals to the jet drivers in the attitude and translation control assembly (ATCA) to perform rotation rates command to the reaction control subsystem (RCS). When the ACA controller back to the detent position, LGC maintained new attitude and AGS holds the vehicle (LM) in the new attitude.

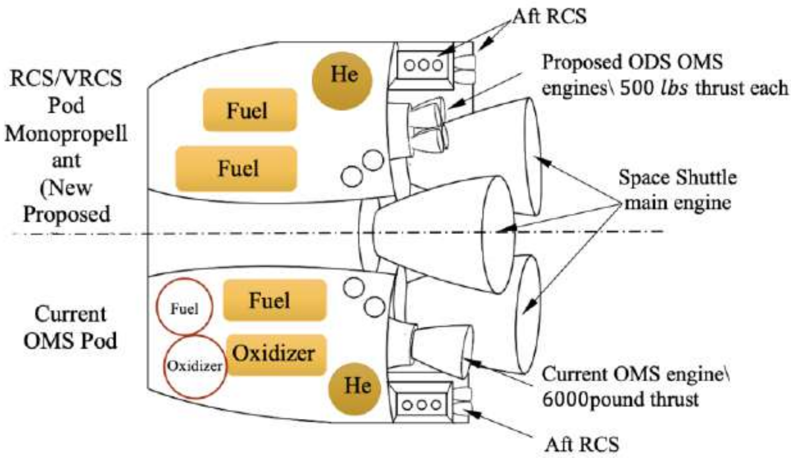

Figure 44- Space shuttle aft fuselage OMS/RCS concepts

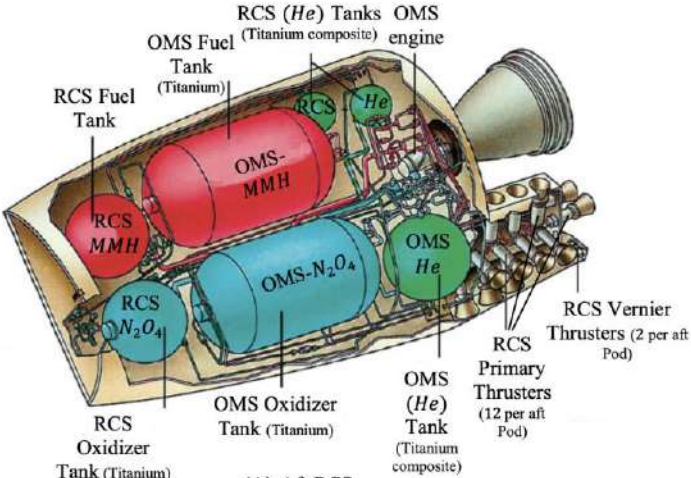

(A) Aft RCS

Current Space Shuttle:
38 Primary thrusters (14 forward, 12 per aft pod).
Thrust Level= 3870 Newtons (870 lb) Vacuum.
6 Vernier thrusters (2 Forward, 4 aft).
Thrust level= 106 Newtons (24 lb) Vacuum

OMS engine characteristic	
Thrust	6000 lb (vacuum)
Specific impulse	313.2 sec
Chamber pressure	125 $Psia$
Mixture ratio	1.65
Gimbal capability	±6° Pitch, ±7° Yaw
ΔV capability	1000 $^{ft}/_{sec}$ (65000 lb Payload)

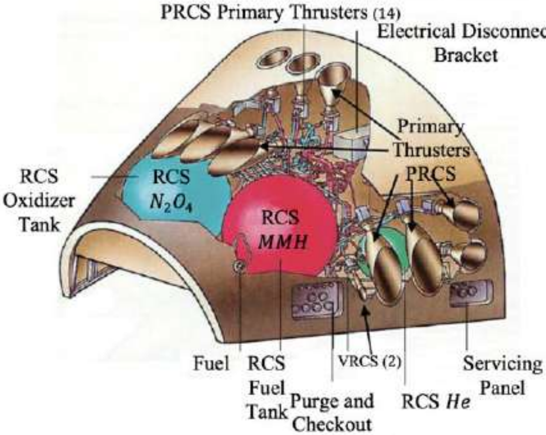

(B) Forward fuselage RCS

Figure 45- Space shuttle RCS. Adapted and modified from Space Shuttle System and Flight Mechanics Ulrich Walter Institute of Astronautics, Technical University, Munich, Germany

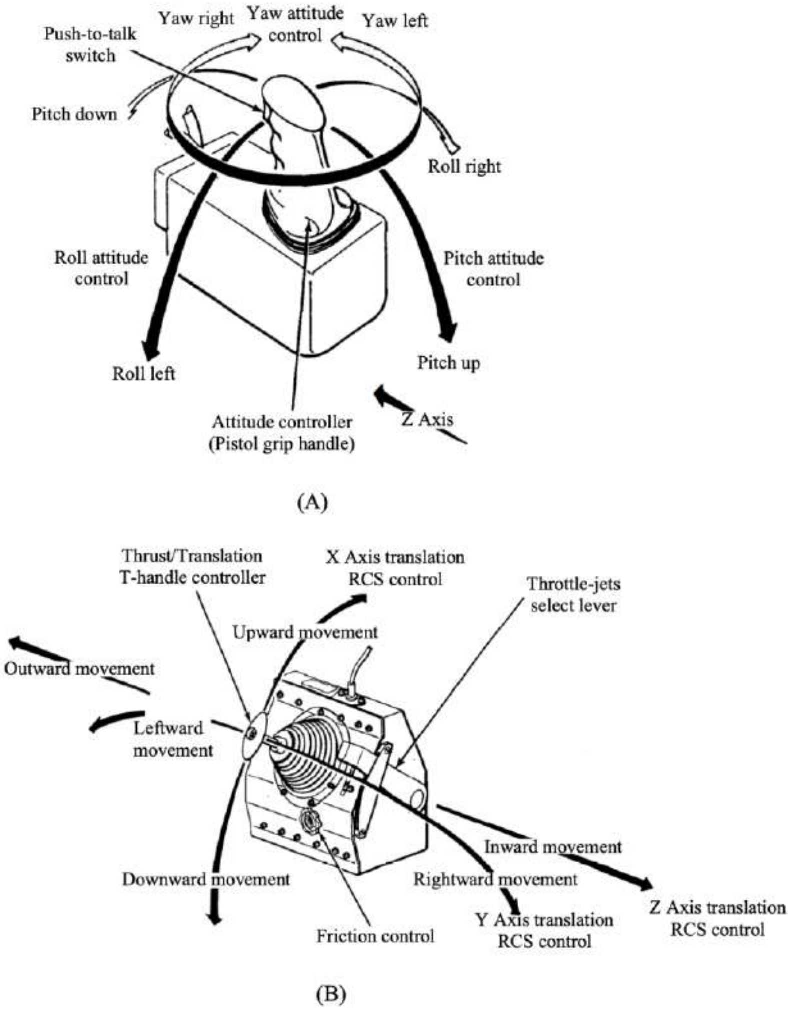

Figure 46- (A) ACA manipulations, (B) Throttle jets select lever. From LMA-790-3-LM 10

In the first OMS thrusting period, both OMS engines are used to deliver the orbiter to the predicted elliptical orbit, and the orbiter altitude is also maintained by gimbaling (swiveling) the OMS engines. It should be noted that during the OMS thrusting operation, RCS attitude control takes effect when the OMS gimbal rate or gimbal limits exceed the allowable limit. However,

if only one OMS engine is used, RCS roll control will be required at the same time. After the end of the OMS-1 period, the flight crew, using the rotational or translational hand controller to null the remaining velocity of the orbiter via an applicable RCS thruster; then RCS provide attitude hold until the OMS-2 thrusting maneuver starts. The second OMS, using both OMS engines near the apogee (an orbit where is established during the OMS-1 period) to circularize the predetermined orbit for that mission. According to the RCS function at the end of OMS-1, the RCSs are reactivated again to null the remaining vehicle speed, and then after providing attitude hold, minor maneuver translation is used if necessary for on-orbit operation. Of course, attitude control in the orbit can be done optionally through the primary or vernier RCS by the flight crew; but, vernier RCS is usually used for on-orbit attitude hold. In the case of direct insertion into the orbit using a single OMS thrusting maneuver, after the main engine cutoff and ending the OMS-1 thruster period, the RCS translation maneuver ($5\, {}^{feet}/_{sec}$) takes place and then the RCS attitude hold maneuver is provided. Therein after, OMS-2 is used for orbit insertion. In case of failure of OMS engines during the OMS thrusting period, aft RCS plus X jets are used.
Each OMS engine also has a gaseous nitrogen storage tank, gaseous nitrogen pressure isolation valve, gaseous nitrogen accumulator, bipropellant solenoid control valves and actuators that control bipropellant ball valves, and purge valves.
From entry interface at 400000 feet, the orbiter is controlled in roll, pitch, and yaw with the aft RCS thrusters. The orbiters ailerons become effective at a dynamic pressure of 10 pounds per square foot, and the aft RCS roll jets are deactivated. At a dynamic pressure of 20 pounds per square foot, the orbiter's elevons become effective, and the aft RCS pitch jets are deactivated. The rudder is activated at Mach 3.5, and the aft RCS yaw jets are deactivated at Mach 1 and approximately 45000 feet, (NASA KSC.STS-newsref).

Each OMS engine has the capability to produce 6000 pounds (ca. 26689.33 kg) of thrust with an oxidant to fuel ratio of about 1.65-to-1. This engine has a dry weight of 260 pounds (117.93 kg), and the chamber pressure of it is about 125 psi with a nozzle area expansion ratio of 55. This engine lifetime is about 100 missions, 1000 stars, or 15 hours of cumulative firing; it can be reused on each mission with only minor repair, refurbishment, and maintenance. These engines are used at altitudes above 7,000 feet (2.13 km) and have the ability to change vehicle velocity of about 3 to 6 feet per second on their own. Each OMS engine consists of two electro-mechanical gimbals actuators that are responsible for controlling the direction of the OMS motor in pitch and yaw; during one OMS engine thrusting period, roll RCS control is also required.

In each of the OMS pods, gaseous helium pressure is supplied to helium isolation valves and dual pressure regulators, which supply regulated helium pressure to the fuel and oxidizer tanks. The fuel is monomethyl hydrazine and the oxidizer is nitrogen tetroxide. The propellants are Earth-storable liquids at normal temperatures. They are pressure-fed to the propellant distribution system through tank isolation valves to the OMS engines. The OMS engine propellant ball valves are positioned by the gaseous nitrogen system and control the flow of propellants in to the engine. The fuel is directed first through the engine combustion chamber walls and provides regenerative cooling of the chamber walls; it then flows into the engine injector. The oxidizer goes directly to the engine injector. The propellants are sprayed into the combustion chamber, where they atomize and ignite upon contact with each other (hypergolic), producing a hot gas and, thus, thrust. (NASA KSC.STS-newsref)

The gaseous nitrogen system is also used after the OMS engines are shut down to purge residual fuel from the injector and combustion chamber, permitting safe restarting of the engines. The nozzle extension of each OMS engine is radiation-cooled and is constructed of columbium alloy. (NASA KSC.STS-newsref) As soon as the fuel reaches the combustion chamber, it enters 102 channels and after passing through it, which causes the regeneratively cooling of the chamber walls, it is sprayed into the chamber through injectors, while oxygen is sprayed directly into the chamber. The nominal values of each engine oxidizer and fuel flow rates are 11.93 and 7.23, respectively, which produce the thrust of about 6000 pounds in a vacuum with a specific impulse of 313 seconds. In these engines, the nozzle extension is bolted through the flange to the rear of the combustion chamber, which is made of columbium alloy and is radiantly cooled.

The platelet injector assembly consists of a stack of plates, each with an etched pattern that provides proper distribution and propellant injection velocity vector. The stack is diffusion-bonded and welded to the body of the injector. The fuel and oxidizer orifices are positioned so that the propellants will impinge and atomize, causing the fuel and oxidizer to ignite because of hypergolic reaction. (NASA KSC.STS-newsref)

NEW PARAMETERS IN ROCKET PROPULSION

Rocket propulsion introduce several new parameters that could not be defined in air-breathing systems. For example, the total impulse, which is defined as the integral of the thrust force at the whole burning time, or thrust-time charts, which can be ascending, descending or cruciform, (figure 48). The specific impulse of the engine can be calculated from the rocket total impulse. Regarding the burning time, it should be noted that during this period, the rocket nozzle ejected mass has a weight equal to w_p, which can be calculated according to the definition of a specific impulse (which is defined as the ratio of thrust force to propellants mass). The mass of the propellants at any given moment is the difference between the initial mass and the exhausted mass.

$$I_t = \int_0^{t_b} F(t)\,dt \tag{140}$$

$$w_P = g_0 \int_0^{t_b} \dot{m}_P\,dt \tag{141}$$

$$\dot{m}_P = \dot{m}_0 - \dot{m}_f \tag{142}$$

Therefore:

$$I_s = \frac{\int_0^{t_b} F(t)\,dt}{g_0 \int_0^{t_b} \dot{m}_p\,dt} = \frac{I_t}{m_p g_0} \tag{143}$$

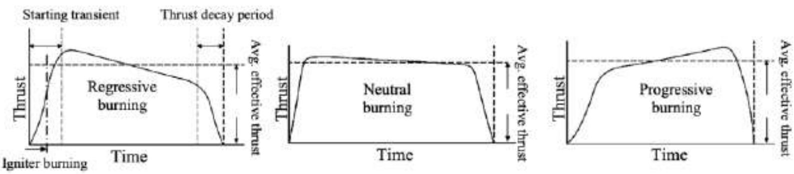

Figure 47- Typical thrust time histories (adopted from Fundamental of Aircraft and Rocket Propulsion)

The shape of the thrust-time diagram for solid propulsion engines is ascending, descending, and converging according to the shape of the propellant particles. In high-performance rockets, the firing time usually starts at 75% of the initial thrust and ends at 5%.

Engine mass ratio, which indicates the rocket's competency, is defined as the ratio of rocket mass after fuel was consumed to the initial mass of the rocket (which includes the propulsion mass and the rocket structure). This ratio can be about 20 for single-stage rockets and more than 200 for multi-stage rockets.

$$MR = \frac{m_f}{m_0} \tag{144}$$

The ratio of the propulsion mass to the initial mass of the rocket is denoted by ξ, which is known as the propulsion mass fraction.

$$\xi = \frac{\dot{m}_{propelled}}{\dot{m}_0} = 1 - MR \tag{145}$$

From the above relation, it can be seen that the higher the mass fraction of the rocket, the more mass is consumed by the propellants, which means that more thrust is produced. The effective exhaust gas velocity obtained from Equation 7 can be rewritten in terms of specific impulse as follows:

$$C = \frac{\dot{F}}{\dot{m}_P} = \frac{\dot{m}_P g_0 I_s}{\dot{m}_P} = g_0 I_s \tag{146}$$

Effective velocity can be obtained in another form. So first we write the trust relationship:

$$F = \dot{m} v_e + A_e(P_e - P_a) \tag{147}$$

In the above equation, the term $\dot{m} v_e$ is called momentum or thrust and the expression $A_e(P_e - P_a)$ is also called pressure thrust. By substituting this equation into the specific impulse formula and by simplifying it, the effective exhaust gas velocity equation is written in terms of actual gas velocity and pressure thrust.

$$c = v_e + \frac{(P_e - P_a)A_e}{\dot{m}_P} \tag{148}$$

Applying Newton's second law for an elementary state of a rocket:

$$F = \frac{dP}{dt} \tag{149}$$

By integrating from the sides of the above equation and simplification:

$$\int F\, dt = P_2 - P_1 \Longrightarrow P_2 = P_1 + \int F\, dt \tag{150}$$

The above equation states that when a force F is applied to a particle, its momentum is equal to the sum of the initial momentum and the impact of the force F on the particle in time t.The same is true for a set of particles, so that the total momentum is the sum of the momentum of the particles and the total impact is the sum of the impact of the particles:

$$P_1 + \sum\int f\, dt = P_2 \rightarrow P_2 = P_1 + \sum F\varDelta t \qquad (151)$$

Now, suppose a rocket at the time (t) with a total mass of M. Its fuel consumption is such that the mass flow rate (q) is exhausted at a relative speed v_e. As a result, at time t, the rocket's mass is equal to $(M - qt)$. In the time interval $\varDelta t$, the nozzle exit mass is $q\varDelta t$, which is moving at absolute speed u:

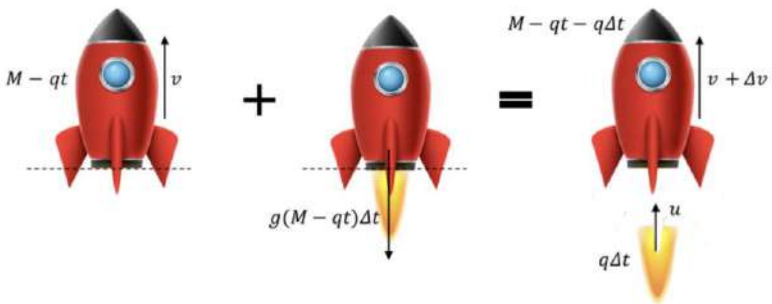

Figure 48- The momentum of the rocket and the mass exhausted of it.

By ignoring air resistance and using momentum and impulse equations, we will have:

$$(M - qt)v - g(M - qt)\varDelta t = (M - qt - q\varDelta t)(v + \varDelta v) + q\varDelta t u \qquad (152)$$

By dividing the sides of the equation (8) by $\varDelta t$ and reducing this time interval $(\varDelta t \rightarrow 0)$, and considering the expression $(u - (v + \varDelta v))$ as the rocket exhausted mass relative velocity (v_e') we have:

$$-g(M - qt) = (M - qt)\left(\frac{dv}{dt}\right) - qv_e \qquad (153)$$

By separating variables and reintegrating at time t and velocity v:

$$\int dV = \int \left(\frac{qv_e}{M-qt} - g\right) dt \tag{154}$$

$$v = v_e \, ln\left(\frac{M}{M-qt}\right) - gt \tag{155}$$

The expression $(-gt)$ is the effect of gravity on the rocket's traction, which is considered zero when the rocket moves in space. It is desirable to use changes in velocity (Δv) instead of the obtained velocity (v). as a result:

$$\Delta v = v_e \, ln \frac{M}{M-qt} \tag{156-a}$$

$$\Delta v = v_e \, ln \frac{m_o}{m_f} \tag{156-b}$$

Usually, the effective exhaust velocity is used instead of the actual exit velocity:

$$\Delta v = C \, ln \, {}^{m_o}/_{m_f} \tag{157}$$

This equation is known as Tsiolkovsky rocket equation. Figure 50 shows a plot of this equation for different effective velocities.

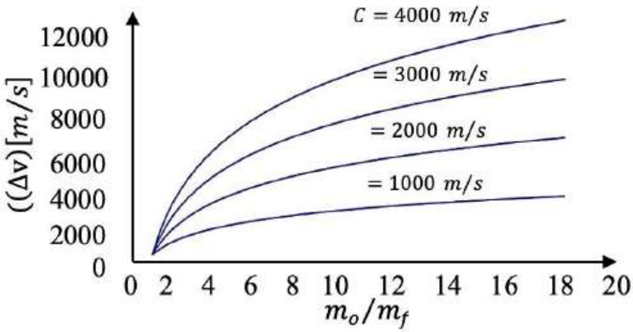

Figure 49- Tsiolkovsky rocket equation.

In addition, these equations are obtained for the initial and final mass:

$$m_f = m_o e^{-\frac{\Delta v}{c}} \tag{158}$$

$$m_o = m_f e^{\frac{\Delta v}{c}} \tag{159}$$

The right time to achieve a certain speed change (or burning time) will also be obtained as follows:

$$t = \frac{m_o}{q}\left[1 - \frac{1}{e^{(\Delta v/c)}}\right] \tag{160}$$

The maximum vehicle speed is shown in the absence of gravity (less gravity) and drag-free space for different specific impulses and mass ratios.

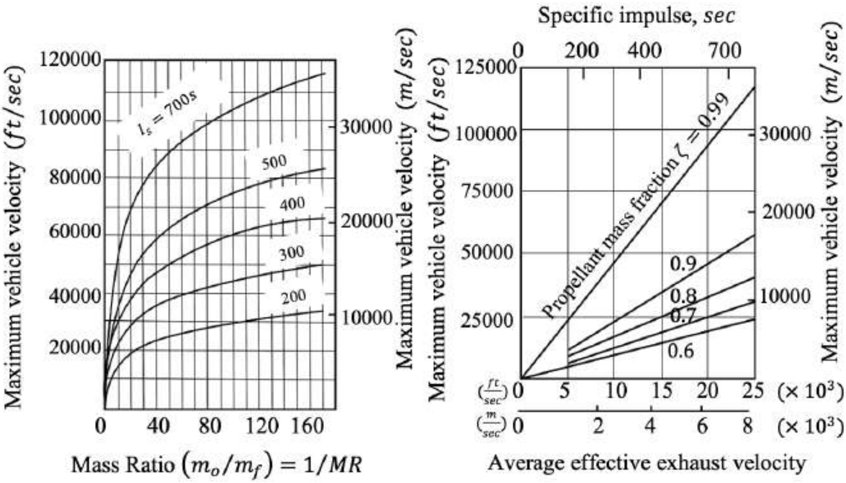

Figure 50- Maximum vhicle velocity changes about (a) specific impulse and mass ratio. (b) Average effective exhaust velocity, specific impulses, and propellant mass fraction. `Adopted from Rocket Propulsion Elements

Kerosene or RP-1 is commonly used as fuel in most aircraft engines. Consider the stoichiometric combustion equation of crocin ($C_{12}\,H_{26}$) under which the maximum flame temperature will be provided. However, the use of rich fuels is often desirable in rocket engines. According to the definition of fuel ratio, for kerosene:

$$C_{12}H_{26} + 125O_2 \rightarrow 12co_2 + 13H_2O$$

$$\frac{m_0}{m_f} = \frac{12.5\times 32}{170} = 2.35$$

The most favorable fuel ratio is achieved when the engine has the best efficiency or, in other words, the engine has the highest specific impulse. However, sometimes using a different air-to-fuel ratio (O/F) for the system does not work. When liquid hydrogen is used, a large volume is required due to its low density. For such cases where volumetric constraint is created, by increasing the air to fuel ratio (O/F), a significant effect on volume reduction is observed, but in this case, the loss and reduction of performance are more important than the requirement of the fuel tank to be Compensated.

Momentum thrust is defined as the product of the velocity of the exhaust gases multiplied by the mass flow of the propulsion, which the velocity refers to the ideal exhaust velocity, namely:

$$v_e = \sqrt{\left(\frac{2k}{k-1}\right)\left(\frac{R' T_C}{M}\right)\left(1 - \left(\frac{p_e}{p_C}\right)^{\frac{k-1}{k}}\right)} \qquad (161)$$

Which (k) is the specific heat ratio and R' 'is the universal constant of the gases $(47720 \frac{ft\ lb}{slug\ mol\ R^O}\ \ or\ 8314.51 \frac{Nm}{kg\ mol\ k})$. Combustion temperature is denoted by (T_C) and (M) is the average molecular weight of the exhaust gases. (p_C) and (p_e) are also the combustion chamber pressure and the nozzle outlet pressure, respectively. The specific heat ratio depends on the composition and temperature of the exhaust gas but is usually considered to be 1.2. The combustion chamber temperature is almost thermodynamically difficult to obtain, but the flame temperature is approximately $2500\ °C$ to $3600\ °C\ (4500\ °F - 6500\ °F)$.

Combustion chamber pressure can be between 7 and 250 atm. The outlet pressure must be equal to the ambient pressure, as mentioned earlier. According to equation (161), the higher the pressure and temperature of the fuel consumed inside the combustion chamber, or the lower the molecular weight, the higher the exit velocity and the higher the thrust produced. This is one of the reasons why liquid hydrogen is so popular as rocket fuel.

SPECIFIC IMPULSE

As mentioned, the specific impulse is defined as the ratio of the generated thrust to the propellant weight. Rocket engines have two different specific impulses in a vacuum and in the atmosphere, and the reason is that in the thrust equation, the effect of atmospheric pressure is effective.

$$I_{s_p} = \frac{F}{qg} \qquad \& \qquad g = 9.80665 \frac{m}{s^2} \qquad (162)$$

Since there are always losses in all systems, there are also losses in the rocket engine. The main factor is related to the incomplete reaction in the combustion chamber and the losses related to the nozzle and pump. The effect of these losses is manifested in the engine-specific impulse reduction. By considering the ideal nozzle and the completeness of the combustion reaction, the difference between these two states becomes clearer in the ratio of the actual specific engine shock to the theoretical specific shock. From relation (162) it can be concluded:

$$I_{s_P} = \frac{F}{\dot{m}g} \overset{F=qC}{\rightarrow} I_{sp} = \frac{C}{g} \quad or \quad C = I_{sp}g \tag{163}$$

Since the specific impulse of the motor is considered as a parameter of the motor and is already known, the value of (C) can be easily obtained, which is very efficient for use in relations (157) and (161).

Another parameter used to measure the superiority of rockets is the **characteristic-velocity** of the exhaust (C^*), which indicates the amount of energy available during the combustion process. For a mass flow passing the nozzle throat by chamber pressure, the characteristic-velocity is formulated namely:

$$C^* = \frac{P_C A_t}{q} = \sqrt{\frac{RT_C}{k}\left[\frac{k+1}{2}\right]^{\frac{k+1}{2(k-1)}}} \tag{164}$$

(P_C) and (A_t) in this formula are the pressure of the combustion chamber and the cross section of the nozzle, respectively. The value of (C^*) is about 1333 $^m/_s$ for single hydrazine propellant and slightly larger than 2360 $^m/_s$ for cryogenic hydrogen / oxygen. (C^*) is used far beyond the assumptions of chocked flow due to its measurability and computability. The left-hand side of the equation is a function of the measurable variables of chamber static pressure (P_C) and the throat cross-section area (A_t) and mass flow rate, while the right-hand side of the equation is a function of the inherent property of gas $(R, k, T(static\ temperature))$. In fact, (C^*) is a tool that can be used to calculate the terms on the right of the equation by knowing the left of it.

Actual values of C^* and I_{sp} delivered from the engine are significantly less than the theoretical values due to factors such as (1) two-phase flow losses in which the particles are unable to achieve kinetic and thermal equilibrium, (2) heat losses to the engine hardware and (3) combustion inefficiencies. These losses that occur upstream of the nozzle throat plane could be expressed as the performance factor η_θ for C^*. In-nozzle performance drop is also expressed by λ as the drop correction factor due to nozzle divergence, while the normal motor efficiency (η_F), which is measured experimentally, is in the range of 0.96 to 0.99. An accurate estimate of the delivered specific impulse to the engine will be obtained as follows:

$$I_{Spd} = \eta_{\mu}\ I°_{Spd} \tag{165}$$

I_{Spd}: Delivered propellant specific impulse, $lbf.sec/lbm\ (N.\frac{Sec}{Kg})$
η_{μ}: Deliverable motor efficiency ($\approx \eta_{\theta}.\eta_{F}$)
$I°_{Spd}$: Theoretical delivered propellant specific impulse, $lbf.sec/lbm\ (N.\frac{Sec}{Kg})$

The value of I_{Spd} is the corrected value of the standard specific impulse (I_{Sps}) , which means the specific impulse delivered at 1000 $psia$ at sea level condition for an optimum nozzle without divergence losses. The correction between I_{Sps} to I_{Spd} is also in accordance with Equation 42, which requires the calculation of the thrust coefficient (C_f) and the characteristic exhaust velocity (C^*) under standard conditions of I_{Sps} and engine conditions of I_{Spd}. g_c in the following equation is a gravitational conversion constant, 32.17 $lbm.ft/lbm.sec^2$.

$$I_{Sp} = \frac{C^* C_f}{g_c} = \frac{C_f}{C_D} \tag{166}$$

The specific impulse can be defined as the difference in enthalpy changes of the entire propulsion system from the combustion chamber to the nozzle outlet, as follows:

$$I_{Sp} = \sqrt{2J\,\frac{(H_c - H_e)}{g}} \tag{167}$$

In the above relation, H_c and H_e are the enthalpies of combustion products before and after expansion (in [Btu/lbm] or [j/kg]), respectively, and J is the mechanical equivalent of heat, which is equal to 778 $ft\ {}^{lbm}/_{Btu}$ or 0.101988 $kg\ {}^{m}/_{j}$. Two sets of conditions, including the combustion chamber and the expansion nozzle, are considered to calculate the performance:

1. Combustion Chamber:
   Using the propellant initial conditions to the combustion chamber (composition, temperature, physical state, mixture ratio) along with the combustion chamber pressure, the properties, composition of the output products, chamber temperature, and hot gas reaction can be understood. However, this information denotes the initial

conditions of the nozzle are used to calculate the specific impulse and velocity of the exhaust gases. It also provides information about engine design, heat transfer estimations, flow parameters, and nozzle expansion. According to thermodynamic knowledge, it should be noted that by employing equilibrium equations of mass, pressure, energy and by applying chemical equilibrium data in the adiabatic combustion process a good estimation of the flame temperature can be obtained. By defining the enthalpy of products as a power series in terms of temperature, the energy equation will be written as follows:

$$\sum_{i,propellant} n_i \{[(H_{Tc}^{\circ} - H_0^{\circ}) - (H_{T0}^{\circ} - H_0^{\circ})] + (\Delta H_F^{\circ})_{T0}\}_i = \sum_{j,reaction\ product} n_j \{[(H_{Ti}^{\circ} - H_0^{\circ}) - (H_{T0}^{\circ} - H_0^{\circ})] + (\Delta H_F \delta)_{T0}\}_j \quad (168)$$

Tc: Combustion adiabatic flame temperature.
Ti: Propellant temperature.
$T0$: Reference temperature ($298K$).
$H^{\circ} - H_0^{\circ}$: molar enthalpy. (Table 3)
ΔH_F: heat of formation.
n_i, n_j: amounts of reactants (propellants) and combustion products, respectively.

To calculate the unknowns Tc and n_j, all these equations are solved simultaneously using thermochemical equilibrium data.

2. Expansion nozzles:
   In the nozzles, the gases undergo isentropic expansion so that their sensible enthalpy is converted into kinetic energy, resulting in a drop in temperature and pressure. When no chemical dissociation, recombination, or condensation occurs during this process, the composition remains constant from the combustion chamber to the nozzle outlet. These processes are known as frozen equilibrium. If the chemical and fuzzy equilibrium continues in such a way that during the nozzle expansion process with varying temperature and pressure, chemical dissociation, recombination, or condensation occur, as a result, the composition of combustion products will change. Maintaining this dissociation and recombination adds to the total chemical energy that is converted into kinetic energy,

which in turn increases the performance of the equilibrium system known as the shifting equilibrium. In fact, rocket performance usually falls into the central region between these two equilibrium states, which might be further reduced due to other losses (such as incomplete combustion, heat loss, nozzle friction, and nozzle divergence angle).

Two simplifying assumptions are used to perform frozen equilibrium calculations:

1. Isentropic process: Due to the constant gas composition throughout the nozzle, the process is considered as isentropic in which the entropy does not change.
2. Heat capacity.

Writing the entropy changes equation for the perfect gas, result in:

$$ds = C_P \frac{dT}{T} - R \frac{dP}{P} \tag{169}$$

And also given that the specific heat is constant,

$$S_2 - S_1 = C_{P0} \ln \frac{T_2}{T_1} - R \ \ln \frac{P_2}{P_1} \tag{170}$$

In an isentropic process that happens adiabatically, the left-hand side of the equation tends to be zero, so

$$\ln \frac{T_2}{T_1} = \frac{R}{C_{P0}} \ln \frac{P_2}{P_1} \tag{171}$$

According to the definition of specific heat ratios for perfect gas:

$$k = \frac{C_P}{C_v} \tag{172}$$

And by considering the relation between C_P and C_v, i.e., $C_P - C_v = R$, the ratio of $\frac{R}{C_{P0}}$ attain in terms of k:

$$\frac{R}{C_{P0}} = \frac{k-1}{k} \tag{173}$$

By substituting the above relation in Equation 171 and simplifying it, result in:

$$\frac{T_2}{T_1} = \left(\frac{P_2}{P_1}\right)^{\frac{k-1}{k}} \tag{174}$$

From the above relation, it is clear that for a selected nozzle, referring to the exit pressure, the flame temperature can be obtained. Therefore, calculate the specific impulse by equation 167 which is in terms of the enthalpy changes during the combustion (that appeared in temperature variation).

In shifting equilibrium calculations, as the temperature and pressure decrease, species and chemical compounds change from the combustion chamber to the nozzle outlet. Due to recombination, the chemical energy of the whole system, which is converted to kinetic energy, increases. The equilibrium equations of mass, pressure and chemical equilibrium are the same as prior and are employed to calculate the exit temperature, except that instead of using the energy equilibrium equation, the expression of entropy conservation is deployed to solve the exit temperature and the exhaust combinations:

$$\sum_{k,exhaust} n_k [S_{Te} - R \ \ln P]_k = \sum_{j,chamber} n_j [S_{Tc} - R \ \ln P]_j$$

(175)

Where Te and Tc are the nozzle exit and combustion chamber temperatures, S_{Tc} is the net molar entropy of j particles at the chamber temperature and pressure of $1atm$, and S_{Te} is the net molar entropy of k particles at the exit temperature and pressure of $1atm$. R is the gas constant. n_k and n_j are the numbers of moles of particle k in the nozzle output and particle j in the chamber. P_j and P_k are the partial masses of particles per unit atmosphere. As a result, with the temperature and composition of the exhaust products, the enthalpy drop and the specific impulse can be calculated. Using equations 167 to 175, the specific impulse equation is expressed as follows:

$$H = C_P T \tag{176}$$

$$I_{sp} = \sqrt{\frac{k}{k-1} \frac{2RT_c}{gm} [1 - (\frac{P_e}{P_c})^{\frac{k-1}{k}}]} \tag{177}$$

Given the above equation, it’s obvious that the specific impulse is proportional to the square roots of the ratio of the chamber temperature to the average molecular weight of the exhaust products ratio, which is a merit approximation for the propellants' comparison.

THRUST COEFFICIENT

According to equation (164), it can be seen that there are many similarities between the definition of effective velocity and specific impulse, namely:

$$C^* = \frac{P_C A_t}{\dot{m}} \sim \frac{T}{\dot{m}} = C \tag{178}$$

Another parameter is defined as the thrust coefficient, to determine the dependence of C and (C^*). In fact, it indicates the amount of generated thrust, with the static pressure in the combustion chamber at the cross-section of the nozzle, which is defined as follows:

$$C_f = \frac{T}{P_e A_t} \tag{179}$$

From equations (165) and (166), we can get the C and (C^*) relation:

$$C = \frac{T}{\dot{m}} = \frac{C_f\, P_C\, A_t}{\dot{m}} = C_f C^* \tag{180}$$

As mentioned, (C^*) represents the rocket's potential to generate thrust production, which depends on the thermodynamic characteristics of the propulsion system, while (C_f) represents the nozzle's ability to convert combustion products and gases into thrust and is highly dependent on the geometry of the nozzle and its physical condition. Therefore, we are faced with two problems, the first of which is the choice of propellant type (C^*) and the second is the choice of nozzle and chamber pressure. The following equation can also be written for the trust coefficient:

$$C_f = \frac{C}{C^*} = \frac{(P_e - P_0)\frac{A_e}{\dot{m}} + u_e}{\frac{p_C A_t}{\dot{m}}} = \left(1 - \frac{P_0}{P_e}\right)\frac{P_e A_e}{P_C A_t} + \frac{u_e}{C^*} \tag{181}$$

Which, the terms $(\frac{P_e}{P_C})$, $(\frac{u_e}{C^*})$, and $(\frac{A_e}{A_t})$ are related to the isentropic expansion of the nozzle exhaust gases. By simplifying and defining the mentioned terms based on Mach number and specific heat ratio, the main and accurate formula for calculating the thrust coefficient can be achieved. First, each of these ratios is expressed in Mach as follows:

$$\frac{u_e}{C^*} = \frac{k M_e}{\sqrt{1 + \frac{k-1}{2} M_e^2}} \left[\frac{k+1}{2}\right]^{\frac{k+1}{-2[k-1]}} \tag{182}$$

$$\frac{P}{P_C} = \left(1 + \frac{k-1}{2} M_e^2\right)^{\frac{-k}{k-1}} \tag{183}$$

$$\frac{A_e}{A_t} = \left[\frac{k+1}{2}\right]^{\frac{k+1}{-2[k-1]}} \left[\frac{\left(1 + \frac{k-1}{2} M_e^2\right)^{\frac{k+1}{+2[k-1]}}}{M_e}\right] \tag{184}$$

By substituting relations (182), (183), and (184) in equation (181) and simplifying:

$$c_f = \frac{\left(\frac{k+1}{2}\right)^{\frac{k+1}{-2(k-1)}}}{M_e\sqrt{1+\frac{k-1}{2}M_e^2}}\left[kM_e^2 + 1 - \frac{P_0}{P_e}\right] \quad (185)$$

The above equation states that all terms $(\frac{P_e}{P_C})$, $(\frac{u_e}{C^*})$, and $(\frac{A_e}{A_t})$ depend on Mach number, and unlike (C^*), they are all independent of propellant properties such as absolute temperature and molecular weight. The exit Mach number will be obtained by relation (186):

$$M_e^2 = 2\left(\frac{\left(\frac{p_e}{P_0}\frac{P_0}{P_t}\right)^{\frac{1-k}{k}} - 1}{k-1}\right) \quad (186)$$

The velocity and pressure equations in the nozzle throat are obtained from Equations (187) and (188):

$$v_t = \sqrt{\frac{2gk}{k+1}RT_c} \quad (187)$$

$$P_t = P_c\left[\frac{2}{k+1}\right]^{\frac{k}{k-1}} \quad (188)$$

c_f can also be obtained using the conservation of mass equation. Therefore, the mass flow rate inside the nozzle throat must first be determined from the following equation:

$$\dot{m}_P = \sqrt{\frac{k}{R}}\frac{P_C}{\sqrt{T_C}}A_{th}\left(\frac{2}{k+1}\right)^{\frac{k+1}{2(k-1)}} \quad (189)$$

In the second step, the output velocity, given that the isentropic expansion occurs in the nozzle, is obtained from the nozzle throat to its exits, namely:

$$T_C = T_2 + \frac{{v_2}^2}{2C_P} \quad (190)$$

$$v_2 = \sqrt{2C_P(T_C - T_2)} = \sqrt{2C_P\left[1 - \left(\frac{p_2}{p_C}\right)^{\frac{k-1}{k}}\right]} \quad (191)$$

Therefore, given that the momentum thrust is the product of the mass flow and the output velocity, and by using equations (189) and (191), we will arrive at another relation for c_f:

$$C_f = \frac{\dot{m}_P v_2 + (P_e - P_0) A_2}{P_C A_{th}} \tag{192}$$

And after substitution and simplification:

$$C_f = \sqrt{\left(\frac{2k^2}{k-1}\right)\left(\frac{2}{k+1}\right)^{\frac{k+1}{k-1}}\left[1 - \left(\frac{P_e}{P_c}\right)^{\frac{k-1}{k}}\right]} + \frac{P_e - P_0}{P_C}\left(\frac{A_e}{A_t}\right) \tag{193}$$

Inasmuch as the most optimal state of thrust is when the nozzle outlet pressure is equal to the ambient pressure ($P_e = P_0$), hence:

$$C_{f,opt} = \sqrt{\left(\frac{2k^2}{k-1}\right)\left(\frac{2}{k+1}\right)^{\frac{k+1}{k-1}}\left[1 - \left(\frac{P_e}{P_c}\right)^{\frac{k-1}{k}}\right]} \tag{194}$$

In Figure 52, the changes in the optimal thrust coefficient are shown as a function of the nozzle pressure ratio (NPR) at different nozzle expansion area ratios, based on specific heat, under optimal expansion conditions ($P_e = P_0$). The expression inside the brackets in equation (194) represents the thermal efficiency of the Brighton cycle, which operates between (P_e) and (P_c). Therefore, for the nozzle that has the highest area expansion ratio to reduce its outlet pressure, and has a very high combustion chamber pressure, the thermal efficiency value tends to zero, which means that the thrust coefficient has reached its maximum value and only is a function of k. For such an optimal nozzle, the maximum thrust coefficient can be calculated from Equation (196).

$$\eta_{th} = 1 - \left(\frac{P_2}{P_C}\right)^{\frac{k-1}{k}} \tag{195}$$

$$c_{f,oPt,max} = \sqrt{\left(\frac{2k^2}{k-1}\right)\left(\frac{2}{k+1}\right)^{\frac{k+1}{k-1}}} \tag{196}$$

From the above equation, the maximum optimal trust coefficient will decrease with increasing the specific heat ratio.

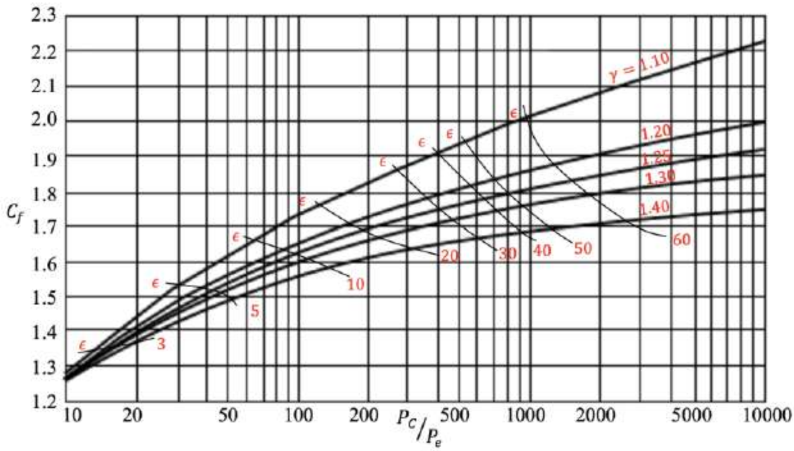

Figure 51- Variation of optimum thrust coefficient for different nozzle pressure and area ratios at the various gas ratios of specific heat. Adopted from Rocket Propulsion Elements

FLIGHT PERFORMANCE

The desirable change of velocity relation (Eq. 157) can be used when the effects of atmospheric drag and gravitational force are ignored. But with these effects in mind, Newton's second law for the same rocket would be written as follows:

$$m\frac{dv}{dt} = F - D - mg\sin\theta \tag{197}$$

The first, second, and third terms on the right side of the equation are the propulsive force, the drag force, and the gravitational force in the direction perpendicular to the rocket's motion, respectively. The propulsive force caused by the propellant burning is also defined as follows (the mass passage of the propulsion is the same as the rate of weight reduction of the rocket):

$$F = \dot{m}_P c = -\frac{dm}{dt}c \tag{198}$$

The thrust force can be expressed as a product of the effective output velocity in the amount of rocket mass reduction. The Drag, which is related to the dynamic pressure $(\rho v^2/2)$ and the front surface of the rocket, is replaced with a correction factor, called the drag coefficient:

$$D = C_D\frac{\rho v^2}{2}A_f \tag{199}$$

The drag coefficient is a function of the Mach number. It should be noted that the shape of the exhaust nozzle has a significant effect on the pressure distribution, so the drag coefficient is examined in the absence of exhaust. Also, the presence of wings creates the lift force, and the lift coefficient, which is a function of Mach number and angle of attack, appears. The effect of the angle of attack (α) and Mach number on the lift and drag coefficients (prepared for the German V-2 missile in jet off and without exhaust plume effects), has been shown in Figures 53.

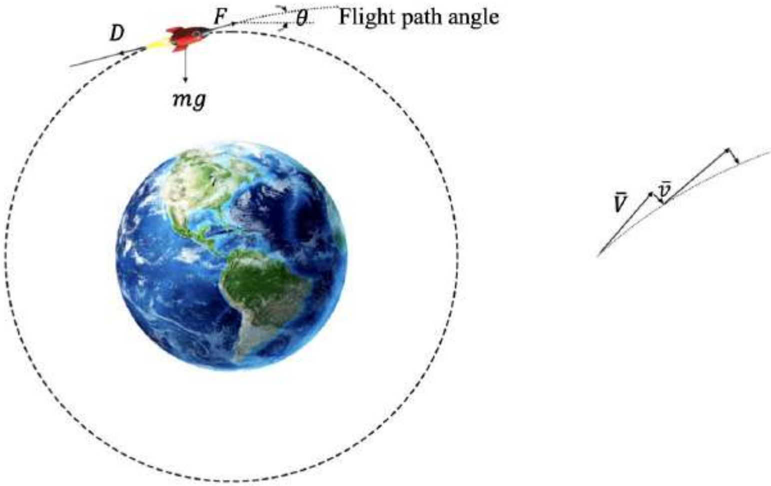

Figure 52- Definition sketch of flight path line.

The important point is that, at high Mach's, some aerodynamic characteristics, such as pressure coefficient, lift and drag coefficients, shock wave shape, and Mach number pattern, are completely independent of Mach number. This is called **Mach number independence in hypersonic Mach's**.

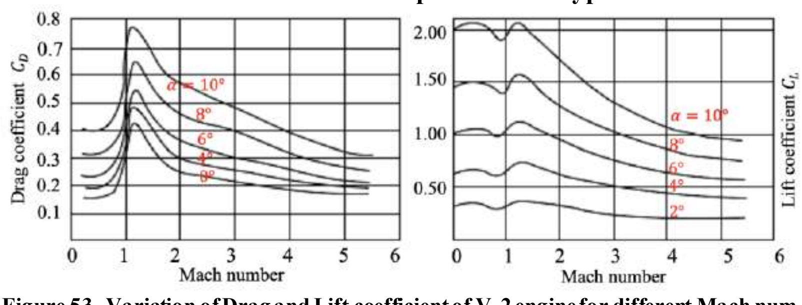

Figure 53- Variation of Drag and Lift coefficient of V-2 engine for different Mach numbers as a function of angle of attack. Adopted from Rocket Propulsion Elements.

By substituting the relation (198) and (199) in (Eq. 197) and dividing the sides of the obtained relation by $\left(\frac{dm}{dt}\right)$:

$$dv = -C\,\frac{dm}{m} - \frac{C_D\,\rho v^2\,A_f}{2m}\,dt - g\sin\theta\,dt \tag{200}$$

The equation of velocity change is obtained by once integrating the above relation and then solving it, namely:

$$\int_{v_0}^{v_f} dv = -\int_{m_0}^{m_f} C\,\frac{d_m}{m} - \int_0^{t_b} \frac{C_D\,\rho V^2\,A_f}{2m}\,dt - \int_0^{t_b} g\sin\theta\,\,dt$$

(201)

$$\Delta v = -\bar{c}\,ln(MR) - (g\,sin\,\theta)_m t_b - \int_0^{t_b} \frac{C_D\,\rho V^2\,A_f}{2m}\,dt \tag{202}$$

To solve the expression within integral in the resulting formula, a relation must be written for the rocket weight
over time (given that the rocket mass changes over time). Since the mass of the propellants is continuously decreasing, the instantaneous mass of the rocket is equal to the difference between the amount of mass output at time t and the initial mass of the rocket. That's mean:

$$m_t = m_0 - \left(\frac{m_p}{m_t}\right)t = m_0\left(1 - \left(\frac{t}{t_b}\right)\varsigma\right) \tag{203}$$

The sign (ς) (read sigma) in the above relation indicates the mass fraction of the propellant. It should be noted that the drag coefficient and the rocket velocity both depend on Mach number (which is a function of altitude), and the density has different values at different altitudes. And since time and altitude are interdependent, then the equation of motion is written as follows:

$$\Delta v = -\bar{c}\,ln(MR) - (g\,sin\,\theta)_m t_b - \frac{A_f}{2m_0}\int_0^{t_b} \frac{C_D\,\rho V^2}{1-\varsigma\frac{t}{t_b}}\,dt \tag{204}$$

The rocket path angle, which is affected by the gravitational force, will always change so that, at each time step, a new path of the rocket must be obtained. This force, which always acts perpendicular to the rocket surface, will change the angle of the rocket by as much as θ, so that this displacement consists of two components Δx and Δy, in each time step. To calculate this amount of deviation, we use the superposition principle, in a direction perpendicular to the direction of rocket motion:

$$m\frac{dv}{dt} = mg\ sin\,\theta \tag{205}$$

By once integration from this equation:

$$\Delta v = -(g\,cos\,\theta)_m t \tag{206}$$

The amount of displacement that the rocket travels in each time step is also equal to:

$$\Delta x = \bar{V}\Delta t \tag{207-a}$$

$$\Delta y = \bar{v}\Delta t \tag{207-b}$$

Therefore, assuming the dynamic pressure is constant and using the average drag coefficient, the motion relation will be written as follows:

$$\Delta v = -ln(1-\varsigma)\left[gI_s - \left(\frac{A_f}{m_0}\right)\left(\frac{\rho v^2}{2}\right)\left(\frac{t_b}{\varsigma}\right)\bar{C}_D\right] - (g\,sin\,\theta)_m t_b$$

(208)

The expression in brackets in the above equation contains the contribution of the trust and the aerodynamic drag penalty. Reduction of the dynamic pressure decreases the aerodynamic drag penalty as well as increases the high initial mass per unit frontal area, i.e., $\left(\frac{m_0}{A_f}\right)$. this requirement tends to produce long slender vehicles for low frontal cross-sectional area. Also, low drag coefficient (C_D) is desirable in achieving high terminal speed, which implies a slender conical nose or tangent Ogive to reduce the vehicle drag coefficient, (from AIRCRAFT PROPULSION,2009).

TOTAL, PROPULSIVE AND THERMAL EFFICIENCY

The ratio of thrust power to the sum of thrust power and residual kinetic power is called the **propulsive efficiency**. The residual kinetic power is the kinetic power as observed by a stationary observer, i.e., (from AIRCRAFT PROPULSION,2009)

$$\eta_p = \frac{\dot{m}_P c\cdot v}{\dot{m}_P\left(c\cdot v - \frac{(c-v)^2}{2}\right)} = \frac{c\cdot v}{c\cdot v - \frac{(c-v)^2}{2}} = \frac{2\left(\frac{v}{c}\right)}{1+\left(\frac{v}{c}\right)^2} \tag{209}$$

From the above equation, it can be concluded that when the flight speed and the products speed are equal, then the thrust efficiency will be 100%. The main difference between rocket propulsion systems and air-breathing systems is that in air breathing systems, unlike rockets, the flight speed is less than the exhaust velocity, and this difference is due to the presence of Ram Drag in the thrust equation. The **total efficiency** for rockets also defines as the ratio of the generated thrust power to the total power consumed in the combustion chamber, which is to generate the thrust and the propulsive kinetic power in the injector plate (this term is usually omitted compared to chemical energy in the combustion chamber).

$$\eta_{Overall} = \frac{Fv}{\dot{m}_p Q_R + \dot{m}_p \frac{V_{Inj}^2}{2}} \approx \frac{c \cdot v}{Q_R} \tag{210}$$

It will take huge energy to send any object into space. For the rocket, the conversion of chemical energy into kinetic energy takes place in the combustion chamber. Thermal efficiency defines to show this conversion energy quantitatively, which indicates how much of the energy received from combustion converts into kinetic energy, namely:

$$\eta_{Thermal} = \frac{\dot{W}_{exhaust}}{P_{in}} = \frac{\dot{m}\frac{C}{2}}{P_{in}} \tag{211}$$

(P_{in}) in the above phrase indicates the amount of energy released, regardless of what type of propulsion (electrical, chemical, nuclear, etc.) is used. For chemical rockets, it's to be calculated as follows:

$$P_{in} = \dot{m}\Delta h \tag{212}$$

Δh represents the amount of energy inside the combustion chamber. By substituting the last two equations (Eq's (211) and (212)) in the quantitative formula of thermal efficiency (Eq. 210), the result will be simplified as follows:

$$\eta_{Thermal} = \frac{\frac{2k}{k-1} RT_t \left[1 - \left(\frac{P_e}{P_t}\right)^{\frac{K-1}{k}}\right]}{2\Delta h} \tag{213}$$

Since the temperature inside the nozzle throat is proportional to the ratio of energy to specific heat capacity, i.e.,

$$T_t \sim \frac{\Delta h}{\bar{c}_P} \tag{214}$$

Therefore:

$$\eta_{Thermal} = \frac{k}{k-1}\frac{R}{\bar{c}_P}\left[1-\left(\frac{P_e}{P_t}\right)^{\frac{K-1}{k}}\right] \tag{215}$$

The thermal efficiency relationship is very useful for electric propellants, but in chemical propellants, the thermal efficiency depends on the fuel and propellants used. In addition, in comparison with thermal engines with chemical propulsion, since in rockets the speed and acceleration of the rocket are much more important than the acceleration of the exhaust gases, therefore, in chemical rockets the propulsive efficiency will be used instead of thermal efficiency. The total efficiency will be also defined as the product of the propulsive and thermal efficiencies, namely:

$$\eta_{Overal} = \eta_{Thermal} \times \eta_{Propulsion} \tag{216}$$

MULTISTAGE ROCKETS

Multi-stage missiles are a group of missiles in which each stage of the missile includes its own engines and propellant. The reason for using this type of rocket is that; Instead of using a very large engine, several smaller engines can be used in different stages. Today, most high-range ballistic missiles, as well as rockets used for space travel, fall into this category. By using multi-stage rockets, flight efficiency can be greatly improved. They are divided into two categories, series, and parallel, based on the arrangement of the stages. In multi-stage rockets, which use in series, the rocket stages start igniting one after the other. So that after the first stage of igniting completion, which has the largest engine and nozzle chamber, the upper retaining cap splits, sending hot gas onto the next stage, burning it, the lower stage will be separated from the rocket. This process continues until the last stages, which take place outside the atmosphere. For example, the Saturn V uses the same series configuration with 5 stages, and the first stage of it consists of five (F1) engines. In the Apollo 11 mission by this rocket, it used three stages in space to land astronauts on the moon. Another advantage of this model is that, with the passing of time and separation of each stage, the total mass of the rocket will be reduced. As mentioned, this configuration use to generate trust instead of using a giant engine. It should be noted that each stage consists of a set of motors that are turned on simultaneously to generate more thrust. Another category of multi-stage motors, known as parallel configurations, uses multiple interconnected rockets. Boosters, which usually use for the initial lift-off from the ground, are referred to as step-zero, and the first stage starts firing at the beginning of the mission to increase the initial thrust. After the ending of each step, they will be dissociated from the main body and returned to the ground. For example, for this category, we can mention the Atlas V, which includes 3 solid boosters, a liquid booster and uses two engines RD 180 and RL 10.1. One of the most common techniques in the development of launch vehicles to boost large payloads with a minimal first stage in contrast to a large engine to generate great power for lift-off is to use the clustering method. In other words, using two or more engines in a group that starts together simultaneously is more efficient, as opposed to engines in succession mode. On the other hand, rocketry clustering makes it possible to combine several smaller engines, which have lower costs and are more reliable as opposed to using a single larger engine. Generally, four engines are the most that should be used in a model rocket, since more engines make ignition less reliable, (from Technical report TR-6 cluster techniques). Two basics in the designing of the cluster rocket are the considerations of symmetrical design and the spacing of the engines. Failure to comply with any of these basics will cause the rocket to deviate from its path. The first one means that the centerline of the rocket plays an important role since any asymmetry of the thrust about it (e.g., using two unlike engines on both sides of the centerline in the cluster system with 3 parallel engines) will lead to the rocket veering off course. However, a slight amount of imbalance or misalignment can be offset by using extra-large fins or a small amount of spin angle on the fins, (from Technical report TR-6 cluster techniques). The second refers that the designer should avoid spacing the engines several inches apart. Namely, the interval from the center of one cluster engine nozzle to the center of any other one should not exceed 10% of the rocket's length. This limit preserves the rocket from thrust variations.

The overall advantages of using multi-stage missiles compared to single-stage missiles are as follows:

1. Prevention of the use of extra thrust to accelerate these loads due to the detachment of extra loads during each stage of the flight.
2. As both effective aerodynamic area and atmospheric drag force decrease, the rocket achieve higher speeds and a greater range.
3. Since each engine has the highest efficiency at a specific pressure and the engine of each stage starts at a certain height (pressure), it is possible to adjust the engine of each stage to the height that turns on.
4. Because in solid-fuel rockets it is necessary to change the mass flow of fuel in each step of the flight (especially in the early stage) and high thrust requirement, hence by multi-staging the rocket, fuel mass flow can be changed for each step.

5. By multi-staging the rocket, there is more possibility to optimize the rocket in terms of specifications and dimensions or economically.
6. Greater range or higher speeds could be recovered by precise multi-stage missile design, which also reduce additional costs and construction time. (Higher number of staging is beneficial for large rockets with smaller propulsion systems relative to the weight of the tanks).

The active stage is the stage that must go through the rest of the path, on the contrary, the inactive stage is the stage in which its mission is over and must be jettisoned from the active one. The function of separation systems is to separate components that are not needed in the rest of the mission anymore, such as protection systems that were needed in certain circumstances, for instance, the protective cap of the explosive warhead of missiles. These separations could be done by active or passive separation systems.
For a rocket with (n) stages, the velocity changes equal the sum of the velocities of all stages, namely:

$$\Delta v = \sum_{i=1}^{N} \Delta v_i = \sum \left(C_{eff}\right)_i ln\left(\frac{1}{MR}\right)_i = g\Sigma\left(I_{sp}\right)_i ln\left(\frac{1}{MR}\right)_i$$

(217)

Assuming that the effective exhaust velocities are equal in all stages, and since the final mass of each stage is equal to the initial mass of its next stage, therefore by simplifying the above relation, for a series multistage rocket with N stages, the mass of the last stage is the payload mass(M_L), so the change in speed is as follows:

$$\Delta v = -NCLn\left(\frac{m_L}{m_0}\right) \tag{218}$$

Since the total mass is equal to the sum of the masses of each stage:

$$\dot{m}_T = \sum \dot{m}_i \tag{219}$$

$$T_i = \dot{m}_T (C)_{avg} \tag{220}$$

As a result, the average effective exhaust gas velocity can be obtained from the above equation, and by substituting this relation into the Tsiolkovsky (Equation 32), the parallel multistage rocket equation obtain as follows:

$$\Delta v = (C)_{avg} \, ln\left(\frac{m_0}{m_f}\right) \tag{221}$$

It should be noted that boosters often use in order to create more thrust for lifting, and the use of multi-stage mode complicates the manufacturing process and, due to more separate processes such as the combustion, collision, and separation disorders, the possibility of failure increases, during flight. Several models of how the steps are arranged are shown in the figure 55.
As mentioned earlier, according to the formula for the velocity changes and figure (51-a), a single-stage rocket has the best efficiency when the mass ratio decreases, i.e., the final mass reaches its lowest level. Since the mass of the rocket is due to the masses of the propellant, structure, and payload, the maximum flight efficiency achieves when the propellant is fully consumed. The best flight efficiency for a single-stage rocket is when its mass ratio is 5%. Given that, at the beginning of each stage, the mass of its earlier stage separates, thus reducing the remaining mass in the final stage, so that the mass ratio in multi-stage rockets to 0.01 and even less arrives. According to figure (51-a), the changes in velocity and consequently flight efficiency, for a multi-stage rocket with an inverse mass ratio of 100 ($MR = 0.01$), compared to the best case of a single-stage rocket with an inverse mass ratio of 20 ($MR = 5\%$), increases significantly. (This diagram shows the optimum nozzle when the speed of the rocket is equal to the velocity of the exhaust gases. In this case, all kinetic energy spends on moving the rocket, but outside this range, always part of the energy will be wasted.)
One of the advantages of using a multi-stage rocket is that once the fuel is exhausted, it reduces the total mass in each stage by separating the previous stage. Therefore, the performance is improved by removing the dead mass, so the thrust of the next stage operates more efficiently than accelerating a single large rocket with heavier structural weight. Ability to reduce thrust in mid-flight, which in turn prevents excessive acceleration of the flight crew and equipment is on other advantages of this method. On the other hand, staging requires the vehicle to lift the engines at the first stage which are not ignited yet; also staging makes the rocket more complex and contains some possibility of failures such as failure in separation, ignition, and stages collision.

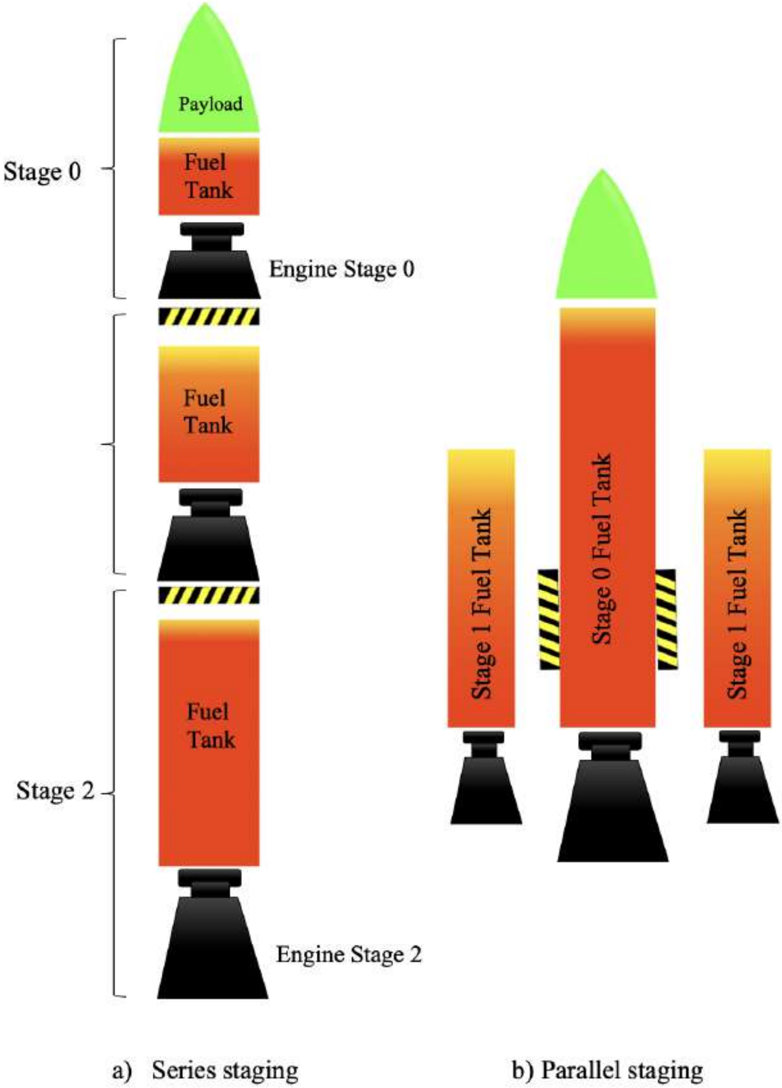

Figure 54- definition sketch of rocket staging

ROCKET COMBUSTION CHAMBER

CHEMICAL ROCKET COMBUSTION CHAMBER

The thrust chamber of rockets with liquid propellants is the most important part of a rocket, which has a great impact on increasing the efficiency of the rocket. This section consists of parts such as injector plate, combustion chamber, and outlet nozzle. The injector plate in the rocket engine is responsible for atomizing and combining fuel an oxygen so that combustion takes place in the combustion chamber. When the high-energy gases go through the nozzle, their energy converts in to kinetic energy. Therefore, the appropriate thrust will be generated. Combustion inside the combustion chamber will cause a sharp rise in temperature inside the thrust chamber, and especially in the combustion chamber, which is assisted by using propellants to be cool. In fact, the latent heat of evaporation of the propellants and their change to a gaseous phase cools the thrust chamber. For example, oxygen and hydrogen can be used as cryogenic propellants. Preheating the propellants along the path before the combustion chamber will also increase the combustion temperature, resulting in increasing the production of thrust and greater rocket efficiency. Unlike liquid propulsion systems, which cool by their liquid propellant, solid propulsion rockets, due to the lack of such cooling, need to end their combustion very quickly after reaching the planned goal and detach from the main body. Of course, these rockets contain parts such as liners, insulators, inhibitors to help cool, but due to the high heat and fuel in this type of rocket and the structure of these rockets in which the propulsion isn't controllable, the time range of operation of these rockets, as a booster, is short and almost shorter than 2min. Another reason for using liquid propellants is to minimize stored volume. Rocket engines have many components, but one of the most basic and important parts is the injector plate, which causes the combustion of liquid propellants to be more stable and creating higher efficiency. Combustion chamber stabilization occurs when a large static pressure drop occurs inside the injector plate (so that the static pressure inside the combustion chamber is 20% less than the feed pressure of the propellant upstream of the inlet to the injectors plate). This relatively large static pressure drop separates small pressure fluctuations in the combustion chamber from propulsion pressure fluctuations. This type of instability is known as chugging. It should be noted that before combustion, the three processes of Atomization, Vapor stream formation, and Liquid stream impingement inside the injectors must be performed in the most optimal way. Several examples of injector plate design are shown in the figures below:

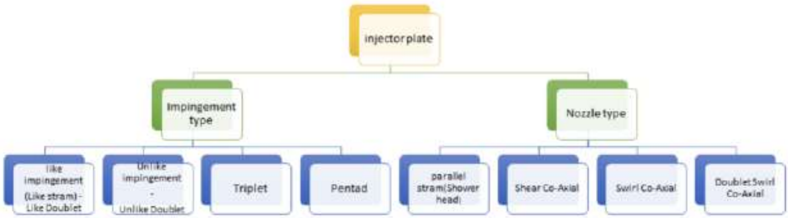

Figure 55- Types of injector plate design

INJECTOR

Liquid rocket engine injectors by atomizing and combining fuel with oxidizer create stable and efficient combustion, which will produce the required thrust without endangering the durability of the structure. Some injector's operation period up to a few minutes, while some are pulsed for a short time (milliseconds), and some have been deeply throttled. Injector design includes ring-type faces, solid faces, and porous faces. The requirement to be met by the injectors is attaining the required efficiency without compromising the combustion stability, durability of the injector, the chamber wall, and baffles. It should be noted that durability has been developed through improved film or barrier cooling effectiveness, more uniform injectant distribution, and improved fabrication technique and materials. Stability has been upgraded due as the combustion processes are better known as well as due to the use of stabilizing devices such as baffles, acoustic absorbers. In general, injector design includes the main two steps of injector flow system design and the development of the injector assembly. The geometry of the injector flow system, which causes the combustion stability and durability of the chamber, includes 1) the total element pattern, 2) the unique geometry of the orifice, and 3) the manifolding system of the orifices. The following figure shows the relationship of the various injector components to the flow system.

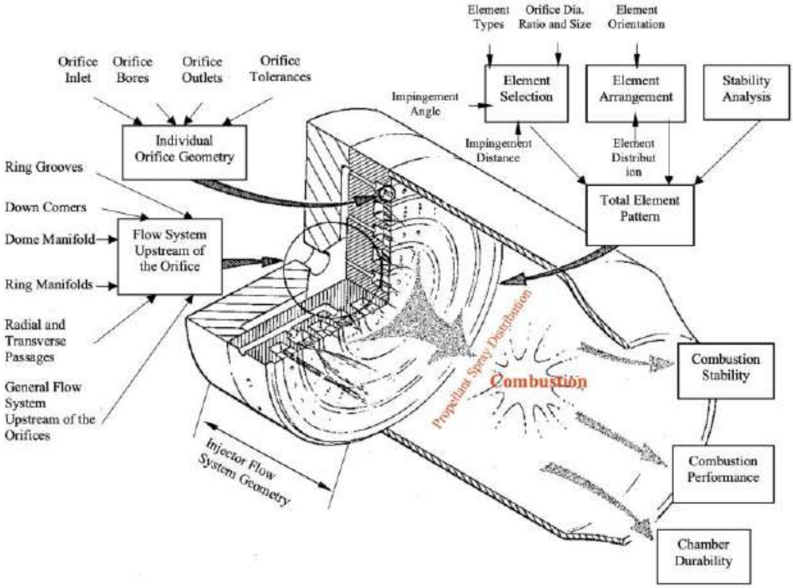

Figure 56- Relation of injector components to total injector flow system. From SP8089

The design of the flow system determines the mass ratio of the mixture, the drop size distribution, and the baffle arrangement.

Design of the total element pattern consist of (1) selection of the injector element, including the type and designation of all geometric parameters. (2) arrangement of the elements, including the orientation of an element with respect to the chamber wall and to other elements as well as element distribution across the injector face, and (3) provision for stabilization devices, such as baffles, acoustic absorbers, and feed-system resistors, that are integral parts of the injector. Proper design of the total pattern ensures that the propellants will mix in the desired manner and result in high performance, stable operation, and chamber and injector durability. (From SP 8089)

Experimental results show that the level of combustion performance is a function of the propellant spray distributions (i.e., mixture mass ratio and drop size). High combustion performance requires a high mixture mass ratio. The drop size also depends on the chamber geometry, operating conditions, and uniform mass distribution. Low performance is also the result of incomplete evaporation or poor dispersion of the mixture ratio. Factors such as the local mixture ratio and the mass distribution along with the injector plate or chamber wall, as well as the radial and transverse winds (i.e., the gases that flow from high-pressure region to the low-pressure regions), affect the durability of the hardware. Impingement of highly reactive propellant on the chamber wall can cause catastrophic failure of the chamber as a result of a high rate of chemical reaction or erosion of material, (from SP 8089). The mixing ratio and the distributions of the propellant mass near the chamber wall are controlled by the injector element, its position, and orientation on the injector face. Changes in the local mixture ratio and the mass distribution at baffle/baffle or wall/baffle junction, as well as the non-uniform distribution design to tailor the amount of propellant in the particularly acoustic mode significantly affect the degree of stability. The selection of the element is done according to the application. The parameters affecting the selection of the element that directly or indirectly affect the performance, heat transfer, compatibility, and stability of the chamber wall materials are as follows:

- Propellant Types: hypergolic, cryogenic, storable.
- Propellant state: liquid, gaseous, gel.
- Chamber wall cooling method: uncooled, ablative, regeneratively cooled.
- Operation conditions: mixture ratio, chamber pressure.
- Throttling requirements.
- System pressure drop limitation.
- Engine Life: total duration and restarts.

In general, the elements are divided into four categories: like impinging, unlike impinging, non-impinging, and hybrid; each method has its own mixing and atomization process.

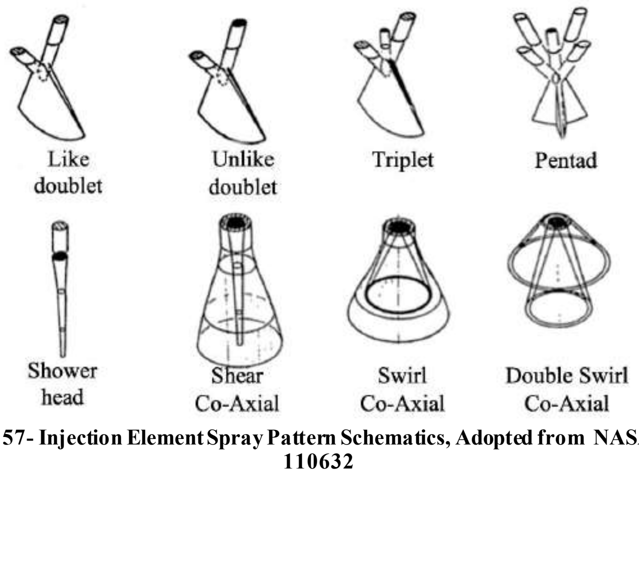

Figure 57- Injection Element Spray Pattern Schematics, Adopted from NASA-TM-110632

UNLIKE IMPINGING

In this case, direct mechanical mixing and atomization are done by direct impingement of fuel and oxidizer jets, which causes all mixing and atomization to take place in the immediate vicinity of the point of collision near the injector face. As a result, unlike impinging, it causes a high heat flux to the injector plate. The use of hypergolic propellants in all unlike impinging elements causes a blow apart phenomenon (reactive stream separation), whose mechanism is not yet well understood. Unlike impinging doublet is one of the most widely used elements for storable propellant engines. This element is composed of a single oxidizer and fuel jets that collide at a certain distance from the injector plate at a predetermined angle (most of the angles used are 60°, 45°, and 90°, respectively). The advantages of this element include simple design and convenience for manifold and uniform mixing. One of the problems that occur during the use of this element is the durability of the chamber when these elements are used near the wall of the combustion chamber and create a non-uniform ratio of the local mixture. To overcome this problem, the orientation of the element near the wall is changed so that the flow is sprayed axially, also shower head fuel orifices in the outer ring are used to create a compatible environment near the chamber wall by spraying a fuel-rich mixture. Unlike impinging triplet is another example of this element in which two jets (usually oxidizer) with a certain angle are designed to collide with the central axial jet (usually fuel) at one point, and thus resulting in axially directed resultant spray under all operating conditions. In this model (two external oxidizer jets and a central fuel jet), while overall mixing uniformity slightly improved over the use of the impinging doublet, its use near the chamber wall is not desirable. As a result, by considering the reverse design, i.e., external jets as fuel jets and central jet as oxidizer, the heat flux on the wall is reduced. unlike-impinging quadlet is commonly used in space vehicle engines and acts like, the unlike-impinging doublet. unlike-impinging panted is very attractive for applications with different mixing ratios (other than one). The design of this element is such that four orifices are equidistant from a central axial orifice and meet at a common point. Using this element creates more uniform mixing than triple doublet. Disadvantages of these injectors include manifolding complexity, high heat flux to the injector plate, and chamber durability due to the local mixture ratio gradient. High heat flux near the injector plate causes injector destruction. Using this element with liquid/gas bipropellants provides highly efficient atomization and uniform mixing with relatively large thrust per element.

The following equation concretizes the general correlation used for the unlike impinging element, which is relating maximum mixing efficiency (MME) to the orifice area ratio and used to define $(\frac{d_c}{d_{ou}})$ that produce optimum mixing, designed for the collision angle of 60°:

$$(\frac{d_c}{d_{ou}})^2_{MME} = M[\frac{\rho_{ou}}{\rho_c}(\frac{\dot{W}_c}{\dot{W}_{ou}})^2]^{0.7} \quad (222)$$

Where:

d_c: diameter of the center orifice (for 1:1 and 2:2, either side by side or opposed, the center orifice is assigned arbitrarily to either leg and the area is that an individual orifice)

d_{ou}: diameter of the outside orifices

M: The mixing factor, which is obtained experimentally. (Typical values are listed in table below)

$\dot{W}_c$ and $\dot{W}_{ou}$: Total mass flowrate through all center and outside orifices, respectively.

Element Type	1-on-1,2-on-2	2-on-1	3-on-1	4-on-1	5-on-1
M	1	1.6	3.5	9.4	27.5

Table 5- Experimentally mixing factors

Because the size of the orifice affects the level of mixing, for hypergolic propellants and large orifices ($d > 0.030\ in$), it causes a reactive stream separation phenomenon (blow apart), whereas the very little effect is observed in small orifices ($d < 0.030\ in$). The diameter of the orifice and the ratio of the diameter influence drop size, which the following expression shows this relation for an unlike impinging doublet element with an impingement angle of 60°:

$$D_f = 2.9 \times 10^4 (V_f)^{-0.766} (\frac{P_c}{P_j})_f^{-0.65} d_f^{0.293} P_D^{0.165} (\frac{d_o}{d_f})^{0.023} K_{Prop} \quad (223)$$

Where:

$\bar{D}$: Mass median drop size in micron

V: Injection velocity $[{}^{ft}/_{sec}]$

P_c and P_j: Dynamic pressure, and mean dynamic pressure of jet, respectively $[psi]$

$\frac{P_c}{P_j}$: Velocity profile parameter

P_D: Dynamic pressure ratio $(\frac{\rho_f V_f^2}{\rho_o V_o^2})$

K_{Prop}: Correction factor for propellant physical properties

$$K_{Prop} = \left[\left(\frac{\mu\sigma}{\rho}\right)_{Propellant} \Big/ \left(\frac{\mu\sigma}{\rho}\right)_{Shellwax} \right]^{\frac{1}{4}} \tag{224}$$

Where μ is dynamic viscosity $[\frac{lbm}{ft.sec}]$, and σ is surface tension $[\frac{dynes}{cm}]$. For the shell wax 270 as a reference material μ, σ, and ρ are $2.69 \times 10^{-3} [\frac{lbm}{ft.sec}]$, $17 [\frac{dynes}{cm}]$, and $47.7 [\frac{lbm}{ft^3}]$, respectively.

LIKE IMPINGING

In these elements, mixing is done downstream of the impingement point of the jets because mixing occurs as a result of intermixing of adjacent fuel and oxidizer spray fans. Mass and mixture ratio distributions are functions of element size, spacing between oxidizer and fuel fans, and fan inclination or cant angle. Atomization is also a function of orifice size, injection velocity, impingement angle, and distance, (from SP 8089). Examples of applications for this element include the F-1 and the Atlas first-stage booster and sustainer, as well as the first-stage Titan-1 engine. In these elements due to the fact that the orifice sizes of the impinging jets are equal, the diameter ratio is not a design parameter, but the orifice diameter is effective at the level of atomization and mixing. Experiments have shown that for elements with jets between 0.02 and 0.03 inches (0.76 mm), there is no significant increase in mixing. Equation 223 for a like impinging element, when designed for an included impingement angle of 60°, rewrite as follows:

$$\overline{D} = 1.6 \times 10^5 (V_j)^{-1} \left(\frac{P_c}{P_j}\right)_f^{-0.10} d_j^{0.57} K_{Prop} \tag{225}$$

Where V_j and d_j are mean jet velocity and jet diameter, respectively. It should be noted that drop size is roughly proportional to the square root of the orifice diameter.

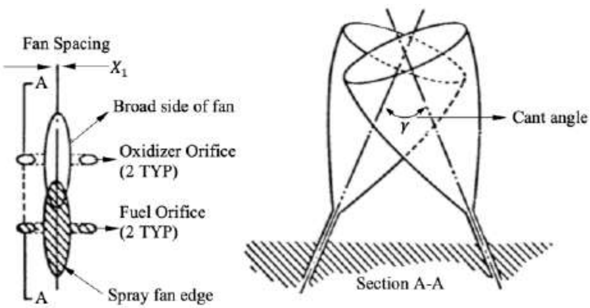

Figure 58- Design variables for like impinging doublet. From SP 8089

NON-IMPINGING ELEMENTS

Non-impinging elements include the shower head and concentric tube. The showerhead element is used near the wall as a cooling film. Examples of this model include the German V-2, Aerobee sustainer engine, and x-15 engine. showerhead contains only axillary directed orifices. The atomization and mixing process is the result of the collision of combustion gases with the injected jet. For engines using this type of injector, a longer combustion chamber is selected to create a turbulent zone that allows for better mixing. Concentric-tube element is also widely used in liquid/liquid and liquid/gas bipropellants applications. Examples of its application in liquid/liquid include the Surveyor vernier engine (MIRA 150 A), although the concentric-tube element with swirler is widely used for booster engines. Other examples of concentric element use include j-2, M-1, and RL-10, which are gas/liquid applications. Several examples of the construction of these concentric elements are shown in the figure 60. These elements have high stability and durability, and despite their simple appearance, they have a complex design so that with a small change in the geometry, the stability, and performance of the chamber, as well as heat transfer to the wall, changes drastically. In showerhead, unlike the previous two elements, the ratio of orifice diameters has no effect on mixing and atomization, while the size of the element affects both. Orifices are generally made to the smallest possible extent with manufacturing constraints to increase mixing and performance. For the concentric tube element, the equivalent of diameter ratio is the ratio of the width of the annulus gap to the diameter of the center jet. Element size is equivalent to the center-jet diameter, (from SP 8089). In these elements, the mixing decreases with increasing diameter ratio, because increasing the thickness in this design, increases the external surface (outward expansion of the flow from the annulus jet), which in turn increases the amount of energy lost in the flow.

High performance designs resulting in low ΔP have been found insufficient for distributing the liquid oxidizer in the feed manifold and sometimes insufficient to meet system stability requirements. To overcome the problems resulting from low ΔP, a small orifice for flow control is placed at the forward end of the center liquid tube (i.e., at the manifold outlet into the tube), with a large outlet area at the exit end of the tube to inject the liquid at low velocity, (from SP 8089).

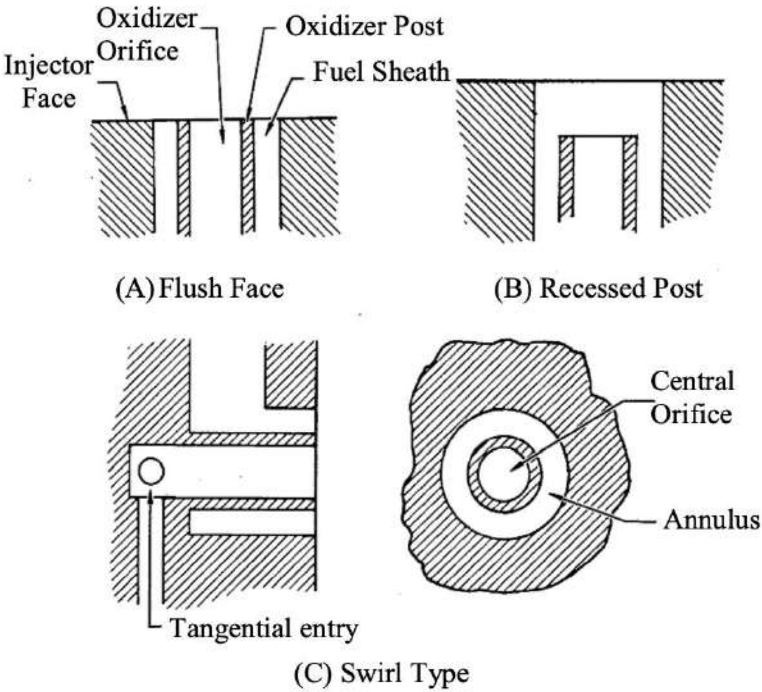

Figure 59- Three configurations for concentric tube element. From NASA SP 8089

HYBRID ELEMENTS

This type of element consists of a combination of previous elements that are divided into two categories of the pintle and splash-plate injectors. Pintle injector applications include Lance sustainer engine and LEM descent engine. These injectors have lower performance, injector plate burning, and wall streaking due to irregularities in the feed-system upstream geometry and variations in local element mixture ratio under throttled conditions. One of the problems with this injector is that it is difficult to build due to many details in the design. The splash plate injector also has many applications, such as the early version of the Lance booster engine and the Gemini maneuvering engine. Other applications of this element include the construction of a large thrust chamber for high performance with a very simple injector manifold system. These elements have been used extensively at low thrust levels in production thrust chamber assemblies where the total number of orifices was very small, primarily to improve ablative wall durability and secondary to reduce variation in performance induced by inadequate injector hydraulic control (from SP 8089). One of the major problems with the splash plate injector that occurs in the combustion chamber and gas generators is the burning of the splash plate face when the point of collision of the fuel and the oxidizer is above the splash plate face. The orifice diameter and its diameter ratio are determinants of mixing control and atomization. For all elements, small orifices have a higher evaporation rate and a more uniform mixture ratio due to the smaller droplet size, therefore have a higher performance. This is while the heat flux on the injector plate is higher due to the higher combustion rate near the injector plate. For the pintle element, the equivalent diameter (figure 61) ratio is the ratio of internal to the external curvature, which in the LEM descent engine, for example, is the ratio of the width of the outer annulus (A) to the width of the inner slot (S). Experience has shown that the correlation of the unlike impinging element can be applied for these injectors, or in other words, the momentum balance between the internal and external streams causes optimum mixing.

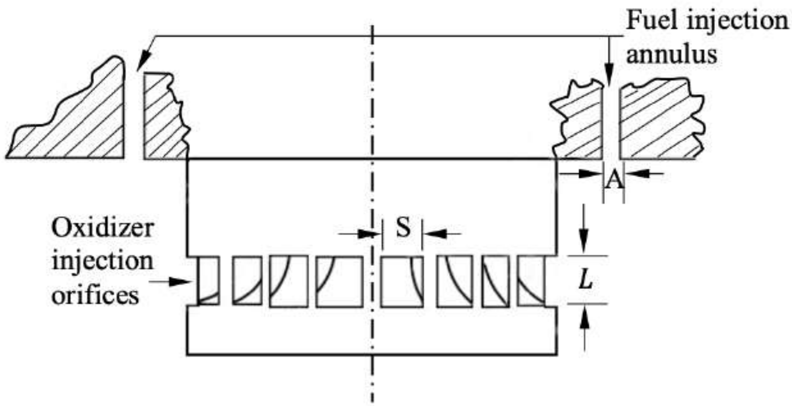

Figure 60- illustration of pintle element showing inner slots and outer annulus. from SP 8089.

For liquid/liquid bipropellant, which is also true for gas/liquid, the oxidizer correlation injected through the slots is written as follows:

$$\frac{\rho_f V_f^{\,2}(AS+2lC)}{\rho_o V_o^{\,2} Sl} = 1 \tag{226}$$

In the above equation, A and S are widths of the fuel and oxidizer slot annulus in inches, respectively, L is the length of the slot which is measured also in inches, and C is the cross-influence term. For splash-plate, laboratory results have shown that the overall performance increases with increasing orifice size until the diameter of the oxidizing jet is less than 0.08.

The precise design of the injector plate creates a suitable mixing ratio of oxidant and fuel at the desired distance from the injector plate and a suitable angle to the axis of the combustion chamber. Any misalignment in the geometry of the orifices and their angle causes poor combustion performance and insufficient fuel composition and the type of chemical reaction in the combustion chamber wall, resulting in structural failure, which occurs due to insufficient cooling. In contrast, the proper design of the injector plate creates a backsplash and heat transfer to the combustion chamber wall, which stabilizes the combustion and increases efficiency. Using Bernoulli's equation and considering the viscous fluid rules inside the injectors, the injection velocity of the fuel and oxidizer obtained by the following equations:

$$v_f = C_{df}\sqrt{\frac{2\Delta P_f}{\rho_f}} \tag{227-a}$$

$$v_O = C_{dO}\sqrt{\frac{2\Delta P_O}{\rho_O}} \tag{227-b}$$

In the above relation, the term C_d represents the discharge coefficient, which is a function of the Orifice geometry and the Reynolds number. The mass flow rate at the Orifice's inlet obtains by writing the mass conservation equation, namely:

$$\dot{m}_f = \rho_f v_f A_f = C_{df} A_f \sqrt{2\Delta P_f \rho_f} \tag{228-a}$$

$$\dot{m}_O = \rho_O v_O A_O = C_{dO} A_O \sqrt{2\Delta P_O \rho_O} \tag{228-b}$$

The ratio of the mass flow rate of oxygen to fuel knows as the mixture ratio (r) and is calculated as follows:

$$r = \frac{\dot{m}_O}{\dot{m}_f} = \frac{C_{dO}}{C_{df}}\frac{A_O}{A_f}\sqrt{\frac{\Delta P_O \rho_O}{\Delta P_f\, \rho_f}} \tag{229}$$

When this ratio is equal to its stoichiometric value, the resulting temperature in the combustion chamber reaches its maximum, but because a rich mixture often uses in rockets, hence $(r < r_{st})$ and the amount of molecular mass of the mixture will be less than its stoichiometric value, which will cause more specific impulse. The thermochemical calculations of oxygen and hydrocarbon fuel RP-1 are shown in figure 65 at a full expanded nozzle with the pressure of 1000 psi and sea-level conditions. According to the figure, two modes use for the nozzle calculations. Frozen equilibrium calculations use assuming that the chemical composition of the products inside the nozzle is constant, i.e., the equilibrium molar fraction in the combustion products remains constant with respect to the expansion of the gases. The sifting equilibrium calculation, however, allow for chemical reaction in the nozzle as a result of flow expansion, thus it represent a more accurate description of the rocket thrust chamber performance. In either case, we note that the specific thrust has reached maximum at either the mixture ratio of ~2.3 for frozen equilibrium or 2.5 for the shifting equilibrium calculations. Based on the choice of the mixture ratio (r) is based on maximum specific thrust (I_s) rather than the maximum chamber temperature (T_c).

IMPINGING ANGLE

The angle of impingement depending on the type of element used, affecting the amount of propellant backsplash, the uniformity of the resulting mixture, and atomization. For unlike impinging elements, as the collision angle increases, the amount of mixed propellant flowing back from the collision point toward the injector plate is increases. The following figure shows a schematic of this concept.

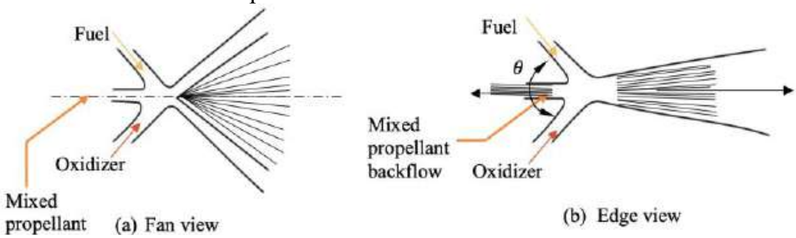

Figure 61- Two-dimensional flow field for a typical unlike impinging element. From SP 8089.

As can be seen in the figure, the mass flowing backward is proportional to the cosine of the collision angle. Experimental results have shown that by increasing the collision angle more than 90°, the amount of heat flux to the injector plate increases and over the range of the impingement angle from 0 to 40°, with decreasing collision angle, the mixing increases. For gas / liquid bipropellant with collision angle of θ in optimal condition (i.e., two fuel jets plus central gas jet):

$$\cos(90-\theta) = 0.2\frac{d_g}{d_L}\frac{V_g}{V_L}(\frac{\rho_g}{\rho_L})^{\gamma_i} \tag{231}$$

For the like impinging element, the backsplash does not cause the previous problems because the process of mixing the propellants occurs after the intermixing of the spray fans. As shown in Figure 59, these elements contain a collision angle (the angle between two fuel jets with two oxidizing jets) and a cant angle (the angle between the centerline of the oxidizing jet and the fuel fans). It should be noted that in these elements, changing the initial angle of impingement has no effect on mixing. The effect of the initial collision angle on the drop size is expressed as follows:

$$D_o = (1.44 - 0.00734\ \theta)\overline{D}_{60} \tag{232}$$

Where θ in the above equation is an impingement angle, and $\overline{D}_{60}$ is the value of drop size which is calculated from equation 225. according to equation 232, it can be understood that the droplet size decreases linearly with increasing collision angle. As mentioned earlier, the like impinging element, similar to the unlike one, uses the collision angles of 60° and 19° (as the lower angle). According to experimental results, cant angle, which has a significant effect on mixing, has shown that by increasing it from 0 to 41°, the uniformity of mixing increases from 30 to 40 and further increasing it reduces the uniformity of mixing.
As can be seen from the showerhead geometry, the impingement angle will not work, and the equivalent of this angle in the concentric-tube injector is the inner post chamfer angle shown in Figure 63. This chamfer angle causes the diffusion of an internal liquid flow into the gas, and it's about 5°.

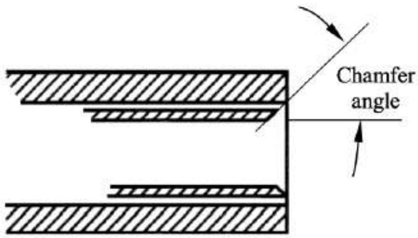

Figure 62- illustration of inner-post chamfer angle in a concentric tube element. From SP 8089.

A schematic of the pintle injector geometry is shown in the figure below. The angle of impingement in these elements, which is an important design parameter, plays a very important role.

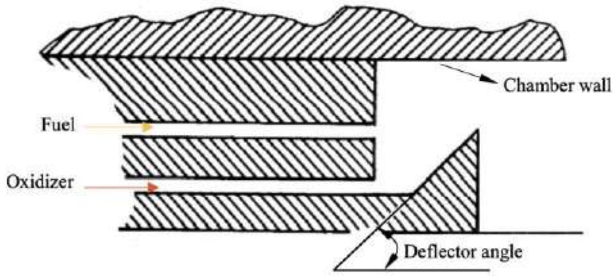

Figure 63- Schematic of Pintle deflector angle. From SP 8089.

As this angle further increases, the heat flux of the wall will be increasing due to the collision of the oxidizer to the chamber wall, hence in the case of the wall with ablation cooling causes wall erosion. Another consequence of increasing this angle is the backflow of the propellant. As shown in Figure 65, these elements can be sprayed radially through the slots, in which case the collision angle is the angle between the slot axis and the deflector. In the other category of hybrid elements (i.e., splash plate injector), the impingement angle is the same as the splash plate angle. Experimentally results show that by increasing the splash plate angle from 20° to 27°, the performance will not change, and by further increasing the splash plate angle, atomization and mixing uniformity will both be affected.

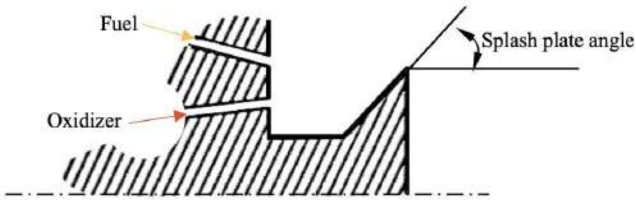

Figure 64- Illustration of splash-plate angle. From SP 8089

Figure (67) shows Injector discharge coefficient for different orifice geometries that are suitable for rocket propulsion applications. For preliminary injector plate calculation purposes, we use the law of the momentum conservation applied to colliding jets mass flow rate. Figure (69) is a definition sketch of two impingement jets, their angles γ_o and γ_f, and collision distance (d) from the wall. The real impingement jets, however, exhibit some backsplash as well as complex turbulent interactions, as schematically indicated in figure (69-b). The resultant jet is assumed to emerge at angle δ with respect to chamber axis, as shown. The momentum balance in the direction of the axis of the chamber and perpendicular to it is: (Adopted from Rocket Propulsion,2009)

$$\dot{m}_f v_f \cos\gamma_f + \dot{m}_o v_o \cos\gamma_o = (\dot{m}_f + \dot{m}_o) v_r \cos\gamma \qquad (233\text{-a})$$

$$\dot{m}_f v_f \sin\gamma_f - \dot{m}_o v_o \sin\gamma_o = (\dot{m}_f + \dot{m}_o) v_r \sin\gamma \qquad (233\text{-b})$$

Which the resultant jet flow angle can be calculated as follows:

$$\tan\gamma = \frac{\dot{m}_f v_f \sin\gamma_f - \dot{m}_o v_o \sin\gamma_o}{\dot{m}_f v_f \cos\gamma_f + \dot{m}_o v_o \cos\gamma_o} \qquad (234)$$

As mentioned earlier, the temperature inside the combustion chamber is very high, and since rocket combustion uses a fuel-rich mixture of propellant, an extra fuel injects adjacent to the combustion chamber wall as means of wall thermal protection. The geometry of the design of the injector is in such a way that they spray the fuel to the axis of the chamber walls to reduce the thermal effect on it. Figures 68-a and 68-b show the concept of this scheme. The backsplash inside the collision injector plate can damage the structure of the injector plate, and because this amount of fuel near the wall participates in the chemical reaction, it causes shock and an increase in temperature. Therefore, some design constraints consider to preventing the occurrence of these accidents, which include restrictions on the collision distance and the total collision angle $(\gamma_o + \gamma_f)$:

$$d \sim 5\ to\ 7\frac{(d_0 + d_f)}{2} \tag{235}$$

$$(\gamma_f + \gamma_o) < 60^{\circ} \tag{236}$$

Also, to reduce the chugging pressure, we design a large pressure drop $\Delta P_{inj} = 0.2P_c$ inside the injector plate, and for better atomization, the diameter of the orifices should be assumed to be smaller $(0.2 - 2.4_{mm})$, although a very small Orifice will create a bifurcated stream. The Orifice's diameter ratio of $(\frac{d_0}{d_f} = 1.2)$ is also considered the most desirable case for unlike impinging.

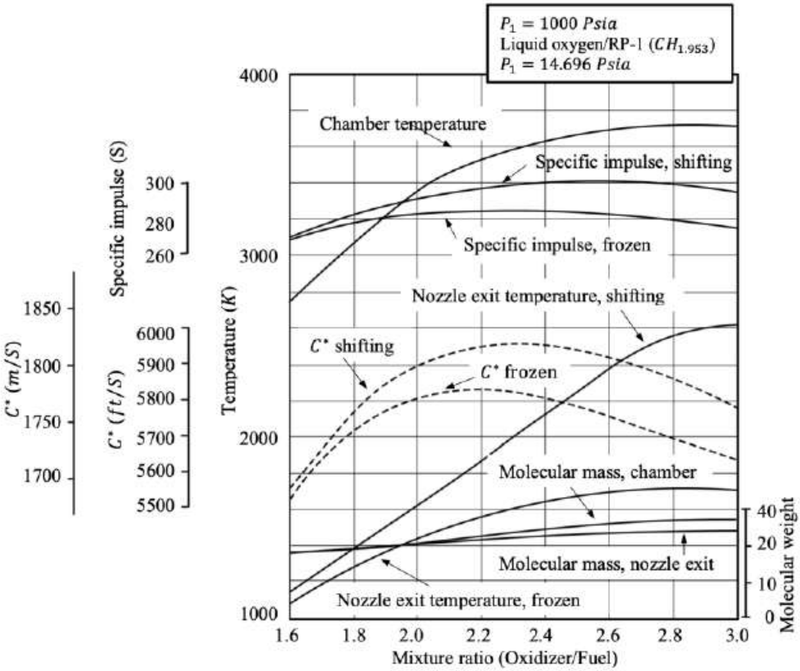

Figure 65- Thermochemical calculation for Oxygen- 〖RP〗_1 combustion. Adopted and redesign From Aircraft Propulsion 2009

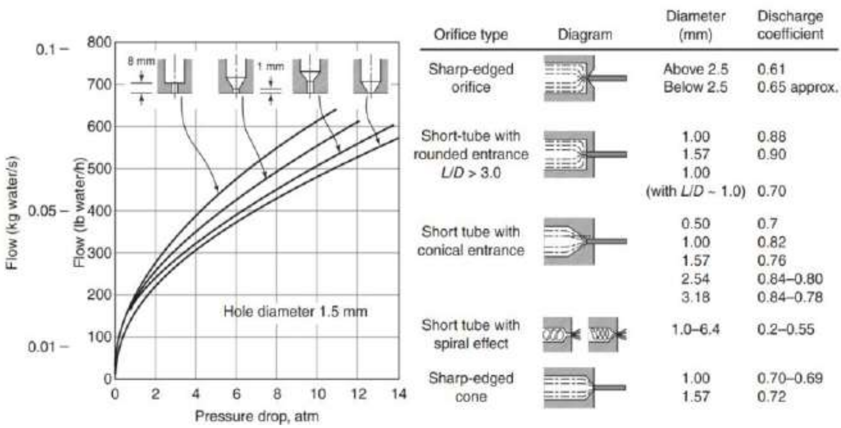

Figure 66- Discharge coefficient for typical injector orifice geometries, based on water test. (From Sutton and Biblarz 2001)

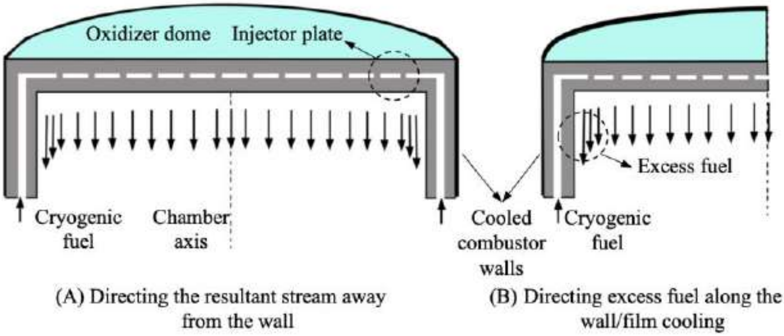

Figure 67- Schematic drawing of possible propellant injection pattern in the combustion chamber. Adopted and redesign from Aircraft Propulsion 2009 .

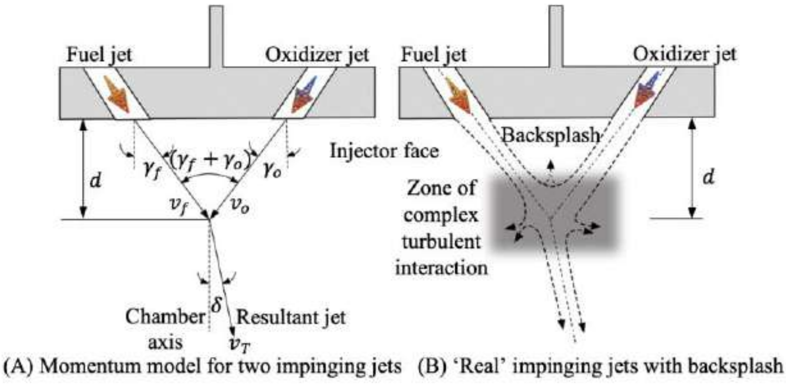

Figure 68- Definition sketch of two impinging jets. Adopted and redesign from Aircraft Propulsion 2009.

COMBUSTION CHAMBER INSTABILITY

Instability in the combustion chamber of chemical rockets will be divided into three categories based on the frequency range. The first type, which is in the frequency range of 10 to 200_{Hz}, is due to the coupling of the pressure feed oscillation with the combustion chamber pressure oscillations, which is known as chugging. To prevent this instability, the static pressure drop should be approximately 20% of the combustion chamber pressure along the injector plate. This type of instability in car movement appears as (pogo) instability. The second type of instability inside the combustion chamber will occur in the frequency range of 200 to 1000_{Hz}, which can be due to mechanical vibration of the propulsion system as well as coupling between the turbulent vortices of the combustion chamber and the spray pattern of the injector plate, and known as buzzing, acoustic, or entropy instability. The third type of instability is due to the pattern of energy released inside the combustion chamber and the sounds and resonances caused by the cavities inside the combustion chamber and has a frequency of more than 1000_{Hz} and is known as screaming or screeching instability. To prevent this instability from occurring, baffles use on the injectors, which are shown in the figure below.

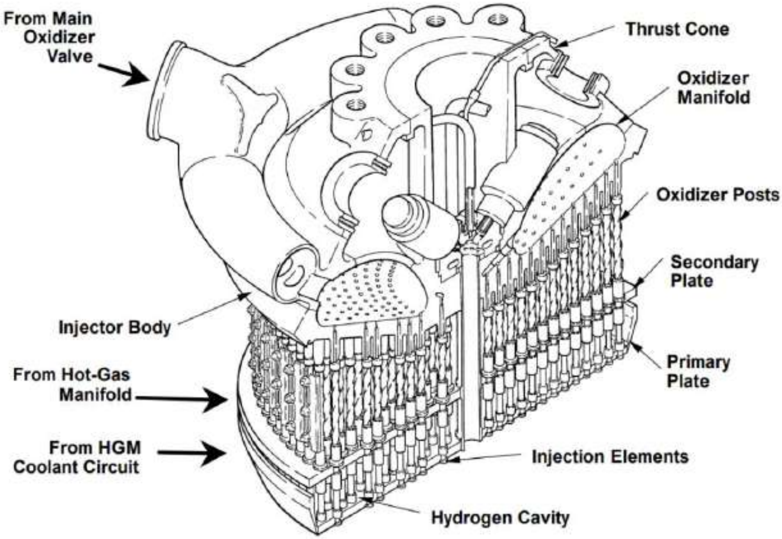

Figure 69- SSME_Presentation_2

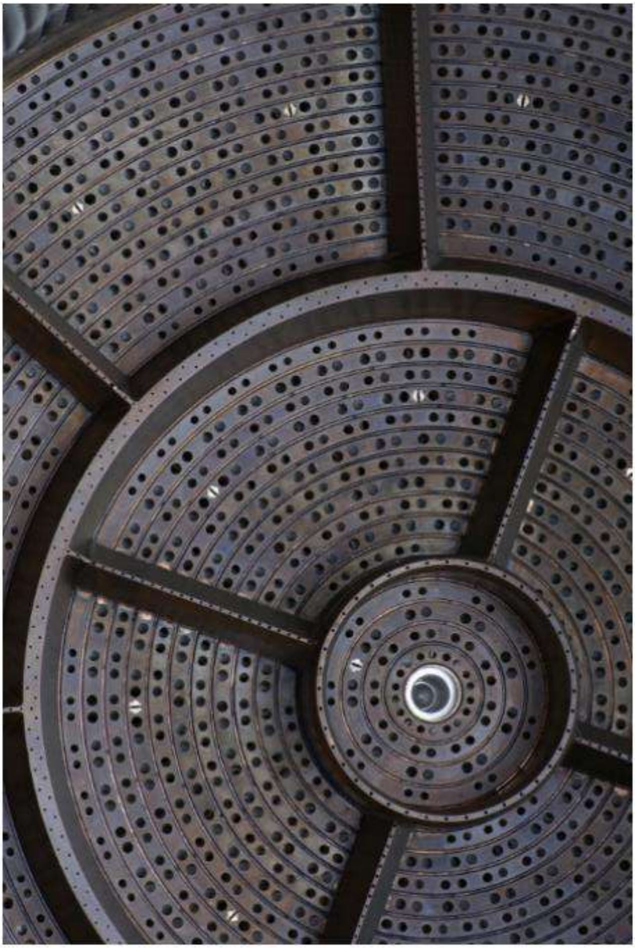

Figure 70- F1 engine by Davidson Center for Space Exploration

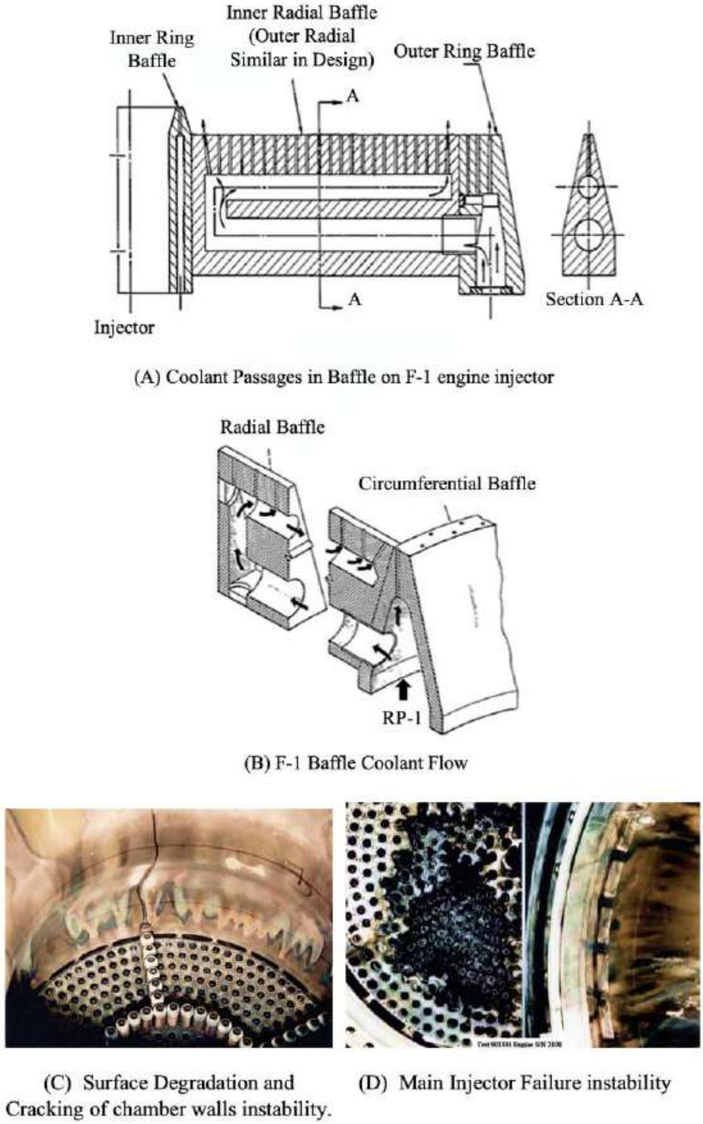

Figure 71 -Baffle concept and main chamber instabilities. Adopted from NASA TN D-4730- NASA SP 8113 and Designing Liquid Rocket Engine Injectors for Performance, Stability, and Cost, respectively.

SOLID PROPELLANT COMBUSTION CHAMBER

Solid propellants consist of oxidizers, fuels, and binders in the solid state, which can be divided into three categories depending on the type of composition. The first group is known as double-base (DB), a homogeneous mixture of fuel and oxidizer and binder, and some additives include metal particles and oxides such as (Al) that will increase the combustion rate. A heterogeneous mixture of fuel and oxidant, binders, and additives such as ammonium perchlorate (AP) classify as composite propellants in the second group. The last one is the composite modified double base (CMDB), which is a combination of the previous two groups. Table (7) shows some.
The combustion rate of a solid propellant, which means the rate of chemical reaction and burning, can be defined as combustion that progresses perpendicular to the surface of the propellant grains. Therefore, the continuity equation for this mass transition due to combustion (or the mass flow rate of the emerging gas from the combustion of solid propellant grains), with due attention to the recession of solid grains perpendicular to its surface as well as the density of the grains:

$$\dot{m} = \rho_b r A_b \tag{237}$$

In this equation, the mass flow rate is proportional to the surface area of the burned grains, the rate of propellant recession surface, and the density of the grains. There is an experimental formula that expresses the combustion rate based on the combustion chamber conditions for the final burning grains:

$$r = aP_c^n$$

(238)

(a) and (n) indices will vary according to the type of selected propellant, with (a) a function of the propellant grain temperature and (P_c) representing the chamber pressure. Since the flow rate through the nozzle is proportional to the combustion chamber pressure, if the combustion chamber pressure decreases, then the flow rate decreases, which also reduces the combustion rate, while if it is $(n \leq 1)$, It will increase the pressure in the chamber, which is called stable operation. However, if it is $(n > 1)$, the burning rate will decrease faster, which will further reduce the chamber pressure and is known as unstable conditions. Therefore, for stable conditions, the power n for the chamber pressure must be less than 1. The table below shows the dependence of the combustion rate on the chamber pressure for several types of solid propellants, which confirms the validity of the previous equation. According to the table, the changes in combustion rate relative to the chamber pressure for the (Plateau DB) propellant have a constant value, meaning that the pressure exponent in equation (238) is zero $(n = 0)$.

By equating the flow rate which is passing through the nozzle throat with the amount of produced gas by the combustion of solid propellants (obtained mass flow rate in equation 237), result in

$$\dot{m} = \rho_b r A_b = P_1 A_{th} \sqrt{\frac{\gamma}{RT_1}\left[\frac{2}{\gamma+1}\right]^{\frac{\gamma+1}{\gamma-1}}} \tag{239}$$

Therefore, the ratio of the burning area to the throat area obtains from the following equation:

$$\frac{A_b}{A_{th}} = \frac{P_1}{\rho_b r}\sqrt{\frac{\gamma}{RT_1}\left[\frac{2}{\gamma+1}\right]^{\frac{\gamma+1}{\gamma-1}}} = \frac{P_1{}^{1-n}}{\rho_b a\sqrt{RT_1}}\sqrt{\gamma\left[\frac{2}{\gamma+1}\right]^{\frac{\gamma+1}{\gamma-1}}} \tag{240}$$

The right-hand side of the above equation represents the dependence of the area ratio on the three terms of pressure and temperature and the characteristics of the propellants, whereas the combustion chamber pressure itself is a function of the area ratio:

$$P_1 \propto \left(\frac{A_b}{A_{th}}\right)^{\frac{1}{1-n}} \tag{241}$$

Since $n < 1$, the pressure inside the combustion chamber will increase as the area ratio increases. Due to this, sudden changes in the burning surface can cause structural failure.

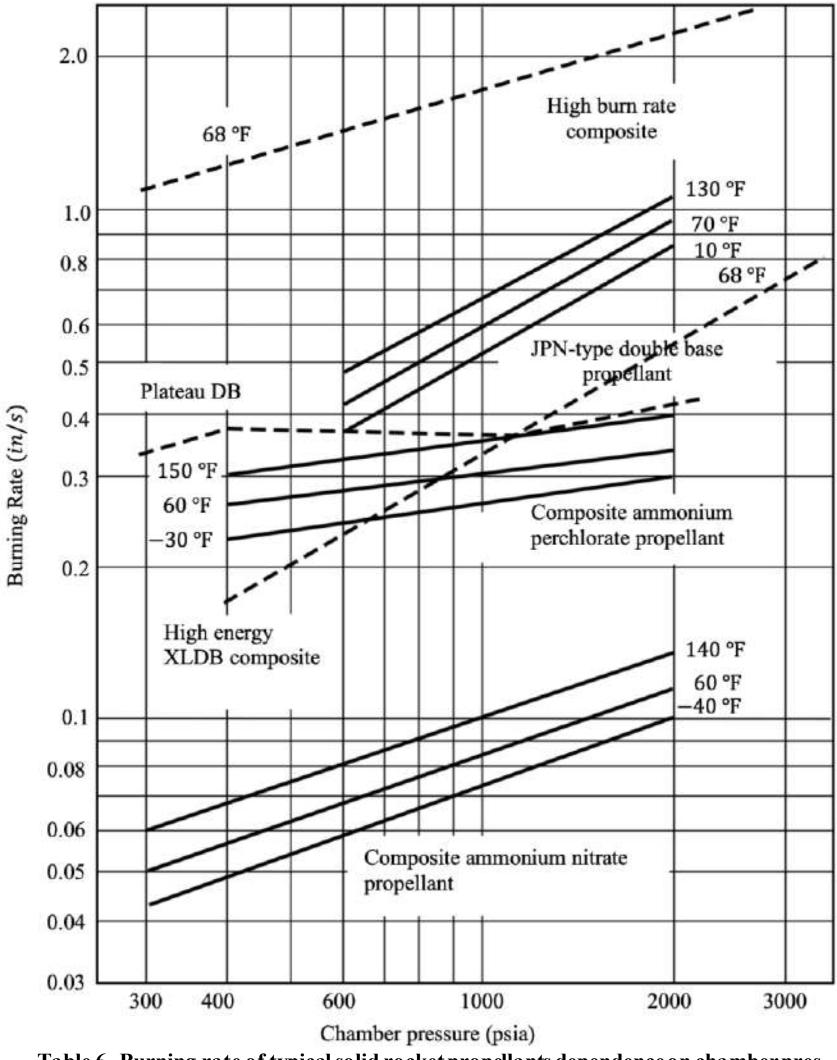

Table 6- Burning rate of typical solid rocket propellants dependence on chamber pressure and initial grain temperature. Adopted from Aircraft propulsion 2009.

Propellant Type[a]	I_a Range (sec)[b]	Flame Temp.[c]		Density or specific gravity		Metal content (wt%)	Burning rate[c,e] (in/s)	Pressure exponenet[c] n	Hazard classification	Stress (psi)/ Strain (%)		Processing method
		(°F)	(K)	(lb/in^3)	$(Sp.gr.)$					−60°F	+150°F	
DB	220-230	4100	2550	0.058	1.61	0	0.05-1.2	0.30	1.1	4600/2	490/60	Extruded
DB/AP/AI	260-265	6500	3880	0.065	1.80	20-21	0.2-0.1	0.40	1.3	2750/5	120/50	
DB/AP-HMX/AI	265-270	6700	4000			20	0.2-1.2	0.49	1.1	2375/3	50/33	Solvent cast
PVC/AP/AI	260-265	5600	3380	0.064	1.78	21	0.3-0.9	0.35	1.3	369/150	38/220	Cast or extruded
PU/AP/AI	260-265	5700	3440			16-20	0.2-0.9	0.15		1170/6	75/33	Cast
PBAN/AP/AI	260-263	5800	3500			16	0.25-1.0	0.33		520/16 (at -10 °F)	71/28	
CTPB/AP/AI	260-265	5700	3440	0.064	1.78	15-17	0.25-2.0	0.40		325/26	88/75	
HTPB/AP/AI				0.067	1.86	4-17	0.25-3.0			910/50	90/33	
PBAA/AP/AI				0.064	1.78	14	0.25-1.3	0.35		500/13	41/31	
AN/Polymer	180-190	2300	1550	0.053	1.47	0	0.06-0.5	0.60		200/5	NA	

a: Al, aluminum; AN, ammonium nitric; AP, ammonium perchlorate; CTPB, carboxy-terminated polybutadiene; DB, double base; HMX, cyclotetramethylene tetranitramine; HTPB, hydroxyl-terminatd polybutadiene; PBAA, polybutadiene-acrylic acid polymer; PBAN, polybutadiene-acrylic acid- acrylonitrile terpolymer; PU, polyurethane; PVC, polyvinyl chloride.
b: At 1000 psia expanding to 14.7 psia, ideal or theoretical value at reference conditions.
c: At 1000 psia.

Table 7- Characteristics of some solid propellants

HYBRID PROPULSION HEAT TRANSFER

According to the hybrid propellant characteristics, heat transfer will occur in the boundary layer basin. The heat transfer due to the flame region inward the solid fuel draws it back to evaporate and regression, which feeds the combustion. The energy conservation for the equilibrium between gaseous fuel and heat transfer to the solid fuel wall will be written according to equation 242, in which the terms m and h represent the rate of fuel and the effective heat for gasification, respectively. Where the effective heat in term includes three parts:

1. The heat is used to warm up the fuel wall.
2. Heat exchange that is spent on phenomena such as polymerization before gasification.
3. Evaporation heat.

$$Q_w = \dot{m}_f . h_v \xRightarrow{\dot{m}_f = \rho_f . \dot{r}} Q_w = \rho_f . \dot{r} . h_v = (\rho \dot{r})_w h_v \qquad (242)$$

Where Q_w is the total heat flux toward the surface and terms h_v and $\dot{r}$ are the heat of gasification and the regression rate of the solid grains, respectively. For the case where the solid surface cannot vaporize, h contains only the heat that shifts the temperature of the grains from ambient to the solid surface temperature. Hence, the convection heat transfer equation on the wall is expressed as follows:

$$Q_c = C_H \rho_b u_b \Delta h \qquad (243)$$

In the above equation, C_H is the Stanton number. ρ_b and u_b are also representatives of the density and velocity of the gas in the flame region within the momentum boundary layer, respectively. The specific enthalpy changes between the flame region and the wall are expressed in terms of Δh. The evaluation of Stanton number employed in this equation is the same as the friction coefficient in conventional pipe flows, but with two major modifications:

1. The heat source is located within the boundary layer:

$$C_H = \left(\frac{C_f}{2}\right) \frac{\rho_e {u_e}^2}{\rho_b {u_b}^2} \qquad (244)$$

2. The second correction is due to the blowing effect that the fuel vapor moves from the wall surface toward the core of the flame in the combustion zone.

$$B = \frac{(\rho v)_w}{\left({}^{C_f}/_2\right).\rho_e u_e} = \frac{\dot{r}\rho}{\left({}^{C_f}/_2\right).G} = \frac{\dot{m}_f}{\left({}^{C_f}/_2\right).G} \tag{245}$$

Where the terms $\dot{m}_f$ and G are the mass flow of gas from the surface and the total mass flux, respectively. For the case where the predominant convective flow occurs, the blowing effect in the equation of gaseous mass flux from the surface is represented as follows:

$$\dot{m}_f = \dot{r}\rho = \left({}^{C_f}/_2\right).G.\left(\frac{u_e}{u_b}\frac{\Delta h}{h_v}\right) \tag{246}$$

The expression in parentheses is called the mass transfer number (B), which can be evaluated in terms of thermodynamic quantities. The speed ratio $(\frac{u_e}{u_b})$ used in the above relation has fewer changes than the $(\frac{\Delta h}{h_v})$ term, and its approximate value for different systems varies between 1.5 to 1.7. The coefficient of friction used is also obtained from the turbulent empirical law in the absence of the blowing (i.e., $Pr = 1$) by equation 247, where (μ) represents the viscosity and G represents the mass flux at a distance of x.

$$C_{fo} = 0.06.\left({}^{\mu}/_{Gx}\right)^{0.2} \tag{247}$$

To find out the relation between C_f and C_{fo}, we return to equation 244, which represents the blocking effect on the heat transfer coefficient, hence $(C_H/C_{Hb}) = (C_f/C_{fo})$.
The general equation of regression rate is expressed as follows:

$$\dot{m}_f = \dot{r}\rho = \left({}^{C_f}/_{C_{fo}}\right).0.03.\left({}^{\mu}/_{x}\right)^{0.2}.G^{0.8}.B \tag{245}$$

According to Figure 73, the above equation can be simplified as follows:

$$\frac{C_f}{C_{fo}} = \left(\frac{\ln(1+B)}{B}\right)^{0.8}\left(\frac{1+1.3B+0.364\,B^2}{(1+B/2)^2(1+B)}\right)^{0.2} \tag{246}$$

$$\dot{m}_f = \dot{r}\rho = 0.03.\left({}^{\mu}/_{x}\right)^{0.2}.G^{0.8}.B^{0.32} \tag{247}$$

Due to the small power of the blowing characteristic (it's raised to the power of 0.32), the regression rate is not very sensitive to the blowing and as a result to the vaporization heat of the fuel. Therefore, the following practical engineering approximation can be used instead of equation 247:

$$\dot{r} = aG^n x^m \tag{248}$$

Where a, n, and m are the constants that are determined empirically. G In this relation is the sum of the oxidizer and the fuel fluxes, which by substituting them into it, results in:

$$G(x) = G_o + G_f(x) \tag{249}$$

$$G_f(x) = \frac{4}{\pi D^2}\int_0^x \dot{r}(x, D)\, dx \tag{250}$$

$$\dot{r} = \frac{a}{(1+m)} G_o{}^n x^m \left(1 + \frac{\frac{2na}{1+m}\rho x^{1+m}}{D G_o{}^{1-n}}\right) \tag{251}$$

Given that the expression in parentheses is small, the final formula for the regression rate is simplified as follows:

$$\dot{r} = G_o{}^n x^m \tag{252}$$

It should be noted that the theoretical values of m and n are -0.2 and 0.8, respectively, which neutralize the effect of increasing the flux and provide an almost uniform regression rate. As mentioned in obtaining the coefficient of friction, the above equation is valid for circular sections, while for non-circular sections, the hydraulic diameter should be used according to the area and circumference of the section, namely:

$$D_H = \frac{4A}{P} \tag{253}$$

To investigate the effect of radiative heat transfer from the fuel surface, the radiative heat transfer equation is written as follows:

$$\dot{Q}_r = \sigma\varepsilon_w\left(\varepsilon_g T_r{}^4 - T_w{}^4\right) \cong \sigma\varepsilon_w\varepsilon_g T_r{}^4 \tag{254}$$

In which σ is the Stephan Boltzmann's constant, ε_w and ε_g are the amount of radiation from the fuel surface and gas, respectively. T_w and T_r are the fuel surface temperature and the average temperature of the gases, respectively, which are omitted due to the smaller temperature T_w compared to T_r. Due to the presence of a non-uniform area within the boundary layer (i.e., the presence of a relatively thin layer of combustion), the temperature average is employed instead of a single temperature. However, the results of this equation differ from the experimental data, so by utilizing correction factors, the results attain higher compatibility.

From Equation 242, it is easy to figure out that the amount of heat transfer will increase as the mass flow through the wall increases. Since increasing the value of n according to equation 245 increases the blowing, the amount of convection heat transfer will decrease. Therefore, the net amount of increase in wall heat transfer should be sought in increasing radiation heat transfer. However, evidence has shown that the rate of increase $\dot{r}$ does not increase $\dot{Q}_r$ proportionally (due to increased obstruction). Also, a conduction heat transfer (due to high optical absorptivity in solids) will occur in the presence of the radiation field (Q_{cr}). Therefore, in the radiation state study, the energy equation, assuming that a reasonable estimate of $\dot{Q}_r$ is available, will be rewritten as follows:

$$Q_r + Q_{cr} = \dot{m}_f h_v = \dot{r}\rho h_v \tag{255}$$

Whereas, the approximate relation between the relative values of r and q in terms of no radiation does occur (net convection) is equal to:

$$\frac{\dot{r}}{\dot{r}_c} = \exp\,(0.37\frac{Q_r}{Q_c}) \tag{256}$$

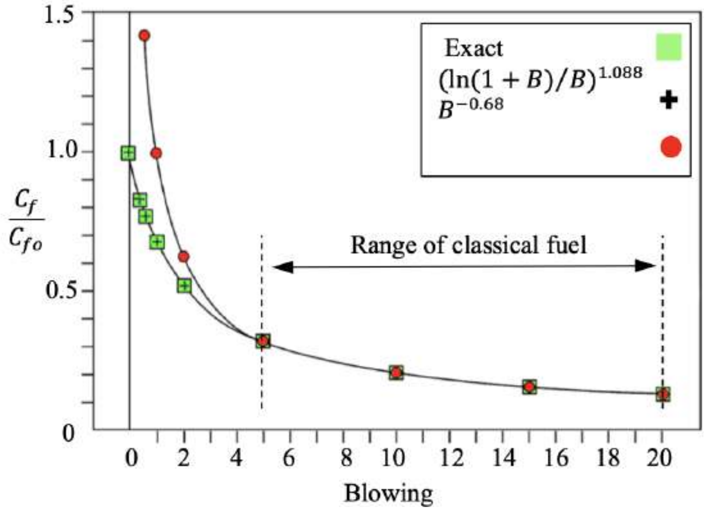

Figure 72- Blocking parameter versus the blowing term. The simple expression $\frac{C_f}{C_{fo}} = B^{-0.68}$ shows an excellent fit in the range of $5 < B < 20$ for most hybrid fuels.

In general, temperature sensitivity is investigated in two parts: burning rate and chamber pressure, which is dependent on ambient temperature. In solid propellant rockets, due to the non-throttling feature, the maximum expected operating pressure (MEOP) for engine case design to sustain the highest pressure during the operation is very critical. In hybrid rockets, since the latent heat of evaporation of gas is greater than the changes in heat content due to extreme ambient heat, the initial temperature has only a small effect on the rate of regression. The regression rate is expressed in such a way that the total effective heat of gasification (h_v) is calculated at the reference temperature (T_0), namely:

$$\dot{r} \sim [h_v - C(T - T_0)]^{-0.32} \tag{257}$$

The following equations express the temperature sensitivity of burning rate and pressure:

$$\sigma_P = \frac{1}{\dot{r}}\frac{\partial \dot{r}}{\partial T} = \frac{0.32C}{h_v - C(T - T_0)} \tag{258}$$

$$\pi_k = \frac{1}{P}\frac{\partial P}{\partial T} = \frac{\sigma_P}{1 + {}^{O}/_{F}} \tag{259}$$

The result of equation 258 is expressed as the percentage of change in fuel consumption relative to fuel weight. In solid rockets, the denominator of equation 259 is omitted because both fuel and oxidizer are temperature dependent, while in hybrid systems the amount of fuel consumption depends on the change in ambient temperature. Like solid propellants, hybrid propellants are pressure-dependent, where this dependence is reflected in the regression rate. Pressure dependency arises from two main reasons:

1. Radiative emissivity.
2. Combustion kinetics.

As mentioned earlier about radiative heat transfer and the presence of thermal conductivity in the radiational field, one of the factors reducing the high optical absorption of a solid is the dependence of the emissivity on the pressure in the following manner:

$$\varepsilon_g = 1 - e^{-apz} \tag{260}$$

In the above equation, p is the pressure, and z (as an engine parameter) represents the length of the optical path between the wall and the flame. Other effective factors such as flame temperature, composition, and percentage of metal are expressed as constant a, which change with both the O/F ratio and the port diameter. In normal diffusion combustion where the reactants are not pre-mixed, the reaction rate is much faster than the diffusion rate of the species and the reactants in the boundary layer, in which case the combustion rate will be limited to the diffusion. In hybrid systems with limited diffusion, because the mass flux determines the diffusion rate, so at high mass flux and low pressure, the kinetics can determine the regression rate with a kinetic pressure dependency as follows:

$$\dot{r} = \dot{r}_c + k(1 - e^{-apz}) = \dot{r}_c + kaz \quad \text{where}, apz < 1 \tag{261}$$

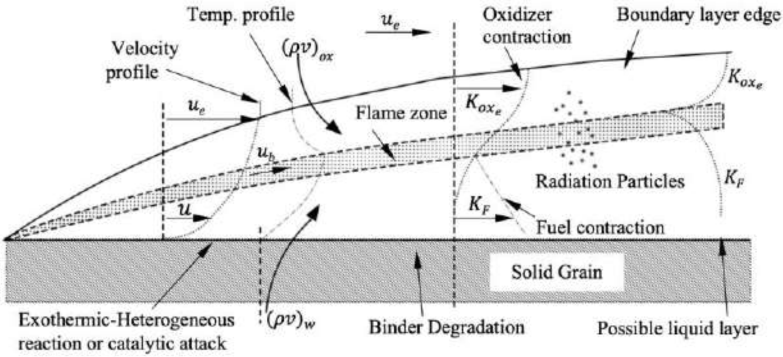

Figure 73-Hybrid Propulsion Boundary Layer

The following figure shows a logarithmic diagram in which both radiative and kinetic effects at different regression rates are plotted as a function of mass flux (G). It can be perceived that the pressure sensitivity appears at opposite ends of the mass flux, however, most of the hybrid fuel falls into the central diffusion-limited region.

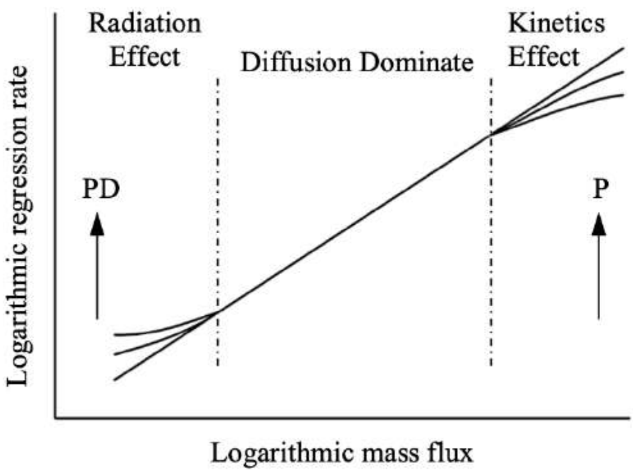

Figure 74- Pressure sensitivity versus regression rate. Adopted from Hybrid Rocket Propulsion

Now, in this section, let's take a closer look at what has been said:

First, we write the convection heat transfer equation of the wall in terms of the thermal conductivity of the gas as follows:

$$\dot{Q}_c = -\left(\frac{k}{\bar{C}_P}\left(\frac{\partial h}{\partial y}\right)\right)_w \tag{262}$$

$\dot{Q}_c$: Convective heat flux to the surface.
$\bar{C}_P$: Average specific heat of the gas.
k: Thermal conductivity of the gas.
y: Distance normal to the grain surface.

The Stanton number for heat transfer from the flame to the wall in the presence of mass addition is:

$$C_H = \frac{\dot{Q}_c}{\rho_b u_b \Delta h} \tag{263}$$

$$\Delta h = (C_P T)_b - (C_P T)_w \tag{264}$$

Δh: Sensible enthalpy difference between the flame and the wall.
ρ_b, u_b: Velocity and the density of the gas at the flame zone.
Given the equality of Equations 242 and 262 and by applying Equation 263 for the dominant convection mode, we will have:

$$\dot{Q}_c = \dot{Q}_w \Rightarrow \rho_f . \dot{r} = \frac{\dot{Q}_c}{h_v} = \frac{\dot{Q}_w}{h_v} = C_H \rho_b u_b \frac{\Delta h}{h_v} \tag{265}$$

Given that the Stanton number used in the presence of the blowing is a function of the friction coefficient of the surface, namely:

$$C_H = f(C_f) \tag{266}$$

Using Reynolds analogy in the boundary layer with the presence of blowing (i.e., $Le = 1$):

$$\frac{\dot{Q}}{\rho \frac{\partial h_T}{\partial y}} = \frac{\tau}{\rho \frac{\partial u}{\partial y}} Pr^{-0.67} \tag{267}$$

h_T: Total enthalpy. τ: Shear stress. Pr: Prandtl number. Le: Lewis number.

Whereas, this relation is written at the wall zone as follows:

$$\frac{\dot{Q}}{Q_w} = \frac{\tau}{\tau_w} \tag{268}$$

By substituting the relation 267 in 268 and integrating from the wall to the flame zone:

$$\frac{\dot{Q}_w}{\Delta h_T} = \frac{\tau_w}{u_b} Pr^{-0.67} \tag{269}$$

Given that there is no combustion between the flame region and the wall, and by placing equation 269 in equation 265, the Stanton number will be obtained in terms of Prandtl number:

$$C_H = \frac{\tau_w Pr^{-0.67}}{\rho_b {u_b}^2} \tag{270}$$

Which, is reflecting the heat transfer from the flame zone to the wall. By employing the momentum transfer from the edge of the boundary layer to the wall, the surface friction coefficient can be obtained. Therefore:

$$\tau_w = \frac{1}{2} C_f \rho_e {u_e}^2 \tag{271}$$

By simplifying and combining equations 265, 270, and 271:

$$\dot{m}_f = \rho_f \dot{r} = \frac{1}{2} C_f \rho_e u_e \; B \; Pr^{-0.67} \tag{272}$$

Where *b* is a thermodynamic parameter and according to the specific composition of each propellant is defined as follows:

$$B = \frac{u_e}{u_b} \frac{\Delta h}{h_v} \tag{273}$$

Now, it's time to set the value of C_f. For the turbulent flow of the boundary layer with mass addition and in the absence of blowing:

$$C_{fo} = 0.06 \; {Re_x}^{-0.2} \tag{274}$$

Marxman developed an expression for $\left({C_f}/{C_{fo}}\right)$ that is used in an approximate range of blowing:

$$\frac{C_f}{C_{fo}} \approx 1.2(B')^{-0.77}, \;\; 5 < B' < 100 \tag{275}$$

Where:

$$B' = \frac{(\rho v)_w}{(C_f/2)\rho_e u_e} \quad (276)$$

Smooth et al. used Spalding's thin-film model to express the effect of the blowing on the surface friction, which ultimately led to the following ratio:

$$\frac{C_f}{C_{fo}} = \ln\left(\frac{1+B\prime}{B\prime}\right) \quad (277)$$

Comparing the approximate and exact relations of 275 and 277, it should be noted that for $B' < 5$, the value obtained from the Smooth relation is more realistic, whereas for $10 < B' < 25$, both relations report the same value. However, the value of B 'for most hybrid engines is in the range of 7 to 15. Therefore, by combining Equations 275 and 277 and substituting them in Equation 272, the result is:

$$\dot{m}_f = \rho_f \dot{r} = 0.366\ {Re_x}^{-0.2}\ B\ Pr^{-0.67} (B')^{-0.77} \quad (278)$$

Where $G = \rho_e u_e$ is the total mass flux per unit area and the Reynolds number at distance x is equal to:

$$Re_x = \frac{\rho_e u_e x}{\mu_e} = \frac{Gx}{\mu} \quad (279)$$

Also, by placing the relation 277 in Equation 272, we get the relation between B and B' in terms of Prandtl number:

$$B' = B\ Pr^{-0.67} \quad (280)$$

Therefore, since the value of $Pr = 1$, using Equation 279, Equation 272 is rewritten to this form:

$$\dot{m}_f = \rho_f \dot{r} = 0.366\ G\ {Re_x}^{-0.2} B^{0.23} =$$

$$0.036\ G^{0.8} \left(\frac{x}{\mu_e}\right)^{-0.2} B^{0.23} \quad (281)$$

This equation is true for an incompressible flow in which fluctuations in fluid properties are negligible. Marxman states the following quasi-experimental relation for the state in which the properties of the fluid in the boundary layer change:

$$\dot{m}_f = \rho_f \dot{r} = 0.036\ \left(\frac{\bar{\rho}}{\rho_e}\right)^{0.6} \left(\frac{x}{\mu_e}\right)^{-0.2} G^{0.8} B^{0.23} \quad (282)$$

Where $\bar{\rho}$ is the reference density, and the density ratio is varying in the range of 1 to 1.1.
For the case where the solid fuel has particles that cannot evaporate, the wall heat transfer equation (Eq. 242) is written as follows:

$$\frac{Q_w}{\dot{r}} = \rho_f h_v = \rho_v h_{v\,eff} = \rho_v (h_{v\,b} + C_m \Delta T \frac{k}{1-k}) \qquad (283)$$

$\Delta T = T_s - T_0$ = Surface Temp. – Temp. deep in the grains.

C_m: Specific heat on non-vaporizing component.

$$\rho_v = \frac{m_v}{V} = \frac{\text{mass of vaporization}}{\text{grain's volume}} =$$

bulk density of vaporization component.

$$k = \frac{m_p}{m_f} = \frac{\text{mass of solid additives}}{\text{total mass of grains}}$$

In this case, the binder starts to warm up from T_0 to evaporate, while the solid particles heat from T_0 to T_s. For this case, Equation 282 will be turned to:

$$\rho_v \dot{r} = \rho_f (1-k) \dot{r} = \frac{\dot{Q}_w}{h_{v\,eff}} =$$

$$0.036 (\frac{\bar{\rho}}{\rho_e})^{0.6} (\frac{x}{\mu_e})^{-0.2} G^{0.8} B^{0.23} \qquad (284)$$

Where

$$B \equiv \frac{u_e}{u_b} \frac{\Delta h}{h_{v\,eff}} \qquad (285)$$

As mentioned earlier, the mode of operation and evaporation in the boundary layer for hybrid propellants include both the concepts of convection and radiation heat transfer, which lead to regression. However, the direct sum of the effects of $\dot{Q}_r$ and $\dot{Q}_c$ is not possible because $\dot{Q}_c$ is a function of surface mass addition. Increasing the heat flux to the wall will increase the regression rate and thus increase the blowing in the boundary layer, which in turn will reduce the convection heat transfer and increase the radiation heat transfer. By the summation of equations 254 and 278 to the right-hand side of Equation 242, given that $(\frac{\bar{\rho}}{\rho_e})^{0.6}$ is insignificant and that $Pr = 1$:

$$\rho_v \dot{r} = \frac{\dot{Q}_w}{h_{v\,eff}} = 0.036\; G\; Re^{-0.2} (B'_r)^{-0.77} B + \frac{\sigma \varepsilon_W {T_r}^4 (1 - e^{-aPz})}{h_{v\,eff}} \tag{286}$$

Given that B is a thermochemical property of propulsion, its changes will not be significant compared to the increase in $\dot{Q}_r$, but B' will increase as a blowing parameter, namely:

$$B'_r = \frac{(\rho v)_w}{\rho_e u_e (^{C_f}/_2)} = \frac{\rho_v \dot{r}}{\rho_e u_e \left(^{C_f}/_2\right)} \tag{287}$$

Which, by substituting the equation of 287 in 286, result in:

$$h_{v\;eff} B'_r \rho_e u_e \frac{C_{f\,r}}{2} = h_{v\;eff}\; 0.036\; G\; {Re_x}^{-0.2} (B'_r)^{-0.77}\; B + \dot{Q}_r \tag{288}$$

From the equality of Equations 272 and 281:

$$\dot{Q}_c = \frac{1}{2} C_f \rho_e u_e\; B\; Pr^{-0.67} = 0.366\; G\; {Re_x}^{-0.2} B^{0.23} h_{v\,eff} \tag{289}$$

Dividing the above equation by equation 288, for the absence of radiation $(\dot{Q}_r = 0)$:

$$\frac{C_{f\,r}}{C_f} = \left(\frac{B\prime_r}{B}\right)^{-0.77} \tag{290}$$

Hence:

$$\frac{B\prime_r}{B} = 1 + \frac{Q_r}{Q_c} \left(\frac{B\prime_r}{B}\right)^{0.77} \tag{291}$$

Which can be approximated by the following expression:

$$\frac{B\prime_r}{B} \approx e^{1.3 \frac{\dot{Q}_r}{\dot{Q}_c}} \tag{292}$$

By simplifying equation 286 and placing the above relation on it, the result is:

$$\rho_v \dot{r} = \frac{\dot{Q}_c}{h_{v\,eff}} \left(\frac{B\prime_r}{B}\right)^{0.77} + \frac{\dot{Q}_r}{h_{v\,eff}} = \frac{\dot{Q}_c}{h_{v\,eff}} \left(\exp\left(-\frac{\dot{Q}_r}{\dot{Q}_c}\right) + \frac{\dot{Q}_r}{\dot{Q}_c}\right) \tag{293}$$

Combustion in hybrid propulsion by the diffusion flame increases the grain length, which in turn changes the O/F ratio, causing fluctuations in the amount of specific impulse, which may eventually lead to a reduction in rocket performance. The O/F ratio in rockets, like air breathing engines, is defined as the $\dot{m}_o/\dot{m}_f$ ratio. In liquid rockets, m_o and m_f are both variables, and in solid rockets, since the fuel and oxidant contain a solid compound, the O/F value is constant during the process. In hybrid propulsion, however, the regression rate of the fuel depends on the oxidizing flux. The mass flow rate of fuel per unit area for circular and non-circular ports are equal to:

$$\dot{m}_f = \dot{r}\pi DL\rho = a\left(\frac{\dot{m}_o}{\pi\left(D^2/4\right)}\right)^n L^m \pi DL\rho = \frac{k\dot{m}_o{}^n L^{1+m}}{D^{2n-1}}, \text{Circular Port} \tag{294}$$

$$\dot{m}_f = \dot{r}PL\rho = a\left(\frac{\dot{m}_o}{A}\right)^n PL^{1+m}\rho, (\text{Non} - \text{circular port}) \tag{295}$$

Which in the equation 294, k is a constant that depends only on the properties of the material and its value is obtained from the following equation:

$$k = 4^n a \pi^{1-n} \rho \tag{296}$$

As a result, the O/F value for different sections will be equal to:

$$\frac{O}{F} = \frac{\dot{m}_o{}^{1-n} D^{2n-1}}{k\, L^{1+m}}, (\text{Circular port}) \tag{297}$$

$$\frac{O}{F} = \frac{\dot{m}_o{}^{1+n} A^n}{\rho a\, L^{1+m}}, (\text{Non} - \text{Circular port}) \tag{298}$$

From the above equation, it is clear that for a circular port the value of O/F increases continuously with D^{2n-1} while for $n = 0.5$ no shifting will occur for O/F. Figure 76 shows the magnitude of O/F for diameters of 1.2 to 2. This amount of shifting reduces by employing another regressive oxidizer flow is employed, as described earlier.

Another important parameter, as the ballistic of hybrid propulsion, is the stoichiometric length (L_{st}), which is an important design parameter and is defined as the minimum required length to satisfies the desired O/F. A reaction is stoichiometric in which all the reactants are involved in the reaction (i.e., complete oxidation), so $(O/F)_{st}$ is met when all the carbons, hydrogens, and metals react. In fact, when $(O/F)_{st}$ is satisfied by L_{st}, the rocket reaches its optimal specific impulse. The relation between L_{st}, $(O/F)_{st}$, and the specific impulse can be expressed as follows in terms of oxidizer flux (G_o):

$$L_{st} = \left(\frac{{G_o}^{1-n} D}{4a\rho (O/F)_{st}}\right)^{\frac{1}{(1+m)}} \quad (299)$$

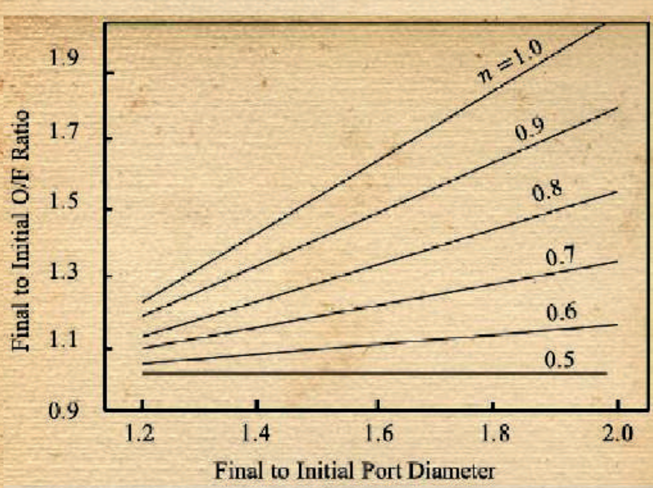

Figure 75- O/F shifting versus port diameter ratio at different n values. Adopted from Rocket Motor, Hybrid

Given the small negative value of m, the above equation with the assumption ($a_0 = aL^m$)is rewritten as follows:

$$(\frac{L}{D})_{st} = \frac{G_o^{\ 1-n}}{4a_0\rho(O/F)_{st}} \tag{300}$$

The $(\frac{L}{D})_{st}$ value for polymer fuels varies between 20 and 30 for the best specific impulse. For high-regression rate fuels that use thick grids (i.e., $(\frac{L}{D})_{st} < 10$), the result is:

$$P = \dot{m}\frac{C^*}{A_t} \tag{301}$$

$$F = mgI_{sp} \tag{302}$$

In terms of thrust variations, it should also be noted that to achieve the best specific impulse, combustion must take place in fuel-rich conditions, which leads to an increase in $\dot{m}_f$, thus increasing exit pressure and thrust as a result of increasing the characteristic velocity of the exhaust gases. Since the specific impulse changes with the characteristic velocity proportionally, the thrust changes exactly follow the pressure. Table 8 summarizes the practical ballistic parameters of hybrid propulsion.

Parameter	Circular	Non-circular	Description
O/F	$\frac{\dot{m}_o^{\ 1-n}D^{2n-1}}{k\ L^{1+m}}$	$\frac{\dot{m}_o^{\ 1+n}A^n}{\rho a\ L^{1+m}}$	$k = 4^n a\pi^{1-n}\rho$ $a_0 = aL^m$
L_{st}	$(\frac{G_o^{\ 1-n}D}{4a\rho(O/F)_{st}})^{\frac{1}{(1+m)}}$	$(\frac{G_o^{\ 1-n}D_H}{4a\rho(O/F)_{st}})^{\frac{1}{(1+m)}}$	
$(L/D)_{approx.}$	$\frac{G_o^{\ 1-n}}{4a_0\rho(O/F)_{st}}$		
$\dot{m}_f$	$\frac{k\dot{m}_o^{\ n}L^{1+m}}{D^{2n-1}}$	$a(\frac{\dot{m}_o}{A})^n P L^{1+m}\rho$	

Table 8- Summery of ballistic parameters. Adopted from Rocket Motors, Hybrid

COMBUSTION CHAMBER COOLING

This section investigates cooling requirements and challenges in the combustion chamber with solid and liquid propellants.

COOLING IN THE COMBUSTION CHAMBER WITH LIQUID PROPELLANTS

As mentioned earlier, liquid propellant rockets have a longer operating time than solid propellant rockets, which is caused to release higher energy gases with due attention to the propellant type and its composition (some of these characteristics are listed in Table (9)). This production with high static temperature (approximately 3000 to 4700 K) will be caused to the exclusive rising of the chamber wall temperature. It should be noted that inside the combustion chamber and on its surfaces, there are all modes of heat transfer including conduction, conduction, and radiation. The hot gases in the combustion chamber then enter the convergent-divergent nozzle to expand, where the thermal energy from the combustion is converted into kinetic energy to produce the required thrust. The high temperature of the extended section of the nozzle downstream of the throat, which is caused by an extremely high temperature of the combustion gases, needs to be cooled. Fortunately, for liquid-propellant rockets, this problem has been solved more easily by using a coolant that is flowing into the tubes placed around the chamber, this method knows as regenerative cooling. Actually, this method uses the cooling capacity of the coolant, i.e., the amount of heat expended in the phase change of the coolant from liquid to vapor. Figure 77 shows the schematic of a rocket with liquid propellant, which is cooled by convection (regenerative cooling) method. Physics of a Regeneratively Cooled Combustion Chamber is also depicted on figure (77-c).

Stable heat transfer in the cooling process is such that there is a convection process between the combustor inner wall and the hot gases inside the chamber across the film. The chamber wall also includes the conduction and radiation processes that take place towards the cooling wall, and the coolant film heat transfer inside the cooling channels occur convectively. Hence, the one-dimensional net heat flux in the thrust chamber can be expressed as the sum of the conduction and radiative heat transfer as follows:

$$\dot{q}_w = \dot{q}_c + q_r \tag{303}$$

The heat transfer related to the radiation of combustion gases toward the wall is obtained by

$$\dot{q}_r = \varepsilon_g \sigma T_g^4 \quad (304)$$

Where ε_g is the emissivity of the gas (1 for blackbody radiation and less than 1 for graybody radiation), σ is the Stefan-Boltzmann constant, which is $5.67 \times 10^{-8}\, W/_{m^2 k^4}$ and (T_g) is the absolute temperature. Since radiant heat transfer grows with temperature increases exponentially, i.e., (T_g^4).Therefore according to Sutton and Biblarz (2001), radiation accounts for 3-40% of the combustion chamber heat flux for the gas temperature range of 1900-3900 K. This is a reminder that we my not neglect radiative heat transfer unless the gas temperature is low, namely,$\sim 700K$.

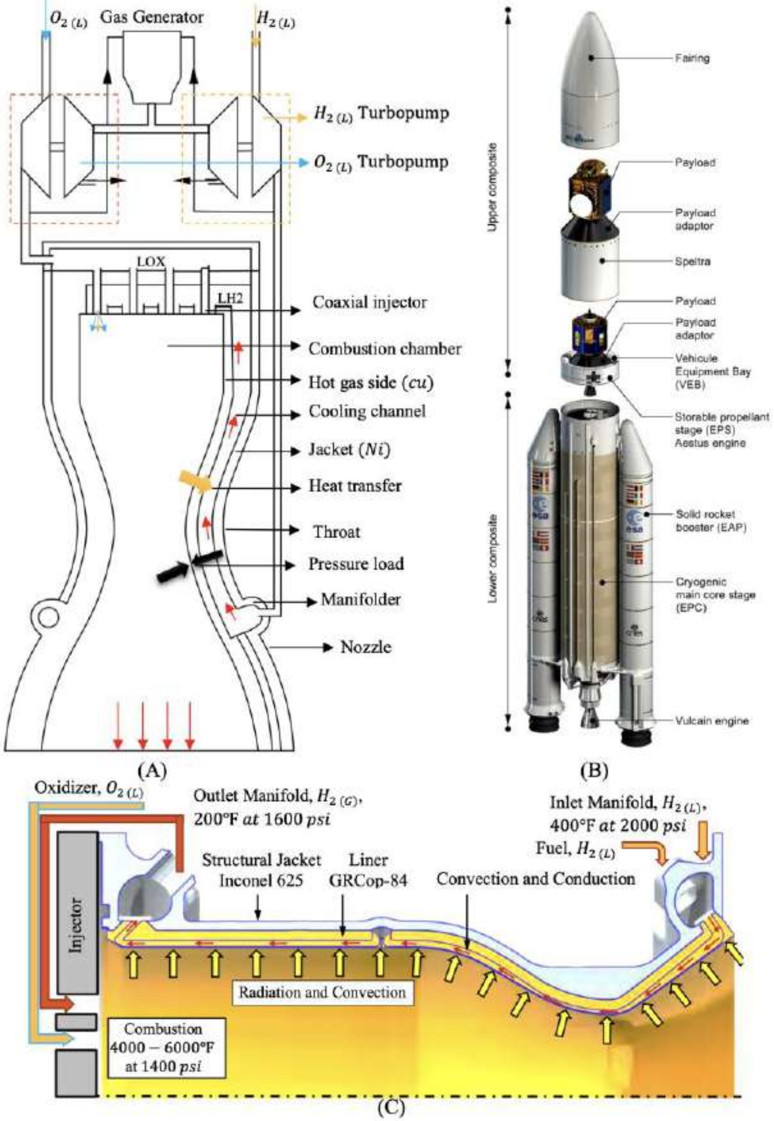

Figure 76-Definition Sketch of a Regenerative Cooling and Components of the Arian 5G Rocket, and physics of the regeneratively cooled C.C. (Top left image is a redesigned version from Thermomechanical Analysis and Optimization of Cryogenic Liquid Rocket Engines and Top right image adopted from ESA-D. Ducros, the bottom image is edited version from Additively Manufactured Rocket Engine Combustion Chamber Structural Analysis)

Oxidizer	Fuel	Mixture ratio		Average Specific Velocity	Chamber Temp. (K)	Chamber c^* (m/sec)	$\mathfrak{M}$ (kg/mol)	I_a (sec)		k
		By Mass	By Volume					Shifting	Frozen	
Oxygen	Methane	3.20 3.00	1.19 1.11	0.81 0.80	3526 -	1835 1853	- -	- 311	296 -	- -
	Hydrazine	0.74 0.90	0.66 0.80	1.06 1.07	3285 3404	1871 1892	18.3 19.3	- 313	301 -	1.25 -
	Hydrogen	3.40 4.02	0.21 0.25	0.26 0.28	2959 2999	2428 2432	8.9 10.0	- 389.5	386 -	1.26 -
	RP-1	2.24 2.56	1.59 1.82	1.01 1.02	3571 3677	1774 1800	21.9 23.3	285.4 -	- 300	1.24 -
	UDMH	1.39 1.65	0.96 1.14	0.96 0.98	3542 3594	1835 1864	19.8 21.3	- 310	295 -	1.25 -
Fluorine	Hydrazine	1.83 2.30	1.22 1.54	1.29 1.31	4553 4713	2128 2208	18.5 19.4	334 -	- 365	1.33 -
	Hydrogen	4.54 7.60	0.21 0.35	0.33 0.45	3080 3900	2534 2549	8.9 11.8	- 410	389 -	1.33 -
Nitrogen tetroxide	Hydrazine	1.08 1.34	0.73 0.93	1.20 1.22	3258 3152	1765 1782	19.5 20.9	- 292	283 -	1.26 -
	50% UDMH-50% hydrazine	1.62 2.00	1.01 1.24	1.18 1.21	3242 3372	1652 1711	21.0 22.6	- 289	278 -	1.24 -
	RP-1	3.4	1.05 1.30	1.23 1.20	3290 3396	- 1747	24.1 22.3	- 289	297 -	1.23 -
	MMH	2.15 1.65	1.00 2.12	1.16 1.35	3200 3175	1591 1594	21.7 24.6	- -	278 258	1.23 1.22
Red fuming nitric acid	RP-1	4.1 4.8	2.48	1.33	3230	1609	25.8	269 -	- 272	- 1.22
	50% UDMH-50% hydrazine	1.73 2.20	1.00 1.26	1.23 1.27	2997 3172	1682 1701	20.6 22.4	279 -	- -	- -
Hydrogen peroxide (90%)	RP-1	7.0	4.01	1.29	2760	-	21.7	-	297	1.19

Table 9- Theoretical performance of liquid rocket propellant combinations. Notes: combustion chamber pressure- 1000 psia (6895 kN/m^2): nozzle exit pressure -14.7 psia (1 atm): optimum expansion. Adiabatic combustion and isentropic expansion of ideal gas. Specific gravity at the boiling point was used for those oxidizers or fuels that boil below 20°C at 1 atm pressure. Mixture ratios are for approximate maximum value of I_s.

Propellant	Formula	Use	Mol. Wt.	Freezing point °F	Boiling point °F	Vapor press., $Psia$	Density gm/cc	Stability	Handling hazard	Storability	Materials compatibility
Aniline	$C_6H_5NH_2$	Fuel, coolant	93.2	21	364	0.25 at 160 °F	1.022 at 68 °F	Good	Good	Good	Al., steel, Teflon, Kel-F
Bromine Pentafluoride	BrF_5	Oxide., coolant	174.9	-80.5	104.5	41 at 160 °F	2.48 at 68 °F	Up to 800°F	Reacts with fuel	Good	Al. alloy, 18-8 stainless steel, nickel alloy, cooper, Teflon
Chlorine trifluoride	ClF_3	Oxide	92.5	-105.4	53.15	80 at 140 °F	1.825 at 68 °F	Up to 600°F	Toxic	Good below 140°F	Al. alloy, 18-8' stainless steel, nickel alloy, cooper, Teflon
92.5% E.A. (ethyl alcohol)	C_2H_5OH	Fuel, coolant	41.25	-189	172	13 at 160 °F	0.81 at 68 °F	Good	Flammable	Good below 130°F	Al., steel, nickel alloy, Teflon, Kel-F, polyethylene
Hydrazine	N_2H_4	Fuel, oxid., coolant	32.05	34.5	235.4	2.8 at 160 °F	1.01 at 68 °F	Up to 300°F	Toxic, flammable	Good	Al., 304.307 stainless steel, Teflon, Kel-F, polyethylene
95% hydrogen peroxide	H_2O_2	Monoprop. , oxid., coolant	32.57	21.9	294.8	0.05 at 77 °F	1.414 at 77 °F	Unstable decomp. at 285 °F	Hazardous skin contact, flammable	Deteriorates at 1%yr.	Al., stainless steel, Teflon, Kel-F
98% hydrogen peroxide	H_2O_2	Same as above	33.42	27.5	299.2	0.043 at 77 °F	1.432 at 77 °F	Same as above	Same as above	Same as above	Same as above
Hydyne (40%" Deta" 60% " UDMH")	NH $(C_2H_4NH_2)_2$ $(CH_3)_2NNH_2$	Fuel, coolant	72.15	-65	140 to 400	16.5 at 160 °F	0.855 at 60 °F	Good	Toxic	Good	Al., stainless steel, Teflon, Kel-F
IRFNA (inhibited red fuming nitric acid)	82% HNO_3 15% NO_2 2% H_2O 1% HF	Oxid, coolant	55.9	-57	150	17.3 at 160 °F	1.57 at 68 °F	Good	Toxic, hazardous skin contact	Good	Al., stainless steel, Teflon, Kel-F, polyethylene
JP-4 (jet propulsion fuel)	$C_{9.66}H_{19}$	Fuel, coolant	128	-76	270 to 470	7.2at 160 °F	0.747 to 0.825 at 60 °F	Good	Vapor explosive	Good	Al., steel, nickel alloy, neoprene, Teflon, Kel-F
MMI (monomethyl hydrazine)	CH_3NH-NH_2	Fuel, coolant	46.08	-63	187	8.8 at 160 °F	0.878 at 60 °F	Good	Toxic	Good	Al., 304.307 stainless steel, Teflon, Kel-F, polyethylene

Table 10- General data of some storeable liquid rocket propellants (continues)

Propellant	Formula	Use	Mol. Wt.	Freezing point °F	Boiling point °F	Vapor press., Psia	Density gm/cc	Stability	Handling hazard	Storability	Materials compatibility
Nitrogen tetroxide	N_2O_4	Oxid.	92.02	11	70	111 at 160 °F	1.44 at 68 °F	Function of temp.	Very toxic, hazardous skin contact	Good when dry	Al., Stainless steel, nickel alloy, Teflon
Pentaborane	B_5H_9	Fuel	63.17	-52.28	140.11	19 at 160 °F	0.61 at 68 °F	Good	Explosive on exposure to air, very toxic	Good	Al., steel, cooper, Teflon, Kel-f, Viton A
Properly nitrate	$C_3H_7NO_3$	Fuel, coolant	105.09	-130.9	231	3.7 at 160 °F	1.06 at 68 °F	Fair	Sensitive to shock	Good	Al., stainless steel, Teflon, Kel-F
RP-1 (rocket propellant)	Mil-Spec. F25576B	Fuel, coolant	165 to 195	-47 to -64	342 to 507	0.33 at 160 °F	0.8 at 68 °F	Auto. Ignition at 470 °F	Flammable	Good	Al., steel, nickel alloy, cooper, Teflon, Kel-f,
TEA (triethylaluminium)	$(C_2H_5)_3Al$	Fuel, start compound	114.15	-49.9	381	0.40 at 160 °F	0.836 at 68 °F	Decomp. Over 400 °F	Ignites on contact with air	Good	Al., steel, cooper, Teflon
TMA (trimethylamine)	$(CH_3)_3N$	Fuel	59.11	-179	37	108 at 160 °F	0.603 at 68 °F	Good	Good	Good	Al., steel, cooper, Teflon
TMB-1. 3-D (NNN' - N' - tetramethylbutane-1,33-dianin)	$(CH_3)_2N - CH_2CH_2 - CH - N(CH_3)_2 CH_3$	Fuel, coolant	144.2	-131	320	1.32 at 160 °F	0.795 at 68 °F	Stable 1 hr. at 500 °F	....	Good	Al., 347 stainless steel, polyethylene
TNM (tetranitromethane)	$C(NO_2)_4$	Oxid.	196.04	57.3	259	2.38 at 165 °F	1.64 at 68 °F	Thermal unstable	Shock sensitive	Good below 100°F	Al., mild steel, Teflon, Kel-F
UDMH (unsymmetrical dimethyl-hydrazine)	$(CH_3)_2NNH_2$	Fuel, coolant	60.08	-72	146	17.6 at 160 °F	0.789 at 68 °F	Good	Toxic	Good	Al., stainless steel, Teflon, Kel-F
WFNA (white fuming nitric acid)	97.5% HNO_3 2% H_2O 0.5% NO_2	Oxid, coolant	59.9	-45	186	9.09 at 160 °F	1.46 to 1.52 at 68 °F	Decomp. above 100 °F	Toxic, hazardous skin contact	Fair	Al., stainless steel, Teflon, Kel-F, Polyethylene

Table 11- General data of some storeable liquid rocket propellants

Propellants	Formula	Use	Mol. Wt.	Freezing point °F	Boiling point °F	Critical press. Psia at 160°F	Critical temp., °F	Density at boiling point gm/cc	Stability	Handle hazard	Materials Compatibility
Ammonia	NH_3	Fuel, coolant	17.03	-108	-28	500		0.683	Good	Toxic, flammable	Al., steel, lead, Teflon, Kel-F, Vitron A
Liquid fluorine	F_2	Oxid.	38.00	-364	-307	808	-200.5	1.509	Good	Very toxic, flammable	Al., 300 series stainless steel, nickel alloy, brass
Liquid hydrogen	H_2	Fuel, coolant	2.016	-434.6	422.9	187.8	-400.3	0.071	Good	Flammable	Stainless steel, nickel alloy, Al., alloy, Kel-F
Liquid oxygen	O_2	Oxid.	32.00	-362	-297.4	735	-182	1.142	Good	Good	Al., stainless steel, nickel alloy, copper, Teflon, Kel-F
Oxygen difluoride	OF_2	Oxid.	54.00	....	-299	719	-72.3	1.521	Good	Very toxic, flammable	Al., 300 series stainless steel, nickel alloy, brass
Ozone	O_3	Oxid.	48.00	-420	-168	804	10.2	1.46	Above 20% explosive	Very toxic, flammable	Al., 300 series stainless steel, Teflon, Kel-F

Table 12- General data of some cryogenic liquid rocket propellants

The presence of solid particles in the rocket combustion chamber increases the emissivity ε_g to its maximum value which is for blackbody. The convective heat transfer is governed by the newton's law of cooling (adopted from AIR PROPULSION-2009):

$$\dot{q}_{conv} = h_g\left(T_{aw} - T_{wg}\right) \tag{305}$$

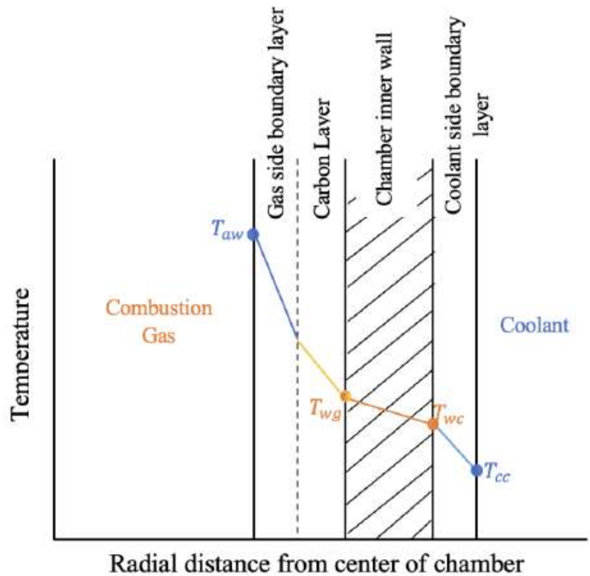

Figure 77- Wall configuration-from Modern Eng.

(T_{aw}) and (T_{wc}) in the above equation are adiabatic wall temperature and gas-side wall temperature, respectively. The heat from the conduction heat transfer through the wall is also written based on Fourier's law as follows:

$$\dot{q}_{Cond} = k_w \left(\frac{T_{wg} - T_{wc}}{t_w}\right) \tag{306}$$

Where k_w is the thermal conductivity of the wall (a property of the wall materials), (T_{wc}) is the wall temperature on the coolant side, and (t_w) is the wall thickness (a design parameter). Note that the minus in the Fourier heat conduction law is absorbed in the parenthesis, i.e., the heat transfer is from the combustor toward the coolant side. Now, by combining these sources of heat flow in a steady-state (one-dimensional) rocket thrust chamber-cooling problem, the wall heat flux equation express as follows, which by eliminating the T_{wc} and T_{wg} the heat flux will be simplified to Eq. (308) (adopted from AIR PROPULSION-2009):

$$\dot{q}_w = h_g\left(T_{aw} - T_{wg}\right) + \varepsilon_g \sigma T_g^4 = k_w \left(\frac{T_{wg} - T_{wc}}{t_w}\right) = h_C\left(T_{wC} - T_C\right) \tag{307}$$

$$\dot{q}_w = \frac{T_{aw} - T_C + \left(\varepsilon_g \sigma \frac{T_g^4}{h_g}\right)}{\left(\frac{1}{h_g}\right) + \left(\frac{T_w}{k_w}\right) + \left(\frac{1}{h_C}\right)} \tag{308}$$

In the above relation (Eq. 308), it can be assumed that the adiabatic wall temperature is equal to the stagnation temperature of the gas $(T_{aw} \approx T_{tg})$ and the rest of the parameters are predetermined and are among the design criteria. The cooling coefficient of (h_g) gas film, which is a function of the product of Reynolds and Prandtl numbers, can be obtained from the following relation:

$$\frac{h_g D_g}{k_g} = 0.026 \left(\frac{\rho_g v_g D_g}{\mu_g}\right)^{0.8} \left(\frac{\mu_g C_{pg}}{k_g}\right)^{0.4} \tag{309}$$

Where D_g is the local diameter of the thrust chamber, k_g is the gas thermal conductivity, $\rho_g\, v_g$ is the average gas mass flow rate per unit area in the combustion chamber, μ_g is the gas coefficient of viscosity, and C_{pg} is the specific heat of the gas at constant pressure. The LHS of the equation 309 is the Nusselt number, whereas the parentheses on the RHS are Reynolds and Prandtl numbers, respectively (adopted from AIR PROPULSION-2009). Since the fluid density and the properties μ_g, k_g, and C_{pg} are function of gas temperature, so average film temperature is used as a reference temperature.

$$T_f = \frac{T_g + T_{wg}}{2} \tag{310}$$

According to what was stated to obtain (h_g)on the gas-side film, to calculate coolant-side film coefficient (h_c) value, it can also be written:

$$\frac{h_c D_c}{k_c} = 0.023 \left(\frac{\rho_c v_c D_c}{\mu_c}\right)^{0.8} \left(\frac{\mu_c \bar{C}_c}{k_c}\right)^{0.4} \tag{311}$$

$\bar{C}_c$ and D_c from this equation are the coolant average specific heat and coolant passage hydraulic diameter, respectively. By expressing the above equation, based on the mass flow rate and the specific heat of the coolant, it'll be understood that as they increase, (h_c) also increases. In other words, the coefficient of coolant film in a given Reynolds and Prandtl number increases directly with the mass flux and specific heat. Optimizing the nozzle cross-section area increases the mass flux, and also by using liquid fuel with high specific heat will increase the film coefficient. Table (13) lists the physical properties of some liquid propellants. From the data in this table, it can be seen that hydrogen has a higher specific heat capacity than other liquid fuels, so it is a good choice for regeneratively cooling rocket thrust chamber.

To obtain the total heat transfer, heat flux integration is used along the wall of the thrust chamber, so that the equation 307 in the axial direction must be integrated. Thus, by dividing the thrust chamber in to axisymmetric cylindrical sections with small axial length where all heat transfer parameters are assumed constant, the total heat flux of this segments is:

$$\dot{Q} = \int \dot{q}\, \mathrm{d}A \approx \sum_{i=1}^{N} 2\Pi r_i \dot{q}_i \Delta x \tag{312}$$

The total heat transfer, which increases the cooling temperature, is obtained from

$$\dot{Q} = \dot{M}_c \bar{c}_c (T_2 - T_1)_c \tag{313}$$

Propellant	Liquid fluorine	Hydrazine	Liquid hydrogen	Methane	Monomethyl hydrazine	Nitric acid[a] (99% pure)	Nitrogen tetroxide	Liquid oxygen	Rocket fuel RP-1	UDMH[d]	Water
Chemical formula	F_2	N_2H_4	H_2	CH_4	CH_3NHNH_2	HNO_3	N_2O_4	O_2	Hydrocarbon $CH_{1.97}$	$(CH_3)_2NNH_2$	H_2O
Molecular mass	38.0	32.05	2.016	16.03	46.072	63.0 16	92.016	32.00	~175	60.10	18.02
Melting or freezing point (K)	53.54	274.69	14.0	90.5	220.7	231.6	261.95	45.5	225	216	273.15
Boiling point (K)	85.02	386.66	20.4	111.6	360.6	355.7	294.3	90.0	460 to 540	336	373.15
Heat of vaporization (kj/kg)	166.26[b]	44.7[b]	446	510[b]	875	480	413[b]	213	246[b]	542 (298K)	2253[b]
Specific heat $(kcal/kg-K)$	0.368 at (85 K) 0.357 at (69.3 K)	0.736 at (293 K) 0.758 at (338 K)	1.75 at (20.4K) —	0.835[b]	0.698 at 293K 0.735 at 393K	0.042 at (311K) 0.163 at (373K)	0.374 at (290 K) 0.447 at (360 K)	0.4 at (65 K)	0.45 at (298 K)	0.672 at (298 K)	1.008 at (273.15 K)
Specific gravity[c]	1.636 at (66 K) 1.440 at (93 K)	1.005 at (293 K) 0.952 at (350 K)	0.071 at (20.4 K) 0.076 at (14 K)	0.434 at (111.5 K)	0.8788 at (293K) 0.857 at (311 K)	1.549 at (273.15 K) 1.479 at (313.15 K)	1.447 at (293 K) 1.38 at (322 K)	1.14 at (90.4 K) 1.23 at (77.6 K)	0.58 at (422 K) 0.807 at (289 K)	0.856 at (228 K) 0.784 at (244 K)	1.002 at (373.15 K) 1.00 at
Viscosity (centipoise)	0.305 at (77.6 K) 0.397 at (70 K)	0.97 at (298 K) Call .913 at (330 K)	0.024 at (14.3 K) 0.0 13 at (20.4 K)	0.12 at (111.6 K) 0.22 at (90.5 K)	0.855 at (293 K) 0.40 at (344 K)	1.45 and (273 K)	0.47 at (293K) 0.33 at (315 K)	0.87 at (53.7 K) 0.19 at (90.4 K)	0.75 at (289 K) 0.21 at (366 K)	4.4 at (220 K) 0.48 at (300 K)	0.284 at (373.15 K) 1.000 at (277 K)
Vapor pressure (MPa)	0.0087 at (100 K) 0.000 12 at (66.5 K)	0.0014 at (293 K) 0.016 at (340 K)	0.2026 at (23 K) 0.87 at (30 K)	0.033 at (100 K) 0.101 at (117 K)	0.0073 at (300 K) 0.638 at (428 K)	0.0027 at (273.15 K) 0.605 at (343 K)	0.01014 at (293 K) 0.2013 at (328 K)	0.0052 at (88.7 K)	0.002 at (344 K) 0.023 at (422 K)	0.0384 at (289 K) 0.1093 at (339 K)	0.00689 at (312 K) 0.03447 at (345 K)

a: Red fuming nitric acid (RFNA) has 5–20% dissolved NO_2 with an average molecular weight of about 60, and a density and vapor pressure somewhat higher than those of pure nitric acid.
b: At boiling point.
c: Reference for specific gravity ratio: $10^3\ kg/m^3$ or $62.42\ lbm/ft^3$.
d: Unsymmetrical dimethyl hydrazine.

Table 13- Physical properties of some liquid propellants. From AIRCRAFT PROPULSION 2009

Where T represents the entrance temperature of the coolant into the jacket, and T_2 is the bulk coolant temperature, when it leaves the cooling jacket and enters the injectors. This temperature as a design parameter should be considered in such a way that it is lower than its boiling temperature. The table (14) lists some of the heat transfer characteristics of liquid propellants. As can be seen, the pressure inside the cooling jacket has a significant effect on the boiling temperature. For example, the boiling temperature of Kerosene at a pressure of 0.101_{MPa} (1_{atm}) is 490_K, while at a pressure of 1.38_{MPa} its boiling temperature changes to 651_K. This pressure inside the cooling jacket is supplied by turbopumps or pressure feed systems, and therefore multi-stage pumps or heavier turbopumps should be used to create a higher-pressure ratio. The maximum amount of heat transfer rate that occurs at the smallest cross-section of the throat is called the critical heat flux. On the other hand, in order to have a lower temperature on the gas side of the wall, we need a higher film coefficient, so based on Equation 311, we will have:

$$h_C \propto \frac{(\rho_C v_C)^{0.8}}{D_C^{0.2}} \tag{314}$$

We need to increase the mass flux. Due to the constant density of the liquid, the cooling rate must be increased.
We need a smaller D_C diameter, i.e., the diameter of the colling tubes should be smaller.
The coolant speed at the throat may be as high as $\sim 15\ to\ 20 m/_s$. The hydraulic diameter of the cooling tubes near the throat scales in millimeters. The must effective throat cooling in regeneratively cooled thrust chamber combined these two effects. Therefore, the cooling jacket is composed of small-diameter tubes with tapered cross-sectional area at the throat with relatively high coolant speed, (adopted from AIR PROPULSION-2009).

Liquid coolant	Boiling characteristics		Critical tamp. (K)	Critical pressure (MPa)	Nucleate boiling characteristics			q_{Max} (MW/m^2)
	Pressure (MPa)	Boiling temp. (K)			Temp. (K)	Pressure (MPa)	Velocity (m/sec)	
Hydrazine	0.101	387	652	14.7	322.2	4.13	10	22.1
	0.689	455					20	29.4
	3.45	540			405.6		10	14.2
	6.89	588					20	21.2
Kerosene	0.101	490	678	2.0	297.2	0.689	1	2.4
	0.689	603					8.5	6.4
	1.38	651				1.38	1	2.3
	1.38	651					8.5	6.2
Nitrogen tetroxide	0.101	294	431	10.1	288.9	4.13	20	12.4
	0.689	342			322.2			9.3
	4.31	394			366.7			6.2
Unsymmetrical dimethyl hydrazine	0.101	336	522	6.06	300	2.07	10	4.9
	1.01	400					20	7.2
	3.45	489				5.52	10	4.7

Table 14- Heat transfer of some liquid propellants (from Aircraft Propulsion 2009)

COOLING IN THE COMBUSTION CHAMBER WITH SOLID PROPELLANTS

Solid propellant rockets may use several nonregenerative methods to protect the thrust chamber walls or motor case against the heat loads in the combustor. The purpose of an inhibitor is to inhibit grain burning where the designer wishes to protect the thrust chamber walls (or as means of controlling thrust-time or vehicle dynamic behavior). The purpose of an insulting layer, i.e., the one with low thermal conductivity, next to the wall is also to protect the wall from excessive heating. In addition to these two techniques, solid propellant grain designer may place the cooler burning grain in the outer shell next to the wall to protect the motor case. However, this is an expensive manufacturing proposition seldom used, (from AIRCRAFT PROPULSION-2009). This material is used in various parts of rockets and acts as a very good thermal protector. In Apollo missions, this material was used as a thermal shield in the command center module, which protected it from the very high heat generated when entering the atmosphere. In these missions, ablative materials consisted of a brazed steel honeycomb structure and a Fiberglass honeycomb shell filled with Phenolic epoxy resin. At the moment of arrival, shell materials are designed to evaporate (disappear) due to friction generated by the atmosphere, to prevent heat from penetrating the crew compartment. Another example is the use of these materials in the combustion chamber and engine throat of the second stage of the Space X-Kestrel rocket, which is a rocket with LOX-RP1 propellants. Today, graphite and ablative materials are used as an erosion resistance in the combustion chamber throat.

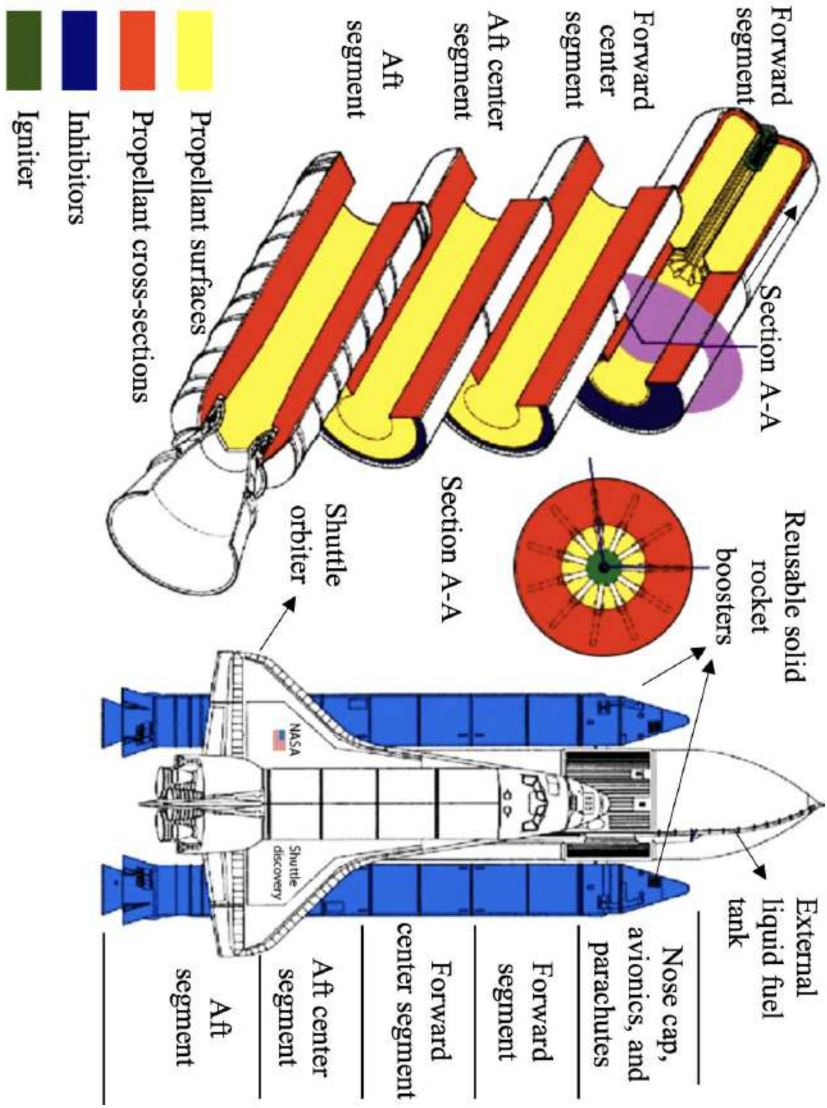

Figure 78- Figure A. The Reusable Solid Rocket Motor (RSRM) is a primary booster for NASA's Space Transportation System (STS). Section A-A shows 11-point slot and fin star grain structure in the RSRM'3s forward segment. Propellant in forward-center and aft-center segments form straight walled cylinders; aft-segment propellant tapers outward to submerged nozzle. Inhibitors between segments are asbestos-filled carboxyl terminated polybutadiene used to tailor burning surface to meet the motor's thrust requirements. (Adopted from Virtual prototyping of solid propellant rockets)

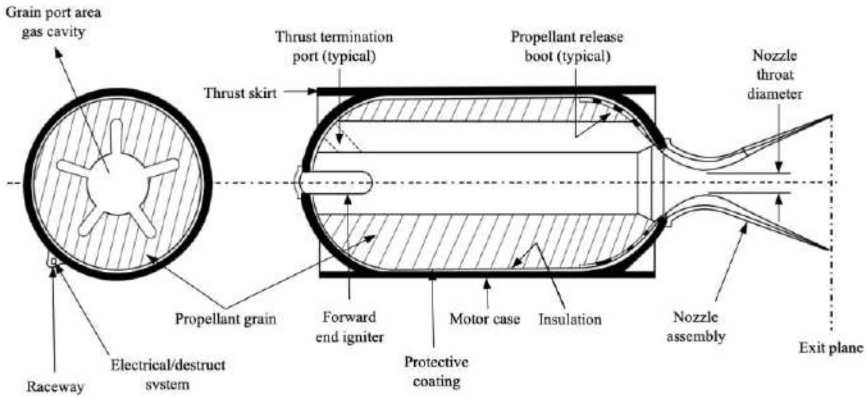

(A)

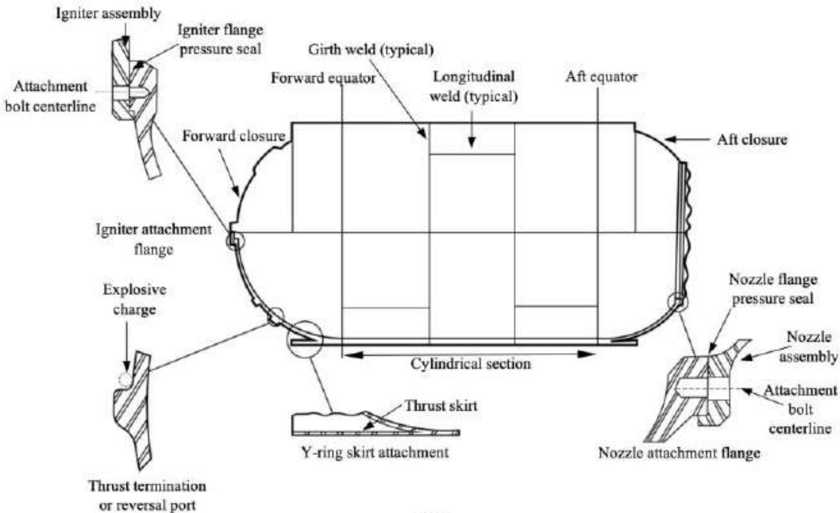

(B)

Figure 79- Typical solid rocket motor case. (Redesigned and adopted from NASA SP-8025)

COMBUSTOR VOLUME AND SHAPE

COMBUSTOR SHAPE

The combustion chamber of chemical rockets, which is cylindrical, has geometric parameters, length L_1 and diameter D_1, effective ratio (contraction) (A_1/A_{th}) towards the nozzle, and contraction ratio of length L_C or contraction angle θ_c. As shown in the figure (81).

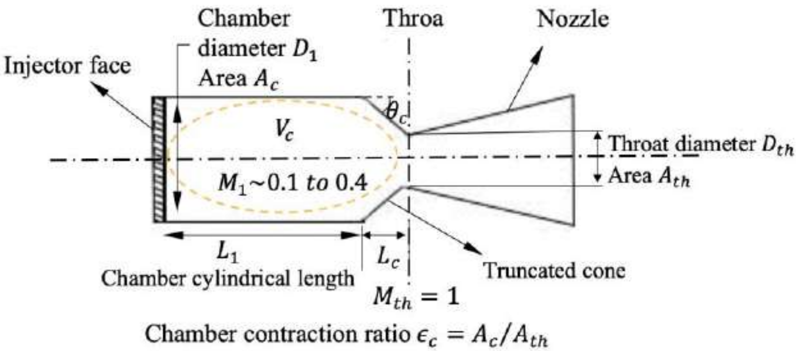

Figure 80- Elements of basic cylindrical combustion chamber (modified and adopted from Design of Liquid Propellant Rocket Engines)

The volume of the combustion chamber includes the cylindrical part and the converging side to the throat. The diameter of the enclosure D_1 is initially determined by the size of the rocket or the size of the thrust, i.e., in the flight efficiency section, the lowest cross-sectional ratio (via $\frac{m_0}{A}$) is determined with the aim of the minimum amount of D_1. Remember that the nozzle throat is acoustic and the area ratio $\frac{A}{A^*}$ determines the Mach value upstream. It is desirable to have the highest cross-sectional area ratio while A_1 still has the lowest possible value. The contraction angle θ_c is determined for a fluid flowing in the throat with a high discharge coefficient. It is desirable to choose a large angle of about $20^\circ - 30^\circ$, which is usually equal to the upper limit and leads to higher efficiency. The length of the combustion chamber L_1 is the minimum length that leads to complete combustion in the rocket with liquid propulsion. Therefore, the length is directly proportional to the products with the average speed of the propulsion in the combustion chamber and the local time of the propulsion, i.e.,

$$L_1 \approx v t_{res} \tag{315}$$

Local time also depends on the times of evaporation, mixing, and reaction, which in turn will strongly depend on the propellant compounds. Another influential factor that affects the local time is the atomization scale related to the design of the injector plate. Therefore, the length of the combustion chamber depends on the design of the injector plate and the type of propulsion. The local time or stay time for different engines is 1-40 ms. The characteristic length is usually defined as the ratio of the total volume of the chamber, namely

$$L^* = \frac{V_C}{A_{th}} \tag{316}$$

Since this number has no physical basis, it is used in comparative cases. A chamber is designed depending on the number of efficiency parameters such as C_f, C^*, and I_{sp} and based on the ratio of the area used to design the throat. The throat is used as the starting point for the dimensional design of the combustion chamber. Characteristic length and contraction ratio are important parameters that were used to determine the length and diameter of the chamber. The ratio for the propellants and the throat section used can be obtained from the table below. The characteristic length range can also be obtained based on the type of propulsion.

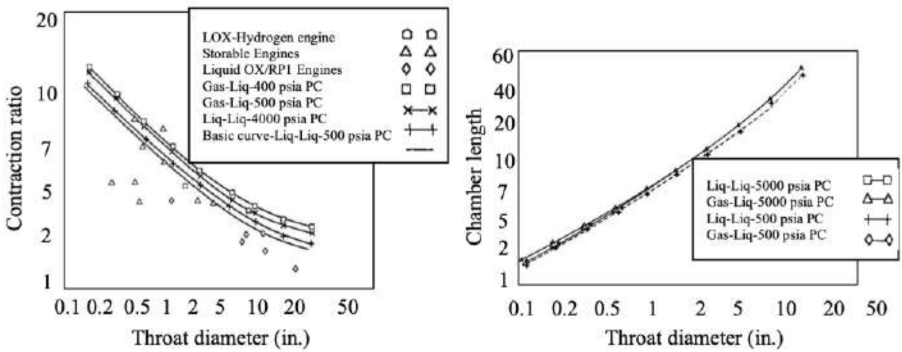

Figure 81- Variation of contraction ratio and chamber length diameter with different throat diameters on several tests (from Modern Eng.)

$$L^* = \frac{V_C}{A_t} = \frac{W_{tc}\ V\ t_s}{A_t} \tag{317}$$

V_C = Chamber volume(ft^3) W_{tc} = Propellant mass flowrate$\left(\frac{lb}{sec}\right)$

V = Average specific volume$\left(\frac{ft^3}{lb}\right)$ t_s = Propellant stay time (sec)

$\frac{A_C}{A_t}$ = Contraction ratio A_C = Cross sectional area of the chamber

Since A_t is approximately directly related to the value of $(W_{tc}\ V)$, therefore, (L^*) is inherently a function of the propulsion stay time, which can only be determined experimentally. Also, if the contraction ratio and the characteristic length (L^*) exceed their limit, they will have a great impact on the pressure drop inside the chamber. The effect of (L^*) on (C^*) in a combustion chamber is shown experimentally (laboratory) in the table below.

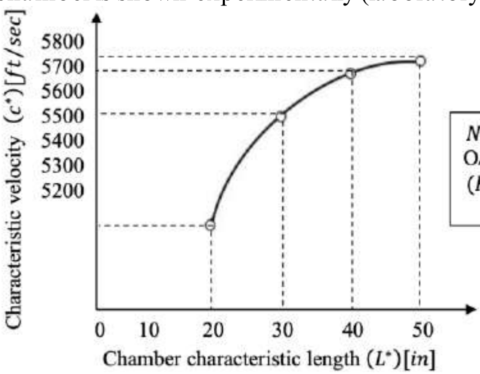

Figure 82- Effect of L* on c* value of experimental thrust chamber. from Design of Liquid Propellant Rocket Engines

The value of (C^*) increases with increasing (L^*) to an asymptotic maximum. Increasing (L^*) beyond a certain point reduces the overall performance of the system for the following reasons:

- Larger L^* will increase the volume and weight of the thrust chamber.
- Larger L^* requires more surface area for cooling.
- The larger L^* has more frictional losses in the chamber wall.

In the actual design, the optimization analysis determines the minimum possible L^* for the combustion chamber in accordance with the efficient combustion. Under a set of operating conditions such as propulsion type, mixture ratio, chamber pressure, injector design, chamber geometry, the required minimum L^* value can only be assessed by the actual firing of the test thrust chamber. A value of L^* proportional to the propulsion residence time between 0.002 and 0.004 Impact can be used between 15_{in} to 120_{in} for design in various combustion chambers. The approximate value of L^* for different propellants is shown in the table below.

Propellant combination	Combustor characteristic length $L^*[m]$
Liquid fluorine/hydrazine	0.61-0.71
Liquid fluorine/gaseous H_2	0.56-0.66
Liquid fluorine/liquid H_2	0.64-0.76
Liquid O_2 /ammonia	0.76-1.02
Liquid O_2 /liquid H_2	0.56-0.71
Liquid O_2 /gaseousH_2	0.76-1.02
Liquid O_2 /RP-1	1.02-1.27
Nitric acid/hydrazine	0.76-0.89
N_2O_4/hydrazine	0.60-0.89
H_2O_2/RP-1 (including catalyst bed)	1.52-1.78

Table 15- Recommended Combustion Chamber Characteristic Length (L*) for Various Propellant Combinations. from Design of Liquid Propellant Rocket Engines

COMBUSTOR VOLUME

The combustion chamber acts as a cover to hold the propellants for a sufficient length of time (stay time) to ensure complete mixing and combustion before entering the nozzle. Therefore, the volume of the combustion chamber has a certain effect on combustion efficiency. And the theoretical volume required for the combustion chamber is a function of the mass flow rate of the propellants and their average density, and also the stay time required for efficient combustion. It is expressed as the following equation:

$$V_c = W_{tc}\ V\ t_s \tag{318}$$

As can be seen in equation (318), the stay time (t_s) is independent of the combustion chamber geometry. Theoretically, for any required volume, the combustion chamber can be of any shape, while in the actual design, the combustion chamber configuration is limited. In a long combustion chamber with a small cross-sectional area, the pressure drop is greater than the non-isentropic flow of gas, which requires a longer thrust chamber and limits the specific space for the injector to be placed. The required number of injectors is designed, while with a small chamber with a large cross-section, the mixing and combustion zone is very short. Other factors such as heat transfer, combustion stability, weight, and ease of construction must also be considered in the final design and configuration of the thrust cham ber.

The five geometric shapes used in the combustion chamber design are shown in figure (79). Spherical and semi-spherical shapes, on the other hand, were used in early European design, and its cylindrical shape was often used in the United States. A spherical or semi-spherical chamber has the advantage of a higher cooling surface area and lower weight compared to a cylinder of the same volume, and also a spherical chamber has the lowest area-to-volume ratio. For a high strength material at an equal chamber pressure, the wall thickness of a spherical chamber is half of the cylindrical chamber. However, a spherical chamber has a more difficult fabrication process and will be less efficient under many conditions. In the design of a cylindrical combustion chamber for a specific A_t and L^*, the value of contraction ratio ($\epsilon_C = \frac{A_C}{A_t}$) can be calculated and optimized according to the following factors:

- Combustion function in combination with injector design
- Need wall cooling
- Combustion stability
- Combustion chamber gas pressure drop
- Weight
- Space envelope
- Ease of manufacturing

For pressurized gas propulsion, the Area contraction ratio is 2 to 5 for systems with low thrust motors and has a lower ratio of 1.3 to 2.5 for systems with higher thrust motors and higher chamber pressure. The following figure shows the basic components of a cylindrical combustion chamber. In general, chamber volume refers to the volume of the combustion chamber, which includes the space between the two injector plates and the throat section. The approximate volume of the combustion chamber can be obtained from the following equation:

$$v_C = A_t\left[L_C\epsilon_C + \frac{1}{3}\sqrt{\frac{A_t}{\Pi}}\cot\theta\left(\epsilon_C^{\frac{1}{3}} - 1\right)\right] \qquad (319)$$

The total surface area of the combustion chamber wall except the injector plate can be approximated by the following formula:

$$total\ area = 2L_C\sqrt{\Pi\epsilon_C A_t} + \csc\theta(\epsilon_C - 1)A_t \qquad (320)$$

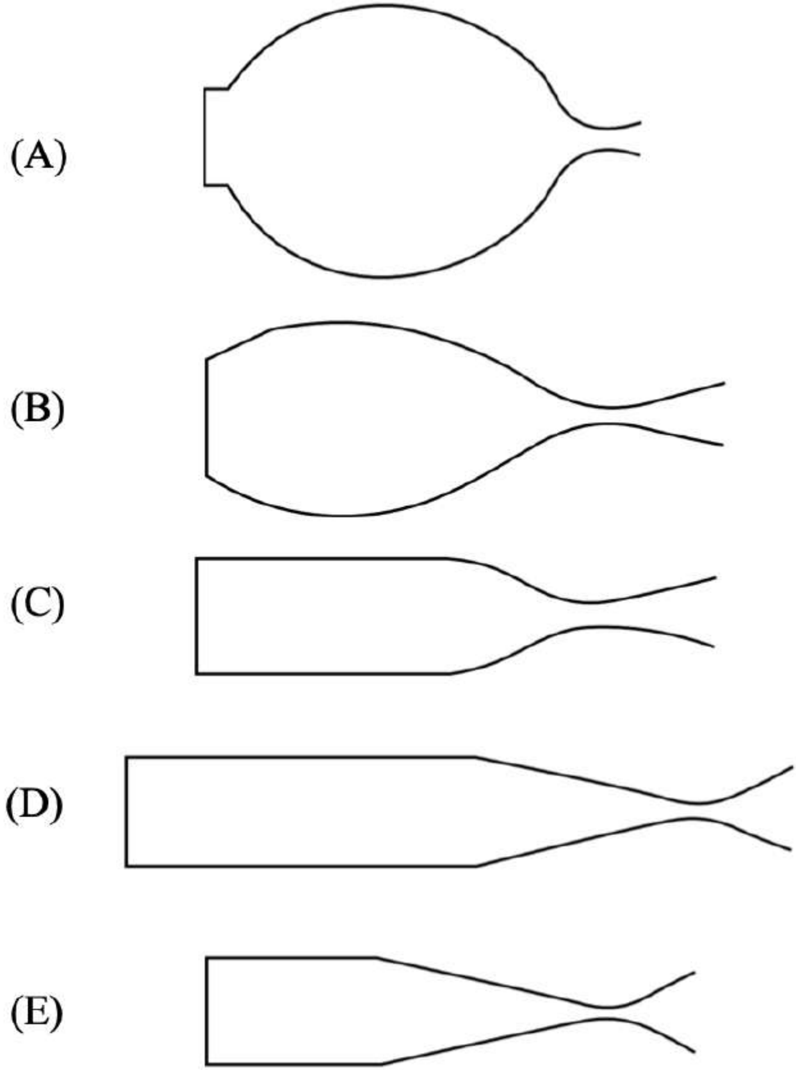

Figure 83-Solid-Wall-Segment Contours. Adopted from confidential NASA 383164

ROCKET NOZZLE

ROCKET NOZZLE WITH LIQUID PROPULSION

The last part of the chemical rocket thrust chamber is its nozzle. They are designed to be able to effectively convert the chemical energy from the combustion of the propellants into kinetic energy, which results in the production of the thrust, and movement of the rocket vehicle. A large part of the rocket engine consists of nozzles, which play an important role in the overall efficiency of the engine and also include a large section of the engine structure. The nozzle design involves solving two matters simultaneously:

1. Wall shape design that forms the expansion surface of the wall.
2. Description and design of the nozzle structure and its hydraulic system.

The nozzle shape starts from the upstream of the throat and extends to its exit. An important aspect of the methods used to produce the geometry and shape of the nozzle wall includes the shapes with the highest efficiency and for the nozzle contours also based on criteria other than efficiency. Structural and hydraulic issues include parts such as regeneratively cooled tube wall nozzles and extensions, which include cooling of the nozzle using turbine exhaust gas, ablation cooling and radiant cooling. Generally, the shape of the nozzle is chosen in such a way as to increase its efficiency without any restrictions on the system, and achieving this goal is easy given the tools available today. The problem starts when unusual requirements impose additional constrains that are not easily controlled. A common example is the tendency to maximize the expansion area ratio to achieve high vacuum performance from the upper stage engine, as well as the ground test of these motors at no extra cost for altitude facilities. For optimization, the cut-and-try method is used to develop the contour of the nozzles that create the best compromise between performance and non-performance. The nozzle structure of a rocket should provide the strength and robustness of a system wherein weight is at a high premium and also the loads that acts on it are not readily predictable. The maximum loads on the nozzle structure often occur during start transients before full flow is established (from 19770009165). The lateral loads (side loads) on the nozzle in the separated flow cannot be accurately predicted in terms of magnitude, direction, or frequency, and therefore a difficult problem for the designer trying to design a structure with the lowest possible weight that will withstand these loads. This structure is often designed overlay strong based on experience with similar nozzles, and restrictions on subsequent weight loss will be included in the original design. The nozzles used in the rocket engine with liquid propellant are inherently very efficient components and can be highly modified and optimized in the current development conditions. (The efficiency of these nozzles has improved by less than 1% in recent years). Striving for higher performance has resulted in a huge increase in area ratio. For example, the J2 engine nozzle used in stages 2 and 3 of the Saturn V rocket had an area ratio of 27, while the nozzle used in the space shuttle orbiter had an area ratio of 77. By increasing the nozzle cross-section ratio in exchange for a small increase in efficiency, the nozzle becomes a relatively large part of the engine. Since the gained efficiency by increasing the surface expansion ratio in the nozzles is very small, so it is tried to use shorter packages with the same efficiency through the short bell nozzle or annular nozzles such as Expansion-Deflection (E-D) and Plug nozzle or aerospikes. The following figure shows the different types of nozzles used in liquid rocket engines. The bell and conical nozzles are standard operational configurations while annular bell and E-D and Plug nozzles are advanced development configurations (from 19770009165).

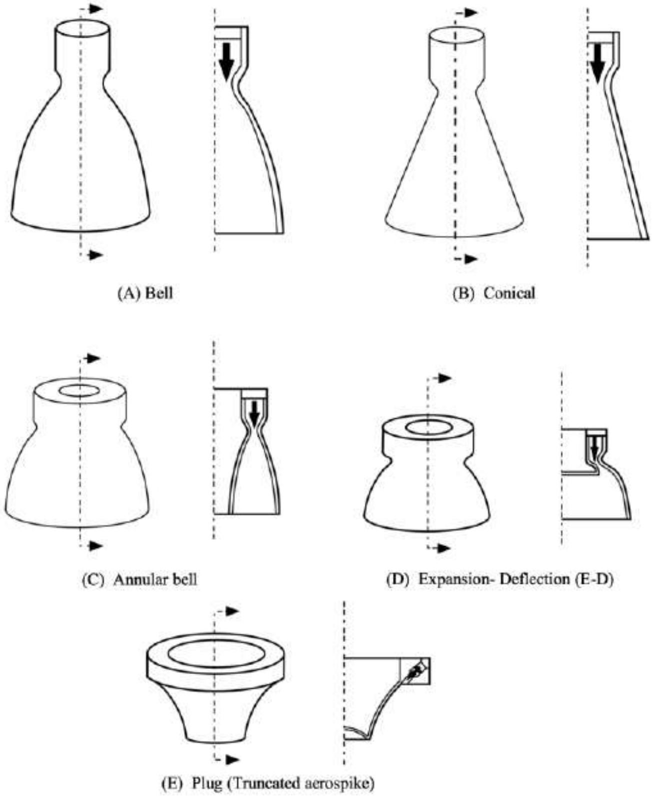

Figure 84- The shape of nozzle types from NASA-Confidential

Tables 16 and 17 show the main characteristics of the nozzles used in most liquid rocket engines. Almost all of these motors use a bell nozzle. Most large motors have tube walls and are regeneratively cooled, while small motors are ablation or radiation cooled.

Engine	System application	Thrust (lbf)	Chamber pressure $(psia)$	Specific impulse $lbf.sec/$	Propellants			A_e/A_{th}	Chamber nozzle joint	Entrance half-angle deg
					Oxidize	Fuel	MR			
RS – 1801	Lunar execution module accent engine	3500 vac	120 vac	310 vac	N_2O_4	50:50	1.60	2.9	Integral	30.0
AJ 10-118	Delta second stage	7575 alt	206 alt	267 alt	IRFNA	UDMH	2.8	3.27	Welded	25
AJ 10-138	Titan III transtage	8000 alt	105 alt	302 alt	N_2O_4	50:50	2.0	2.54	Integral	7.5
VTR - 10	Lunar execution module decent engine	9850 vac	104 vac	305 vac	N_2O_4	50:50	1.6	2.52	-	-
RL10 A- 3-3	Centaur upper stage	15000 alt	400 alt	444 alt	LOX	LH_2	5.0	4	Integral	10.5
YLR81-BA-11	Agena upper stage	15800 vac	506 vac	298 vac	IRFNA	UDMH	2.57	5.335	Welded	-
AJ 10-137	Apollo service module	20500 vac	97 vac	310 vac	N_2O_4	50:50	1.6	2.00	Bolted	7.5
YLR 99-RM-1	X-15 aircraft; Pioneer spacecraft	49390 alt	600 alt	236 alt	LOX	$RP-1$	1.25	4.10	Integral	31.5
YLR 113-AJ-1	Rocket sled	50000-150000 sl	235 to 595 sl	195 to 240 sl	N_2O_4	UDMH	2.1	2.04		25
LR91-AJ-5	Titan II second stage	100000 alt	827 alt	321 alt	N_2O_4	50:50	1.80	2.51		30
LR89-NA-7	Atlas MA-5 booster engine	330000 (2 thrust chambers)	578 sl	254 sl	LOX	$RP-1$	2.28	1.67		-
LR79-NA-11	Thor MB-3	169500 sl	588 sl	256 sl	LOX	$RP-1$	2.15	1.67		10
H-1C and H-1D	S-1 stage of Saturn 1B launch vehicle	204300 sl 228800 alt	705 sl 707 alt	269 sl 301 alt	LOX	$RP-1$	2.23	1.62		-
LR87-AJ-5	Titan II first stage	214400 sl 236400 alt	783 sl 783 alt	263 sl 289 alt	N_2O_4	50:50	1.93	2.04		25
J-2	S-II and S-IV stages of Saturn V	230000 alt	725 (nozzle stagnation)	423 alt 294 sl	LOX	LH_2	5.5	1.58		13.73
F-1	S-IC stage of Saturn V	1522000 sl 1748000 alt	1126 injector 983 throat	274 sl 315 alt	LOX	$RP-1$	2.27	1.307		13

Table 16- (continued)

Engine	D_{th} $[in]$	A_{th} $[in^2]$	Length, throat to exit $[in]$	Exit type	Divergence half angle, deg	D_e $[in]$	A_e $[in^2]$	A_e/A_t	Nozzle extension	Extension/ nozzle joint	Method of cooling nozzle and extension
RS – 1801	4.578	1.65	35.27	72% bell	-	30.9	750	45.6	None	NA	Film and ablation
AJ 10-118	5.25	21.64	23.1	Complex contour		23.5	432.8	20	Optional	Clamped flange	Regenerative to 20:1; radiation to 30:1 or 40:1
AJ 10-138	7.48	43.9	49.61	Bell		47.33	1758.5	40	Yes	Bolted flange	Ablation to extension; radiation thereafter
VTR - 10	8.320	54.34	62.11	72.3% bell, rounded		57.26	2574.0	47.5		-	Ablation to 16:1; radiation to 47.5:1
RL10 A- 3-3	5.14	20.75	46.3	Bell	32.5	38.8	1182.75	57	None	NA	Regenerative
YLR81-BA-11	4.670	17.13	39.8		25.7	31.326	770.32	45	Yes	Bolted flange	Regenerative to 13:1; radiation to 45:1
AJ 10-137	12.447	121.675	111.8		-	98.40	7605	62.5			Ablation to 6:1; radiation to 62.5:1
YLR 99-RM-1	8.64	58.6	-	Conical	20	27.20	574.3	9.8	None	NA	Regenerative
YLR 113-AJ-1	15.25	182.56	35.41		17	36.41	1040.66	5.7			Film
LR91-AJ-5	9.12	65.41	72	Bell		64.0	3217	49.2	Yes	Bolted flange	Regenerative to 13:1; ablation to 49.2:1
LR89-NA-7	16.2	206.0	58	100% bell	-	45.83	1648.8	8	None	NA	Regenerative
LR79-NA-11	16.2	206.0	58			45.8	1646.6				
H-1C and H-1D	16.16	205	55	Bell		45.49	1630		Yes	Bolted flange	
LR87-AJ-5	15.25	182.56	42.46		23	43.14	1461.6		None	NA	Film and regenerative
J-2	14.7	169.6	90		4.226 min 27.5 max	77	4656.6	27.5			Combined film and regenerative
F-1	35	961.4	158		-	140	15400	16	Yes	Bolted flange	Regenerative to 10:1; turbine exhaust to 16:1

Table 16- The Main Characteristics of the Nozzles Used in Most Liquid Rocket Engines

Engine	System application	Thrust (lbf)	Chamber pressure $(psia)$	Specific impulse $lbf.sec/lbm$	Propellants			A_c/A_{th}	Chamber nozzle joint	Entrance half-angle deg
					Oxidizer	Fuel	MR			
Model 8093	Centaur ACS and ullage orientation	1.5 vac	198 vac	155 vac	90% H_2O_2 (mono)		-	17.4	Welded	(0.06 in. radius)
M2-A	Comsat positioning and orientation	1.9 to 3.0 vac	117 to 185 vac	225 vac	N_2H_4 (mono)			44.8	Integral	60
Model 8250 Unit I	Agena-Gemini target vehicle SPS	16 vac	78 vac	252 vac	MON	UDMH	1.1	15.8		40
SE-7	Gemini attitude control	23 vac	132 vac	258 vac	N_2O_4	MMH	0.7	3.8		31.5
PD6000179	Titan III transtage ACS	16.0 vac 26.7 vac	120 vac 200 vac	221 vac 225 vac	N_2H_4 (mono)		-	33.7	Welded	50
Model TD-339	Surveyor vernier propulsion system	30 to 104 vac	70 to 250 vac	287 vac	MON	MMH: H_2O (72: 28)	1.5	10		47
MC-4-610	Ranger Inn mariner propulsion	50 vac	190 vac	235 vac	N_2H_4 (mono)		-	37		60
R-4D	Apollo service module RCS	60 sl 100 vac	96.5 sl 96.5 vac	168 sl 280 vac	N_2O_4	50:50	2.03	4.2	Integral	53
SE-7-1	Saturn SIV D-B ullage	72 vac	101 vac	274 vac		MMH	1.27	3.1		31.5
SE-8	Apollo command module ACS	93 vac	137 vac				2.0			26.1
Model 700800	Saturn SI-B and SIV-B ACS	147 vac	101 vac	292 vac			1.64	5.8		45
Model 8250 Unit II	Agena-Gemini target vehicle SPS	200 vac	94 vac	257 vac	MON	UDMH	1.15	7.9		40
RS-2101	Mariner Mars 1971 spacecraft	300 vac	117 vac	283 vac	N_2O_4	MMH	1.55	4.9	Clamp	44.7
Model 7161 (500 lbf)	Lunar landing training vehicle ACS	500 sl	325 sl	122 sl	90% H_2O_2 (mono)		-	12.7	Integral	45
LR 101-NA-15 Mod 2	Atlas MA-5 vernier engine	913 sl	337 sl	205 sl	LOX	$RP-1$	1.8	3		10

Table 17- continued

Engine	D_{th} $[in]$	A_{th} $[in^2]$	Length, throat to exit $[in]$	Exit type	Divergence half angle, deg	D_e $[in]$	A_e $[in^2]$	A_e/A_t	Nozzle extension	Extension/ nozzle joint	Method of cooling nozzle and extension
Model 8093	0.075	0.0044	0.344	Conical	18	0.293	0.0674	15	None	NA	Radiation
M2-A	0.105	0.0086	0.9		15	0.662	0.34	40			
Model 8250 Unit I	0.377	0.1118	3.715	80% bell	29	2.832	6.28	56.2			
SE-7	0.358	0.1008	2.599	80% bell (scarfed)	31.6	2.27	4.05	40.2			Ablation
PD6000179	0.313	0.0772	3.0	Optimized bell	15	2.20	3.8	49			Radiation
Model TD-339	0.54	0.23	6.5	Overturned bell	37	5.09	19.7	86	Yes	Welded	Regen. to extension;
MC-4-610	0.437	0.15	4.05	Bell	23.6	2.904	6.623	44	None	NA	Radiation
R-4D	0.868	0.592	6.98		8	5.46	23.41	40	Yes	Bolted flange	
SE-7-1	0.710	0.3959	-	80% bell (scarfed)	-	4.49	15.85		None	NA	Ablation
SE-8	0.710		2.190	82% bell	36 entrance 10.6 exit	2.13	3.563	9	Yes	Bolted flange	
Model 700800	1.040	0.849	6.350	Bell	32	6.06	28.84	33.9	None	NA	
Model 8250 Unit II	1.423	1.59	-	80% bell	27	4.9	18.85	11.86			Radiation
RS-2101	1.354	1.44			44.75	8.56	57.5	40	Yes	Clamp	Film and
Model 7161 (500 lbf)	1.195	1.121	1.640		15	2.078	3.39	3	None	NA	Radiation
LR 101-NA-15 Mod 2	1.63	2.09	4.75	Conical		3.86	11.70	5.6			Regenerative

Table 17- The Main Characteristics of the Nozzles Used in Most Liquid Rocket Engines

To improve the cooling process of the nozzles in areas that require high heat dissipation, there is always an effort to reduce the area and increase the thermal conductivity of the wall surface of ducts exposed to hot gases. Space shuttle main engine (SSME) has been designed for milled axial coolant channel in the main combustion chamber and throat up to an expansion area ratio of 5 and tube walls from area ratio of 5 to 77 (from 19770009165). Significant work has been done in the field of nozzle development, but the development process and activities in the field of E-D nozzles are less than plug nozzles. This development also includes smaller bell shape nozzles. Regarding the use of these nozzles, it should be noted that, with the exception of bell nozzles, which are almost always used, and also, for example, the annular bell nozzle used in lance boosters, plug nozzles to date. And E-D has not been used in operational engines, however, the possibility of using them with high efficiency in future engines is not far from the mind and is achievable.

NOZZLE CONFIGURATION

The appropriate nozzle configuration for a particular operation depends on several factors, including the altitude regime at which the nozzle will operate, the diversity of stages for using the same nozzle, and the development time limitation or funding. Mixture ratio, chamber pressure, propellant composition, and thrust level are in most cases based on factors other than nozzle configuration and are used as input for the nozzle-selection study. These parameters have a minor effect on the configuration, but are very effective in choosing the method of cooling the nozzles. Payload from a given propulsion system is nearly constant over a wide range of any independent variable (e.g., chamber pressure) in the vicinity of the optimum value for that variable. Nozzle parameters therefore can be selected based on preliminary optimization studies (from 19770009165). The following figure shows a schematic of a typical bell nozzle configuration.

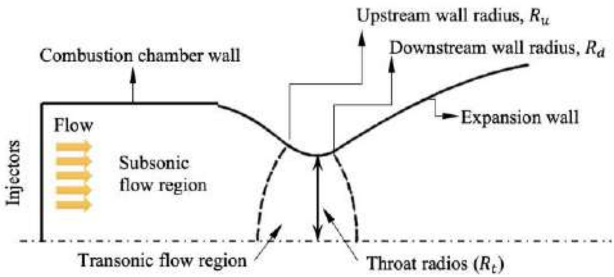

Figure 85- Sketch illustrating basic nozzle configuration and nomenclature

GEOMETRY

The nozzle throat is the region where the flow is transient from subsonic to ultrasonic, and for most nozzles, the mass flow rate and consequently the rate of heat transfer to the wall have their maximum value in this section. The geometry of the nozzle wall in the vicinity of the throat will determine the characteristics and distribution of the exhaust gas properties across the nozzle at the throat. It should be noted that the geometry of this throat flow-field is independent from the nozzle geometry downstream of the throat and for a distance of about one throat radius upstream of the throat (from 19770009165). Usually, the nozzle wall adjacent to the throat usually consists of an upstream circular arc that is tangent to the geometry of the downstream circular arc. Fixed-radius arches are used to shape the throat-approach wall. A small radius is desirable both for minimum overall length and for minimum wall area exposed to the high heat fluxes associated with flow near Mach 1 (from 19770009165). However, the smaller the radius, the more difficult it will be to obtain an accurate solution for the transonic flow field. Existing methods for solving transonic flows for radius ratios of about one provides accurate answers, while computer solutions that use power-series expansion to solve parabolic partial differential equations in transonic flows are shown the value of the nozzle aerodynamic efficiency for the radius ratio $\left(\frac{R_u}{R_t}\right)$ in the range of 0.6 to 1.5 will remain constant. In annular nozzles, the throat section is annulus and exits a circular shape with radius R_t. The width of the annular throat is called the throat gap (G_t), which has the same design effect as R_t. For circular nozzles with two convex walls with equal radii, the ratio of the radius of the upstream wall to the throat gap $\left(\frac{R_u}{R_t}\right)$ greater than 1.0 will be used, and this ratio will be greater than this value when the convex radii are not equal. The flow rate through the nozzles is directly proportional to the cross-sectional area of the aerodynamic flow in the throat. This area of the flow is denoted by (A_t^*), which is the same as the geometric area of the flow in the throat section (A_t), with the difference that, this is a corrected amount of transonic non-uniform flow effects. The ratio $\left(\frac{A_t}{A_t^*}\right)$ is called the potential discharge coefficient, which is given in the figurer 87. It should be noted that the mass flow rate of the nozzle will decrease with decreasing ratio of radius.

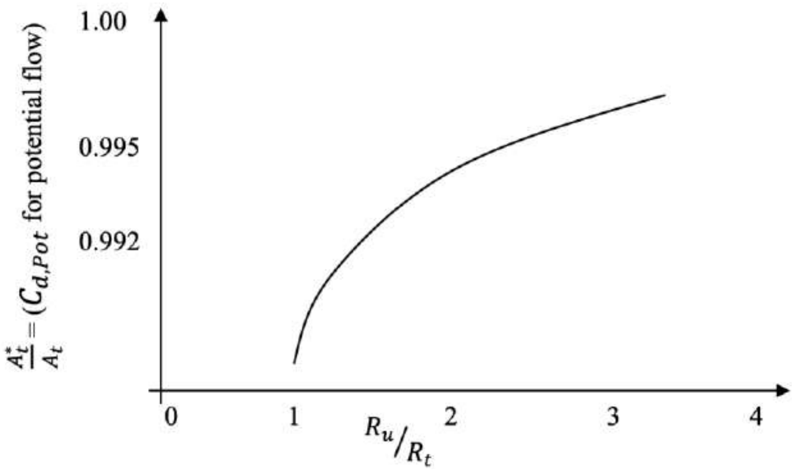

Figure 86- Variation of A t/A t with Ru/R t. from SP8120

The downstream to throat radius ratio of 0.4 is a very good compromise between construction difficulty and the minimum nozzle length for the tube wall area. For round tubes made of relatively ductile materials such as stainless steel, nickel or copper, a minimum bending radius of twice the outer diameter of the tube is required. Difficult-to-work materials should be limited to a larger bending radius. For elliptical sections, the bending radius of the tube must be more than twice the principal dimension of the tube section. For ablative materials, the radius must be large enough to prevent shearing of the material during firing. When the gas density is relatively low (chamber pressure is low) or the nozzle is relatively small, the downstream radius ratio $\left(\frac{R_D}{R_t}\right)$ should be large enough for the expansion to be slow enough to keep the chemical compounds close to equilibrium, (From 19770009165). If this expansion occurs rapidly and there is a significant deviation from the equilibrium composition near the bottleneck, significant and large reductions in the performance of some high-energy engines will occur. The geometry of the downstream wall is chosen primarily according to the exchange of chemical (kinetic) performance, which increases with the radius ratio, and then the aerodynamic performance, which decreases with the pressure ratio. Another consideration that should be considered in the design of nozzles with a circular throat arc and a conical divergent section is that the geometry of the nozzle wall downstream of the throat has a significant effect on heat transfer downstream because the geometry may Can affect the boundary layer by reverse pressure gradient. Experimental data in (ref

10,11 From 19770009165, Page26) for nozzles with a conical angle of 15 ° show that the ratio $\left(\frac{R_D}{R_t}\right)$ should not be less than about 0.75.

EXPANSION GEOMETRY

As we know, the nozzle functions in such a way that it converts the thermal and chemical energy produced in the combustion chamber into kinetic energy. In fact, the nozzles accelerate the exhaust gases by the expansion geometry that extends from the nozzle throat to the nozzle exit, which is dropping down the pressure and temperature in this short distance. Since thrust is a product of mass and speed, the higher the speed, the better the result. As seen in Figures 85 and 86, the nozzles consist of a converging section and a divergent section, so that the smallest flow section between these sections is known as the nozzle throat, and the end of the nozzle from which the gas came out is called the nozzle exit. The length of the nozzle is usually large enough to cause the necessary pressure drop so that the nozzle outlet pressure is equal to the outside ambient pressure. Since the thrust has its maximum value, it is called adapted, which is known as optimum or correct expansion. Both engine length and specific impulse strongly influence the payload capability of rocket vehicles, (From 19770009165). Conical nozzles are generally used in small missiles, and similar to those in Tables 16 and 17, bell nozzles are often used for larger systems. The expansion surface of this type of nozzle is limited between a length for optimal performance, so that the nozzle is given a specific bell shape (characteristic bell shape). The length of the bell nozzle is generally specified as a percentage so that this percentage determines the length of the bell nozzle as a percentage of the length of a conical nozzle with an angle of 15 ° with the same area ratio. Plug nozzles and reverse plug nozzles such as Forced-Deflection or reverse-flow nozzles are not yet operational, however, these nozzles are of interest because they can be made to flow full at large area ratio at sea level. When the outlet pressure (P_e) is less than (P_a), the nozzle is called under-extended, and if the opposite is true, it is called over-extended, therefore, a nozzle is designed for the height at which it should work. At sea level and atmospheric pressure $(14.7\ psi\ or\ 1MPa)$ the discharge of exhaust gases is limited by the separation of the jet from the nozzle wall, while in a vacuum there is no physical limitation, so there must be two different types of engines and nozzle. When the mass flow rate and propellant and the operating conditions are already known, assuming the theory of complete gas law, the cross-section of the nozzle throat (A_t) can be obtained as follows:

$$A_t = \frac{q}{P_t}\sqrt{\frac{R^* T_t}{Mk}} \tag{321}$$

In this equation, q is the propulsion mass passage, P_t is the gas pressure in the nozzle throat, T_t is the gas temperature in the nozzle throat, R^* is the global constant of gases and k is the specific heat ratio. P_t and T_t are calculated from the following equations:

$$P_t = P_c\left(1 + \frac{k-1}{2}\right)^{-\frac{k}{k-1}} \tag{322}$$

$$T_t = \frac{T_c}{1+\frac{k-1}{2}} \tag{323}$$

Where P_c and T_c are the combustion chamber pressure and temperature, respectively.
The hot gases from the combustion inside the divergent part of the nozzle must be expanded to produce maximum thrust, and at the same time the gas pressure reduce because its energy is used to accelerate the gas, the surface in which the inside nozzle pressure is equal to the ambient atmospheric pressure, known as nozzle exit area. Using the ideal gas law, we can obtain a relation for the Mach number (N_m), which is a ratio of the velocity of the gas to the local velocity of sound, as follows:

$$N_m^2 = \frac{2}{k-1}\left[\left(\frac{P_c}{P_a}\right)^{\frac{k-1}{k}} - 1\right] \tag{324}$$

Therefore, the nozzle exit area will be obtained according to the Mach number in the nozzle exit:

$$A_e = \frac{A_t}{A_m}\left[\frac{1+\left(\frac{k-1}{2}\right)\times N_m^2}{\frac{k+1}{2}}\right]^{\frac{k+1}{2(k-1)}} \tag{325}$$

For lunch vehicles (especially the first stages) where the ambient pressure is constantly changing during the burning time, the optimal exit pressure is estimated using rocket trajectory (path line) calculations. However, the maximum allowable diameter for the nozzle outlet is an additional constraint, which in some cases is also a limiting constraint. It is very important that the diameter of the nozzle opening in each stage should not be larger than the diameter of the nozzle opening of the previous stage (lower stage). In space engines where the ambient pressure is zero, the thrust always increases as the nozzle expansion ratio increases. In these motors, the nozzle expansion ratio generally increases until the extra nozzle weight has a longer performance than the excess thrust produced. Since the flow velocity of the gases in the convergent part of the nozzle is relatively low, in this part, unlike the contour of the divergent part of the nozzle, where there is a very high flow velocity, less energy will be lost. As a result, the divergent part of the nozzle will have a greater impact on its performance. Generally, an optimal nozzle shape for a given expansion ratio can be selected with the following considerations:

1. The gas flow at the nozzle outlet is considered to be uniform, parallel and axial for the maximum amount of momentum.
2. The least amount of separation and turbulence losses inside the nozzle is considered.
3. The shortest possible length selection for the nozzle so that space envelope, weight, wall friction losses are minimized.
4. Ease of manufacturing

The operating conditions of the rocket nozzle are completely different from those of the air-breathing system, since the rockets must operate at sea level to vacuum. Therefore, the nozzle pressure ratio (NPR) in rockets is approximately (~ 50) at sea level, and its infinite in a vacuum. As a result, chemical rockets with such a high-pressure ratio also require a large surface expansion ratio to produce maximum thrust. For space applications, the surface expansion ratio is considered to be about 100 or more. Because rocket weight and ambient pressure are not constant during a chemical rocket mission, variable surface nozzle design is a challenge due to its mechanical complexity. One successful example is the motor (RL-10B-2), which consists of two expandable nozzles and is shown in the figure below.

Axial thrust will not be created for all nozzle geometries except bell nozzles, where the exhaust velocity field is the same as the non-axial outlet motion. For example, as shown in the figure below, the flow exiting a conical nozzle is a divergent jet stream. According to its radial velocity pattern, jet flow from a virtual source whose velocity is constant at $(r = cte)$ can be considered.

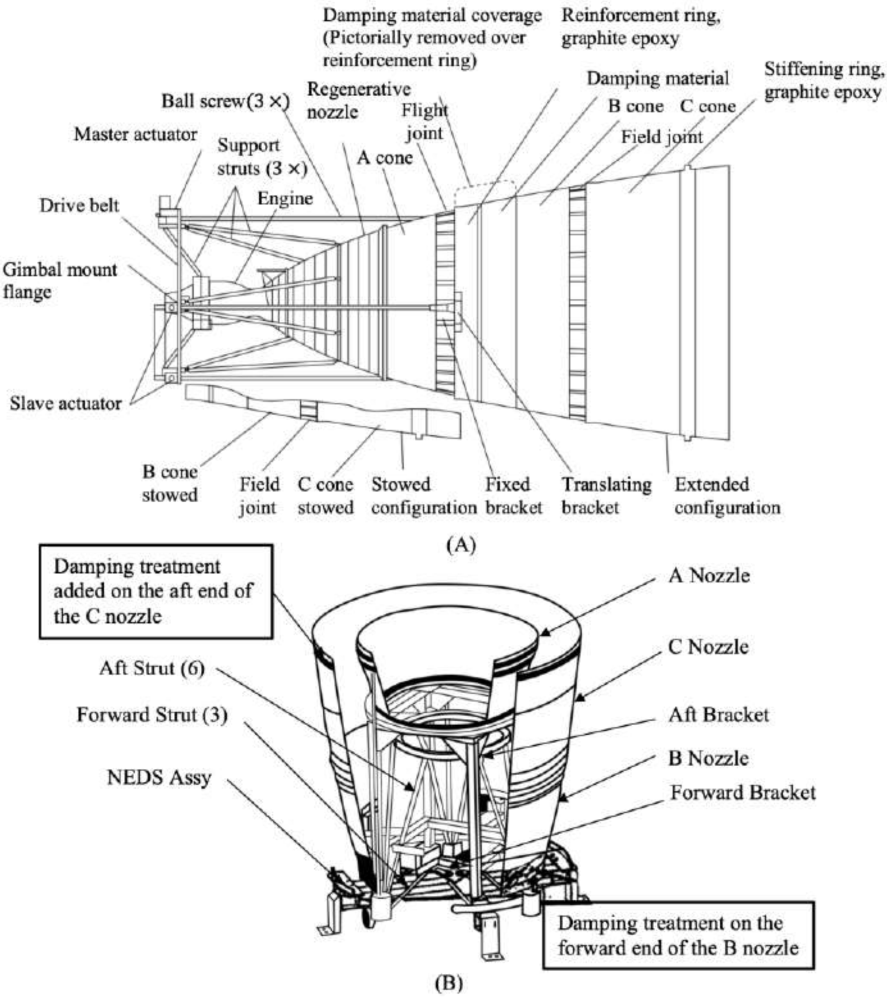

Figure 87-from Carbon/Carbon Extendible Nozzles† M. Lacoste‡, A. Lacombe And P. Joyez Soci5et5e Europ5eenne De Propulsion, Bp 37, 33165 Saint Medard En Jalles, Cedex, France And R. A. Ellis, J. C. Lee And F. M. Payne Pratt & Whitney, Csd, San Jose, Ca, Usa & Aiaa

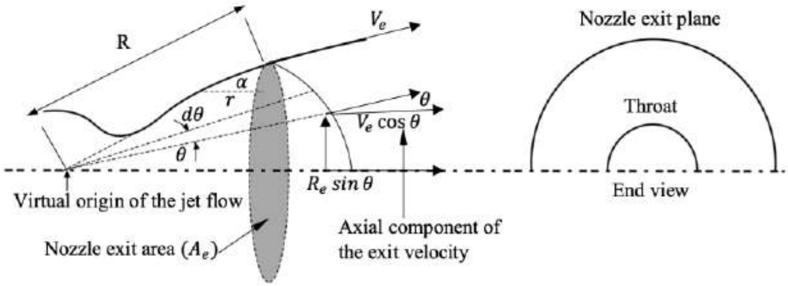

Figure 88- Working sketch used to derive flow angularity loss (or divergence correction factor) for a conical nozzle of half angle in attached exit flow- AIRCRAFT PROPULSION 2009

The angularity loss coefficient is defined as a factor coefficient as the ratio of axial momentum thrust to momentum thrust equivalent to the bell shape nozzle:

$$\text{Thrust: } F_g = C_A \dot{m}_e v_e + (P_e - P_a)A_e \quad (326\text{-a})$$

$$C_A = \frac{\int v_e \cos\theta \, d\dot{m}}{\dot{m} v_e} \quad (326\text{-b})$$

Considering the output surface which is spherical so that the velocity component v_e is perpendicular to it, we can write for the surface unit:

$$dA = 2\pi R \sin\theta \cdot R \, d\theta \quad (327)$$

According to the mass flow rate equation (law of mass conservation) of the nozzle exit and by its first integration, the total mass flow rate in the nozzle can be obtained:

$$d\dot{m} = \rho_e v_e \, dA = 2\pi R^2 \rho_e v_e \sin\theta \, d\theta \quad (328\text{-a})$$

$$\dot{m}_c = \int_0^\alpha 2\pi R^2 \rho_e v_e \sin\theta \, d\theta = 2\pi R^2 \rho_e v_e (1 - \cos\alpha) \quad (328\text{-b})$$

According to Equation (328-a), the axial thrust is calculated as follows:

$$\int v_e \cos\theta \, d\dot{m} = \int_0^\alpha 2\pi R^2 \rho_e v_e \sin\theta \; cos\theta \, d\theta =$$

$$\pi R^2 \rho_e v_e \sin^2\alpha \quad (328\text{-c})$$

By placing the relations (328-b) and (328-c) inside the relation (326-b), the angularity loss coefficient will be obtained as follows:

$$C_A = \frac{\sin^2\alpha}{2(1-\cos\alpha)} = \frac{1+\cos\alpha}{2} \quad (329)$$

For a two-dimensional convergent-divergent nozzle, the angularity loss coefficient can also be obtained according to what was done in the previous case. According to the figure, by considering a cylindrical element of the surface at the output of the nozzle and re-expressing the passing mass rate and the total mass rate passing through the nozzle, the angularity loss coefficient can be gained in this way:

$$dA = L' d\theta W \tag{330}$$

$$d\dot{m} = \rho_e v_e L' d\theta W \tag{331-a}$$

$$\dot{m} = 2\int_0^{\alpha} \rho_e v_e L' W d\theta = 2\rho_e v_e L' W \alpha \tag{331-b}$$

$$C_{A_{2D-CD}} = \frac{2\int_0^{\alpha} v_e \cos\theta\, \rho_e v_e L' W d\theta}{2\rho_e v_e^2 L' W \alpha} = \frac{\sin\alpha}{\alpha} \tag{332}$$

Nozzles are divided into two categories: center body and without center body, the second category of which includes bell shape, partial bell, and conical nozzles. A conical nozzle with a half-cone angle of 15 ° produces an angularity loss coefficient of less than 1.7%, however, at low flight altitudes, i.e., over expanded mode, the operation of conical nozzles involves creating a shock inside the nozzle, which will lead to flow separation. Bell shape nozzles include two categories of full-bell and partial-bell contours which have a more difficult manufacturing process, but due to the smaller exit angle, the momentum thrust performance of this nozzle is more than conical nozzles with the same area ratio or length. It should be noted that in the operation of bell nozzles at sea level, and the output is full flow is accompanied by oblique shock at the edge. Another type of nozzle is known as the center-body, and it can categorize to plug, aerospike, or expansion-deflection nozzles. The advantage of this category over the without center body type is the tendency for higher off-design efficiency at all heights. In fact, there is no shock at the exit of these nozzles to cause separation, and as a result, the flow The off-design efficiency in aerospike and other nozzles in the center body category is higher than the bell or cone nozzles, but the factor that makes this category less used than without center bodies is their cooling. to the end of the path is fully attached to the nozzle.

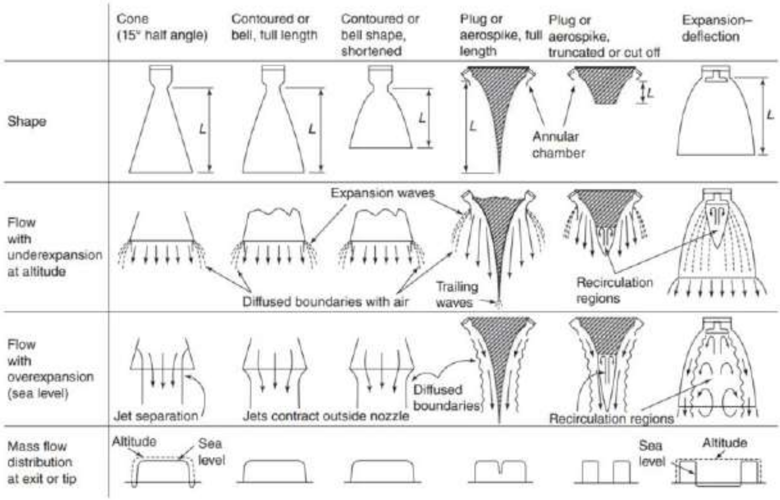

Table 18-Rocket nozzle configuration and their altitude performance. from AIRCRAFT PROPULSION 2009

More information on a linear truncated aerospike is given in the figure below. This design is related to the XRS-2200 aerospike in the rocket engine, which has 20 individual thrust cells or modules and 2 regeneratively fuel cooled external expansion ramps.
The truncated base is porous, which is filled by the gas flow generating device through the turbopump system. The distribution of pressure on the ramps indicates the presence of compressive and expansion waves. The reason for the separation phenomenon does not occur is that the shock waves, which are in the form of shock, are the result of the return of the expansion waves from the jet boundary or shear layer. However, the presence of pressure waves on the ramp increases the heat transfer in the wall, which requires a conservative approach to fuel-coolant. The upstream and downstream radius of curvature of the nozzle throat, the inlet and outlet angle of the bell nozzle and the angularity loss coefficient parameters in the conical and bell nozzles are shown in the figure below. These curves are used in the preliminary design of many nozzles and the study on them.

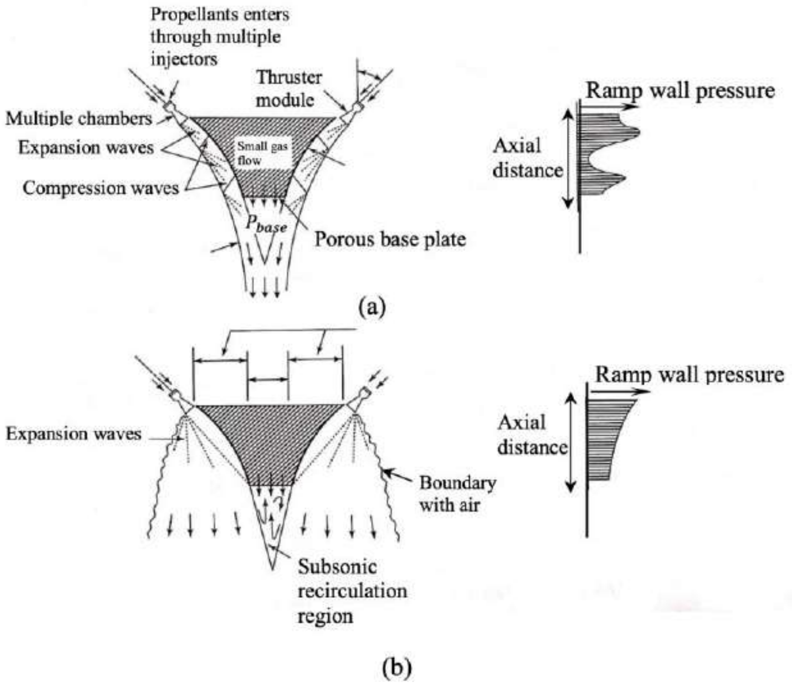

Figure 89- Flow pattern and pressure distribution in a linear aerospike nozzle. from AIRCRAFT PROPULSION 2009

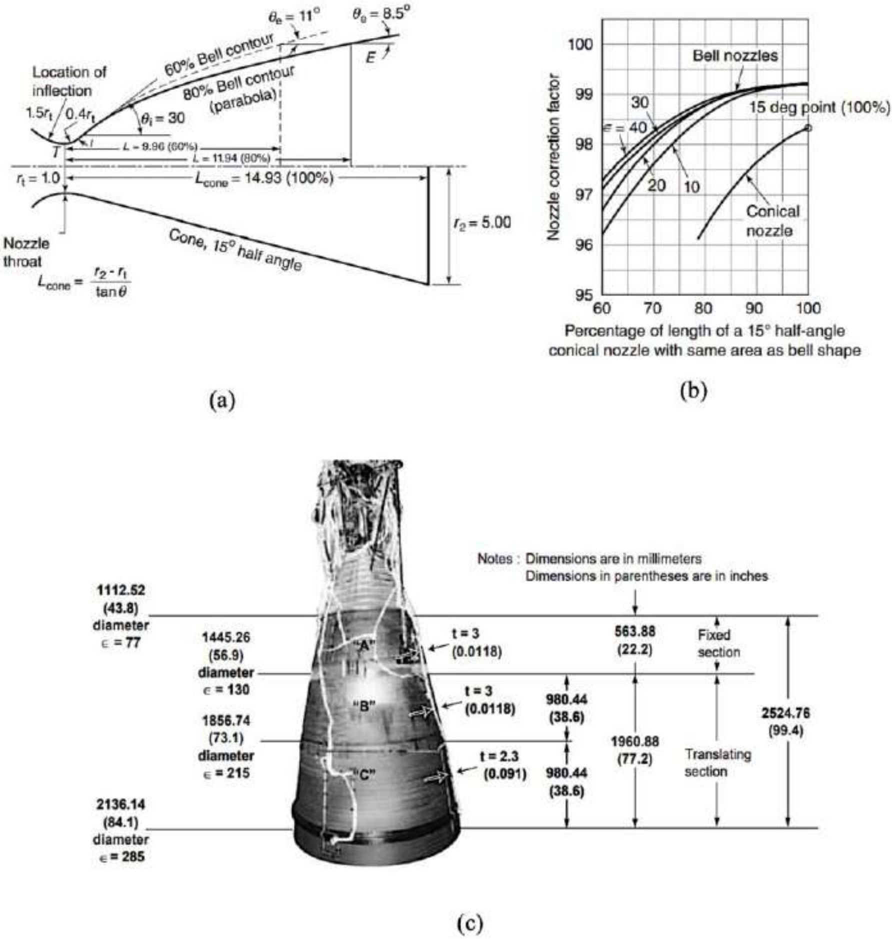

Figure 90- (a), (b) From Air Propulsion System & Carbon/Carbon Extendible Nozzles† M. Lacoste‡, A. Lacombe And P. Joyez Soci5et5e Europ5eenne De Propulsion, Bp 37, 33165 Saint Medard En Jalles, Cedex, France And R. A. Ellis, J. C. Lee And F. M. Payne Pratt & Whitny, Csd, San Jose, Ca, Usa

MULTIPHASE FLOW IN ROCKET NOZZLE

In the studies we have done so far about rocket nozzles, we considered the nozzle output to be gaseous, when in fact the nozzle outputs exist in all three forms: solid, liquid, and gas. Liquid and gas particles can have three sources.

The first is fuel, which is intentionally embedded as gaseous, in such a way as to increase rocket performance through the higher specific impulse. The presence of these particles in the propellant will increase the combustion rate and increase the combustion temperature. The next case occurs in the combustion process so that after combustion, there is always a fraction of the output in the form of soot or other chemical compounds, and the third case is related to the appearance of solid droplets (mainly frozen). The reason for this is that by increasing the ratio of the area of the sections, the pressure and static temperature will decrease and as a result, the gas particles will condense and become solid (frozen) particles. Generally, in the science of heat transfer and fluid dynamic, the two-phase reaction in the fluid (which here includes gas and solid) complicates matters, but by applying some limiting conditions and assumptions, the result of the effect of multiphase flow on the rocket performance will be clearer. Here are four limiting hypotheses that state only the state of heat transfer and the momentum of the particles leaving the nozzle:

1. When solid particles leave the nozzle, they reach a temperature equal to the temperature of the exhaust gases, which means that they are in heat equilibrium with each other.
2. Solid particles at the exit of the nozzle reach a speed equal to the speed of the exhaust gases, i.e., they have reached the momentum equilibrium.
3. Solid particles maintain their temperature so that they do not have any heat exchange with gaseous particles.
4. Solid particles retain their momentum along the nozzle, meaning that their acceleration is not related to gases.

According to the above assumptions, solid particles do not change phase in the nozzle and are frozen around the nozzle exit. For a closer look, we write the conservation principal equations in one dimension on a slab in fluid. The following figure shows the design of the slab in a two-phase flow with zero friction and heat transfer (adiabatic and reversible). The flow rate is constant and as follows:

$$\dot{m}_g = \rho_g v_g A = (\rho_g + d\rho_g)(v_g + dv_g)(A + dA) \qquad (333\text{-a})$$

$$\dot{m}_s = \rho_s v_s A = (\rho_s + d\rho_s)(v_s + dv_s)(A + dA) \qquad (333\text{-b})$$

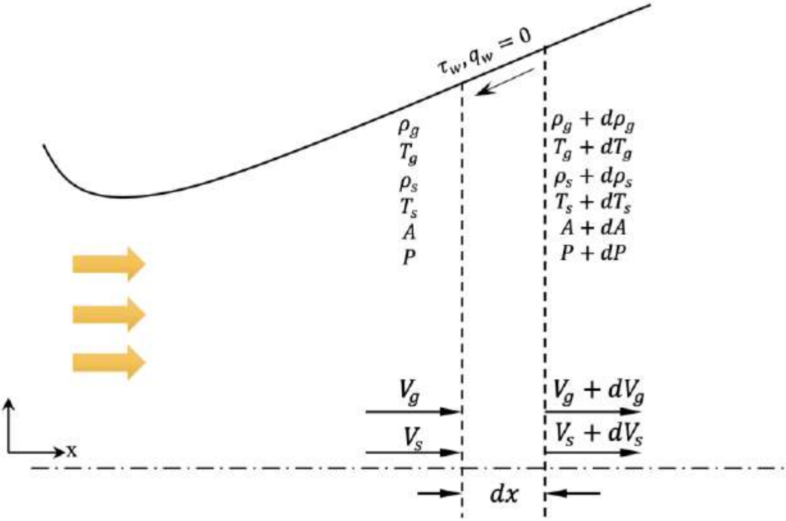

Figure 91- Definition sketch of a slab in a two-phase flow in a nozzle

It is important to note that the density of gas and solid particles is the mass of gaseous and solid particles in the gas-solid mixture. According to the form of the momentum survival equation, the conservation of the momentum on the slab will be written as follows:

$$(\dot{m}_g(v_g + dv_g) + \dot{m}_s(v_s + dv_s)) - (\dot{m}_g v_g - \dot{m}_s v_s) = PA - (P + dP)(A + dA) - \left(P + \frac{dP}{2}\right) dA \qquad (334)$$

The last expression to the RHS of the above equation is related to the compressive force of the side wall on the fluid. By simplifying the above equation, the momentum equation is rewritten as follows:

$$\dot{m}_g dv_g + \dot{m}_s dv_s = -AdP \qquad (335)$$

By dividing the sides of the equation by the area of the stream (A), the above equation is simplified as follows:

$$\rho_g v_g dv_g + \rho_s v_s dv_s = -dP \qquad (336)$$

The steady state energy equation for perfect gases and solid particles in the flow is written as the balance between the net flux of power in the solid and gas states and the rate of energy exchange through heat transfer and mechanical shaft power:

$$\left[\dot{m}_g\left[C_{pg}\left(T_g+dT_g\right)+\frac{\left(v_g+dv_g\right)^2}{2}\right]+\dot{m}_s\left[C_s(T_s+dT_s)+\frac{(v_s+dv_s)^2}{2}\right]\right]-\left[\dot{m}_g\left[C_{pg}T_g+\frac{v_g^2}{2}\right]+\dot{m}_s\left[C_sT_s+\frac{v_s^2}{2}\right]\right]=\dot{Q}_w-P_s$$

(337)

The energy equation is also simplified as follows:

$$\dot{m}_g\left(C_{pg}\,dT_g+v_g dv_g\right)+\dot{m}_s(C_s\,dT_s+v_s dv_s)=0 \qquad (338)$$

The fraction of solid particles in a two-phase fluid, denoted by (X), is as follows:

$$X=\frac{\dot{m}_s}{\dot{m}_s+\dot{m}_g}=\frac{\rho_s v_s}{\rho_g v_g+\rho_s v_s} \qquad (339)$$

Given the limiting assumption we had about the stability of solid particles (frozen), we write the energy equation in the form of the mass fraction of solid particles, namely (X):

$$(1-X)\left(C_{pg}\,dT_g+v_g dv_g\right)+X(C_s\,dT_s+v_s dv_s)=0 \qquad (340)$$

By rewriting the term $\rho_s\, v_s$ in terms of mass fraction of solid particles (X) and placing it in the momentum equation obtained from equation 336 we have:

$$\rho_s v_s=\frac{X}{1-X}\rho_g v_g \qquad (341\text{-a})$$

$$v_g dv_g=-\frac{dP}{\rho_g}-\frac{X}{1-X}v_g dv_s \qquad (341\text{-b})$$

By dividing the sides of equation (340) by (1-X) and substituting equation (341-b) instead of the term $v_g\,dv_g$ in it, the momentum equation is written as follows:

$$C_{pg}\,dT_g+\frac{X}{1-X}C_s\,dT_s+\frac{X}{1-X}\left(v_s-v_g\right)dv_s=\frac{dP}{\rho_g} \qquad (342)$$

Now, considering the limiting cases that we mentioned, we will examine the rocket performance in the above equation. According to the first case, where is said gas and solid particles are in heat equilibrium, i.e., ($dT_s-dT_g=dT$), so the energy equation (342) is reduced to:

$$(C_{pg} + \frac{X}{1-X}C_s)dT + \frac{X}{1-X}\left(v_s - v_g\right)dv_s = \frac{dP}{\rho_g} \tag{343}$$

There are two scenarios for the momentum of solid particles inside the nozzle. The first scenario is when solid particles are accelerated by gaseous particles to reach a velocity equal to the velocity of the gases at the nozzle exit $\left(v_s = v_g\right)$. Thus, the above equation is simplified as follows:

$$(C_{pg} + \frac{X}{1-X}C_s)dT = \frac{dP}{\rho_g} \tag{344}$$

Assuming it is perfect gas (i.e., $\rho_g = \frac{P}{R_g T}$) and by integrating from the above Eq:

$$\frac{P_2}{P_C} = \left(\frac{T_2}{T_c}\right)^{\frac{\left(C_{pg} + \frac{X}{1-X}C_s\right)}{R}} \tag{345-a}$$

$$\frac{T_2}{T_c} = \left(\frac{P_2}{P_c}\right)^{\frac{R}{(C_{pg} + \frac{X}{1-X}C_s)}} \tag{345-b}$$

Also, equation (340) when $v_s = v_g = v$ and $T_s = T_g = T$ will be

$$[(1 - X)C_{pg} + XC_s]dT + vdv = 0 \tag{346}$$

We integrate from the equation obtained from the combustion chamber (where $v_c = 0$) to the nozzle output (v_2):

$$v_2 = \sqrt{2[(1 - X)C_{pg} + XC_s](1 - \frac{T_2}{T_c})T_c} \tag{347}$$

The nozzle exit velocity can also be expressed in terms of pressure ratio using Equation (345-b):

$$v_2 = \sqrt{2[(1 - X)C_{pg} + XC_s]T_c[1 - \left(\frac{P_2}{P_c}\right)^{\frac{R}{(C_{pg} + \frac{X}{1-X}C_s)}}]} \tag{348}$$

Since solid particles reach a velocity equal to the velocity of gases, so the specific impulse ratio, no matter the presence of gaseous particles in the flow, is the ratio of the velocity of the exhaust in these two cases, namely:

$$\frac{I_s(x)}{I_s(D)} = \sqrt{(1 - X + X\frac{C_s}{C_{pg}})[\frac{1-\left(\frac{P_2}{P_c}\right)^{\overline{\frac{R}{(C_{pg}+\frac{X}{1-X}C_s)}}}}{1-\left(\frac{P_2}{P_c}\right)^{\overline{\frac{R}{C_{pg}}}}}]} \tag{349}$$

The second scenario for acceleration of solid particles is that it is assumed that solid particles are not accelerated by gases, and therefore when their temperature is equal to the temperature of the gas then $(dv_s = 0)$. Using equation 340 in this scenario, the energy equation expresses the changes in gas velocity in terms of the mixture temperature, i.e.,

$$[(1 - X)C_{pg} + XC_s]dT + (1 - X)v_g dv_g = 0 \tag{350}$$

By integrating the above equation and solving the equation, the velocity of the nozzle exhaust gases can be obtained:

$$v_{g2} = \sqrt{2[C_{pg} + \frac{X}{1-X}C_s]T_c[1 - \left(\frac{P_2}{P_c}\right)^{\overline{\frac{R}{(C_{pg}+\frac{X}{1-X}C_s)}}}]} \tag{351}$$

The average velocity of the nozzle output current for a perfectly expanded nozzle will be obtained from the relationship between the two-phase current trusts that move the gas phase at v_{g2} and the solid phase at v_s:

$$\bar{v}_2 = \frac{F}{\dot{m}_g + \dot{m}_s} = \frac{\dot{m}_g v_{g2} + \dot{m}_s v_s}{\dot{m}_g + \dot{m}_s} = (1 - X)v_{g2} + X(v_s) \tag{352}$$

Given that we assume that solid particles will not accelerate during motion and also the small solid mass fraction, the relationship between the average velocity of the nozzle output is simplified as follows:

$$\bar{v}_2 \approx (1 - x)v_{g2} \tag{353}$$

By writing the specific impulse equation in terms of the average velocity we have:

$$I_s = \frac{F}{g_0 \dot{m}_p} = \frac{\bar{v}_2(\dot{m}g + \dot{m}_s)}{g_0(\dot{m}_g + \dot{m}_s)} = \frac{\bar{v}_2}{g_0} \approx (1 - x)\frac{v_{g2}}{g_0} \tag{354}$$

Therefore, the specific impact ratio of a stream with/without solid particles that are in thermal equilibrium together, but the solid particles are accelerated by the gas is as follows:

$$\frac{I_s(x)}{I_s(0)} = (1 - X)\sqrt{(1 + \frac{X}{1-X}\frac{C_s}{C_{pg}})[\frac{1-\left(\frac{P_2}{P_c}\right)^{\overline{\frac{R}{(C_{pg}+\frac{X}{1-X}C_s)}}}}{1-\left(\frac{P_2}{P_c}\right)^{\overline{\frac{R}{C_{pg}}}}}]} \tag{355}$$

As a result, the specific impulse ratio for the solid particles states to accelerate or not is shown in the figure below.

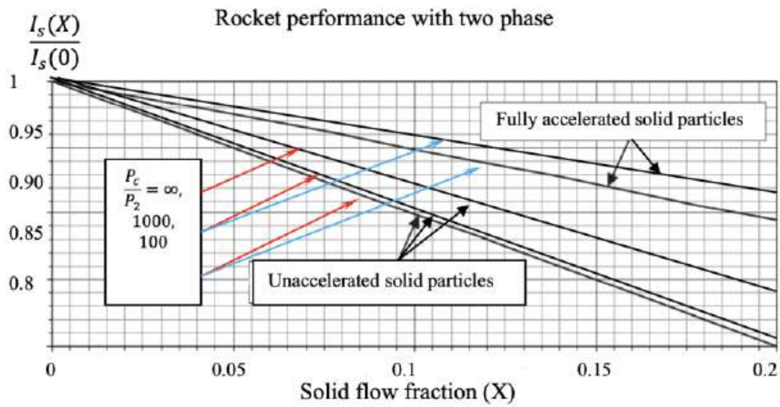

Figure 92- Variation of specific impulse with solid flow fraction in the gaseous exhaust nozzle

From this diagram, it can be concluded that as the mass fraction of solid particles increases (frozen particles increase), the rocket performance decreases and the effect of the pressure ratio is less than expected. And the specific impulse for the state that the gas particles do not accelerate decreases, and the rate of recession increases with increasing mass fraction of solid particles. In the second case, it was assumed that the solid particles were not in thermal equilibrium, that is because there was no heat transfer between the solid particles and the gas, the temperature of the solid particles remained constant ($dT_s = 0$).Therefore, the energy equation for this case will be equal to:

$$C_{pg}\, dT_g + \frac{X}{1-X}(v_s - v_g)dv_s = \frac{dP}{\rho_g} \tag{356}$$

According to the above conditions, for both scenarios where the solid particles accelerate and reach the gas velocity $(v_s = v_g)$ and the case where they do not accelerate $(dv_s = 0)$, the temperature-pressure relation will be gained by the solving of the above equation.

$$\frac{T_2}{T_1} = \left(\frac{P_2}{P_1}\right)^{\frac{c_{pg}}{R_g}} \tag{357}$$

The energy equation (Equation 340), assuming that the particles are accelerating and reach the gases' velocity, is equal to:

$$(1-X)C_{pg}\,dT_g + v_g\,dv_g = 0 \tag{358}$$

By solving the above equation, the exit velocity will be obtained:

$$v_{g2} = \sqrt{2(1-X)c_{pg}T_c[1-\left(\frac{P_2}{P_1}\right)^{\frac{c_{pg}}{R_g}}]} \tag{359}$$

Therefore, the specific impact ratio is

$$\frac{I_s(x)}{I_s(0)} = \sqrt{1-X} \tag{360}$$

For the case where solid particles do not accelerate $(dv_s = 0)$, Equation (340) is written as

$$C_{pg}\,dT_g + v_g\,dv_g = 0 \tag{361}$$

Which by solving it

$$v_{g2} = \sqrt{2c_{pg}T_c[1-\left(\frac{P_2}{P_1}\right)^{\frac{c_{pg}}{R_g}}]} \tag{362}$$

As can be seen from the above equation, the velocity of the exit gases is not affected by the solid particles. By writing the trust equation at the average velocity of nozzle exit, the effect of the solid particles present in the thrust term will be demonstrated:

$$\bar{v}_2 = \frac{\dot{m}_g v_{g2} + \dot{m}_s v_s}{\dot{m}_g + \dot{m}_s} = (1-X)\,v_{g2} + Xv_s \tag{363}$$

Similar to the previous case, due to the fact that the velocity of solid particles (v_s) is negligible, the specific impulses ratio will be

$$\frac{I_s(x)}{I_s(0)} = \frac{\bar{v}_2(\dot{m}_g + \dot{m}_s)}{\dot{m}_P} = \bar{v}_2 \approx 1-X \tag{364}$$

The changes in specific impulse ratio in terms of mass fraction of solid particles for this case is shown in the figure below, which indicates that, unlike the previous case, when the gas particles are not in thermal equilibrium with the gases, the specific impulse ratio has no dependence on pressure. For the case where solid particles do not accelerate, the specific impulse ratio decreases more than when they accelerate. This is because accelerated particles have a high momentum that will participate in the thrust equation, while for non-accelerating particles the output momentum is very small. These cases which are discussed so far, examines only a range of effects of multiphase flow on the rocket performance, and as mentioned at the beginning of this section, the presence of multiphase flow within the fluid cause complex relations and equations in heat transfer and fluid dynamics approaches, which requires simulation and computational approach solutions.

FLOW EXPANSION IN ROCKET NOZZLE

The reaction of combustion products continues after entering the nozzle and is not limited to the combustion process, in fact, the conversion of thermal energy into kinetic in the nozzle causes the temperature to drop as a result of the pressure drop which affects the reaction rate of combustion products. Therefore, chemical reactions from the combustion chamber to the nozzle are constantly occurring. Sometimes the nozzle reverses some reactions performed in the combustion chamber. For example, the separation operation that results from the high temperature of the combustion chamber inside the nozzle leads to a recombination process due to a drop in temperature. In addition, to simplify problems, the reactions of chemical compounds are often considered in equilibrium, the use of which can be questioned. Because chemical equilibrium depends on the chemical kinetics and reaction rate in the mixture, and also because the process of expansion inside the rocket occurs in a very short period of time (milliseconds) due to the very high rate of reaction and convection. Such environments are questionable. Of course, there are computational approaches to complex chemical reactions that provide a detailed analysis of mixed chemical reactions in different thermal environments. In preliminary analyzes and rocket design calculations often use solids (condensed gases) (known as frozen chemical models). According to the computational results (Sutton and Biblarz, 2001 or Olson, 1962) shown in the figure below, the corrected specific impulse for both oxygen-hydrogen and oxygen-jp4 increases due to chemical reactions in the nozzle. Also, the corrected results of Olson, 1962 experimental data show that the equilibrium state overestimates actual performance, which means the conservative estimation of rocket.

THRUST VECTORING NOZZLE

The conventional gimbals of the entire rocket thrust chamber are swiveled by using hydraulic or electromechanical actuators with a range of control authority of approximately $\pm$ 7°. Injection of inert gases and propellant into the nozzle, called secondary injection, causes oblique shock and requires a secondary injection thrust vector controller (SITVC) system with the controller authority range of 5 °. The use of cluster motors is also a success that can be used, especially in rocket vehicles. Jet deflectors can be used as jet vans or jet tabs in rocket burn time due to very hot exhaust gases for a short time. The operating range of the vans is approximately ± 10 °. Linear-aerospike, which consists of many engine cells (up to 20), compared to the use of bell nozzle, has a higher thrust and off-design performance and has better thrust vectoring. The following figure shows the variation of thrust coefficient in terms of nozzle pressure ratio for aerospike, which indicates in the same pressure ratio, the linear aerospike has a higher nozzle thrust coefficient compare to the bell nozzle and also has more agreement with the ideal nozzle.

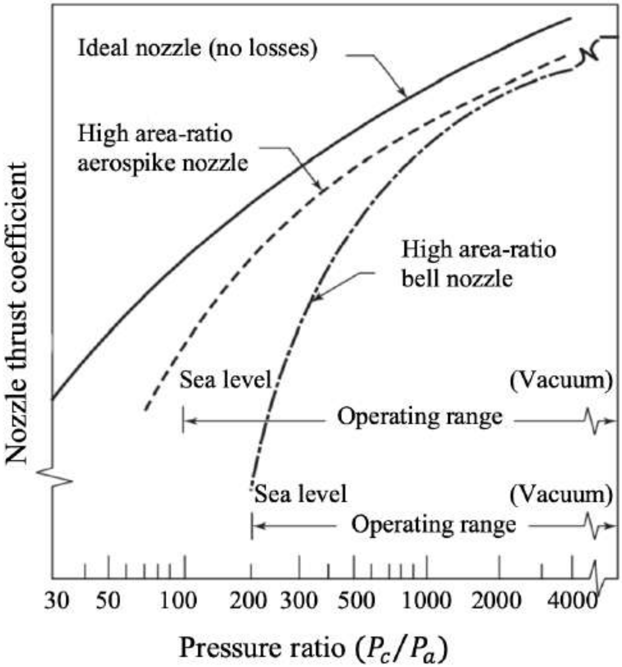

Figure 93-variation of Nozzle thrust coefficient with pressure ratio. from AIRCRADT PROPULSION 2009

BELL NOZZLES

The supersonic area of a bell nozzle can be designed through many computer programs (e.g., ref14). These geometries are a mathematical method based on maximizing the computational variations described in Sources 6, 15, and 16. Although the mathematical solutions are performed accurately, the initial conditions obtained from the transonic solution and the properties of the gas are approximate. However, the nozzle geometry is not sensitive to these parameters. Existing computer programs made it possible to select the most optimal nozzle expansion geometry at the lowest possible cost. As mentioned in the previous sections, the properties of equilibrium gases are used to perform the most optimal wall state calculations. However, programs for non-equilibrium gas compounds are also obtained in Reference 17, although their application in rocket nozzle design is unclear. In choosing the length of the nozzle and its expansion ratio, the effect of the viscous reaction caused by the expansion of the gases on the performance of the nozzle should be considered. The results show that the boundary layer analysis methods are strongly dependent on the coefficients of friction and heat transfer obtained from the experimental method. The functional losses due to viscous drag in the bell nozzle are shown in the figure below.

Nozzle viscosity losses will be obtained by solving the momentum integral equations and the energy equation. This loss rate is expressed as a percentage of the nozzle trust and plotted against a parameter that is approximately proportional to the Reynolds number. To more accurately predict the performance of the nozzle, the displacement thickness of the boundary layer is calculated, and in the case where the boundary layer is often thicker than the size of the nozzle, the wall is going point-to-point to outward as much as the displacement thickness of the boundary layer (i.e., the nozzle section size gets bigger). High combustion temperature propellant compounds (fluorine/hydrogen) in some materials caused a 5 to 10% drop in nozzle performance. To prevent that the wall downstream of the throat is designed to keep the rate of expansion slow enough to keep the compounds in balance near the equilibrium. For the area ratio of 2 to 5, a technique for direct performance improvement for non-equilibrium gas reactions is given in Reference 17 but is very complex and is not commonly used. The method used for high-energy propellants is to select downstream geometry, which expands much more slowly than the minimum radius configuration. Then at a certain specific point, the controlled expansion wall is terminated, and the rest of the nozzle wall is design by the equilibrium method. The resulting configuration has a greater downward curvature of the throat than is required for expanded gas at equilibrium. The advantages and disadvantages of this method are that the kinetic performance of this method is high, but it has low aerodynamic performance because less given length from the throat to the nozzle is used for optimum aerodynamic contour. By selecting a number of controlled expansion walls and termination points, the final design will be based on both kinetic and aerodynamic performance, which is caused the final product composition in the flow at the end of the controlled section to be constant (freezes). According to the experimental programs, this nozzle has produced high performance and is near optimum performance for the actual flow.

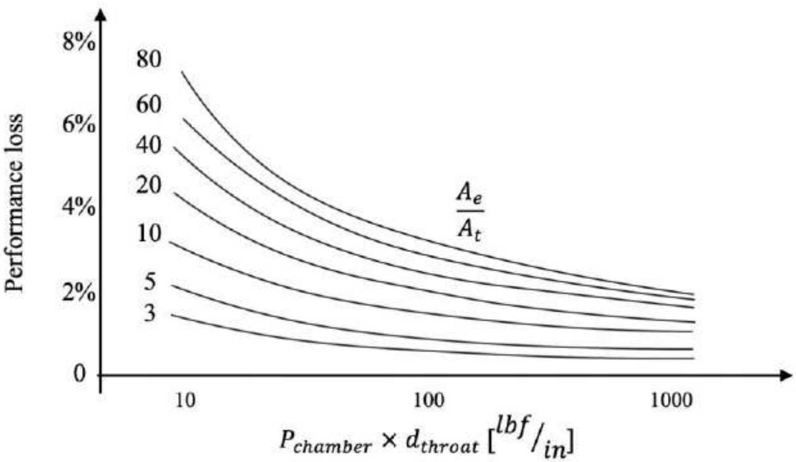

Figure 94- Computed performance loss due to viscous-drag effects in bell nozzles (storable propellants). From SP8120

NON-OPTIMUM CONTOUR

Existing optimization methods are often based on just a general approximation of the actual conditions, bell nozzle contours that are obtained based on approximate mathematical methods and optimal design, and change only slightly with the properties of the gases. For a given ratio of area and length, a canted parabola approximates a very close approximation of the optimal contours of the various chamber conditions present in the rocket engine. For engineering purposes, the use of near-optimum parabolic contour is almost suitable and applicable in many operations without the need for a computer. The figure below shows a canted parabolic contour, in which the initial and final angles of the wall for a range of area and length ratios are specified.
Mathematically optimized nozzles cannot be used in any situation. In fact, the design of these nozzles for values less than a certain length will fail, and this minimum length increases with increasing area ratio. The following figure compares the local angle variation of flow with the local Mach number, (over which the mathematical-optimum design method of (ref 16) will produce an acceptable design).
Another method is used in the design of nozzles, which has the same effect as the ideal nozzle design method, although these types of nozzles are

sometimes known as optimal nozzles. These nozzles are such that an ideal nozzle with a cross-sectional area ratio greater than the required is used, so that if we truncate it to reach the required cross-sectional area ratio, then the correct nozzle length will be obtained (ref 14), which is called high performance nozzle. The advantage of these nozzle (truncated-ideal nozzle) over optimal mathematical nozzles is that they can be used in the shortest desired length. As mentioned, conical nozzles are used when performance and length are not critical and minimum fabrication time and cost are desirable (from NASA Confidential). In a small area ratio, conical nozzles have a small performance drop. The effect of area ratio on divergence performance at different wall angles is shown in the figure below, which indicates that with increasing area ratio, oscillation in nozzle performance increase with the small wall half-angle of the wall.

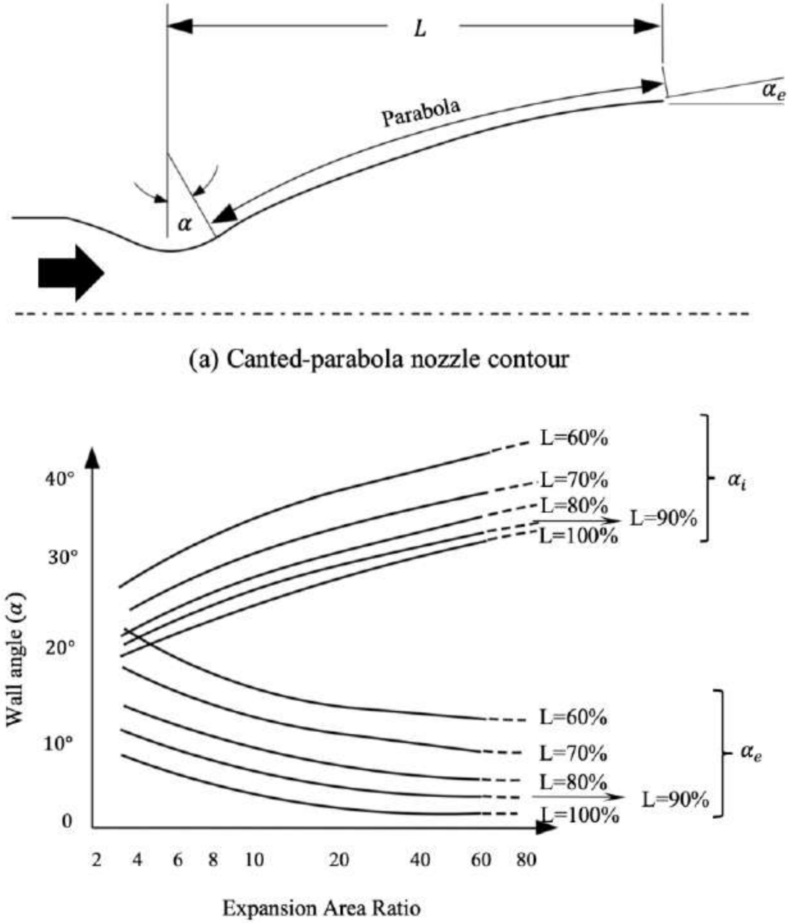

(a) Canted-parabola nozzle contour

(b) Wall angles for parabolic contour as a function of expansion area ratio and nozzle length

Figure 95- Canted-parabola contour as an approximation of optimum bell contour. From SP8120

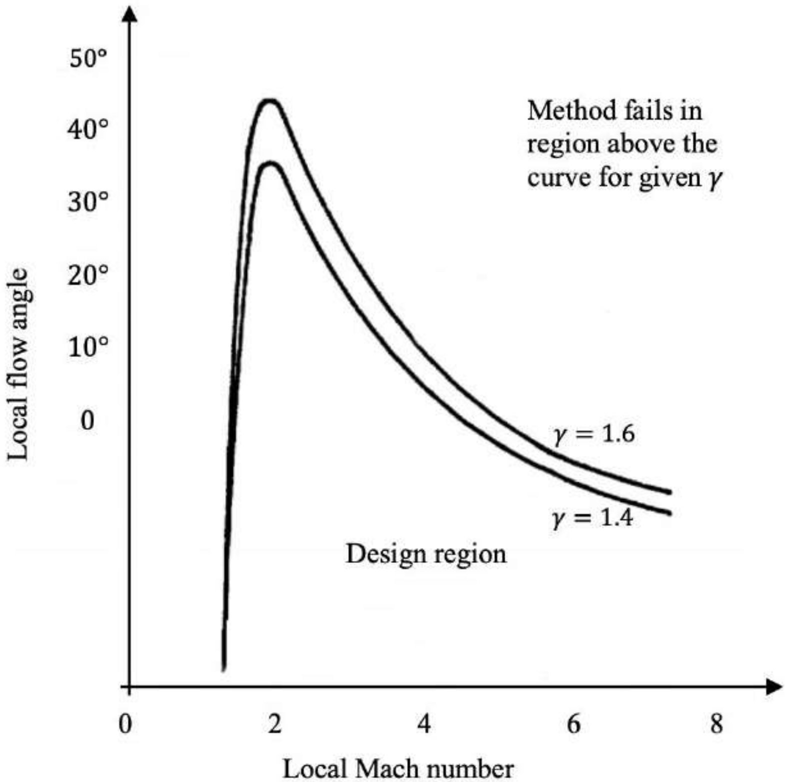

Figure 96-Graphic display of region over which the mathematical-optimum method for contour design can be used. From SP 8120

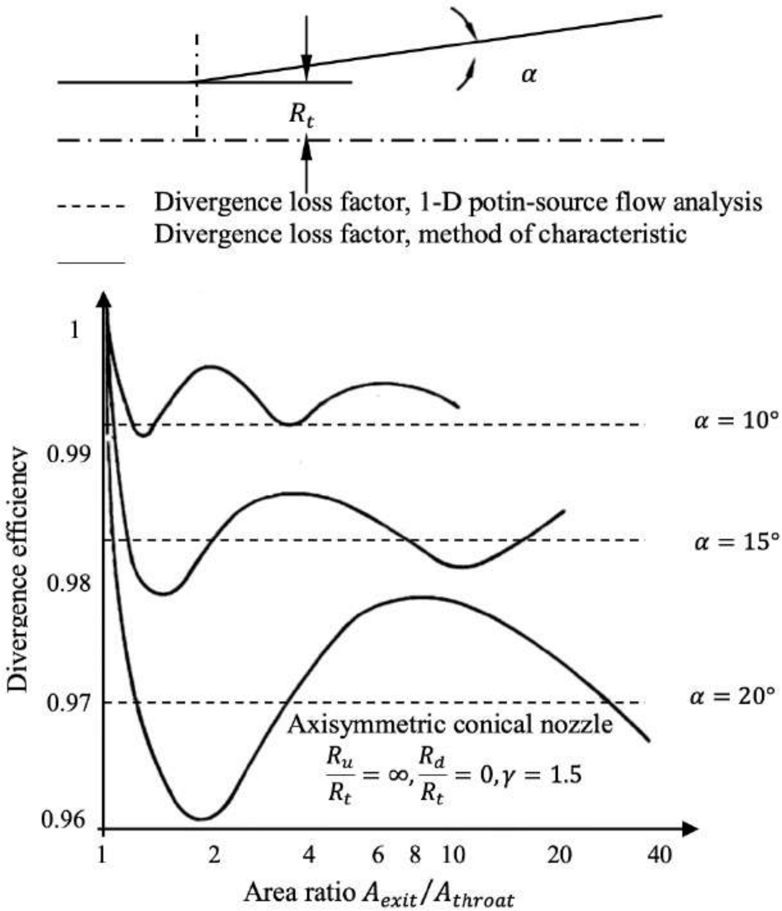

Figure 97-Variation of theoretical nozzle divergence efficiency with area ratio and divergence half-angle. From SP 8120

OVER-EXPANDED NOZZLE

The nozzles are designed to have a large area expansion ratio in a vacuum to achieve a high specific impulse. Engines are ground tested for optimization and development. During this ground test, altitude engines are over-expanded, often to the point where the exhaust gas separates from the nozzle wall. This flow separation causes serious problems. For example, a non-optimal parabolic contour was selected for the J-2 nozzle in order to increase the exit wall pressure, the high-exit-pressure nozzle was supposed to run

unseparated at an area ratio of 27 with a chamber pressure of 700 psi, (from NASA Confidential). The minimum wall pressure produced at the expansion ratio of 14 at the nozzle outlet created unstable flow conditions that led to unstable asymmetric separation, especially during start-up. The result of these instabilities was the large forces acting on the thrust chamber, which led to the failure of various parts of it. All this while the test stand was attached to the nozzle skirt to absorb the separation loads during start-up.
Separation of gas flow within the boundary layer occurs when it cannot reach ambient pressure. The exact atmospheric pressure at which the flow separates from the nozzle wall cannot be accurately predicted. Various rules have been proposed to distinguish separation, but no agreement has been reached between them, but according to a basic law, there is a separation line when the ratio of exit pressure to ambient pressure is 0.4. Subsequent methods are based on fitting experimental data to calculate the over-expansion obtained by increasing the Mach number. A fit of experimental data for short contoured nozzles over a broad range of nozzle area ratios (ref. 24) indicates that separation will occur when, (from NASA Confidential):

$$\frac{P_{wall}}{P_{amb}} = 0.583\left(\frac{P_{amb}}{P_c}\right)^{0.195} \tag{365}$$

NOZZLE EXTENSIONS

Two types of extensions are used in rocket nozzles. In the first type, which has a wider application, the nozzle contour is selected from the throat to the nozzle outlet in such a way that it has maximum design performance. The purpose of the extension is to divide the nozzle into two parts between the throat and the exit. This breaking is at the point where the cooling method of the wall also changes (19770009165). For example, from the throat to the point of separation, where the temperature is very high, the regenerative cooling method is used, and from the breaking point, a passive cooling method (such as radiation) is used. The use of these extensions is also used in cases with the aim of minimizing weight and reducing costs, as well as reducing the total heat input to the active coolant. Of course, it should be noted that in this method, different methods are available to build the combustion chamber and nozzles. The second type of extension is used to increase the altitude performance so that this happens without changing the nozzle used in the engine and only by increasing the ratio of the expansion area. For area ratios larger than 15, straight-wall extensions produce nearly the same performance as optimized contoured extensions (19770009165).

SMALL NOZZLE

The use of analytical methods used in nozzles with conventional sizes (conventional, normal) when the rocket size is reduced, due to the increasing importance of the effects of viscous flow (viscous flow) have low accuracy, so the use of these nozzles in There are situations where the relatively large effects of viscosity affect performance, for example, these nozzles are used to control the height and rotation of satellites. For nozzle analysis, it is very important to pay attention to the Reynolds number because for nozzles with Reynolds less than 500, the slip velocity profile and temperature jump as well as the curvature of the boundary layer affect the nozzle analysis. In fact, for nozzles with a low Reynolds number, the throat boundary layer increases, and the discharge coefficient decreases as the radius ratio increases. Figure (99) shows the discharge coefficient changes, which here are the ratio of the actual mass flow to the one-dimensional non-viscous mass flow in the nozzle in terms of the Reynolds number in the ratio of different radii. In Reynolds less than 100, it is not possible to use boundary layer analysis methods for non-viscous flow because the thickness of the boundary layer produced in the throat is larger than its radius. It is also important to note that flow calculations are performed in a manner that includes the effects of viscosity on the generation of the flow field.

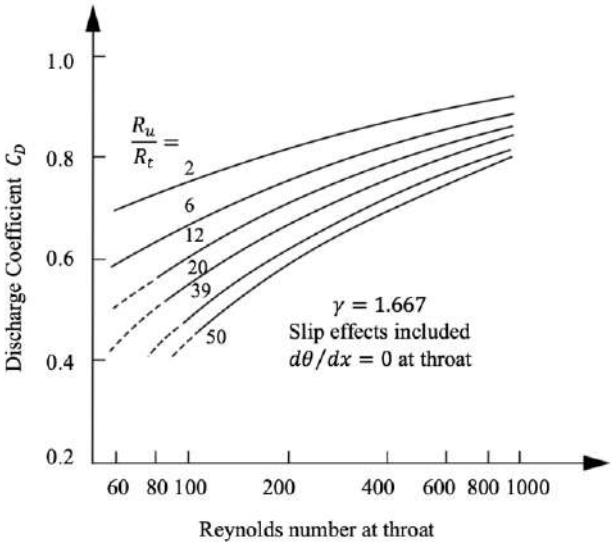

Figure 98- Nozzle discharge coefficient as a function of Reynolds number at throat for various values of Ru/R t. from SP8120

PLUG NOZZLE

The basis of such a nozzle is attaining thrust from a free or unconfined expanding supersonic jet flow, which was mooted in the mid-1940s. External expansion nozzle or plug nozzle is based on the 1908 Prandtl-Meyer corner expansion fan theory. Figure 100 demonstrates an unconfined expanding supersonic jet stream in a corner to a lower pressure environment. This expansion in the corner will continue until the stagnation pressure of the supersonic stream reaches the stagnation pressure of the environment (Fig. 100-b). By tilting the primary flow axis, the exhaust gases expand to a perfectly axial supersonic stream, resulting in maximum velocity and thrust. One of the unique features of the plug nozzle is the expansion process control method. If designed properly, the external flow field streamline is essentially an axial profile that is controlled by Prandtl-Meyer characteristics and ambient pressure. This axial flow is the result of tilting the internal expansion control modules inward at the proper angle. The Prandtl-Meyer expansion waves that remain at the internal expansion output expand and continue in the axial direction by tilting these modules and under the control of the plug contour, which is designed by the conventional method of characteristic for producing free shock expansion. Therefore, unlike bell nozzles where the expansion control is on the outside of the flow field, in plug nozzles, it is done on the inside of the flow field. It should be noted that due to the fully developed gases, the expansion surface will have nothing to do with the environment surrounding, thereby increasing the freedom of action in the design of the plug. Among the measures taken in the design of these nozzles is the shortening of the nozzle sequence (known as truncating the plug), as a result of which the captured gases in the base zone are pressurized by internal recirculated gases. Experience has shown that shortening the nozzle to 20% of its isentropic length is associated with minimal performance loss. As mentioned earlier, in bell or conical nozzles, designers consider the nozzle length to be larger to increase the area ratio, while in plug nozzles this is done in reverse, namely, in small nozzle lengths, one can also have a large area expansion ratio. Eventually, this shortening of plug nozzles will solve many integration problems produced by bell nozzles such as long interstage structures, long loading legs, large flimsy nozzle extensions, high evaluation platforms to unload the stage on the lunar surface.

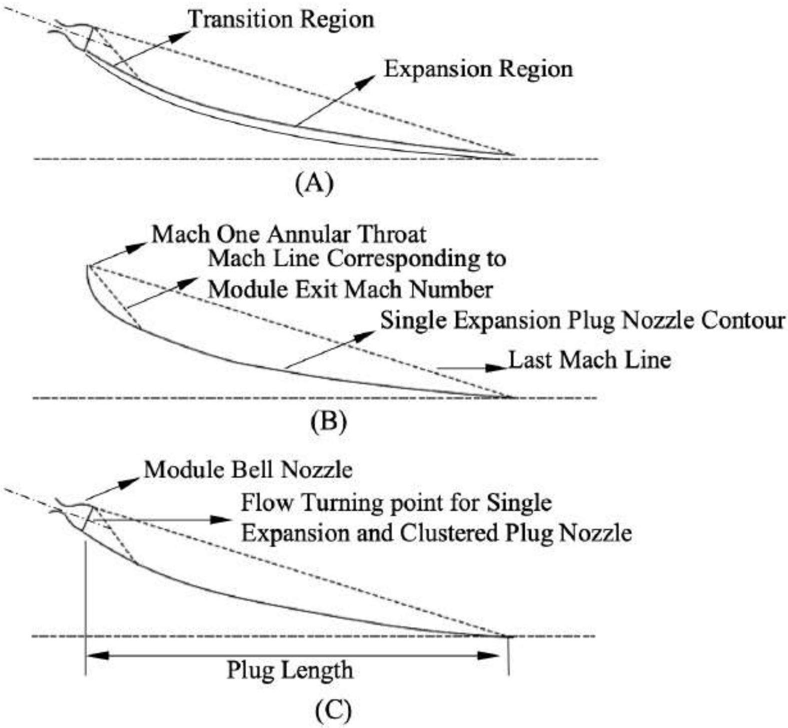

Figure 99- Internal and External Expansion Process for Plug Nozzle.

The two main applications of plug nozzles are the use in the first stage where the effective area expansion ratio increases as the vehicle move up due to the external expansion (known as altitude compensation) and also its use in spacecraft due to the small drop in the performance of truncated plug nozzles in a vacuum. In general, the goals of optimal design include high reliability, high performance in a minimum volume, and a propulsion system that can be confidently developed on schedule and within cost restraints. High reliability in a propulsion system means that components are lesser presumably to fail, and if an individual component fails, the system will still continue to perform. Failure due to heavy loads is one of these factors. These loads may be chamber pressure, chamber heat transfer rate, pump pressure, and turbomachine speed. However, most of these failures are traceable due to design features at high loads. By reducing the chamber pressure as a key parameter, these destructive loads could be minimized. These motors might also be used in clusters, whereas they cover the entire diameter of the vehicle, thus leading to less chamber pressure. Figure 101 shows an example of a plugin cluster configuration. The design configuration is in such a way that the exhaust gases from the thrust modules, which are in the form of axisymmetric bell nozzles, touch the plug contour. These modules cover the contour of the plug, in such a way that they are staying in touch with each other in almost a circular geometry; So that the flow of expanded gases is directed almost annularly on the plug contoured surface at a correct angle. These modules' exit touch is essential to maximize performance. The performance of the nozzle is determined by its overall area ratio, whereas the ratio of the internal or modular area ratio, contour, and length, which controls the flow field, is not important except for determining the weight of the module nozzle surface. Figure 102 determines a module configuration in terms of total thrust, area ratio, and maximum vehicle diameter. For the cluster design, the overall area ratio could be obtained:

$$E = \frac{A_{D\,v}}{N\,A_t} \tag{366}$$

E: the overall vehicle area ratio.
$A_{D\,v}$: the area of the vehicle nozzle section (diameter D) that modules are installed.
A_t: module throat area.
N: number of modules.
The total thrust is determined in terms of chamber pressure (P_C) and nozzle thrust coefficient(C_f), which is a function of overall area ratio(E) and the isentropic expansion factor (γ) for an ideal gas, are as follows:

$$F = N \times P_C \times A_t \times C_f \tag{367}$$

Given the design parameters, the chamber pressure is:

$$P_C = \frac{1}{N} \times \frac{1}{A_t} \times \frac{F}{\eta_{Cf}} \times \frac{1}{C_f = f(\frac{P_C}{P_x}, \frac{A_{D\,v}}{A_t}, \frac{1}{N})} \tag{368}$$

Where, $\frac{P_C}{P_x}$ is the nozzle pressure ratio.

Figures 96 show how the chamber pressure will decrease as the number of modules increases. For instances, if the throat diameter is arbitrarily considered to be 2.5 inches, a logical design with 16 modules at a pressure of 510 psi could be utilized, which is a very desirable value. Also, this system is capable of producing a specific impulse of $480s$. The diagrams dictate that in a very large number of modules, the minimum chamber pressure will be uniform. Experience has also shown that pressures less than 300 psi are obtained for vehicles with a diameter greater than 32 ft.

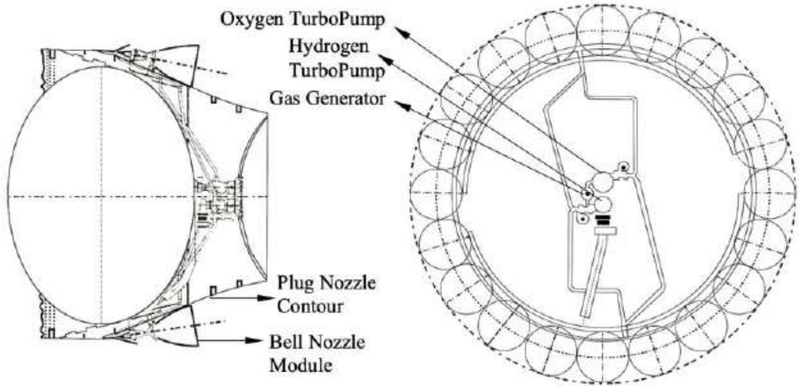

Figure 100- Plug Nozzle Clustered Configuration

These nozzles, unlike other nozzles, offer altitude compensation up to a good area ratio, theoretically. Various design approaches include plug nozzles with annular and throat enclosures (with and without truncation) and plug nozzles with a set of circular bell nozzles or quasi-rectangular nozzles. The second approach is more practical because of the minimal losses between individual modules and the flow field interactions downstream of the module exit. However, compared to the two geometries of the bell and quasi-rectangular nozzles, the rectangular cross-section has a smaller performance drop than the circular cross-section. Besides these advantages, plug nozzle design has inherent disadvantages; the main drawbacks of this design are as Inability to control combustion instability in the annular combustion chamber, cooling of the annular throat with small throat slits and slit control, constant of the throat during fabrication, and thermal expansion leading to lateral loads and thrust vector deflections.

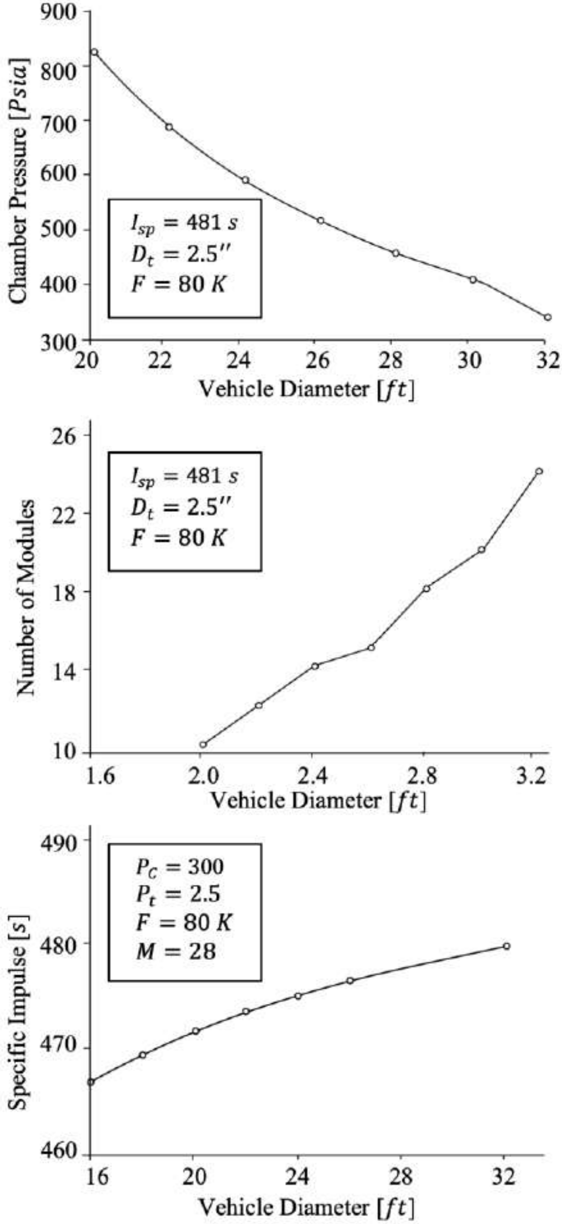

Figure 101 - Modules Configuration in Terms of Chamber Pressure, Number of Modules, and Specific Impulse With Respect To The Vehicle Diameter.

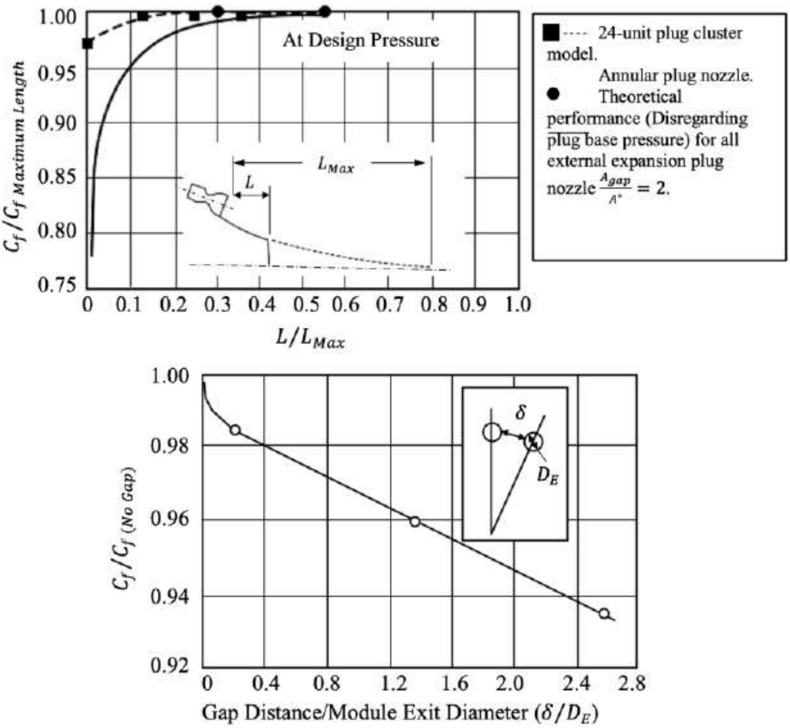

Figure 102-Thrust Coefficient Variation with Plug Length and The Gap Distance

The following figure shows the nozzle phenomena of the plug with respect to the different pressure ratios so that when the pressure is less than its design value, the flow expands near the surface of the plug contour without detachment, which is introducing a set of shock waves and expansion fans, that eventually reduce the pressure to the amount of ambient pressure. The shear layer grows downstream of the throat as a result of the interactions of these compressive and expansion waves along the nozzle contour.

In the design pressure ratio, a hypothetical straight line is considered as the characteristic line that has a fixed Mach number starting from the center of the plug body to the tip; and the shear layer continues parallel to the centerline. Although methods have been proposed in various references to design these contours in this case, it should be noted that Prandtl-Meyer relationships are only valid for planar flows and there is also a homogeneous flow in the throat that affects the output flow profile, while these are not considered in most designs.

At pressures higher than the design pressure, the pressure distribution remains constant, and the plug nozzle will act like conventional nozzles.

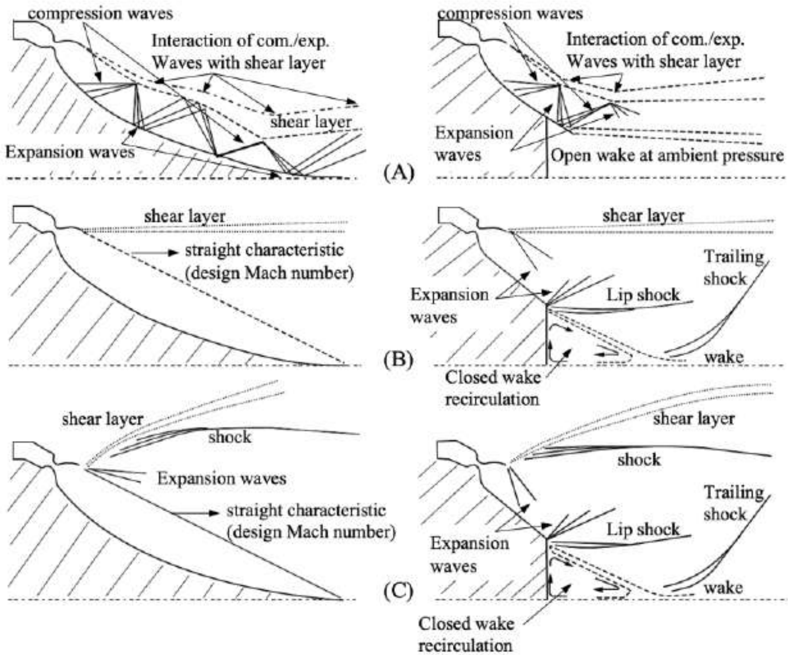

Figure 103- Plug Nozzle Phenomena at different Pressure Ratios, from Advanced Rocket Nozzles

These phenomena related to the different pressure ratios will be explained more in the annular nozzle section.

Different nozzle operation, and different flow will occur after truncating the nozzle end, as both the length and weight of the structure are reduced. The small pressure ratios are associated with open wake formation and pressure drop to ambient pressure. At a pressure ratio close to the full-height nozzle design pressure, the base flow profile changes abruptly so that it is no longer affected by ambient pressure. Calculations have shown that shorter plug bodies with longer truncation cause faster flow wake deformation at a lower pressure ratio than the design pressure. In the transition zone, the pressure in the wake changes to less than the ambient pressure, causing a negative thrust in the base region. Beyond the transition zone, the pressure inside a closed wake remains constant while the pressure in the base zone exceeds the ambient pressure, and eventually, a positive thrust is generated.

EXPANSION-DEFLECTION NOZZLE

These nozzles were once thought to be able to altitude compensation like plug nozzles because the expansion of the gas occurs at a free constant pressure boundary, and as a result, the expansion process is controlled by ambient pressure and consequently height. Whereas, unlike plug nozzles, in E-D nozzles the expansion process is controlled from inside the nozzle. At low altitudes, high ambient pressures limit gas expansion, resulting in a low effective area ratio, hence the exhaust gas is adapted to the environment by recompression systems and expansion waves. At high altitudes, low ambient pressure leads to more expansion of the gases inside the nozzle and, consequently, to the higher effective expansion area ratio. However, it should be noted that in E-D nozzles, the pressure in the wake caused by the central plug due to aspiration is always less than the ambient pressure. This occurs at low pressure ratios when wake is open and leads to loss of aspiration. Furthermore, as the flow of exhaust gases expands to the base pressure (pressure greater than ambient pressure), the downstream exhaust gases expand too much, leading to over-expansion losses. As the pressure ratio increases, the closed wake zone is formed so that it is completely isolated from the environment. In the transition zone, from open wake to closed wake, the manner is quite similar to plug nozzles, where at the closed wake again the base pressure becomes independent of ambient pressure. Experimental and laboratory studies have shown that the ability to altitude compensation in E-D nozzles is weaker than plug nozzles due to aspiration losses and excessive expansion. Also, E-D nozzles perform better than conventional bell nozzles due to higher divergence and lower profile losses. In addition to these advantages of E-D nozzles, it should be noted that the heat flux in the throat of the E-D nozzles (such as toroidal plug nozzle) is higher than the bell type; However, by using the clustering concept, this defect is partially eliminated. Also, a smaller motor housing without moving parts is another benefit of these nozzles.

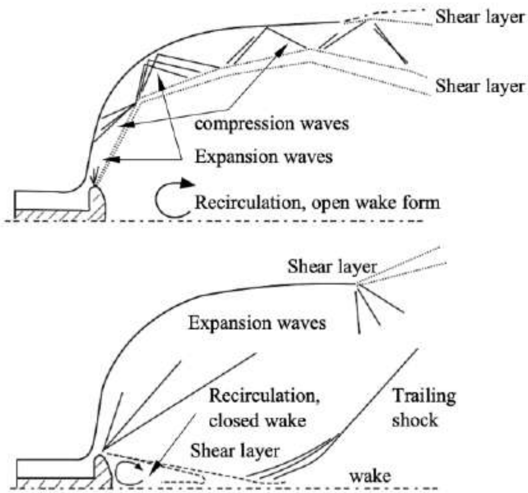

Figure 104- Expansion-Deflection nozzle phenomena at different pressure ratios

NOZZLE EXPANSION AREA RATIO

Atmospheric systems, such as boosters operating at or near sea conditions, have only one optimal nozzle surface expansion ratio at that altitude at those ambient pressure, while all parameters are to be constant at a given chamber pressure. Since the ambient pressure is not constant, the designer must know the rocket trajectory or the height of the rocket at any time to obtain the first optimal expansion area ratio of the nozzle to achieve the best result in the whole path. It should be noted that factors such as weight, size, ease of construction, and cooling are effective to achieve the desired amount of surface expansion.

CONICAL NOZZLE

These nozzles have a simpler geometry, so they do not need to redesign the nozzle contour with large changes to change the area expansion ratio, so they have been more satisfied. These nozzles configurations are shown in the figure (106). According to the figure, the throat section of the nozzle consists of a circular contour with radius R, the value of which can be 0.5 to 1.5 times the throat radius (R_t). This nozzle consists of two angles in the convergent and divergent parts, the size of which is approximately between 45 ° to 20 ° and 18 ° to 12 °, respectively. The nozzle length, which is the length of the throat to the outlet of the nozzle, is:

$$L = \frac{R_t}{\tan\alpha}\left(\sqrt{\varepsilon} - 1 + \frac{R_1}{R_t}\left(\frac{1}{\cos\alpha} - 1\right)\right) \quad (369)$$

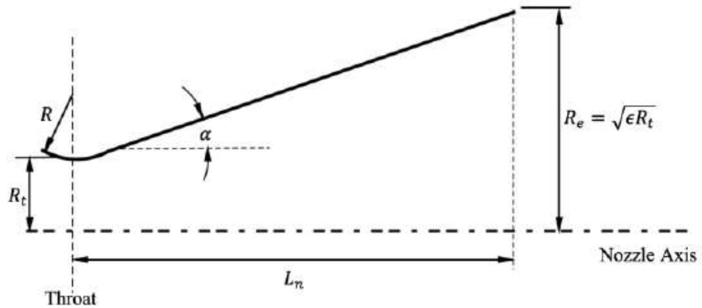

Figure 105- Conical nozzle contour. From Design of Liquid Propellant Rocket Engines

From the above equation (Eq. 369), it can be seen that by increasing the α half-angle α, the $(\frac{L}{R_t})$ fraction will decrease, which will result in a decrease in trust. The following diagram in figure 107 shows the relevance between $(\frac{L}{R_t})$ and the α (λ) half-angle. One of the disadvantages of these nozzles is the decrease in their efficiency, which is due to the non-axiality of the velocity component in the nozzle output. Therefore, a correction factor (λ) is used to calculate the momentum of the exhaust gases. This correction factor is defined as the momentum ratio of the gas output in a conical nozzle to an ideal nozzle with axial exhaust gas flows. Using this correction factor, the thrust relationship will be rewritten as follows:

$$F = \lambda \dot{m} u_e + (p_e - p_A)A_e \quad (370\text{-a})$$

$$\lambda = \frac{1-\cos\alpha}{2}, \text{(For spherical expansion)} \quad (370\text{-b})$$

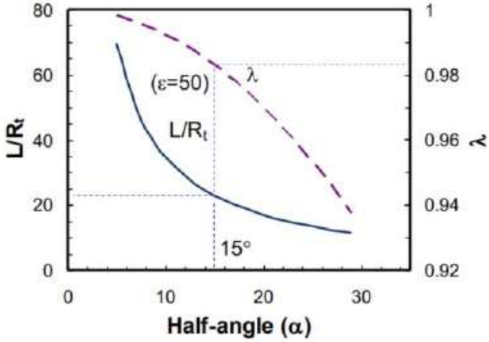

Figure 106- The Effect of The Coefficient Factor on Efficiency for Certain $\frac{L}{R_t}$ and Half-angle.

According to the above diagram, it can be seen that the most ideal state of a conical nozzle with the highest value $\lambda = 0 \cdot 983$ occurs at a half-angle of the convergence angle of 15° with an expansion ratio of 50 , whereas without considering the correction factor at the same angle of 15°, the $(\frac{L}{R_t})$ value will reduce by about 65%. According to the definition of correction factor λ, at a convergence angle of 15 °, the gas outlet velocity from the nozzle reaches 98.3% of the gas exit velocity from the nozzle, which is calculated from Formula 36 for the ideal nozzle. It should also be noted that in a vacuum environment where friction losses and flow losses are very small, the nozzle vacuum thrust coefficient is directly related to the generated thrust or the velocity of the nozzle exhaust gases. As a result, the theoretical vacuum thrust coefficient in a conical nozzle with a half-angle of 15 ° will be 98.3% of the ideal nozzle thrust coefficient obtained by Equation 55.

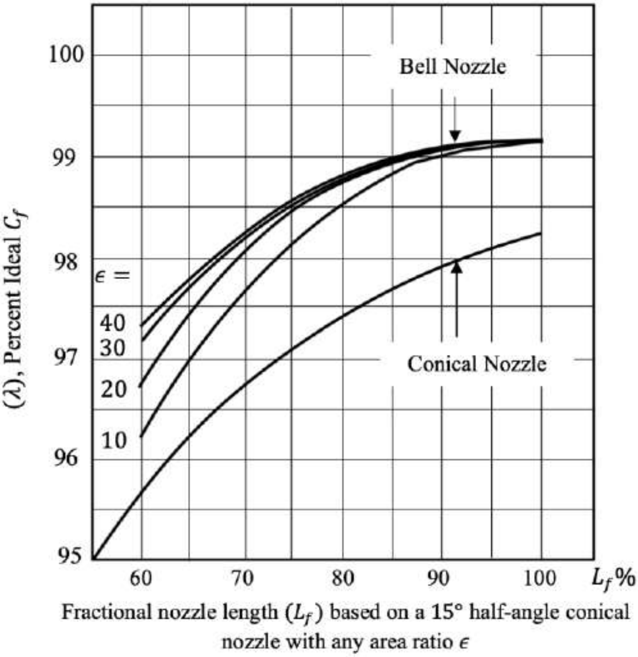

Figure 107- Thrust efficiency versus bell nozzle length. (Shown for comparison: effect of shortening conical nozzle, increasing half-angle. From Design of Liquid Propellant Rocket Engines.

METHOD OF CHARACTERISTICS

As we saw in Figure 108, in conical nozzles, the increase in efficiency is accompanied by an increase in length, and these nozzles have low efficiency due to the axial flow in the nozzle exit, so consider another geometry as the nozzle, which is the bell nozzle. In these nozzles, the length is shorter and the efficiency is higher. Bell nozzles are designed so that expansion will occur faster and radial flows at the beginning of the divergent section of the nozzle will cause the nozzle exit flow to be uniform and axial and also, another advantage of these nozzles is their wall contour, which prevents oblique shocks due to their gradual change. The geometry of this nozzle can be divided into three general parts so that the first part is just before the throat and the second and third parts include the divergent part of the nozzle. The contour geometry of this nozzle can be seen in the figure below.

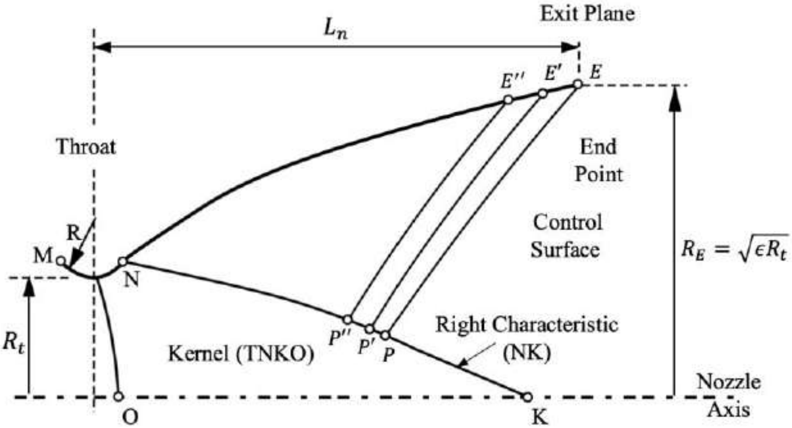

Figure 108- Bell nozzle contour. from Design of Liquid Propellant Rocket Engines

The first section is a circular arc with radius (R_1) that is selected for the upstream contour of the throat (TM). The second section (TN) is the part where the initial expansion occurs and according to the figure, it can be seen that it has a smaller radius (R_2) than the previous section. The third part (NE), which is the basis for choosing these nozzles instead of conical nozzles, causes the flow to be axial. Since the Mach number in the throat is 1, as a result of this operation, the Mach line (TO) is formed. Depending on the fluid conditions on the Mach line (TO) and the solid boundary (TN), an area of the nozzle containing ultrasonic fluid $(TNKO)$ will be formed, the contour of which will be determined entirely by the throat conditions. Specific design characteristics are used to define the line (NK) in the area. To find the point N, we first consider the point (E) at the end of the nozzle (end of the NE contour), which is determined using the ratio of the nozzle surface expansion and the nozzle length (distance between the throat and the nozzle outlet). Define the control surface of (PE) so that the point P is on the line NK so that the mass flow rate through PE is equal to the mass flow rate through NP and the maximum amount of thrust is generated in the nozzle. With such conditions, we can find the points P', P'', ..., which have the same conditions during their control surface, i.e., $(P'E', P''E'', \dots)$ As a result, contours can be designed from this data using a computer. To design bell nozzles, the base design of a conical nozzle with a half-angle of 15° is used. Nozzle length (distance from throat section to nozzle exit plane) which is previously expressed as a percentage, meaning that for example, the length of an 80% bell nozzle is equal to 0.8 of the length of a conical nozzle with a half-angle of 15°, with same expansion ratio and throat cross-section area. The following figure shows the thrust performance compared to the nozzle length fraction for both conical and bell nozzles. As shown in the figure 108, for length fractions greater than about 80 °, the effect of length fractions on thrust performance is negligible.

CHARACTERISTIC METHOD PROCEDURE

To understand the concept of the characteristic method, consider a steady, compressible, inviscid fluid flow in two-dimensional space. The velocity potential equation governing this flow is written as follows:

$$\left[1-\frac{1}{a^2}\left(\frac{\partial\phi}{\partial x}\right)^2\right]\frac{\partial^2\phi}{\partial x^2}+\left[1-\frac{1}{a^2}\left(\frac{\partial\phi}{\partial y}\right)^2\right]\frac{\partial^2\phi}{\partial y^2}-\frac{2}{a^2}\frac{\partial\phi}{\partial x}\frac{\partial\phi}{\partial y}\frac{\partial^2\phi}{\partial x\partial y}=0$$

(371)

Where $\emptyset$ is velocity potential and u, v are velocity vector along x, y direction respectively.

$$u=\frac{\partial\phi}{\partial x} \quad (372\text{-a})$$

$$v=\frac{\partial\phi}{\partial y} \quad (372\text{-b})$$

By substituting relations (372-a, b) in the equation of velocity potential (Eq. 371), and then rewriting it in terms of $\frac{\partial u}{\partial x}$:

$$\left[1-\frac{u^2}{a^2}\right]\frac{\partial u}{\partial x}+\left[1-\frac{v^2}{a^2}\right]\frac{\partial v}{\partial y}-\frac{2uv}{a^2}, \qquad \frac{\partial u}{\partial y}=0 \quad (373\text{-a})$$

$$\left(\frac{\partial u}{\partial x}\right)_{i,j}=\frac{\frac{2uv}{a^2}\frac{\partial u}{\partial y}-\left(1-\frac{v^2}{a^2}\right)\frac{\partial v}{\partial y}}{1-\frac{u^2}{a^2}} \quad (373\text{-b})$$

And since the velocity potential and its derivatives are functions of x and y, i.e.,

$$\frac{\partial\phi}{\partial x}=f(x,y) \quad (374\text{-a})$$

$$\frac{\partial\phi}{\partial y}=f(x,y) \quad (374\text{-b})$$

By defining the exact differential for the (f) function and according to its definition in the above two relations, we will have:

$$df=\frac{\partial f}{\partial x}\mathrm{dx}+\frac{\partial f}{\partial y}\mathrm{dy} \quad (375\text{-a})$$

$$d\left(\frac{\partial\phi}{\partial x}\right) = du = \frac{\partial^2\phi}{\partial x^2}\mathrm{dx} + \frac{\partial^2\phi}{\partial x\partial y}\mathrm{d}y \qquad (375\text{-b})$$

$$d\left(\frac{\partial\phi}{\partial y}\right) = du = \frac{\partial^2\phi}{\partial x\partial y}\mathrm{dx} + \frac{\partial^2\phi}{\partial y^2}\mathrm{dy} \qquad (375\text{-c})$$

To numerically solve Equation (375-b) as shown in Figure (109-a), consider particle $A(i,j)$ in the fluid flow domain moving at velocity (V) with an angle of θ with respect to an axial direction. According to the CFD basics, to calculate the axial velocity changes in the X direction (and also in Y direction) at point A, we need to calculate the velocity component at the next point (point D in the diagram). So, we write the Taylor series for this point:

$$u_{i+1,j} = u_{i,j} + \left(\frac{\partial u}{\partial x}\right)_{i,j}\Delta x + \frac{1}{2}\left(\frac{\partial^2 u}{\partial x^2}\right)(\Delta x)^2 + \cdots \qquad (376)$$

By ignoring the higher-order terms in the Taylor series at both X and Y directions, and again by using some CFD basics such as forward, backward, or central difference concepts we can calculate $\partial u/\partial y$ and also $\partial v/\partial y$ which is used to obtaining $\partial u/\partial x$ in the equation (373-b). But the point is when the denominator of the equation (373-b) goes to zero, $\partial u/\partial x$ will be indeterminate, and this is happening in a case where the axial velocity of point (A) be sonic (like the nozzle throat), i.e.,

$$1 - \frac{u^2}{a^2} = 0$$

So,

$$u = a = sonic \qquad (377)$$

Therefore, the hypothetical line where points A, B, and C are position, that has $\partial u/\partial x = 0$ is called characteristic line, and the orientation (X and Y direction) doesn't matter on this line. Suppose that this line has made an angle (μ) with the velocity vector at point (A). According to the schematic shown in figure 109-b, it can be understood that in such cases characteristic line is meant Mach line physically.
By solving the set of the system of simultaneously equations (Eq. 373-a and with expressions 375-b, 375-c) for $\emptyset_{xy}$:

$$\frac{\partial^2 \phi}{\partial x \partial y} = \frac{\begin{vmatrix} 1-\frac{u^2}{a^2} & 0 & 1-\frac{v^2}{a^2} \\ dx & du & 0 \\ 0 & dv & dy \end{vmatrix}}{\begin{vmatrix} 1-\frac{u^2}{a^2} & -\frac{2uv}{a^2} & 1-\frac{v^2}{a^2} \\ dx & dy & 0 \\ 0 & dx & dy \end{vmatrix}} = \frac{N}{D} \tag{378}$$

This expression says that when the denominator goes to zero, the derivative $(\frac{\partial^2 \phi}{\partial x \partial y})$ will be indeterminant. The indetermination of the derivative is physically impossible but like what we assumed for obtaining $\partial u/\partial x$ before, the indeterminacy of the derivative in such case means to characteristic line existence. Therefore, if the denominator is zero, so the determinant will be zero, which by solving it we have:

$$\frac{dy}{dx} = \frac{-\frac{uv}{a^2} \pm (\sqrt{\left(\frac{u^2+v^2}{a^2}\right)} - 1)}{1-\frac{u^2}{a^2}} \tag{379}$$

Where $(u^2 + v^2)$ in the fraction is the particle total velocity (V), so this equation can be rewriting as follows

$$\frac{dy}{dx} = \frac{-\frac{uv}{a^2} \pm (\sqrt{M^2 - 1})}{1-\frac{u^2}{a^2}} \tag{380}$$

In other words, this equation expresses that when the determinant for the chosen value of dx and dy goes to zero, the characteristic line orientation will be obtained by this equation or how we can locate this characteristic line. According to the expression within the integral in the above equation, three cases will occur:

1. $M > 1$: in this case, we have two real roots which are mean two characteristic equations where $\frac{dy}{dx}$ is its slope. The Characteristic lines are hyperbolic PDEs. (This is our case since it corresponds to supersonic flow)
2. $M = 1$: this case has one real root, which is a mean physically sonic flow. And the equation will be parabolic PDE.
3. $M < 1$: imaginary roots with elliptical PDEs will be expressed. (Subsonic case)

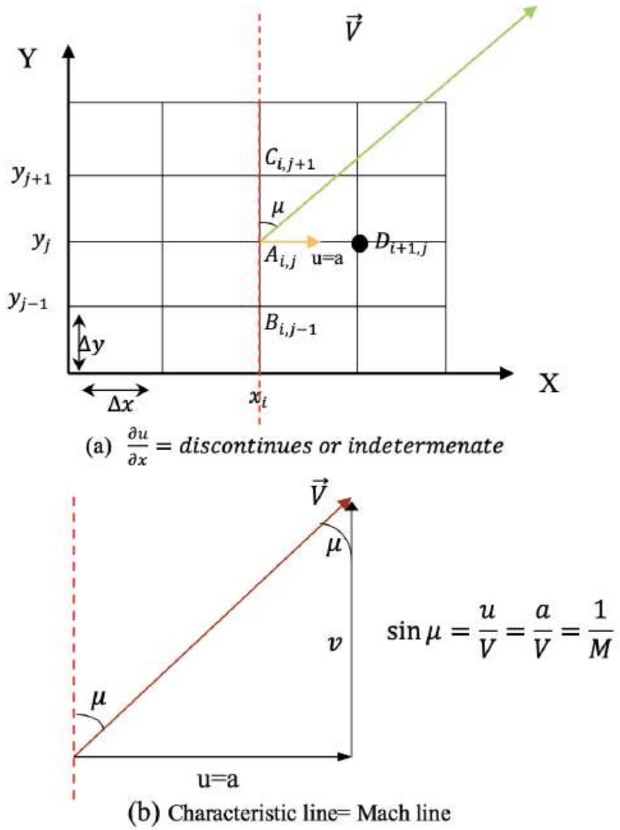

Figure 109- (a)Grid points, (b) the concept of the characteristic line and the Mach line

Therefore, according to case (1), we have two characteristic lines which have hyperbolic states and according to what we said earlier about the characteristic line for point (A), which deviates by (μ) degree from the total velocity vector. Therefore, according to Figure 110, Equation 380 is also written as follows:

$$\frac{dy}{dx} = \tan(\theta \mp \mu) \tag{381}$$

The above equation can be obtained by considering $u = V.\sin\theta$, $v = V.\cos\theta$ and $\sin\mu = \frac{1}{M}$ then substituting these expressions in Equation 172, as well as by several mathematical and simplification operations. The negative and positive signs in the above equation correspond to the right-running Mach waves and the left-running Mach waves, which are denoted by $(C_-)$and (C_+), respectively.

If we plot the changes in axial velocity (u) in terms of X (Figure 111), given that the axial velocity is constant along the axis (i.e., $\frac{\partial u}{\partial x} = 0$), and the velocity obtained indeterminate according to our assumptions (Which for simplicity we assume it has a constant value of C) and given that the velocity in the axial direction is continuous, therefore, for the continuity (u), its value changes between 0 and C, and also for the derivative to be finite but still indeterminate, it should be at least zero, namely $(N = 0)$.

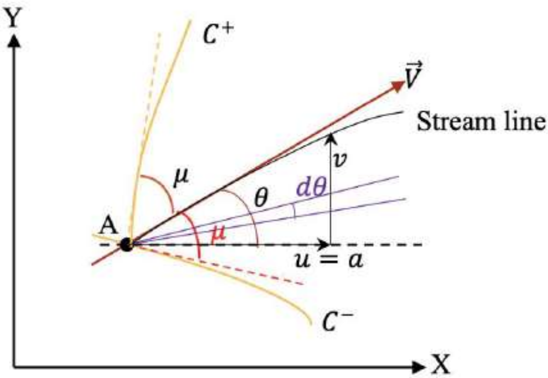

Figure 110- Left, and right-running characteristics lines from point A

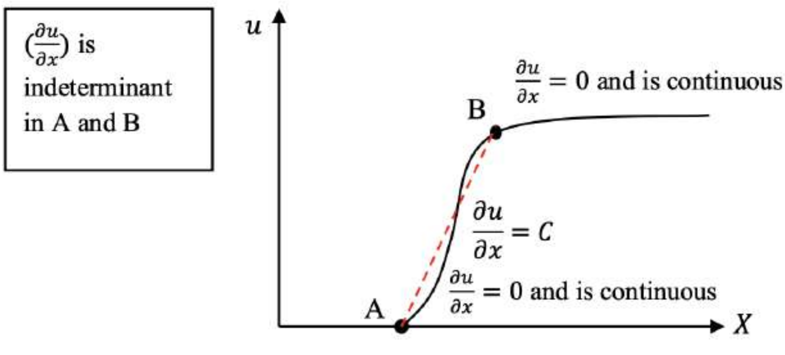

Figure 111- Continuity condition of the axial velocity

$$\emptyset_{xy} = \frac{\partial u}{\partial y} = \frac{\partial v}{\partial x} = \frac{N}{D} = indeterminant \tag{382}$$

When N is zero from Equation 378, the following expression will be obtained

$$\frac{dv}{du} = \mp\sqrt{M^{2-1}}\frac{dv}{v} \tag{383}$$

According to Figure 110 it can be seen that $(\frac{dv}{du})$ is equal to $d\theta$, i.e.,

$$d\theta = \mp\sqrt{M^2 - 1}\frac{dv}{v} \tag{384}$$

The above expression represents the compatibility equations along the characteristic lines. By integrating the compatibility equations, it can be expressed in terms of the Prandtl-Meyer function.

$$C^- \equiv \theta - \nu(M) = Constatn = K_- \tag{385-a}$$

$$C^+ \equiv \theta + \nu(M) = Constatn = K_+ \tag{385-b}$$

Where K is a constant parameter along each characteristic line and $\nu(M)$ is the Prandtl-Mayer function

$$\theta = \nu(M_2) - \nu(M_1) \tag{386}$$

$$\nu(M) = \sqrt{\frac{\gamma+1}{\gamma-1}}\tan^{-1}\sqrt{\frac{\gamma-1}{\gamma+1}(M^2-1)} - \tan^{-1}\sqrt{M^2-1} \tag{387}$$

This means that the nozzle contour can be designed just by having the exit Mach number.

NOZZLE CONTOUR DESIGN

In this section, we explain the procedure of nozzle contour designing. Supersonic nozzles are separated into two types of gradually expanded and minimum length nozzle types based on their characteristic lines. That's mean in the second type, unlike the gradually expanded type, characteristic lines intersect each other at smaller length. In the first model, the angle will change so that it reaches its maximum value with some increase and then decrease back to zero, and cancels the waves. This model also generates higher-quality flow at the desired exit conditions, especially at higher Mach numbers ($\theta_{wall} \geq 40°$).The high weight and length penalties of this model make this type of nozzles inefficient for use in rockets.

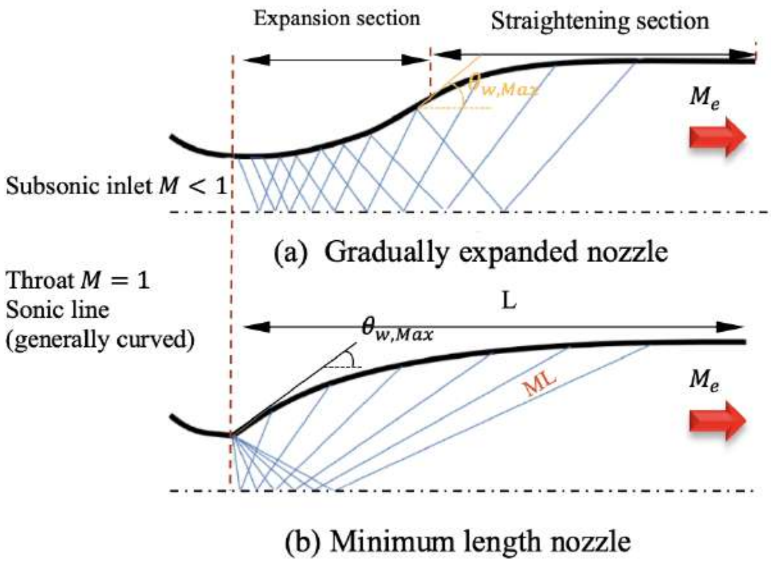

Figure 112- Two Common Types of Nozzle Contour Design

Consider the points inside Figure 113. Since we know the position of points A and B, the properties of the flow field at point C, which is at the intersection of the two characteristic lines C_- from point A and the characteristic C_+ from point B, will be determined. The point is the value of K along each characteristic line has a constant value, i.e.,

$$\theta_A + v_A = (K_-)_A = (K_-)_C \tag{388-a}$$

$$\theta_B - v_B = (K_+)_B = (K_+)_C \tag{388-b}$$

We also write the compatibility equations at point C:

$$\theta_C + v_C = (K_-)_C \tag{389-a}$$

$$\theta_C - v_C = (K_+)_C \tag{389-b}$$

In the above two equations, parameters $(K_-)_C$ and $(K_+)_C$ are known values obtained from Equations (388-a) and (388-b). Hence the unknowns θ_C and v_C will be obtained:

$$\theta_C = \frac{1}{2}[(K_-)_A + (K_+)_B] \tag{390-a}$$

$$v_C = \frac{1}{2}[(K_-)_A - (K_+)_B] \tag{390-b}$$

According to the two values θ_C and v_C , all other properties of the flow field can be obtained at this point, including M_C, P_C, T_C, speed of sound (a_C), and also V_C. Given that the characteristic lines are curvilinear lines, but to simplify the calculations, we assume them as a line whose slope is the average of its two points. In other words, for AC and BC lines, these angles are as follows:

$$AC: \frac{1}{2}(\theta_A + \theta_C) - \frac{1}{2}(\mu_A + \mu_C) \quad (391\text{-a})$$

$$BC: \frac{1}{2}(\theta_B + \theta_C) + \frac{1}{2}(\mu_B + \mu_C) \quad (391\text{-b})$$

Therefore, for given points A and B which are intersecting each other at point C, the location of this point is achieved by this procedure:

$$m_1 = \tan(\frac{(\theta-\mu)_A+(\theta-\mu)_C}{2}) \quad (392\text{-a})$$

$$m_{11} = \tan(\frac{(\theta-\mu)_B+(\theta-\mu)_C}{2}) \quad (392\text{-b})$$

$$y_C = y_A + m_1(x_C - x_A) \quad (392\text{-c})$$

$$y_C = y_B + m_{11}(x_C - x_B) \quad (392\text{-d})$$

$$x_C = \frac{y_1 - y_B + m_{11}x_B - m_1 x_A}{m_{11} - m_1} \quad (392\text{-e})$$

Again, we return to Figure 114 and compare the characteristic lines AE and Ee. Since the values of K_+ at points A, E, and K_- at points E and e are the same, respectively:

$$\theta_A - v_A = \theta_E - v_E \quad (393\text{-a})$$

$$\theta_E + v_E = \theta_e - v_e \quad (393\text{-b})$$

It should be noted that the value of θ_A is the largest angle of the nozzle wall ($\theta_{wall,Max}$), and the value of this angle at point (e) as the last point of the nozzle expansion wall curve is zero. And given that the value of θ on the axis is zero ($\theta_e = 0$). This point, as the last point, has an exit velocity equal to the Mach number, which means that the Prandtl-Meyer function in this Mach number must be calculated for it, i.e., ($v_e = v(M_{exit})$). Therefore, according to Equations 182, we have:

$$\theta_{wall,Max} - v_A = 0 - v_E \quad (394\text{-a})$$

$$0 + v_E = 0 - v(M_{exit}) \quad (394\text{-b})$$

We write the Prandtl-Meyer equation (Equation 387) at point A:

$$\theta_A = \nu(M_2) - \nu(M_1) = \nu(A) - 0 = \theta_{wall,Max} \tag{395}$$

By substituting equations (394-b) and (395) into equation (394-a), then the maximum wall angle will achieve by:

$$\theta_{wall,Max} = \frac{\nu(M_{exit})}{2} \tag{396}$$

Consider figure 108-a to find the position of the points on the wall contour. We write the compatibility equations on the characteristic line C_- at points f and d.

$$(K_-)_d = \theta_d + \nu_d = \theta_f + \nu_f = (K_-)_f \tag{397}$$

Since we have already obtained the angle θ_d, then:

$$\nu_d = \theta_f + \nu_f - \theta_d \tag{398}$$

Therefore, the angles of the left and right running characteristics for this point will be as follows:

$$fd\text{: } \frac{1}{2}(\theta_d + \theta_{wall}) \tag{399-a}$$

$$gd\text{: } \frac{1}{2}\left(\theta_d + \theta_f\right) + \frac{1}{2}(\mu_d + \mu_f) \tag{399-b}$$

Where θ_{wall} is the turning angle at the previous wall location (i.e., point c). The position of the point d can be obtained from Equations 392.

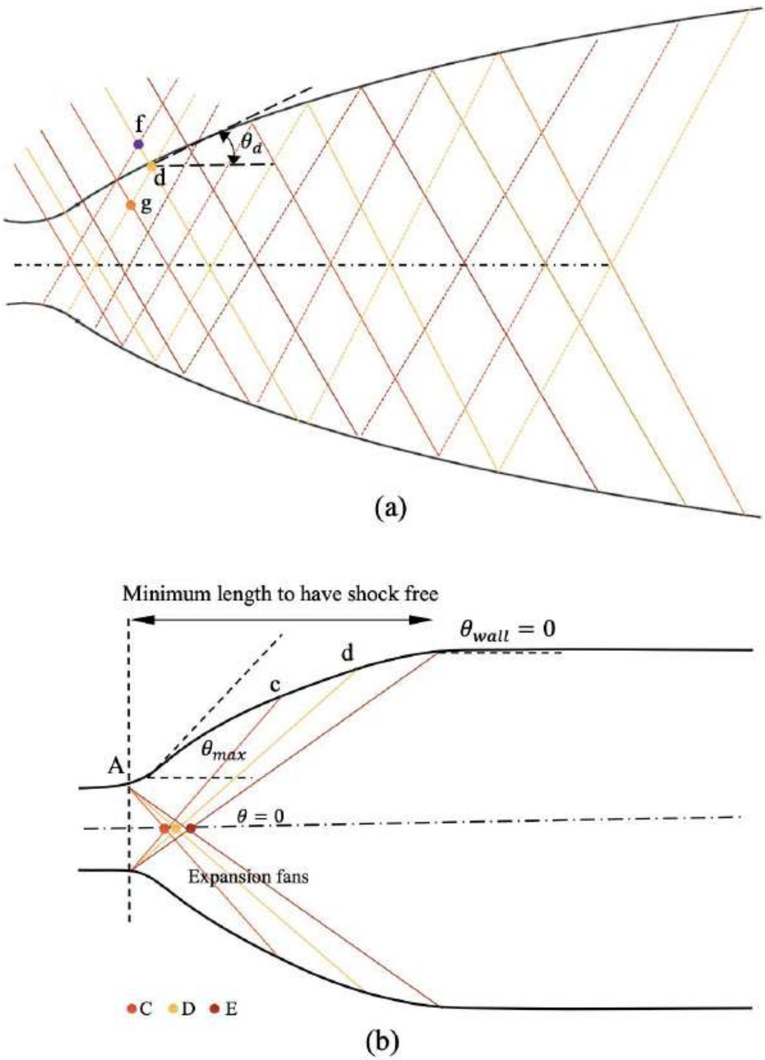

Figure 113- Designing of supersonic nozzles by characteristic s' method. (a) refers to the Gradually expanded nozzle and (b) to the minimum length nozzle.

PARABOLIC APPROXIMATION OF BELL NOZZLE

Another method that can be used almost optimally to design the contour of alarm nozzles is to use the method of parabolic approximations proposed by

Rao. The design configuration of this nozzle with this method is shown in the figure below. According to the top figure, contours are designed according to specific data ratios so that upstream of the nozzle throat consists of a circular arc with radius $0 \cdot 382R_t$ and the second part starts from point (N) and reaches a point on the nozzle output plate (E). Other design parameters in this method include the input angle of the parabolic part (θ_n) and the output angle of the parabolic part of the nozzle (θ_e), which are in degrees and are shown in the figure below in terms of the surface expansion ratio. Another advantage of this method is that due to the experience of the effect of the specific heat ratio on the contour is small, so by selecting the appropriate values, we are able to design without considering the propellant type. (For more information, you can refer to Rao's article).

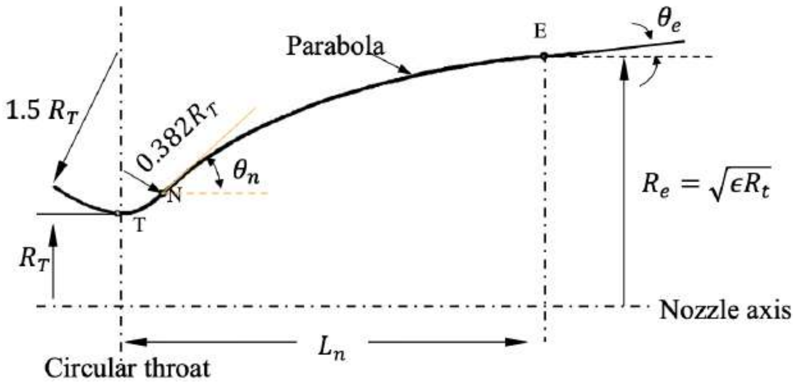

Figure 114- Parabolic approximation of bell nozzle contour. From Design of Liquid Propellant Rocket Engines

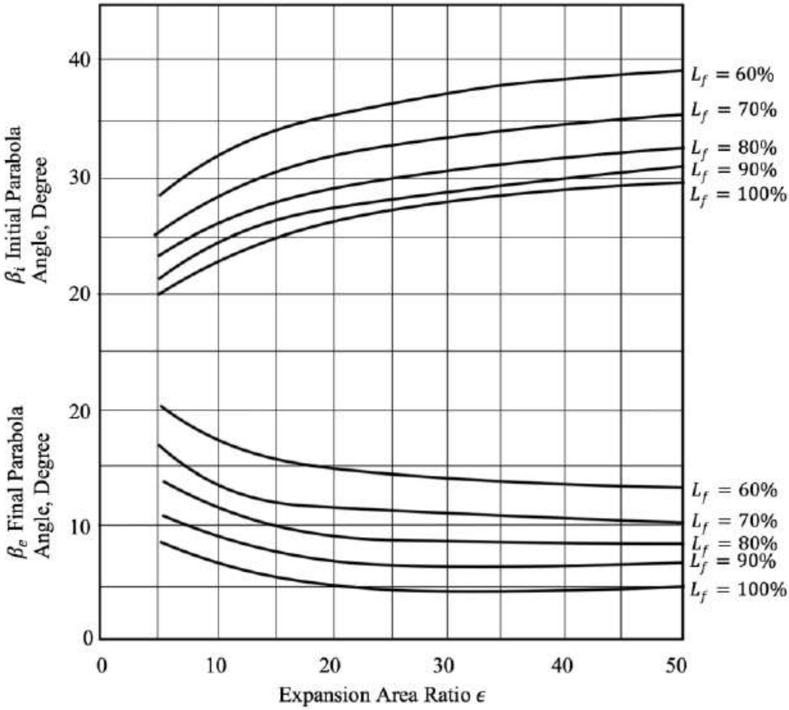

Figure 115- θ_n and θ_e as function of expansion area ratio ϵ. From Design of Liquid Propellant Rocket Engines

ANNULAR NOZZLE

According to momentum conservation theory, the thrust generated in the thrust chamber of an ideal expansion nozzle depends only on the mass flow conditions (velocity and direction of flow) at the nozzle exit. Therefore, in some nozzles, such as annular nozzles, the current inside the nozzle throat is not necessarily parallel to the axis, but at the nozzle output, they have conditions such as bell and conical nozzles, so their output thrusts are the same. These nozzles can be divided into two general categories: Radial in-flow and Radial out-flow, so that the first category includes Spike nozzles and the second category include the nozzles such as Expansion-Deflection (E-D), Reverse Flow (RF), and Horizontal-Flow (HF), which are shown schematically in the figure below, along with the bell and conical nozzles.

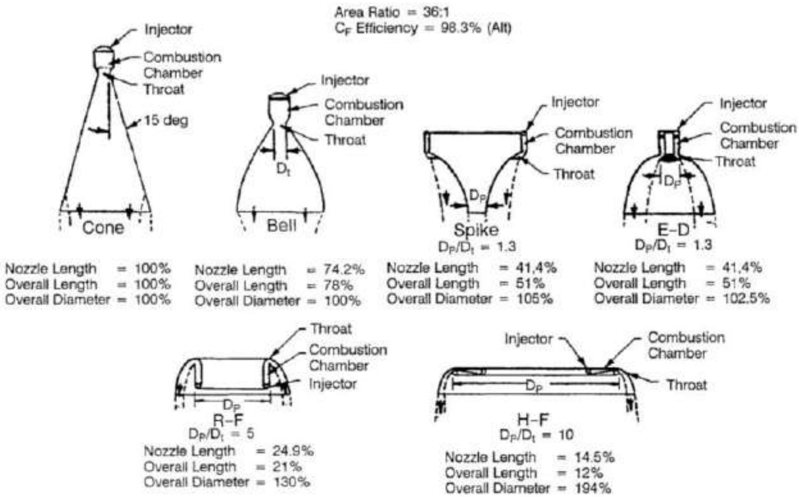

Figure 116- Comparison of bell nozzle. From Design of Liquid Propellant Rocket Engines

To investigate the effect of the type of nozzles on their size, all nozzles are considered to have the same thrust and expansion ratio of the nozzle surface and the performance. According to the geometry of these nozzles, each of them can be used in certain situations, for example, when using shortened nozzles due to the low weight of its structure and due to increasing its efficiency for a certain length, the amount of payload can be increased. Annular nozzle area expansion ratio is defined as the ratio of the projected area of the nozzle wall contour to the throat, which is the difference between the exit area of the nozzle (A_e) and the projected area of the center of the object (A_p) , i.e.,

$$\epsilon = \frac{A_e - A_p}{A_t} \tag{400}$$

Another design parameter in the design of these nozzles is the diameter ratio $\frac{D_p}{D_t}$, in which D_p is the diameter of the center of the body and D_t is the diameter of the throat in an equivalent circular throat. In bell nozzles, the expansion of gases at low altitudes or at atmospheric pressure occurs earlier than the separation occurs, but it is important to note that in this category of nozzles, annular nozzles, due to their special characteristics, does not contain any separation phenomenon. For example, figure (118) shows a schematic of the E-D nozzle. In these nozzles, the pressure behind the center body is known as the back pressure(P_L), which is a function of ambient pressure but generally less than it, and plays a very important role in regulating the pressure inside the nozzle. The expansion of the gases around the arms (C)

downstream will not be effective until the base pressure is reached. After the initial expansion through the fixed Mach line (CD), the gas flows through the base pressure, which separates the flow and controls the inner jet boundary, and the contour (DE) of the nozzle wall, which makes the flow almost axial, will be controlled. The special geometry of these nozzles makes them largely safe from separation. The curvature of the nozzle wall is such that it diverts the gas flow, which increases the local pressure on the nozzle wall. This is especially true for Spike nozzles, which greatly increase the performance of the nozzle at low altitudes. Another feature of these nozzles is the nature of the automatic flow regulation, which makes separation almost impossible compared to normal nozzles.

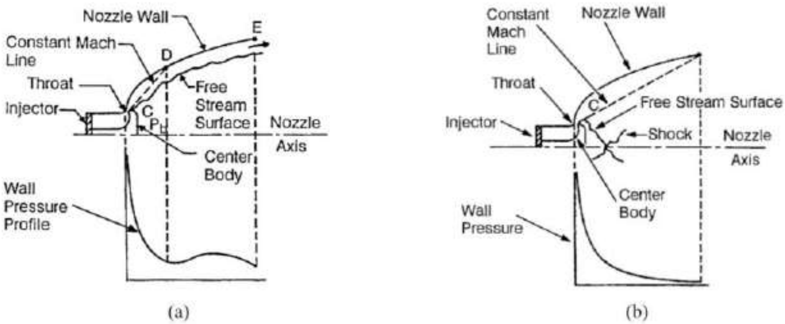

Figure 117- E-D nozzle at low and high-altitude operation. From Design of Liquid Propellant Rocket Engines.

At high altitudes, the base pressure (P_b) will decrease to such an extent that the flow behind the center body will converge, which may even cause a shock wave depending on the flow conditions. However, the expansion of the gases may continue unaffected until the end of the nozzle. There is an improved type of spike nozzle that has an aerodynamic advantage over it, in which the secondary flow occurs on its tail. This type of nozzle is called the aerodynamic truncated spike nozzle. The performance of these nozzles is due to various factors such as geometric parameters and the amount and method of producing secondary flow and the relative energy between primary and secondary flow. Primary and secondary flows are shown in the following figure, where the primary flow characteristics will be determined by the annular geometry of the nozzle, the circular contours of the nozzle, and the ambient pressure. Also, the pressure applied to the base of the nozzle will cause additional thrust, which the thrusts generated in this type of nozzles is well specified in the figure 119.

This initial flow extends beyond the nozzle surface and encloses the recirculating subsonic flow field in the base region. The pressure applied to the nozzle base, which causes additional thrust, is due to the presence of secondary flows and recirculation, which will result in an increase in performance. It should be noted, however, that there is a limit to each configuration that results in an optimal secondary flow. The outer surface of the primary stream is also the free jet boundary, which is a function of ambient pressure, so that at high altitudes, which have a large pressure ratio, the outer free jet boundary of the primary stream extends outwards, which The Prandtl-Meyer rotation angle is obtained in the throat, and at low pressure ratios or at sea level altitudes, high pressure causes compression of the external free jet stream, and this flow compression increases the static pressure, which results in an increase in base pressure on the nozzle, and to some extent it compensates for the negative effects of higher ambient pressure on the back of the nozzle. Figure (94) shows the performance of ideal nozzles and bell and Aero Spike nozzles with large area ratio in different pressure ratios with respect to the thrust coefficient. As can be seen, Aero Spike nozzles follow the ideal nozzle better than the bell nozzles. All nozzles at high altitudes (vacuum) have a large thrust coefficient.

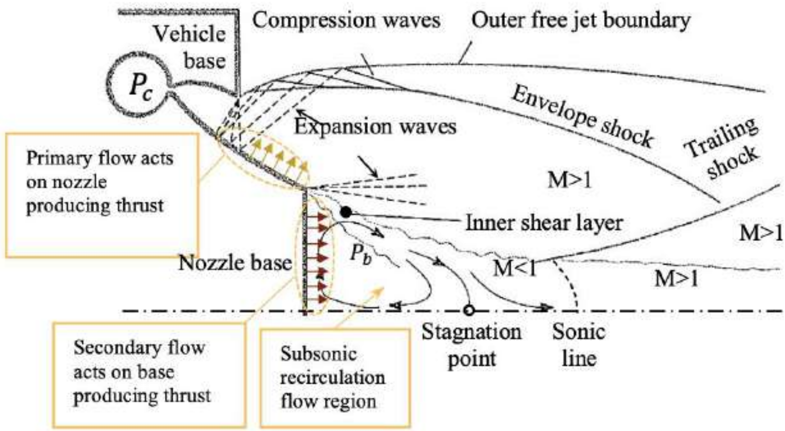

Figure 118- The Plume Physics Behind Aerospike Nozzle Altitude Compensation And Slipstream Effect By J.H.Ruf And P.K. Mcconnaughey.

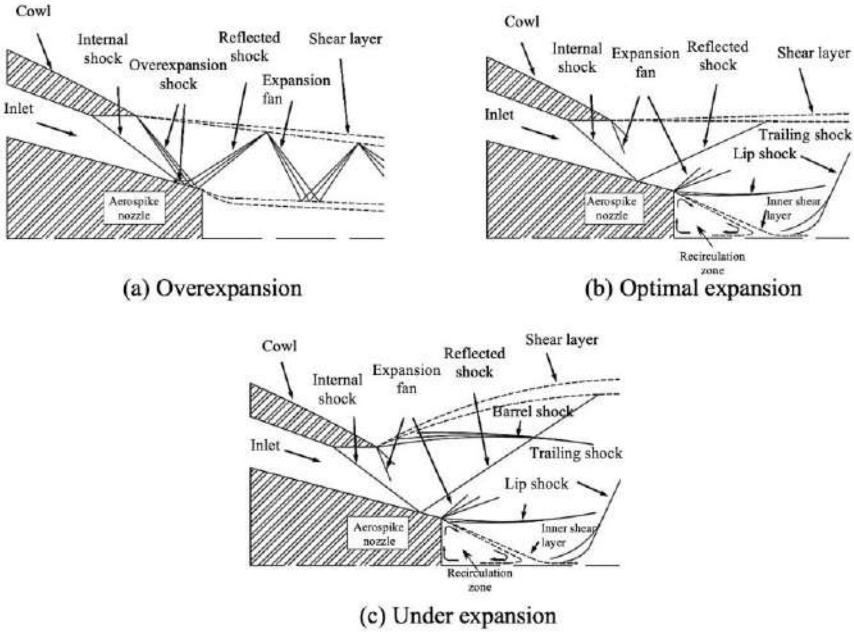

Figure 119- Flow phenomena of a truncated conical aerospike nozzle: a) overexpansion, b) optimal expansion, and c) underexpansion. Study of Conical Aerospike Nozzles with Base-Bleed and Freestream Effects Prasanth P. Nair and Abhilash Suryan and Heuy Dong Kim.

Here are some of the advantages and disadvantages of these nozzles:

1. Have a larger expansion ratio at a given length or have a shorter length for a given specific expansion.
2. They have better performance at low altitudes (sea level) so that an annular nozzle with a large coefficient of expansion can be used in single-stage rockets for missions from sea level to vacuum.
3. The stationary zone created in the nozzle base can be used for circulating turbo pumps and gas generators and installing secondary equipment and turbine gas outlets.
4. The combustion chamber can be made of different parts so that each part cannot be made and tested in the early stages to improve combustion stability.

Disadvantages:

1. Too much cooling requirements due to too many heat fluxes and more surface to be cooled.
2. Heavier structure in some applications
3. Construction difficulties.

THRUST CHAMBER COOLING

The combustion chamber requires a cooling system due to its high temperature (about 4000 to 6000 °F) and the high heat transfer rate of hot gases to the chamber wall (0.5 to 50 $\frac{BTU}{in^2 \cdot \sec}$). Heat sinks can be used in operations of about a few seconds, for example, the fins used on the surface of the chamber prevent the chamber from overheating, but this structure causes the chamber to become heavy and reduces its operating range. For systems that are used for longer periods of time, the use of this method is not suitable and causes system failure, so that for these systems, a steady state cooling system is used. Several examples of these methods are given below:

1. Dump cooling: The way this method works is that some propellants such as liquid hydrogen in engines with $(LO_2 \ / \ LH_2)$ fuel enters the passages embedded inside the wall of the thrust chamber and along the way becomes super-heated. And then expand at high temperatures and speeds, which will also produce some thrust, and eventually exit through the rear openings at the back of the nozzle. This cooling method is used effectively in systems with low pressure hydrogen fuel ($P_C < 1000Psi$) or in Nozzle extension with high pressure systems.
2. Film cooling: Cooling materials such as $(LH_2, RP1, \ldots)$ enter the thrust chamber through porous materials used in the wall or cracks and holes in the wall and cause cooling and lowering the temperature of the exhaust gases. Due to the reactions between the cooling film and the exhaust gases resulting from the transfer of heat and mass, the effective thickness of the cooling film will decrease. Excess coolant is injected at one or more downstream stations to compensate for this deficiency. Of course, in many engines, the fuel itself is used as a coolant, so that several holes are installed on the body of the injector, so that during the operation, some fuel is sprayed towards the walls. This method is more widely used than the previous method, so that in rocket cooling, a combination of cooling methods is often used, and this method is not used alone as a cooling system.

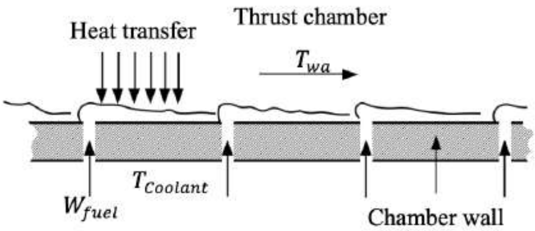

Figure 120- from rocket heat transfer

The adiabatic temperature of the wall cooled by this method is obtained from Equations (401) and (403):

$$\frac{G_c}{G_G} = \frac{1}{\eta_0} \cdot \frac{h}{a\left(1+b^{\left(c_{pvc}/c_{pg}\right)}\right)} \tag{401}$$

Where in this equation, G_c and G_G are, the weight flow rate of the cooling film per unit area from the surface of the wall of the cooling chamber $\frac{lb}{in^2 \cdot Sec}$ and the weight flow rate of combustion gas per unit area from the cross-section of the chamber perpendicular to the flow, respectively. Cooling efficiency is displayed with η_c, which ranges from 30 to 70%. h is also the enthalpy of the cooling film $\frac{BTU}{lb}$ and a and b are also obtained from the following expressions.

$$a = \frac{2v_d}{v_m f} \tag{402-a}$$

$$b = \left(\frac{v_g}{v_d}\right) - 1 \tag{402-b}$$

The terms v_d, v_m, and v_g are the axial velocities of the combustion gases at the edge of the boundary layer and at the middle and the centerline of the combustion chamber and f is the coefficient of friction between the gases and the cooling film. Using the coolant enthalpy, the adiabatic wall temperature in the case of liquid cooling is obtained from this equation.

$$h = \frac{c_{pvc}\left(T_{aw} - T_{wg}\right)}{c_{plc}\left(T_{wg} - T_{co}\right) + h_{fg}} \tag{403}$$

In this equation, c_{pvc} and c_{plc} are the specific heat of cooling in the vapor phase and the liquid phase at constant pressure $(\frac{BTU}{lb\ R})$, respectively, and C_{Pg} in equation (401) represents the specific heat of combustion gases at constant pressure.

For the gaseous state, the adiabatic wall temperature will be obtained by equation (404).

$$\frac{T_{aw}-T_{wg}}{T_{aw}-T_{co}} = e^{-\left(\frac{h_g}{G_c\, C_{pvc}\, \eta_c}\right)} \qquad (404)$$

T_{aw}, T_{wg}, T_{co}, represents the adiabatic wall temperature, the maximum allowable gas-side wall temperature, and the initial cooling temperature in the manifold respectively.

Transpiration cooling: This cooling method, which is a special type of film cooling and has a very wide application, so that the cooling material enters the chamber through the porous walls and will reduce the wall temperature to the desired temperature. To obtain the adiabatic wall temperature, the following proposed models are used, in which Pr_m and Re_b are mean film Prandtl number and bulk combustion gas Reynolds number, respectively.

$$\frac{T_{aw}-T_{co}}{T_{wg}-T_{co}} = [1 + \{1.8(\mathrm{Re}_b)^{0.1} - 1\}\{1 - e^{-37\left(\frac{G_c}{G_R}\right)Re_b^{0.1}}\}][e^{37\left(\frac{G_c}{G_R}\right)Re_b^{0.1}Pr_m}] \qquad (405)$$

Ablative cooling: During the use of this process, the materials on the gas-side wall (Pyrolysis of resins) begin to melt and evaporate due to the very high heat inside the chamber, causes the formation of a boundary layer with lower temperatures near the wall. This method can be used alone in boosters and rockets with solid propulsion and upper stage application in finite chamber pressure $P_c < 300psi$, and for the combined mode, which is used with film cooling, its operating range and pressure increase up to $1000psi$, and in this case, they are even used in liquid propellants.

Radiation cooling: The application of this cooling model is related to the outer wall of the thrust chamber and is mostly used in parts where the heat flux and compressive stresses are low, such as Nozzle extensions and expansion nozzle skirt at large area ratios. In this method of cooling, the availability of materials operation due to the equilibrium temperature of the thrust chamber wall which is reached during the steady state operation is the limiting characteristic. These temperatures, which are sensitive to the nozzle area ratio and the combustion chamber pressure, are plotted for one propellant in the figure below. Chambers with thrust levels less than $100lb$ and the chamber pressure of 90 $psia$ can run under steady state conditions for over an hour with the radiation cooling system.

$$h_g\left(T_{aw} - T_{wg}\right) = \varepsilon\sigma\left(T_{wg}^4 - T_{sur}^4\right) \qquad (406)$$

The most important limit on firing duration is the life of the protective coating used on refractory metals. Actual thrust chamber lives of several hours have been demonstrated with molybdenum disilicide at metal temperatures above 3000°F. (From NAS-7-103).

Heat sink: This method is contained of Inert and Endothermic heat sink cooling. Combustion chamber component temperature may be held below structural limits while heat is being conducted away from the surface and absorbed in the chamber wall. The primary limitation on this concept is he run time available before a limiting surface temperature is reached. Two limiting temperatures are encountered: First, the melting, subliming, or softening temperature at which the material would flow or erode rapidly, and second, the temperature at which the oxidation rate or reaction rate with the combustion gases would be excessive. (From NAS-7-103). Heat sink materials must have properties such as high heat capacity, high thermal conductivity, high structural temperature limits, and compatibility with the combustion gases. The best materials to use in this cooling method are tungsten, and pyrolytic and isotropic graphite. In this method of cooling, oxidation by combustion gases containing H_2O and CO_2 is the most critical problem. Theoretically, the run time is the function of the endothermic heat sink materials such as subliming salt, lithium compounds, and low melting point metals which is capable for absorbing large amount of heat through a phase change from an initial solid state and mostly saturated into porous refractory wall. It should be noted that an inert heat sink is the best way for the low duty cycle of pulsing operation in contrast to an Endothermic heat sink which is not applicable.

HEAT TRANSFER

REGENERATIVE COOLING:

The method that James H. Wilde invented in 1958 as Regenerative Cooling is today the most widely used cooling method for liquid propellant rockets. The description of the operation of this method is that the coolant, which can also be propellants, enters the passages through the inlet manifold located at the outlet of the nozzle, which continues until after the throat area. Then, through the output manifold, they enter the radial passages of the injector plate and are sprayed into the combustion chamber through the orifices on the injector. The nozzle throat section in which has the highest combustion temperature requires the maximum amount of heat flux dissipation. To provide this amount of heat dissipation, the velocity of the coolant must be high, which is provided by reducing the cross-sectional area of the throat. To increase the cooling performance, the coolant enters the passages through the nozzle outlet as well as from the throat or directly from the throat. Generally, two cooling techniques are used for Regenerative Cooling. Cooling passages can be in the form of Cooling adjacent tubes or Separate inner walls. In the first model, the combustion chamber contour consists of cooling pipes with a wall thickness of 0.012 that are welded together to the outer shell. In this method, the closer we get to the throat to dissipate more heat, the lower the cross-section of the pipes to increase speed. In the second model, which is often used for thinner thrust chambers, by milling, rectangular channels are drilled inside the body of the combustion chamber, which is reduced to the area close to the cross-section of the channels, similar to the previous case. In this method, the outer shell is also part of the cooling channels. Initially, the aspect ratio for these channels was 8, which increased to 15 after the introduction of Platelet technology. Today, due to the development of manufacturing technology (especially machining technology), this value has reached 16 (i.e., 8 mm height and 0.5 mm width). (Index.pdf Page 25 [20],[21])

The materials used in the construction of the combustion chamber should be selected so that they are resistant to stresses on the chamber and also have a good heat transfer. Copper as an excellent conductor that does not oxidize in non-corrosive gas mixtures of fuel is the base material of the combustion chamber, which is used to increase the strength of copper alloys with additives such as zirconium, silver, or silicon. For example, Amzirc, which is a copper alloy, contains 0.15% zirconium, which is a strong electrical and thermal conductor that has high strength and hardness at high temperatures. NARloy-Z, as another copper alloy containing 0.5% zirconium and 3% silver, has a higher hardness than Amzirc. Stain Less Steel is used when propellant compounds contain corrosive oxidants, such as nitric acid or nitrogen tetroxide. For example, Steel 4130 and Stainless steel 347 are among the most widely used materials in this field, the first of which can be used to make fuel manifold and tension band, stiffening rings, and outriggers. The structure of the outer wall is also made of nickel alloys. INCONEL-718 is a chromium-nickel-based alloy used in turbojet engines, the outer shell of the thrust chamber, and resists against phenomena such as creep, tension, yield, and creep rapture to high temperatures up to $1000K$ and Cryogenic temp. The following figure shows several examples of cooling channels.

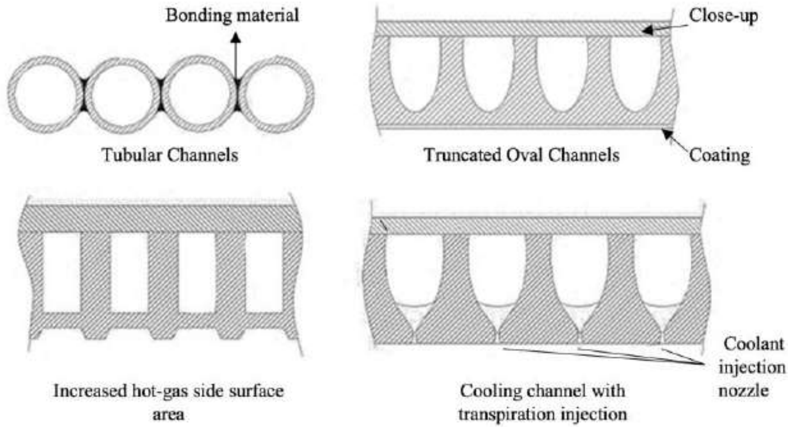

Figure 121- wall cooling channels configuration. From rocket heat transfer

The table (19) also shows the cooling materials used in the thrust chamber wall:

Wall	Close-out	Coating
Copper NARloy-Z SS-347 Glidcop Incone1718 Amzirc Columbium	SS-347 Nickel Copper Monel	Platinum Nicraly Soot Zirconia

Table 19- Wall close out coating coolants slide 12 rocket heat transfer NY slide 14.

Figure 123 demonstrates heat transfer modes inside the thrust chamber. Mainly, heat transfer of the forced transfer type occurs due to the very high velocity of the gases along the chamber wall. Before the combustion gases transfer heat to the wall, the heat energy must pass through a layer of stagnant gas along the wall called the boundary layer. Heat transfer from combustion gases to the chamber wall consists of two terms: heat transfer, radiation, and displacement. As a result, we use the following equation for the displacement term in the previous equation:

$$\dot{q}_g = \dot{q}_{g,Conv} + \dot{q}_{g,Rad} \tag{407}$$

$$\dot{q}_g = h_g\left(T_{aw} - T_{wg}\right) \tag{408}$$

In this equation, T_{aw} and T_{wg} are the adiabatic temperature and the local hot-gas-side temperature of the chamber wall, respectively, which are in the degree of Rankin. Obtaining heat transfer coefficient is one of the challenges that due to turbulence flows inside the chamber, analytical solutions are not consistent with experimental results. This difference is due to the basic assumptions used in the analytical solution, such as that there is a propellant mixture in the injector and that heat transfer to the wall depends on the composition and local temperature of the gases, which is contrary to the assumption of homogeneous gases in analytical calculations. Experience has shown that the heat transfer coefficient is more dependent on the mass transfer of gas per unit area than other factors such as speed and thickness of the temperature boundary layer. This approximation is expressed as the heat transfer coefficient:

$$h_y = (\rho' v)^m \tag{409}$$

In this expression, ρ' and v are the density and local velocity of free flow, respectively. This equation can also be expressed in the form of dimensionless:

$$Nu = C(Re^m Pr)^n, \frac{L}{D} \geq 10\ , 0.7 \leq Pr \leq 160\ , Re \geq 10^5$$

(410-a)

$$Pr = \mu \frac{c_p}{k} \tag{410-b}$$

$$\mathrm{Re} = \frac{\rho' UD}{\mu} \tag{410-c}$$

This expression (equation 410-a) is similar to the heat transfer equation of a fully developed turbulent flow inside a tube. The values of m and n in the above two expressions will be 0.8 and 0.4, respectively. Of course, for cooling, n will change to 0.3, (from Dr. Bartz reference (2)). Due to the large temperature difference inside the rocket, the physical properties are used in the arithmetic mean (am) between bulk temp and wall temp for low-speed problems with a high-temperature difference and high-speed problems with a low-temperature difference. Therefore, h_g will be rewritten as follows:

$$h_g = \frac{C}{D^{0.2}}\left(\frac{\mu^{0.2}\, C_p}{Pr^{0.6}}\right)(\rho_{am}\ U)^{0.8}\ , C = 0.026 \tag{411}$$

Specific heat capacity (C_P) and Prandtl number can be assumed to be constant at stagnation temperature within the boundary layer, while μ_{am} and ρ_{am} generate at stagnation and static temperatures, respectively. To eliminate the effect of the changes μ and ρ in the previous expression, we define the dimensionless number σ in terms of μ and ρ as follows:

$$\sigma = \left(\frac{\rho_{am}}{\rho'}\right)^{0.8} \left(\frac{\mu_{am}}{\mu}\right)^{0.2} \tag{412}$$

As a result, the heat transfer coefficient relationship will be written as follows:

$$h_g = \frac{C}{D^{0.2}} \left(\frac{\mu^{0.2}\, C_p}{Pr^{0.6}}\right) (\rho'\, U)^{0.8} \sigma \tag{413}$$

Using the following equation and two approximations, the equation of heat transfer coefficient will be obtained:

$$T_{am} = \frac{1}{2(T+T_w)} \tag{414}$$

$$\rho \sim \frac{1}{T} \tag{415-a}$$

$$\mu \sim T^{\omega} \tag{415-b}$$

$$h_g = \left[\frac{C}{D_*^{0.2}} \left(\frac{\mu^{0.2}\, C_p}{Pr^{0.6}}\right)_0 \left(\frac{P_C\, g}{C_*}\right)^{0.8}\right] \left(\frac{A_*}{A}\right)^{0.9} \sigma \tag{416-a}$$

$$\sigma = [\frac{1}{2}\frac{T_W}{T_0}\left(1+\frac{\gamma-1}{2}M^2\right)+\frac{1}{2}]^{\frac{\omega}{5}-0.8}[1+\frac{\gamma-1}{2}M^2]^{-\frac{\omega}{5}}$$

(416-b)

It should be noted that the expression inside the bracket in equation (416-a) is always constant in the nozzle, and only the terms $(\frac{A_*}{A})$ and σ change. In the above equations, the dimensionless number (C) has a value equal to 0.026, which is equal to the heat transfer coefficient obtained from Equation (416-a) with the results of turbulent boundary layer analysis, (ref (2) DR. Bartz). The results of the relation obtained by solving the turbulent boundary layer method are shown in the figure below, which are also in good agreement with each other.

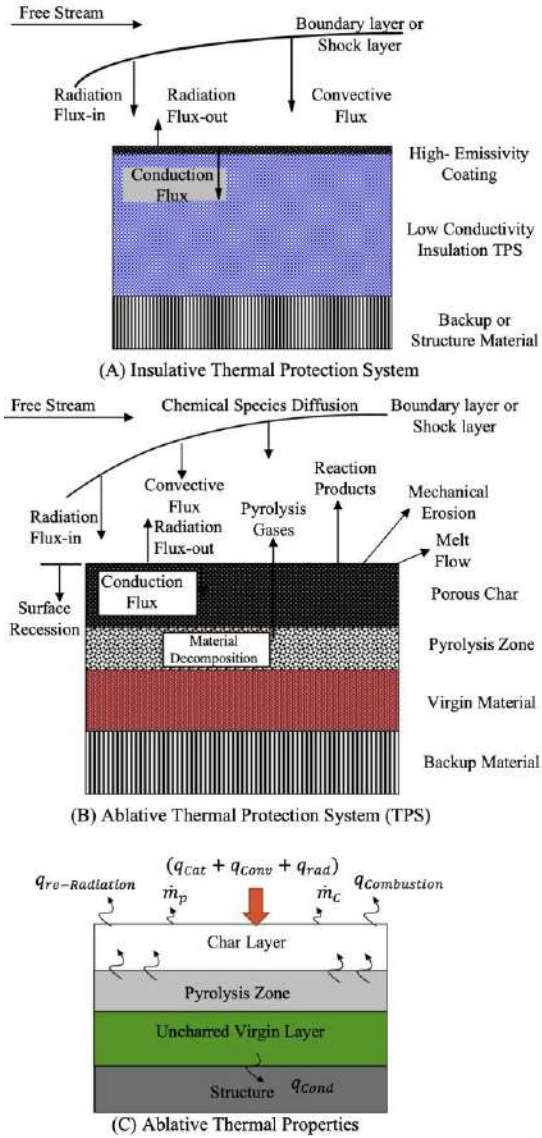

Figure 122- Heat transfer modes, adopted from Thermal Protection Materials: Development, Characterization and Evaluation.

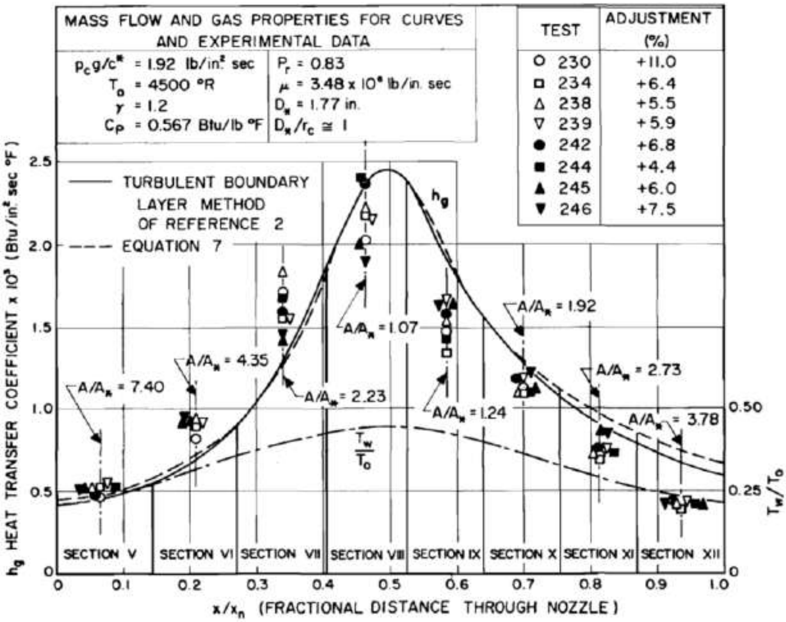

Figure 123- Distribution of heat transfer coefficient for nozzle of Fig. 2, Ref. 2. From D.R. BARTZ

To show the effect of the throat curvature of the nozzle radius (r_c), the above equation is multiplied by $(\frac{D_*}{r_C})^{0.1}$, i.e.,

$$h_g = \left[\frac{C}{D_*^{0.2}} (\frac{\mu^{0.2} C_p}{Pr^{0.6}})_0 (\frac{D_*}{r_C})^{0.1} \left(\frac{P_C\, g}{C_*}\right)^{0.8}\right] \left(\frac{A_*}{A}\right)^{0.9} \sigma \qquad (417)$$

To obtain (Pr) and (μ) for the mixture of combustion gases, especially when data are not available, kinetic theory can be used, the approximate results of which are as follows:

$$Pr = \frac{4\gamma}{9\gamma - 5} \qquad (418\text{-a})$$

$$\mu = (46.6 \times 10^{-10})\ m^{\frac{1}{2}} (T_{\circ R})^{\omega} \qquad (418\text{-b})$$

For $\gamma = 1.2, \gamma = 1.3,$ and $\gamma = 1.4$ at $\omega = 0.6\ lb\ /\ (in.sec)$, the variations $\frac{T_W}{T_0}$ against $\left(\frac{A_*}{A}\right)$ are shown logarithmically in figure 125.

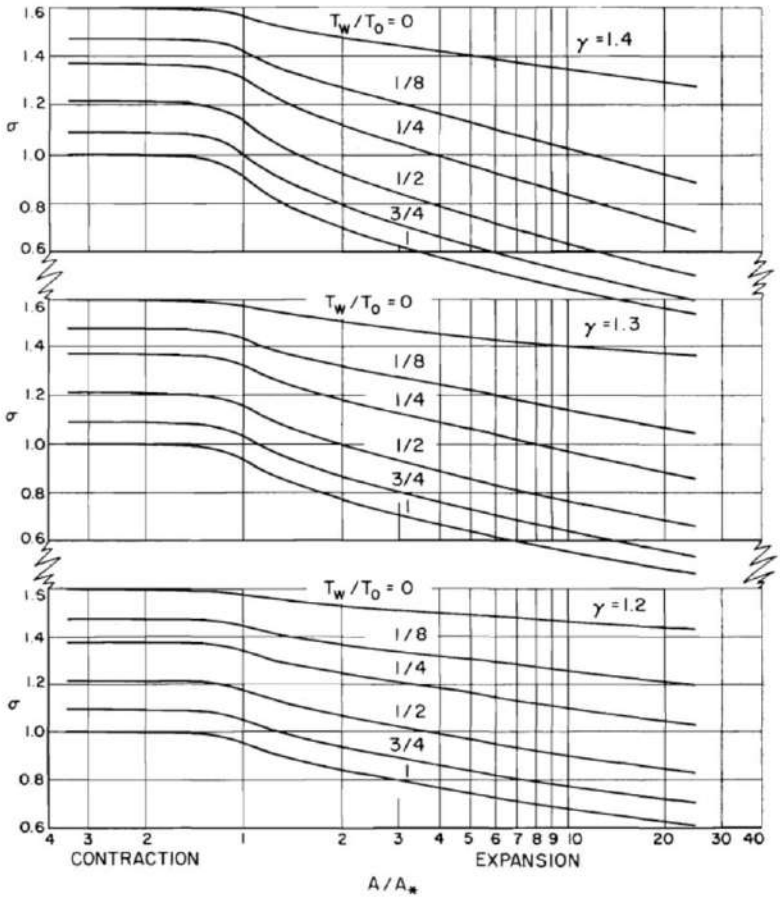

Figure 124- Values of the property's variation parameter σ. From D. R. BARTZ

According to the experimental results obtained from studies (index.cinafar and dobrovoski [29]), the heat transfer coefficient in terms of dimensionless Reynolds and Prandtl numbers is expressed as follows:

$$h_g = \frac{k_g}{d} 0.0162\ Pr_g^{0.82} Re_g^{0.82} (\frac{T_{aw}}{T_{wg}})^{0.35} \tag{419}$$

Adiabatic wall temperature can also be obtained from the following equation:

$$T_{aw} = T_C\left[\frac{1+r\left(\frac{\gamma-1}{2}\right)M^2}{1+\left(\frac{\gamma-1}{2}\right)M^2}\right] \tag{420}$$

Where (r) is called the recovery factor and for turbulent flows is

$$r = Pr^{0.33} \tag{421}$$

For the case that there are solid particles in the exhaust gas or the propellants are in the form of hydrocarbons, the heat transfer coefficient is obtained from the following equation:

$$h_{g_C} = \frac{1}{\frac{1}{h_g}+R_d} \tag{422}$$

The following figure shows the thermal resistance due to carbon deposit for the case where the chamber pressure and mixture ratio are equal to 1000 Psi and 2.35 for LO_2 / $RP1$ propellants in different surface ratios, respectively.

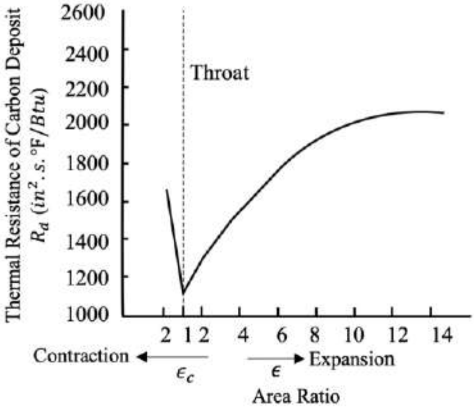

Figure 125- Thermal resistance of carbon deposit on chamber walls LO2/RP-1, mixture ratio = 2.35, (pc)ns - 1.000 psia. From Design of Liquid Propellant Rocket Engines

The thickness of the soot layer in inches for the convergent and divergent parts of the nozzle is:

Converging section:

$$\begin{cases} 0.0041213\left(\frac{A}{A_t}\right) + 0.00410 & 1 < \frac{A}{A_t} < 2 \\ 0.01234 & 2 < \frac{A}{A_t} \end{cases} \tag{423}$$

Diverging section:

$$\begin{cases} 0.0000442\left(\frac{A}{A_t}\right)^2 + 0.0011448\left(\frac{A}{A_t}\right) + 0.007092 & ,1 < \left(\frac{A}{A_t}\right) < 12 \\ 0.01445 & ,12 < \frac{A}{A_t} \end{cases}$$
(424)

As mentioned earlier, gas heat transfer also involves radiation heat transfer. This type of heat transfer, depending on the gas composition and geometry, and chamber temperature, accounts for about 3 to 40 percent of the heat transfer on the wall and is due to the temperature that appears as internal energy. It should be noted, however, that gases with symmetrical molecules such as hydrogen, oxygen, and nitrogen do not participate in this type of heat transfer because they do not absorb radiation. In contrast, heteropolar gases such as water vapor, carbon dioxide, hydrogen chloride, hydrocarbons, ammonia, nitrogen oxides, and alcohol have a significant effect on radiant heat transfer. In fact, the radiation intensity of all gases is directly related to the volume, partial pressure, and the fourth power of the absolute temperature of that gas, so for a smaller thrust chamber, the contribution of radiation heat transfer will be small. It should be noted that the more reactants and reaction products contain more solid particles or liquid droplets, the higher the heat transfer rate (2 to 10 times) will be achieved. Hence, the specific impulse and the efficiency will increase, but the presence of these particles and droplets, especially in the throat and upstream of the nozzle, causes them to collide with the nozzle wall and thus increase heat transfer. In addition, it can cause phenomena such as abrasion and erosion in the nozzle wall. According to the second law of thermodynamics and that radiation energy is a function of its surface properties and temperature, its relationship is expressed as follows:

$$E = f\epsilon\sigma AT^4 \tag{425}$$

Where f is as a geometric coefficient and also to express the surface properties and properties of materials, a dimensionless coefficient ϵ called emissivity is used. σ is also known as the Stephen-Boltzmann coefficient ($5.67 \times 10^{-8}\frac{W}{m^2.K^4}$).

For propellants that contain only hydrogen, nitrogen, oxygen, and carbon, the radiative heat transfer relationships obtain by

$$\dot{q}_{rad} = \dot{q}_{rad_{CO_2}} + \dot{q}_{rad_{H_2O}} \qquad [\frac{Kcal}{m^2.h}] \tag{426-a}$$

$$\dot{q}_{rad_{CO_2}} = 3.5\sqrt{0.6P_{CO_2}D}[\left(\frac{T_{aw}}{100}\right)^{3.5} - \left(\frac{T_{wg}}{100}\right)^{3.5}] \quad (426\text{-b})$$

$$\dot{q}_{rad_{H_2O}} = 3.5(P_{H_2o})^{0.8}(0.6D)^{0.6}[\left(\frac{T_{aw}}{100}\right)^{3} - \left(\frac{T_{wg}}{100}\right)^{3}] \quad (426\text{-c})$$

Heat transfer on the coolant side is also in the form of forced heat transfer. In this cooling model, in which the cooling fluid flows through passages in the body of the chamber, the heat absorbed by the cooling propellant is used to increase its temperature and energy, which increases the enthalpy of these propellants. In general, in the case of propellant used as a coolant, this method can increase the specific impulse and engine efficiency because the propellant is preheated before spraying through the injectors. It should be noted that overheating will cause damage or failure to the chamber body. Generally, the heat transfer equation on the coolant side is written as follows:

$$\dot{q} = \dot{q}_{Conv} = h(T_{wc} - T_{Cb}) \quad (427)$$

The heat transfer coefficient of the cooling side depends on many factors such as surface hardness, entrance effect, curvature effect, cooling channel contraction and expansion, pressure drop, cooling channel turbulence and block channel, which can be obtained only experimentally. Among the major factors affecting heat transfer are the cooling pressure and the wall temperature of the cooling side. The following figure shows the heat transfer of the wall in terms of the difference between Liquid side temperature and Bulk side temperature in pressure and bulk temperature and constant flow velocity, which represents four states of the behavior of the liquid film:

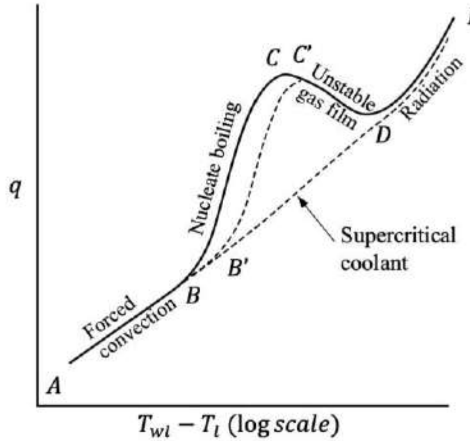

Figure 126-Regimes in transferring heat from a hot wall to a flowing liquid. From Rocket Propulsion Elements

The most ideal cooling mode is when the heat flux on the coolant raises its temperature so that the wall temperature is lower than the boiling temperature of the coolant at that cooling jacket pressure. Line A-B of the diagram shows this. The heat transfer coefficient in this case will be obtained as follows: (Ref 10, Ref 12 Chapter8-Sutton)

$$h = 0.023\overline{C_P}\frac{\dot{m}}{A}\left(\frac{Dv\rho}{\mu}\right)^{-0.2}\left(\frac{\mu\bar{C}}{k}\right)^{-\frac{2}{3}} \tag{428}$$

In this relation, $\dot{m}$, $\bar{C}$, and k represent the fluid mass flow rate, average specific heat, and conduction, respectively, and D also represents the diameter equivalent to the coolant passage. Some physical properties of several propellants are also shown in the table 13.

When the wall temperature is greater than the boiling point of the coolant (approximately 50°F to 100°F), vapor bubbles will form near the wall inside the coolant layer and will grow continuously. And then, they move to a cooler liquid stream, after which the vapor bubbles change to a condensed liquid until the rate of condensation exceeds the rate at which these bubbles form. The presence of these bubbles causes the flow to be turbulent, which results in a change in the characteristics of the liquid and increases the rate of heat transfer in a smaller interval than the temperature difference. This phenomenon is known as nucleate boiling. This mode corresponds to the B-C section of the diagram. The increase in the boiling point of the fluid as a result of the increase in pressure is also shown in the diagram (sections B'-C'). It should be noted that this condition is more common in high-pressure areas such as the throat. During this heat transfer process, if this amount of heat is so high that the population of bubbles inside the film layer increases sharply, and as a result of this high heat, the volume of these gas bubbles increases which, will increase their density, and because these bubbles do not have the ability to leave the film layer quickly, the film layer becomes a vapor layer, which makes this layer act as a thermal insulator and significantly reduces the heat transfer rate. This action increases the wall temperature and causes the melting or burning of the wall material. The region for this type of heat transfer along with the film boiling in the diagram is for the C-D section. If the wall temperature value exceeds the prior step, the heat transfer occurs in the radiation heat transfer range, although even in tests it is difficult to reach the gaseous film state due to its instability, as a result, the radiation heat transfer of the wall is not considered related to this state. And again, it should be reminded that the high temperature of the wall will cause the melting and failure of the wall. The heat transfer rate corresponding to point C is used as q_{max}. In the meantime, there are some coolants, such as liquid hydrogen, that can work above their critical temperature so that during its operation, no bubbles (**nucleate boiling** phenomenon) will be formed, and by increasing the amount of temperature difference, directly the wall heat flux increases (dash line in the diagram). Liquid hydrogen usually enters the passage at a critical pressure and then reaches a critical temperature shortly thereafter. In case the pressure is higher than the critical pressure, if the temperature is less than the critical temperature, the conditions for the operation of the nozzle and the motor are favorable and the cooling is done well. However, if the temperature exceeds the critical temperature, the boundary layer gradually becomes a stable supercritical vapor film that acts as a thermal insulator, as it does at pressures below the critical pressure, reducing the heat transfer coefficient, and increasing the wall temperature. Of course, the temperature that causes the wall to break in this case is lower than the case where the pressure is less than the critical pressure. However, the optimum design is considered to be such that nuclear boiling occurs, i.e., the operating pressure of the coolant is approximately between 0.3 and 0.7 of its critical pressure ($h_{\max}$ corresponds to point C which is the highest value of heat transfer rate). Nonetheless, in systems powered by turbopumps, the cooling pressure is greater than the sum of the injector and combustion chamber pressures and acts super critically. In any pressure range, boiling does not occur when the coolant has a temperature below the critical temperature. When the temperature difference between the fluid and the wall is significant, the changes of viscosity in respect of time should be used in it. Therefore, the improved form of this relation, called the Sider-

Tate equation, in the Dittus-Boelter expression, provides an almost accurate estimate for determining the heat transfer coefficient:

$$Nu_{Dh} = C_1 Re_{Dh}^{\frac{4}{5}} Pr^{\frac{1}{3}} (\frac{\mu_b}{\mu_w})^{0.14} \text{ where } 0.7 \leq Pr \leq 16700 , Re_D \geq 10^5, \frac{L}{D} \geq 10 \quad (429)$$

C_1: a Constant (Selected according to the type of coolant) Nu: Nuselt Number = $\frac{h_c d}{k}$

Re_{Dh} : Reynolds Number = $\frac{\rho v_c d}{\mu}$ Pr: Prandtl Number = $\frac{\mu C_P}{k}$

μ_b: Coolant viscousity at bulk temperature

μ_w: Coolant viscousity at coolant sidewall temperature

d: hydrolic diameter of coolant passage (in)

k: thermal conductivity of coolant ($\frac{Btu}{Sec.in^2 .\frac{°F}{in}}$)

v_C: Coolant velocity ($\frac{in}{sec}$)

C_P: Specific heat of coolant at constant pressure ($\frac{Btu}{lb.°F}$)

For the case where the surface roughness is considered, Gnielinski proposes the following equation:

$$Nu = \frac{\frac{f}{8}\,\mathrm{Pr}\,(Re - 1000)}{1 + 12.7\left(\frac{f}{8}\right)^{0.5}(Pr^{\,2/3} - 1)} \text{ where } 3000 \leq Re \leq 5 \times 10^6, 0.5 \leq Pr \leq 2000 \quad (430)$$

Where the Darcy-Weisbach coefficient of friction is used in it:

Laminar flow($Re \leq 2300$):

$$f = \frac{64}{Re} \quad (431\text{-a})$$

Which is known as Colebrook equation or Darcy-Weisbach friction factor.

Turbulent flow($Re \geq 10000$):

$$\frac{1}{\sqrt{f}} = -2\, log(\frac{\epsilon/_D}{3.7} + \frac{2.51}{Re\sqrt{f}}) \quad (431\text{-b})$$

Although many relationships for the friction coefficient for the turbulent flow are proposed, the obvious Wood relationship is one of the best options:

$$f = 0.094\left(\frac{\epsilon}{D}\right)^{0.225} + 0.53\frac{\epsilon}{D} + 88\left(\frac{\epsilon}{D}\right)^{0.44}\frac{1}{Re^{1.62\left(\frac{\epsilon}{D}\right)^{0.134}}} \qquad (432)$$

In the above equations D and ϵ are the hydraulic diameter and surface roughness, respectively. Moody diagram is used to graphically express the coefficient of friction, which shows the coefficient of friction based on Reynolds number and surface roughness.

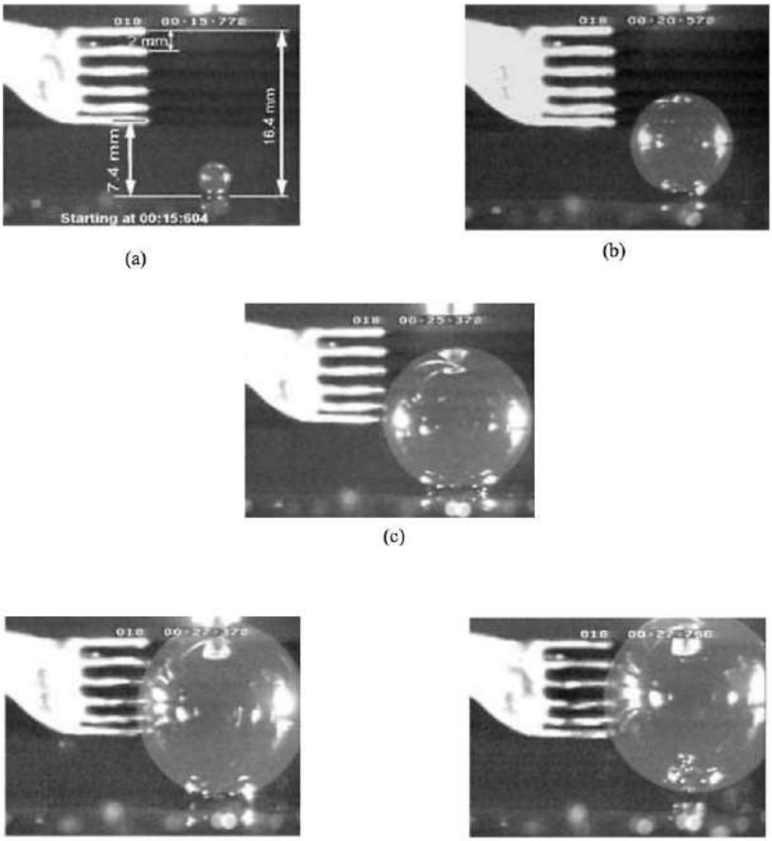

(a) (b) (c) (d) (e)

Figure 127-Selected pictures of a single bubble during a growth-departure cycle inception of nucleation. Nucleate Boiling Heat Transfer Studied Under Reduced-Gravity Conditions by Dr. David F. Chao and Dr. Mohammad M. Hasan. Glenn center

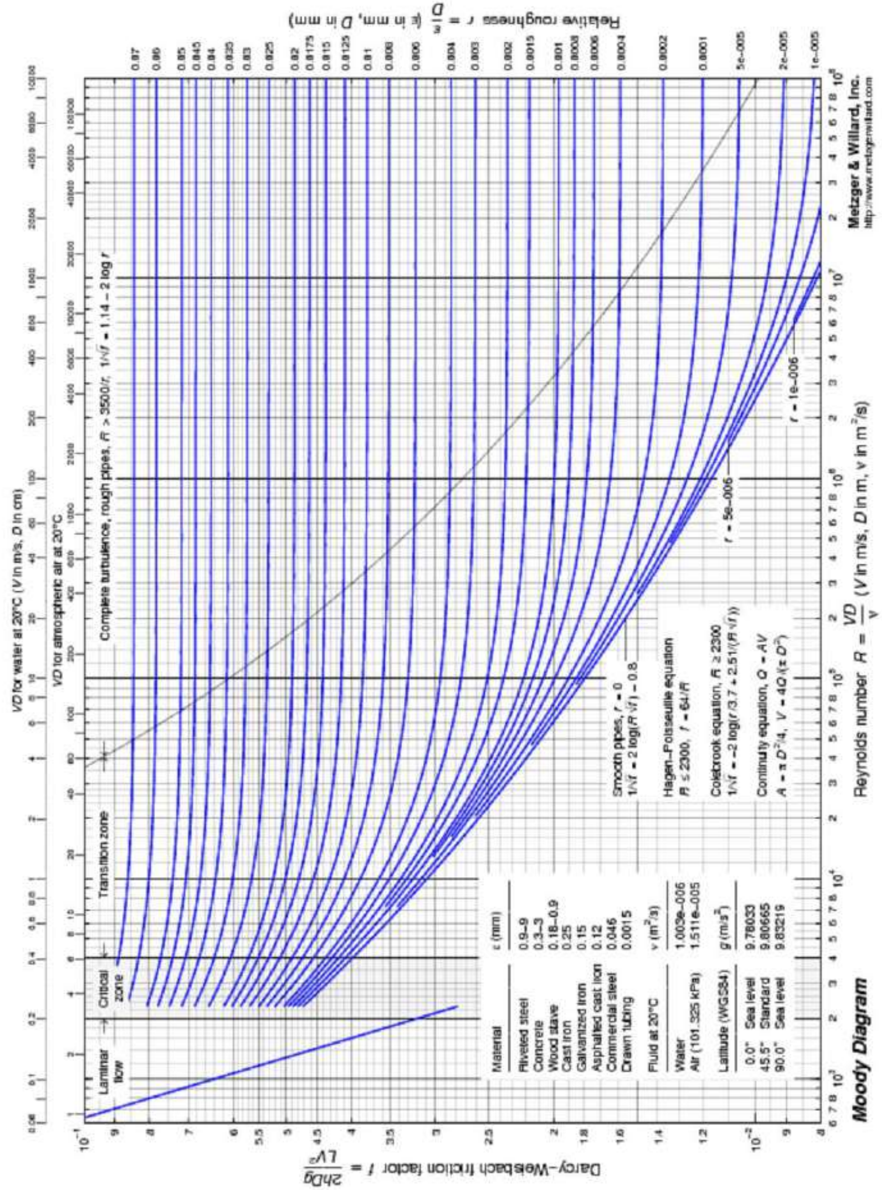

Figure 128- Moody diagram. Tom Davis (2021). Moody Diagram (https://www.mathworks.com/matlabcentral/fileexchange/7747-moody-diagram), MATLAB Central File Exchange. Retrieved September 13, 2021.

The heat flux corresponding to point c can be determined from the following equation:

$$q_{UL} = C_2 q_{NB} \frac{10^4}{P_{Co} G} \tag{433}$$

q_{UL}: heat flux of upper limit of nucleate boiling
q_{NB}: Heat flux for when Nucleate boiling does not occur. $[\frac{Btu}{in^2.sec}]$
P_{Co} : Coolant pressure. $[Psia]$
G: Coolant maximum weight flow rate. $[\frac{lb}{in^2.Sec}]$

Also, at pressures above the critical pressure at which the boundary layer of the vapor film forms, or in other words, the coolant at temperature and supercritical pressure, the following formula expresses the approximation of the heat transfer coefficient of the coolant:

$$h_c = \frac{0.029\, C_p \mu^{0.2}}{Pr^{\frac{2}{3}}} \frac{G^{0.8}}{D^{0.2}} (\frac{T_{co}}{T_{wc}})^{0.55} \tag{434}$$

As mentioned so far, it is desirable that the coolant be at a lower temperature than its critical state so as not to reduce the heat transfer coefficient. Therefore, the cooling capacity when the coolant is in the liquid phase is:

$$Q_c = \dot{W}_c C_p (T_{cc} - T_{c1}) \qquad [\frac{Btu}{sec}] \tag{435}$$

In the above equation, $\dot{W}_c$ represents the coolant mass flow rate $(\frac{lb}{sec})$, T_{cc} and T_{c1} represent the critical temperature and the coolant inlet temperature $(°R)$, respectively.
One of the important factors that should be considered in the design of cooling passages is its pressure drop, which the design conditions should be done in such a way that the pressure drop is minimized. Factors that can cause pressure drop include backflow and sudden change in the flow direction, and expansion and contraction of the cooling surface. The internal pressure drop for a smooth and clean passage can be obtained from the Darcy-Weisbach equation, which is established in both flow regimes:

$$\Delta P = h_f = f \frac{L}{D} \frac{\rho v_{co}^2}{2g} \tag{436}$$

In this equation, f can be determined from the equations (431-a or 431-b) or also the wood expression (Eq. 432), although the coefficient f in turbulent flows is mostly obtained experimentally.

DESIGN OF COOLING PASSAGES

a As mentioned, for areas that need higher heat transfer, by reducing the diameter of the passage, the cooling flow rate can be increased, which results in an increase in heat transfer rate in that area. Therefore, designing suitable geometry for the passages is treated as an important subject. Many models have been proposed for the design of these passages, the two most common types being Axial-flow cooling jackets and coaxial shell, which is shown in figure 130-a. The first model consists of pipes that are placed in the direction of the thrust axis inside the body of the thrust chamber. This geometry is often used for systems that generate high thrust (weight above 3000 lb). In the second model, which is used in smaller thrust chambers, the gap between the chamber walls is used as a cooling passage, which is classified using helical ribs or wires.

Generally, cooling passages establish in tubular or channel construction methods. Some advantages of both methods are listed below.

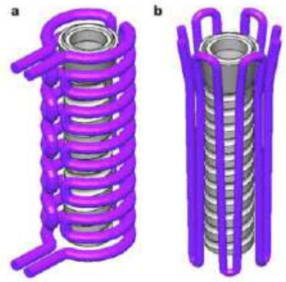

Tubular constriction:

- Light-Weight
- Extensive fabrication experience
- Little conduction between tubes

Channel construction:

- Smooth hot-gas wall (reduce heat load)
- Conduction between channels, which falls into two categories, tolerance to flow variation and tolerance to fabrication variation, respectively.
- Channel flow area can be closely controlled.

Figure 129- Coaxial shell thrust chamber cutaway. Note over-heated and burnt-through spot on clamber wall.

Figure 130-b shows several examples of different geometries used within the chamber.

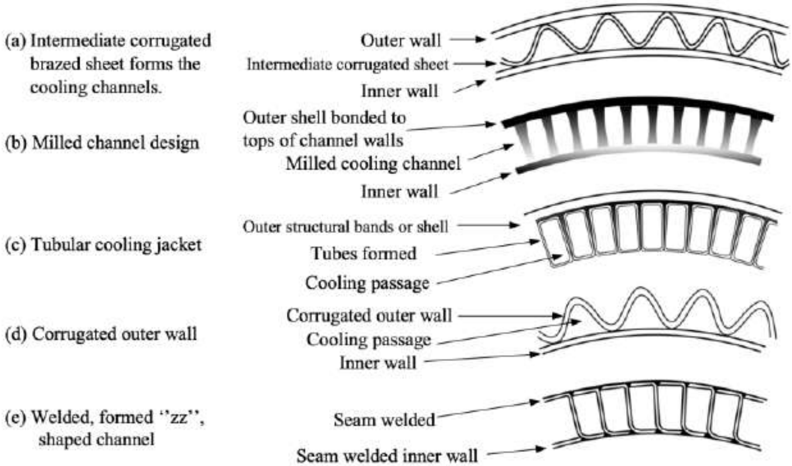

Figure 130- (a) - (b) milled cooling channel

Another commonly used geometry is the use of circular tubes, which are less than the proposed geometries due to the easier manufacturing process and lower applied stresses. The effective stresses such as

1. Hap stress: Stresses due to cooling pressure on the shell wall.
2. Thermal stress: Stress caused by temperature gradient in tubes and walls.
3. Bending stress: Stress due to distortion caused by the pressure gradient on the tubes.

As a result, the maximum tangential stress on the tubes can be obtained according to the following equation:

$$S_t = \frac{(P_{co}-P_g)r}{t} + \frac{E\alpha qt}{2(1-\nu)k} + \frac{6M_A}{t^2} \tag{437}$$

S_t: Combined tangential tensile stress. $(\frac{lb}{in^2})$

P_{co}, P_g : Coolant and combustion gas pressure respectively. $(\frac{lb}{in^2})$

M_A : bending momentum caused by discontinuity. $(\frac{in.lb}{in})$(No effect of pressure differential between adjacent tubes for circular tube design)

k: Thermal conductivity of tube wall material. $(\frac{Btu}{in^2.sec.\frac{°F}{in}})$

q: heat flux. $(\frac{Btu}{in^2.sec})$

t ,r: tube wall thickness & radius. (in)

E: modulus of elasticity of tube wall material. $(\frac{lb}{in^2})$

α: Thermal expansion coefficient of tube wall material. $(\frac{in}{in.°F})$
ν: Poisson ratio of tube wall material.

The important point about stresses is that because the inner shell is exposed to much higher temperatures than the outer shell, it is subject to more stress, hence it undergoes more thermal expansion. However, since the set operates as a continuous system, this excess amount of thermal expansion of the inner shell will be inhibited by the outer shell. But, as a result of this inhibition as well as the greater mass of the outer shell, the inner shell will undergo inelastic thermal buckling. Longitudinal thermal stress can also be estimated as follows:

$$S_1 = E\alpha\Delta T \quad [\frac{lb}{in^2}] \tag{438}$$

Where ΔT is the mean temperature difference (°F) of the two inner and outer shells. This value of longitudinal stress shall not be less than a value of 0.9 critical thermal stress as defined below:

$$S_c = \frac{4E_t E_c t}{(\sqrt{E_t}\sqrt{E_c})^2\sqrt{3(1-\nu^2)r}} \quad [\frac{lb}{in^2}] \tag{439}$$

The E_t and E_c used in the above equation represent the tangential modulus of elasticity at wall temperature and the tangential modulus of elasticity, respectively, which E_c can be obtained from the compressive stress-strain curve at wall temperature. For the case where the cross-section of the tubes is more elongated and out of the circular position, according to the following figure, the equations (437), (438), and (439) are established so that the bending momentum is again in the inner wall of the pipe be maximized and will not dependent on the pressure difference between them.

$$M'_a = M_a + K_a \frac{L\Delta P}{2} \tag{440}$$

M'_a: Combined bending momentum at section A. $[\frac{in.lb}{in}]$
M_a: bending momentum due to discontinuity. $[\frac{in.lb}{in}]$
L: Length of fuel portion on tube wall. $[in]$
K_a: Dimension less design constant based on test results. (Range 0.3 - 0.5)
ΔP: Pressure differential between adjacent tubes. $[\frac{lb}{in^2}]$

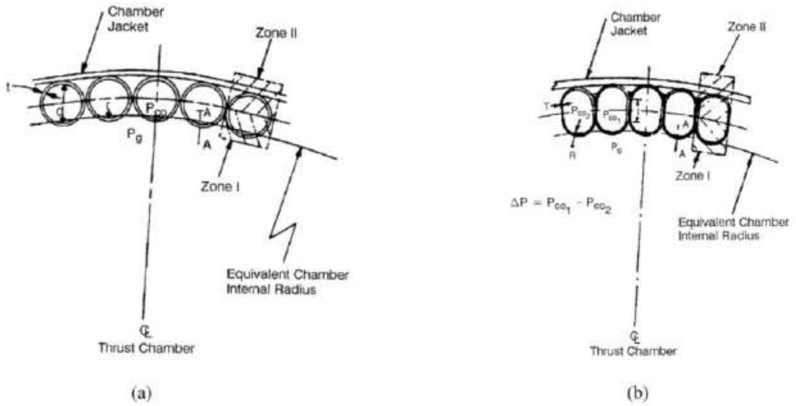

Figure 131-5 Elongated and circular tube wall of regeneratively cooled thrust chamber. From Design of Liquid Propellant Rocket Engines

This pressure difference inside the tubes creates forces on the body and the wall of the chamber that are absorbed by the tension straps wrapped around the chamber, as well as by the chamber jacket. For systems with a coaxial shell combustion chamber, the maximum stress that occurs in the inner shell can be obtained as in equation (411), except that no bending will occur in this type. So that the outer shell is only affected by the hoop stress which is caused by the cooling pressure and the inner shell is also affected by the thermal and compressive stresses caused by the wall temperature gradient and the pressure difference between the coolant and the combustion gases. As a result, the maximum stress in the inner shell in this model will be obtained by:

$$S_c = \frac{(P_{co} - P_g)R}{t} + \frac{E\alpha q t}{2(1-\nu)k} \qquad [\frac{lb}{in^2}] \qquad (441)$$

The process of making these channels was initially in such a way that two shells were placed next to each other and welded (soldered) between them to form the passages. However, due to the very low manufacturing accuracy and the fact that these welds are difficult to inspect, other manufacturing methods are used, one of which is a method in which pre-prepared pipes are used. In this method, numerous tubes are placed side by side on the surface of forming a mold, and on the other hand, another mold covers them so that the set becomes like a sandwich. The set of molds and pipes are placed together in a press, and at the same time, according to the press and the shape of the mold, the pipes are deformed, and the molds are connected to each other. Therefore, the pipes are placed in a relative proportion, although the computer is used to minimize the empty space (gap) between the two pipes.

After this process, the relative position of the pipes is determined and the pipes are placed on a bonding fixture. The following figures show a schematic of this process. (Refer to Figure 132 and 133)

Disadvantages of this method include the design, the many machinations in it, and the fact that each pipe must be welded separately to the manifold, all of which point to the high cost and time-consuming and difficult manufacturing process. To solve this problem, another method is proposed in which molten metal is sprayed on the outer shell of the bunch of pipes and the ends of the pipes are covered with predetermined thicknesses. Then, at the intersection of the pipes and manifold, machining is done to reach the required thickness. The steps of this construction model are specified in figures of 135.

Figure (A) shows side-by-side tubes that are before spraying the molten material on it, the two ends of the pipes are first crimped to prevent the molten material from entering it (3). And in the next step, they start machining the outer shell (5), the manifold is then machined to expose the tubes (6). Figure (E) also shows the final chamber. There is another method in which the distance between the tubes is done through laser powder injection welding, which closes the gap between the tubes and holds them tightly together. This method can even be used to connect the jacket to the tubes. An overview of this process is also given in the following figure. (Figure 135- fig 1…5 WO1995)

Figure 136 shows the cross-section of the tubes along with the thrust chamber, where the cross-section of the tube changes at different points according to the characteristics of the fluid. The formation of these tubes is such that they are first pipes with a circular cross-section filled with wax that is subjected to the hydraulic pressure of the mold to find the desired final shape. (fig 4-31, page 122 from Huzel)

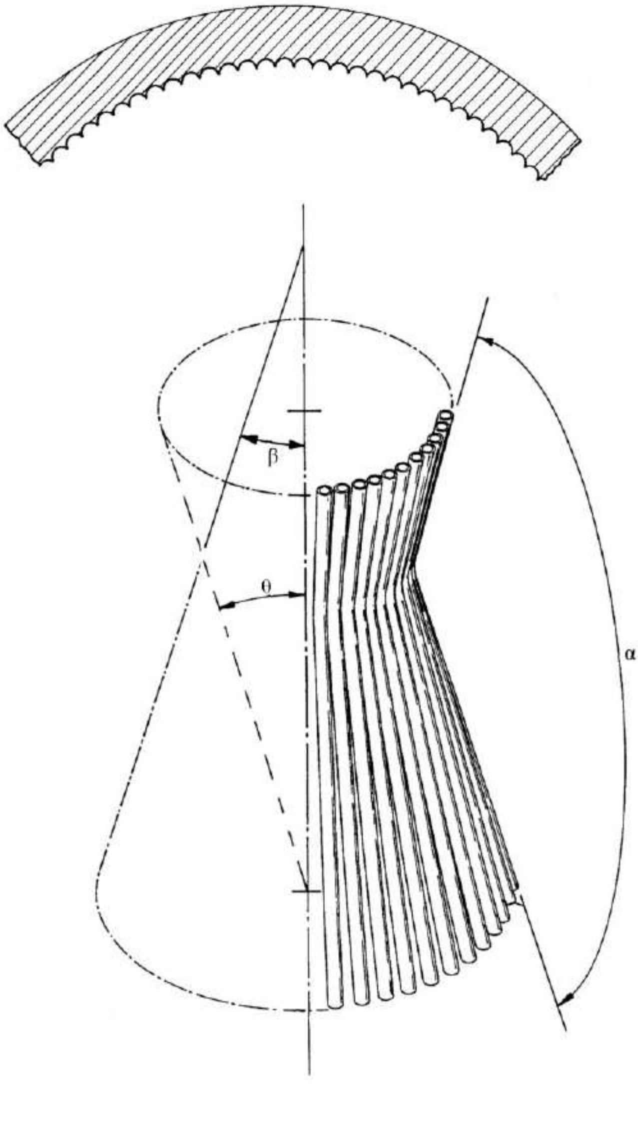

Figure 132- Relative position of pipes, Adopted from US5477613

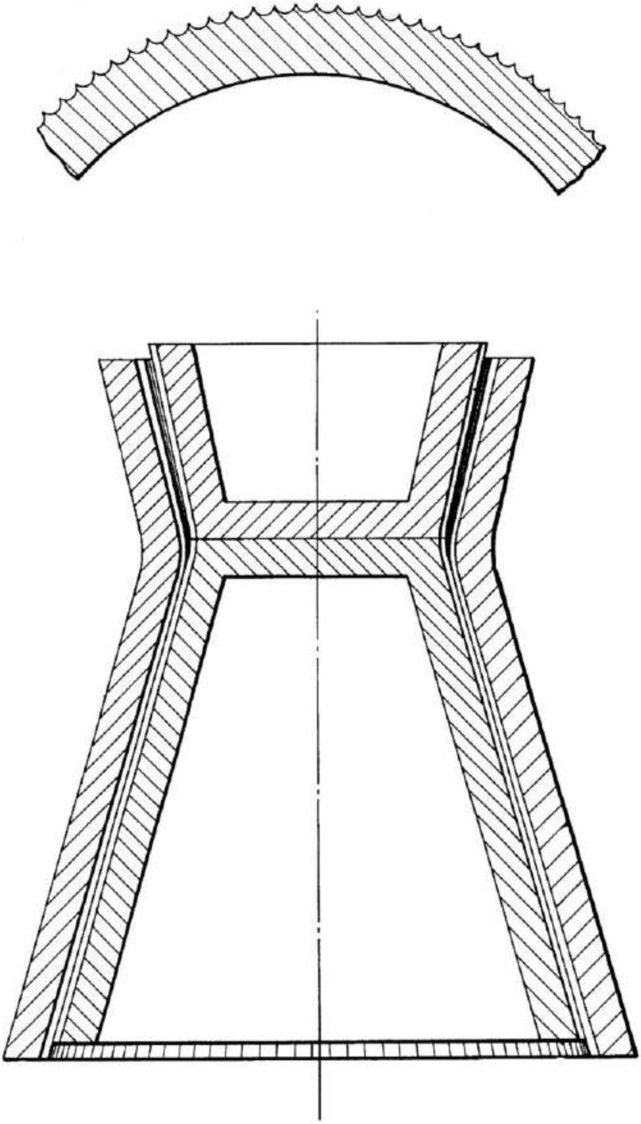

Figure 133- Bounding fixture of pipes, Adopted from US5477613

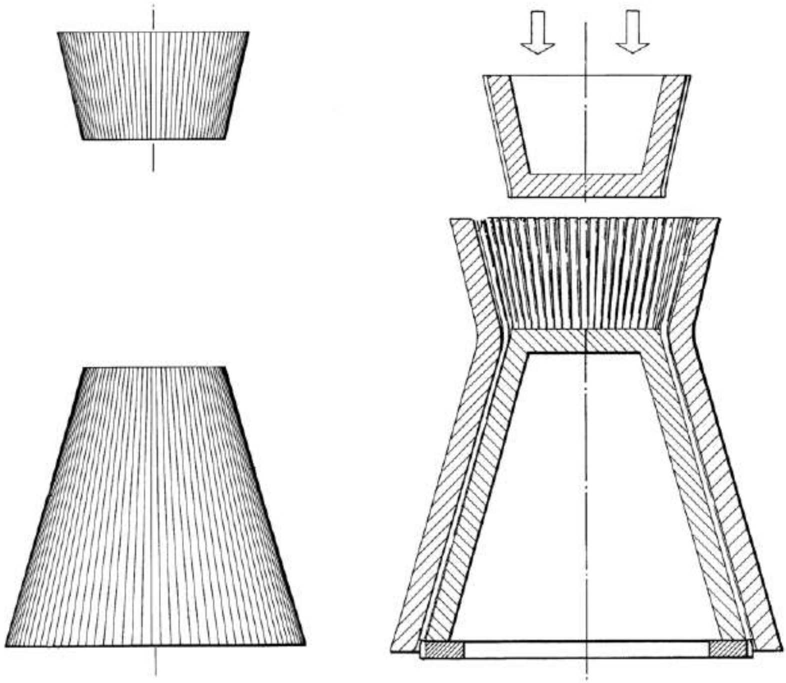

Figure 134- Construction Schematic of the Pipes and Fixture, Adopted from US5477613

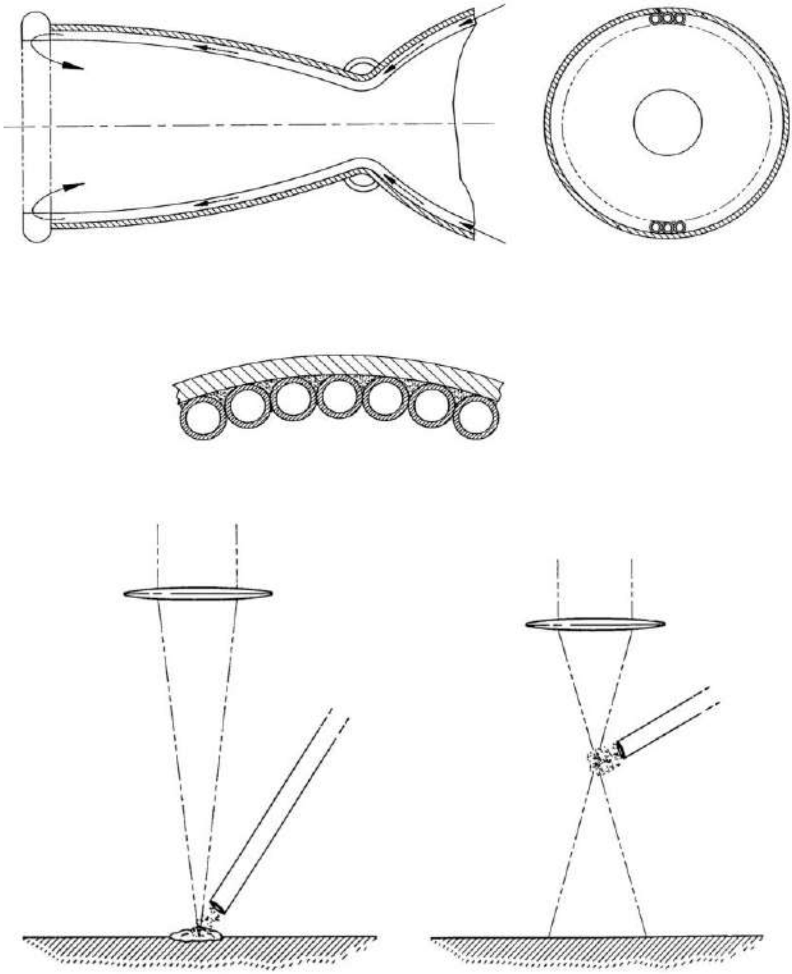

Figure 135- an overview of the construction model, Adopted from WO1995029785A1

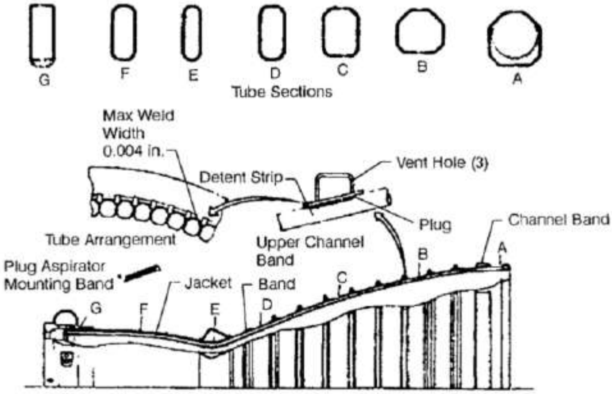

Figure 136- Typical regeneratively cooled tube wall thrust chamber. From Design of Liquid Propellant Rocket Engines

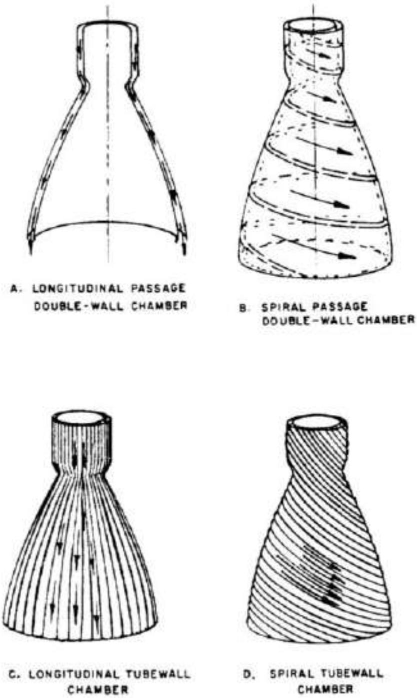

Figure 137- Typical dump-cooled chamber fabrication methods. From Design of Liquid Propellant Rocket Engines

DUMP COOLING:

This cooling method, which is similar to the previous method, can be used effectively in low-pressure nozzles (100 Psi) as well as in high-pressure nozzle extensions, especially for systems that run on hydrogen fuel. In this method, hydrogen enters the cooling passages directly from the feed-system and leaves the end of the nozzle after it becomes superheated. Because hydrogen expands significantly at this temperature and high speed, it will also produce some thrust. In general, this type of cooling is used in axial and circumferential flows. In designing this system, it should always be based on maximum performance and at the same time, factors such as weight, construction difficulty and production and maintenance costs should be considered. In the category of axial flows, two geometry models can be used, in the first model the propellant passes through two walls, and cooling is done (Figure 137-A). In the second model, the propellant flows out through the tubes that are placed on the wall (Figure 137-B). For circumferential flows, superheated hydrogen either passes through two walls with circular paths embedded between them or through tubes wrapped around the nozzle bodies (Figures 137 C and D). Axial flow systems are often used in larger systems, while circumferential flow systems will be used in cases where controlled speed is required.

FILM COOLING:

Stresses are one of the important factors that should be minimized in the design. Thermal stresses can be reduced by decreasing the heat transfer of the chamber wall, for which purpose, the film cooling technique is proposed. The porous walls and the slots or louvers, and holes embedded in the wall of the thrust chamber are also an efficient method for cooling the chamber, which is usually not used alone but has a great effect on cooling. The operation is in such a way that the coolant (about 3% of the propellants) is sprayed through the slots located on the inner wall of the chamber and alters the temperature profile through the Thermal boundary layer, hence the heat flux of the nozzle wall is decreased. In a fully film-cooled design, injection holes are located at incremental distances along the wall length. The holes in each coolant row cover a range from that row to the next row, and the reason for this is that during the flow of these coolants in the chamber wall, the reaction between the coolant and the resulting hot gases formed from combustion reduces the thickness of the cooling film on the wall, so we need to strengthen these coolants, which refers to the row of holes. For cooling by this technique through coolants, another model can be used by spraying some fuel through the hole created in the outer circle of the injector orifices (as shown below) towards the chamber wall, which causes the formation of a fuel-rich gas boundary layer on the wall. Experimental results have shown that the use of cooling film in the liquid phase is more effective than the gas phase in reducing heat transfer to the wall. In this case, the coolant will act like an isothermal heat sink because it evaporates and spreads into the free stream. In liquid film cooling, the vaporized film coolant does not diffuse rapidly in to the main exhaust gas stream but stand out as a protective mass of vapor adjacent to the wall for an appreciable distance downstream from the liquid film latest terminal. This makes the length of the hot gas flow passage protected by the liquid film is significantly longer than that of the liquid film (from N6638728). In comparing liquid film cooling and gaseous film cooling, it should be noted that the basis of these heat transfers is evaporation and sensible heat exchange, respectively. The advantages of liquid film cooling over gaseous film cooling in that the liquid film has a lower density over the gaseous film, which reduces the limitation of tanks, and has more cooling effects due to the much greater latent heat of liquids. It should be noted that liquids (except hydrogen and helium), have a higher specific heat than gases. However, the disadvantages of this method (liquid film cooling) are that the evaporation of the coolant during this process reduces the cooling potential, and also the disturbances that occurred on the surface of the liquid film adjacent to the combustion gases will cause the coolant acceleration to be lost. The use of liquid cooling film has a much higher efficiency than other propellants, and this is the result of film formation and cooling deposits. As mentioned earlier, the presence of solid carbon deposits acts as insulation and reduces heat transfer to the wall. The overall efficiency of liquid coolants obtained through real-time tests is between 30 and 70%.The theoretical equation of Zucrow and Sellers can be used in the thrust chamber design with the liquid film cooling.

$$\frac{G_c}{G_g} = \frac{1}{\eta}\frac{H}{a(1+b^{\frac{C_{pvc}}{C_{pg}}})} \tag{442}$$

$$a = 2\frac{v_d}{v_{mf}} \tag{443-a}$$

$$b = \left(\frac{v_g}{v_d}\right) - 1 \tag{444-b}$$

$$H = \frac{C_{pvc}(T_{aw} - T_{wg})}{C_{plc}(T_{wg} - T_{co}) + \Delta H_{vc}} \tag{445}$$

G_c: Film coolant weight flow rate per unit area of cooled chamber wall surface.$[\frac{lb}{in^2.sec}]$

G_g : Combustion gas weight flow rate per unit area of chamber cross section perpendicular to flow.$[\frac{lb}{in^2.sec}]$
η_c: Film cooling efficiency.
H: Film coolant enthalpy. $[\frac{Btu}{lb}]$
ΔH_{vc}: heat of vaporization of coolant. $[\frac{Btu}{lb}]$
C_{plc}: Average specific heat at constant pressure of the coolant in the liquid phase. $[\frac{Btu}{lb.°F}]$
C_{pvc}: Average specific heat at constant pressure of the coolant in the vapor phase. $[\frac{Btu}{lb.°F}]$
C_{pg}: Average specific heat at constant pressure of the combustion gases. $[\frac{Btu}{lb.°F}]$
f: Applicable friction coefficient for the two-phase flow between combustion gases and liquid film coolant.
v_d: Axial stream velocity of combustion gases at edge of boundary layer. $[\frac{ft}{sec}]$
v_m: Average axial stream velocity of combustion gases. $[\frac{ft}{sec}]$
v_g : Axial stream velocity of combustion gases at the center line of the thrust chamber. $[\frac{ft}{sec}]$
T_{aw}: Adiabatic wall temperature of the gas. $[°R]$
T_{wg} : Gas- side wall temperature and coolant film temperature. $[°R]$
T_{co}: Coolant bulk temperature at manifold. $[°R]$

As mentioned earlier, the liquid film injected through the injector into the combustion gases evaporates due to excessive heat, and as a result, the film will behave like a gas. The Hatch and Papell equations can be used to design a thrust chamber with a gaseous film cooling:

$$\frac{T_{aw}-T_{wg}}{T_{aw}-T_{co}} = exp^{[-\frac{h_g}{G_c C_{pvc}\eta_c}]} \tag{446}$$

T_{wg} : minimum gas- side wall temperature. $[°R]$
T_{co}: initial film cooling temperature. $[°R]$
h_g : Gas-side heat transfer coefficient. $[\frac{Btu}{in^2.sec.°F}]$

The efficiency of the cooling film in this regard is the correction factor for the cooling film of gases that have entered the combustion gases without having a significant effect on the cooling of the chamber. The range of this coefficient is between 25 to 75% depending on the flow conditions and the geometry of the cooling injection (Design of Liquid Propellant Rocket Engines). The above equation indicates the equilibrium between the thermal energy and the coolant temperature increment, which means that if an equilibrium is established, all the heat is used to raise the film temperature and wall temperature will be nearly constant (adiabatic wall condition), and equal to the film temperature. As mentioned earlier, each row of holes on the thrust chamber wall, which is installed to inject the cooling film, has the ability to cool a certain range. And due to the fact that the temperature of the chamber increases along the axis, therefore, in each area, the wall surface temperature will change from the initial temperature of the coolant inlet to the maximum allowable temperature of the wall design.

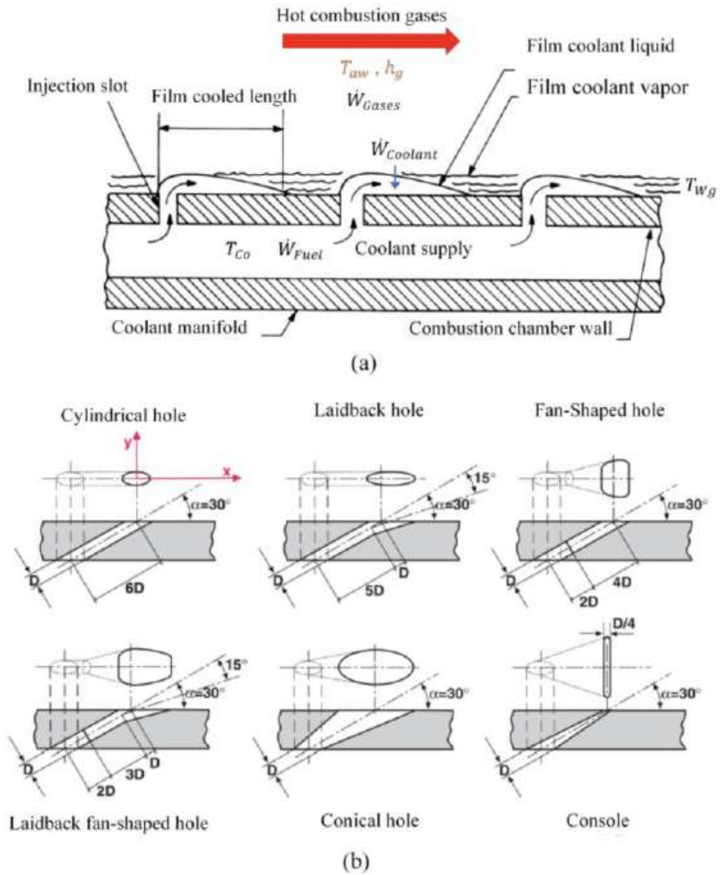

Figure 138-(a) Film cooling model, (b) Film cooling slot shapes. From N66 38728 & Large Eddy Simulation of the Film Cooling Flow System of Turbine Blades: Public Shaped Holes by SIMIRIOTIS Nikolaos.

It should be noted that the most common coolants have two main characteristics; first, they are materials that have a high heat capacity, and second, they have the ability to produce gases with the lowest molecular weight. Some of these materials are listed in table 20. The figure below shows the hydrogen film cooling system in the thrust chamber, which consists of four film-coolant injector rings upstream and one ring downstream. Generally, the use of coolant film in the axial mode has a higher efficiency than normal injection because, in the normal mode, a large part of the coolant with combustion gases will leave the chamber.

Coolants	H_2	He_2	H_2O (g)	NH_3	N_2	air	CH_3OH	Ar	CO_2	$C_3H_8O_3$
Molecular Weight	2	4	18	17	28	29	32	40	44	92
SHC at 370 K $(kJ/kg.K)$	14.45	5.20	2.14	2.22	1.03	1.00	1.72	0.52	0.91	2.40

Table 20- Common coolants and their properties. Adopted from thermal protection by Polezhayev Yu V & Yurevich F B.

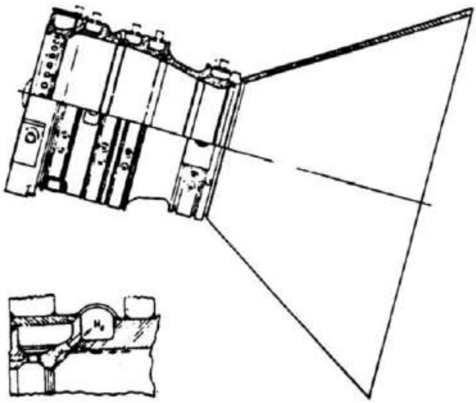

Figure 139- Experimental hydrogen/oxygen, film-cooled thrust chamber. From Design of Liquid Propellant Rocket Engines.

Thermal stresses are caused by the large variations in the wall temperature due to the non-optimum spacing of injection location, and inefficient cooling results from over cooling of the wall in the injector region. Therefore, injection velocity and injector manifold design are important.

Film cooling may be used effectively to protect the combustion chamber and nozzle walls in several ways as follows: (from Selecting Cooling Techniques for Liquid Rockets for Spacecraft CLIFFORD D. COULBERT* The Marquardt Corporation, Van Nuys, Calif)

1. Reduction of the adiabatic wall temperature to a value below the material limiting value.
2. Radiation in the heat flux to a wall which is also cooled by radiation, convection, or a heat sink.
3. Maintaining a non-oxidizing gas adjacent to refractory surfaces otherwise capable of withstanding full combustion gas temperature, such as uncooled tungsten, tantalum, or various carbides.

In general, the advantage of film cooling over other techniques is the no inherent limitation on cooling capacity, time, or chamber pressure.

However, the disadvantage of this method wherein one of the propellants (usually fuel) or inert fluids are used is the performance penalty (specific impulse losses) due to the gas and temperature stratification.
The gaseous film cooling effectiveness (η)in terms of Reynolds number of the cooling fluid at the slot exit ($\frac{V_C y_C}{v}$), the ratio of downstream distance to slot width ($\frac{x}{y_C}$), and the velocity ratio ($\frac{V_C}{V_g}$), where V_C and V_g are coolant and mainstream velocity, respectively.

$$\eta = C(\frac{V_g x}{V_C y_C})^{-0.8}(\frac{V_C y_C}{v})^{0.2} \quad (447)$$

Where C is a constant and η define as follows:

$$\eta = \frac{T_{ad} - T_{ad'}}{T_{ad} - T_C} \quad (448)$$

T_{ad}: Adiabatic wall temperature without film cooling.
$T_{ad'}$: Adiabatic wall temperature with film cooling.
T_C: Temperature of coolant at exit slot.
x, y_C: Distance along wall and width of slot in direction normal to the wall, respectively.

Stolley and El-Ehwany made a simplified derivation which equated the film cooling effectiveness in terms of enthalpy (H). This expression, which obtained good correlation to experimental data, is: (from N6638728)

$$\eta' = 3.09\left(\frac{V_g x}{V_C y_C}\right)^{-0.8}\left(\frac{V_C y_C}{v}\right)^{0.2} \quad (449)$$

Where:

$$\eta' = \frac{H_{ad} - H_g}{H_C - H_g} \quad (450)$$

Spaulding compared most of the authors' theories on predicting the adiabatic wall temperature in film cooling systems. To emphasize the similarity of the theories, he limited his discussion to two-dimensional flows with uniform properties. The proposed relationship for the velocity ratio of coolant to the mainstream from zero to 14 is consistent with the experimental results and data obtained from various forms of geometric arrangements. These results for uniform properties are as follows:

$$X < 7 : \eta = 1 \quad (451)$$

$$X > 7 : \eta = \frac{7}{X} \quad (452)$$

$$X \equiv 0.91(\frac{V_g x}{V_C y_C})^{0.8}(\frac{V_C y_C}{v})^{0.2} + 1.41(\left|1 - \frac{V_g}{V_C}\right| \times \frac{x}{y_C})^{0.5} \quad (453)$$

Although this theory is not accurate, Spaulding has shown that it can be used in a wide range of velocity ratios and geometrical slot arrangements with fair correlation to experimental data.

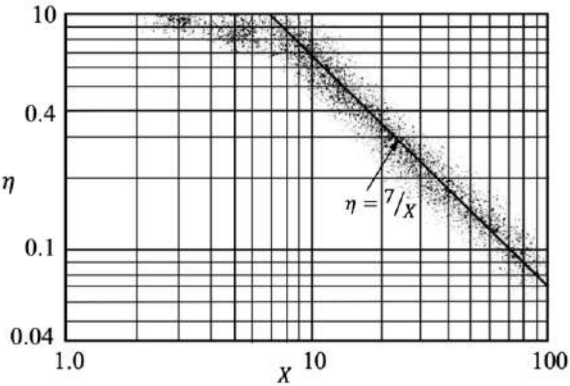

Figure 140- Agreement Between Equation (44) and the Data of Various References. From N6638728

The Hatch and Papell model begin by assuming that the coolant film exists as a discrete layer (no mixing). Two empirical modifications are then made to take care of the mixing phenomenon. This model provides a good basis for correlating experimental data taken reasonably close to the coolant slot $0 < \frac{X}{S} < 150$,where S is the coolant slot height (From N6638728). It should be noted that this method was developed for the flow of high-temperature gases which was used on a simple heat transfer model and was determined by empirical constants and parameters.

Since this method was only developed for tangential injection of the coolant parallel to the adiabatic wall, subsequently considering several other semi-empirical terms by Papell in the equation, the data obtained from the equation with the experimental results obtained from the coolant injection through the angled slots and normal holes matched together. However, these data were limited to subsonic flow with no pressure gradient in the flow direction. Therefore, the Hatch-Papell equation rewrite as follows

$$\ln \eta = \ln\left(\frac{T_{ad} - T_{ad'}}{T_{ad} - T_C}\right) = -\left(\frac{h_g L x}{(WC_P)_c} - K\right)\left(\frac{SV_g}{a_c}\right)^{\frac{1}{8}} f\left(\frac{V_g}{V_c}\right) +$$

$$\ln \cos 0.8\, \beta_{eff} \quad (454)$$

where

$$\beta_{eff} = \tan^{-1}\left(\frac{\sin\beta}{\cos\beta + \frac{(\rho V)_g}{(\rho V)_c}}\right) \tag{455}$$

And

$$f\left(\frac{V_g}{V_c}\right) = \begin{cases} 1 + 0.4\tan^{-1}\left(\frac{V_g}{V_c} - 1\right) & \frac{V_g}{V_c} \geq 1.0 \\ 1.5\left(\frac{V_c}{V_g}\right)\left(\frac{V_c}{V_g} - 1\right) & \frac{V_g}{V_c} \leq 1.0 \end{cases}$$

(456-a, b)

In these equations, all parameters and coolant properties are measured and computed at the temperature and pressure of the coolant in slot location. All angles are in radiant and convective heat transfer coefficient is only $K = 0.04$. Equation 454 can be used for multiple-slot as well as single-slot. Convective heat transfer coefficient for gaseous film cooling is also obtained by

$$h = 0.0265\frac{K_f}{D_h}Re_f^{0.8}Pr_f^{0.3} \tag{457}$$

The adiabatic wall temperature with gaseous film cooling (T'_{ad}) is calculated and then its determined for the next row again, but the adiabatic wall temperature without gaseous film cooling (T_{ad}) is the function of the distance downstream of the slot (x) and is actually the T'_{ad} curve from the original slot. In other words, the T_{ad} at each slot and each time is equal to the T'_{ad} , which is obtained by the previous slot calculation. Sellers, by using $K = 0$ instead of 0.04 in equation 454, has shown that there is good agreement between calculated wall temperature and experimental data for 2,3,4, and 5 slots with different dimensions. Therefore, it can be understood from this experiment that $K = 0.04$ may be too high for rocket heat transfer. To eliminate the effect of slot height (s), which is a basic parameter and could not be applied to the hole configuration data, hence the definition of effective slot height (s') is used as the ratio of the total area of the coolant flow to the width of the first row of holes, i.e., $(\frac{A_c}{t})$. In this case, for a velocity ratio greater than one (i.e., $V_g > V_c$), a correction factor is entered into the equation.

$$\ln \eta = \ln\left(\frac{T_{ad} - T_{ad'}}{T_{ad} - T_C}\right) = -\left(\frac{h_g L x}{(WC_P)_c} - K\right)\left(\frac{SV_g}{a_c}\right)^{\frac{1}{8}} f\left(\frac{V_g}{V_c}\right) + \ln \cos 0.8\, \beta_{eff} - 0.08\left(\frac{V_g}{V_c}\right) \quad (458)$$

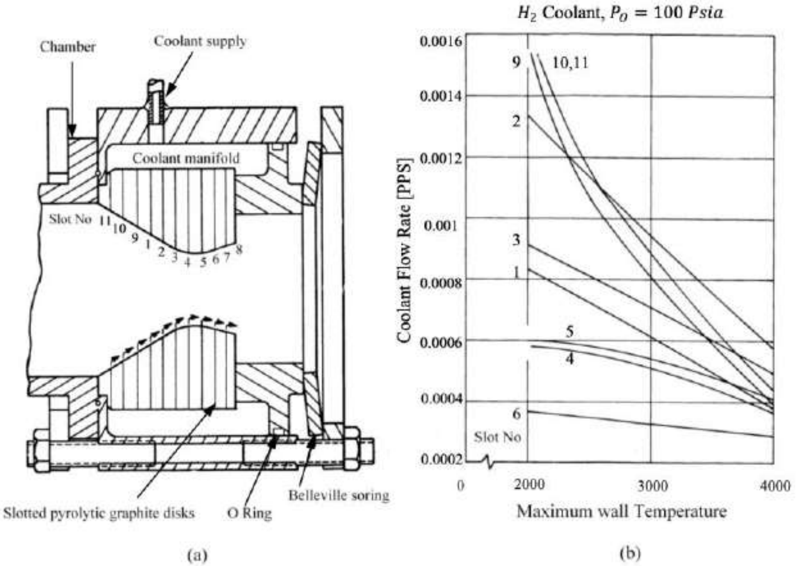

Figure 141-(a) Multi-slot, Filmed cooled pyrolytic graphite nozzle, (b) Gaseous film cooling for standard nozzle with multi-slot cooling. From N6638728

TRANSPIRATION COOLING:

Nozzles were unable to withstand the very high heat flux produced in the engine due to the rapid development of the rocket engine industry against material technology. Cooling of the nozzles is considered very necessary, although the use of cooling systems increases the weight of the rocket and even some penalties in its efficiency. The use of cooling methods often has limitations that force the designer to choose the most appropriate cooling method according to his design. For example, regenerative cooling (convection), which has been successfully used in rockets such as Saturn, Titan, and Atlas, is more commonly used in systems with a heat flux of less than 5000 $\frac{Btu}{ft^2.sce}$, while the heat flux within the nozzles can go beyond this value. This flux limitation is also present in other methods so that the maximum heat dissipation power of the Dump cooling method is 1500 $\frac{Btu}{ft^2.sce}$. Ablation cooling also due to the complexity of the manufacturing process and achieving renewable properties for char and unburned materials, and also due to the low heat flux capability (500 $\frac{Btu}{ft^2.sce}$), has limitations. The use of heat sink cooling also has a time limit and is only responsible for a few seconds at high heat flux. As shown in table 12, the results of studies examining the two methods of film and transpiration cooling on the nozzles indicate that at an equal cooling flow rate, Transpiration cooling has higher efficiency and more heat flux.

The use of these two methods in combination with other methods is common in rockets. In addition to the advantages of these two methods, each of them has design challenges, including the design of very small passages that are too close to each other, as well as the low resistance of porous surfaces in Comparison with integrated solid plates for transpiration cooling, and in liquid film cooling, we can mention the work required for the stability of the film as well as obtaining the highest possible speed ratio (ratio of injected cooling rate to free gas flow rate).

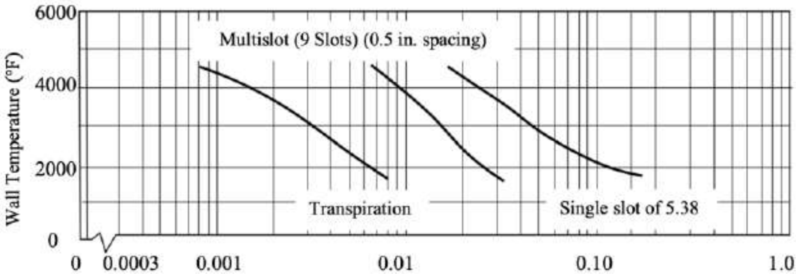

Figure 142- Comparison of Cooling Techniques for Nozzles O_2/H_2 Fuel and H_2Coolant. From N6638728

So that the combined methods (regenerative cooling with film cooling) and (ablation cooling with film cooling) have been successfully implemented on liquid propulsion engines, while so far, no motor has been designed to be able to work on the nozzle at high temperatures only with film or transpiration cooling. Self-cooling is in essence also a type of transpiration cooling method which has been developed by using high-energy metallized propellants. This method is only possible for solid rockets, and so far, there are no examples or indications was found of its use in the nozzle cooling of liquid propellant rockets. Transpiration generally refers to the process whereby a fluid transpires through a porous medium. When this method is used for cooling, there are at least two heat dissipation mechanisms in it. First, the coolant absorbs heat when passing through the porous medium from some reservoir to a wall with higher temperature against the direction of heat flow, and consequently reduces the wall temperature. Second, when the fluid comes out of the wall (emerge), an insulating layer will form between the wall and the hot gases. In other words, gas is blown from the porous surface into the boundary layer, diluting the external hot gas and moving it away from the wall surface. The following figure shows the transpiration cooling mechanism in such a way that the wall is made of porous material and a coolant is blown through the pores, which can move from the porous space inside the wall to hot gases, and form the film cooling layer on the gaseous-side wall, so that the cooling film on the gas side continuously renewed and cooling effectiveness stay constant along the surface. The use of a liquid coolant creates a liquid film, some of which evaporates at the boundary between the film and the hot gases. This evaporation, which causes more cooling, is often known as evaporative-transpiration cooling.

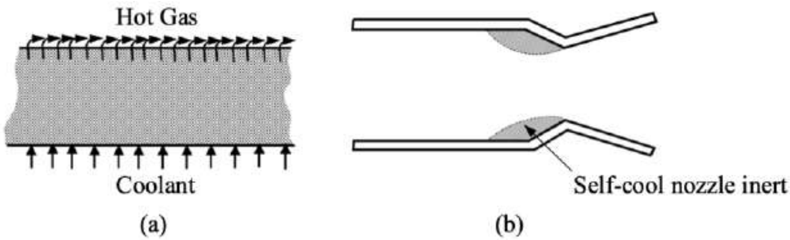

Figure 143- evaporative-transpiration cooling.

Another type of transpiration cooling consists of porous refractory matrices that contain materials that evaporate to create a protective heat sink or gaseous thermal barrier. This method, which is specific to the nozzle of solid propellant engines, can be used for any nozzle application, and one of the biggest advantages of this cooling method is the ability to dissipate high heat flux when it's applied to regeneratively cooled nozzles with a long-firing duration. The matrix is usually made out of high melting point materials such as tungsten in which low melting point materials (such as copper, silver, zinc, etc.) are infiltrated. This method is also referred to as self-cooling or auto transpiration cooling to distinguish it from the type where the entire nozzle wall or chamber is made out of porous material passages, which the coolant within is transpired.
Given the advantages of cooling in this way, the use of this method is very practical but mutually forces the designer to design only the part of the nozzle or chamber that has a very high heat flux (forward surfaces) by transpiration cooling, and for the rest of the surfaces (rearward areas where heating is not severe) use the coolant film introduced into the boundary layer. As

mentioned, a porous material is a solid that has pores and cavities that are almost evenly distributed throughout the material volume. One of the main characteristics of these materials is their porosity, which is the ratio of the volume of pores to the total volume of the body and is expressed as follows:

$$\Pi = \frac{V_\Pi}{V_O} = 1 - (\frac{\rho_s}{\rho_O}) \tag{459}$$

$$1 - \Pi = \frac{V_T}{V_O} \tag{460}$$

V_Π: Pores volume, V_O: Total volume, $V_T = V_O - V_\Pi$: Solid particles volume.

In fact, porous materials are obtained in different ways. For example, metal powder pressing by using spherical particles or woven fiber can be mentioned as two common methods in manufacturing porous materials. For the case where the material is composed of spherical solid particles with a diameter (dt), its volumetric porosity will be obtained from the following equation:

$$\Pi = 1 - N_P \frac{\pi d_P^3}{6} \tag{461}$$

N_P: Number of particles per unit volume.

Today, making porous shapes using sintering is one of the most widely used and modern methods of clay pottery technology, in which a porous material with high mechanical strength is compressed using thermal processing at a temperature of about 0.8 to 0.9 melting temperature. Any metal that can be comminuted to fine powder can be used in this method. Porous materials can be acquired from metal powder using two basic processes. The first method proposed by Meyer-Hartwig is that the metal fabric is mixed with a binder, and formed in a mold to the desired shape, and sintered in a furnace after the mold is removed (from N6638728). The second method was proposed by Martin and Dawes and states that the metal powder is mixed with a gas-evolving compound such as ammonium bicarbonate. The mixture is then pressed to the desired shape and sintered in a reducing atmosphere while still under pressure. It should be noted that reducing atmosphere is an atmospheric condition in which oxidation is prevented by removal of oxygen and other oxidizing gases or vapors, and may contain actively reducing gases such as hydrogen, carbon monoxide, and gases such as hydrogen sulfide, that would be oxidized by any present oxygen. By comparing the above two methods, it can be seen that the first method will cause unlimited deformation in shape, and also shrinkage during sintering can cause cracking or hardening of porosity control. The grains that make up these materials have a special porosity between 8 and 15, which after sintering, taking into account The internal distance of the particles and the distance between them, its amount will change to about 30 to 40. Metals such as stainless steel, tungsten, and nickel are among the most widely used metals, which will be combined with some metal and ceramic carbides to make porous materials. In general, it should be noted that the use of porous materials that arise by weaving method has better conditions compared to spherical particles due to less deviation of the specific surface area, which is expressed as the ratio of the area of porosity to the volume of the material. This parameter plays an important role in calculating the heat transfer between the solid body and the cooling gas. Other advantages of woven materials over spherical particles include higher strength and simpler manufacturing technology, as well as the production of a material with uniform and specific porosity. Another method of producing porous materials without using spherical particles and metal powders is to use wire-mesh screens. This method can also be applied with any ductile metal that can form into wire. Once the wires are put side by side together to the desired contour, they are woven in cloth or gauze and sintered in a furnace. The porosity of these materials can be determined by adjusting the spacing between the wires. Wire-winding and felting techniques have the best strength quality among the methods used to make porous media. The following table presents some advantages and disadvantages of several methods of making porous media by Magnusson, Misra, and Thompson.

In general, the necessary conditions for the fabrication of the porous wall are as follows: (from N66 38728)

1. It must have the necessary properties at the operating temperature to maintain its structural and dimensional integrity.
2. It must be Corrosion and corrosion resistant to the propellant and the coolant at operational temperature.
3. It must be resistant to the thermal shock.

To use any material in high-temperature environments, special attention must be paid to its melting point, so the materials used in such porous media are usually tungsten, molybdenum, and columbium. It should be noted that non-metallic materials are not used due to the difficulty of design and fabrication and that they are often incompatible with the coolant at high temperatures.

Consider a transpiration cooling system in which the coolant with temperature T_0 and flow rate G_0 is blown from the outside to the hot gases and due to the contact of the coolant with the heated surface by the hot gases, the cooling process takes place so that After a while, the temperature of the solid body $T_S(y)$ and the gas $T_g(y)$ reach a steady state. To calculate heat transfer in this type of system, we first examine the characteristics of fluid flow.

Wall material	Advantage	Disadvantage
Woven metal cloth (Regiment)	Uniform porosity.	1. must be fabricated in conical and cylindrical shapes and welded. 2. Does not have unidirectional radial flow 3. Does not have large permeability variation over short distance.
Wound wire (Poroloy)	Uniform porosity.	1. Can be constructed in only limited shapes. 2. Does not have unidirectional radial flow. 3. Does not have large permeability variation over short distance.
Powdered sintered metal Sintered felted short metal fibers Sintered foam metals	Can be fabricated to desired geometrical shape.	1. Uniform porosity is not always achieved. 2. Does not have unidirectional radial flow. 3. Does not have large permeability variation over short distance.
Photoetched washers	1. Controlled porosity. 2. Accurate flow distribution. 3. Permeability only in radial flow direction. 4. Flexibility in choice of materials, flow patterns and washer thickness. 5. Capability of replacing individual washers or washer sections.	1.Weight. 2. Initial cost will be high. 3. Close tolerances complicate fabrica

Table 21- Advantages and disadvantages of various wall materials. From N6638728

Property	Tungsten	Tantalum	Molybdenum	Columbium (Niobium)	Graphite
Theoretical density at 70°F, $\mathbf{lb/in^3}$	0.697	0.600	0.368	0.309	0.082
Melting point, °F	6170	5430	4750	4380	6600 (Sublimes)
Boiling point, °F	9980	9810	8730	8910	-
Linear coefficient of thermal expansion/ °C	4.3×10^{-6}	6.5×10^{-6}	4.9×10^{-6}	7.2×10^{-6}	$2\ to\ 6\times10^{-6}$
Specific heat at 70°F, $\boldsymbol{Btu/\mathrm{lb}-}$°F	0.032	0.036	0.061	0.065	0.18
Thermal conductivity, $\boldsymbol{Btu.ft/\mathrm{hr}.ft^2}$.°F					
Room temp.	97	31	92	31	50 to 90
1000°F	80	37	75	-	40 to 80
1500°F	70	40	65	-	30 to 60
2000°F	65	42	56	-	20 to 50
2500°F	63	43	46	-	20 to 50
3000°F	61	44	39	-	20 to 40
Tensile strength, 1000$\boldsymbol{psi}$					
Room temp.	100 to 500	100 to 150	120	75 to 150	1 to 3
1000°F	180	35	45	30	1 to 3
1500°F	-	25	35	17	1 to 3
2000°F	50	15	25	10	1 to 3
2500°F			10	4	1.5 to 4
3000°F			9		1.5 to 4.5
Young's modulus, $\mathbf{10^6}\boldsymbol{psi}$ at room temp.	59	27	46	12 to 15	1 to 3

Table 22-Properties of some refractory materials

The velocity of the cooling gas flow along the pores of the porous wall with thickness h, which the pressure drop of it is predetermined, is obtained from the Darcy relation:

$$v = \frac{K_\Pi}{\mu}\frac{\Delta P}{h} \tag{462}$$

Where K_Π the porosity coefficient depends on the structure of the porous material and the viscosity μ also depends on the type of coolant.
For the case where the Reynolds number exceeds the critical limit (which depends on the structure of the body and the properties of the cooling fluid), we use the following equation, to which the effect of the inertia component of the resistance in the curved channels is added:

$$\frac{\Delta P}{hv} = \alpha\mu + \frac{\beta\rho_g}{g}v \tag{463}$$

$$Re_{\Pi_{Cr}} = \frac{\rho_g v d}{\mu\Pi} \tag{464}$$

The coefficients α and β for a porous metal body are obtained as follows:

$$\alpha = \frac{7.22\times10^{17}}{\Pi^{3.81}} \tag{465}$$

$$\beta = \frac{1.26\times10^{12}}{\Pi^{6.35}} \tag{466}$$

Another determining parameter in the type of fluid flow is the thermal conductivity, which for porous materials is strongly dependent on the degree of porosity. The reason for using porosity is that due to the lower thermal conductivity of the gas compared to solids, the presence of porosity acts as a barrier against heat penetration. To calculate the thermal conductivity (λ_Σ), we consider the most ideal state of a porous body so that the porous body is considered as gas and solid layers which are put together alternatively. According to this assumption, two different situations will arise for the boundary conditions:

1. Heat flux applies perpendicular to the layers (in this case, there is no thermal connection between the individual elements)
2. Heat flux applies in parallel with the layers.

For these two hypothetical cases, the thermal conductivity relations will be obtained as follows:

$$\lambda_\Sigma = \frac{\lambda_s \lambda_g}{[\lambda_g(1-\Pi)+\lambda_s(\Pi)]} \tag{467}$$

$$\lambda_\Sigma = \lambda_s(1-\Pi) + \lambda_g(\Pi) \tag{468}$$

Given that the coefficient of conductivity of the metal from which the porous body is made, is several times the coefficient of thermal conductivity of the gas filling its pores, Equation (468) is rewritten as follows:

$$\lambda_\Sigma = \lambda_s\left(1-\frac{\Pi}{0.48}\right),\ \Pi < 0.45 \tag{469}$$

Unlike powdered materials, woven porous materials have a weak dependence on the degree of porosity because in such materials the fibers are arranged vertically in the direction of heat transfer and the coefficient of thermal conductivity is determined mainly by the contact resistance between adjacent fibers. Experimental studies have shown that the thermal conductivity of materials with the same porosity depends on the shape and size of the pores. The effect of this parameter is related to the occurrence of free convection inside the pores, which varies between 10 and 15%.

Considering the radiation heat transfer at the porous surfaces and considering the Fourier equation for molecular thermal conductivity and equating these two types of heat transfer with each other for a case where the temperature difference between the surfaces is small:

$$q_R = \lambda_R \frac{T_1 - T_2}{h} = 4\varepsilon^2 \sigma h T_1^3 (\frac{T_1 - T_2}{h}) \quad (470)$$

At low temperatures (λ_R) it is usually much lower than the molecular heat transfer coefficient of the solid (λ_s) but with increasing temperature, the contribution of radiative conductivity in the total conductivity will increase. The shape coefficient will be used to express the effect of the geometry of the porous medium on the radiative thermal conductivity. The shape coefficient is one for cylinders whose axis is in the direction of the temperature gradient, and for the sphere is 0.66, and it's 0.8 for cylinders whose axis is perpendicular to the direction of heat transfer. Considering that the radiation will be scattered in all directions in a cubic pore, the radiative heat conduction coefficient will be:

$$\lambda_R = 2\varepsilon^2 \sigma h T^3 h \quad (471)$$

To calculate the heat transfer in a porous medium, two heat transfer equations are used, which are written separately for the existing phases (solid and gas phases):

$$\frac{d^2 T_s}{dy^2} = \frac{\alpha_v}{(1-\Pi)\lambda_s}(T_s - T_g) \quad (472)$$

$$\frac{dT_g}{dy} = \frac{\alpha_v}{C_g G_g}(T_s - T_g) \quad (473)$$

α_v: Volumetric heat transfer coefficient inside the pores. $[\frac{W}{m^3 K}]$

T_s, T_g: The temperature of the porous material and the cooling gas.

G_g : Coolant gas flow rate. $[\frac{kg}{m^2.sec}]$

The volumetric heat transfer coefficient can also be obtained based on the Reynolds number:

$$\alpha_v = 0.1 \frac{\lambda_g}{\mu_g} \frac{G_g}{d_\Pi} = 0.1 \frac{C_g G_g}{Pr_g d_\Pi}, (1 < Re = \frac{G_g d_\Pi}{\mu_g} < 200) \quad (474\text{-a})$$

$$\alpha_v = 0.6 \frac{\lambda_g}{\mu_g{}^{0.7}} \frac{G_g{}^{0.7}}{d_\Pi{}^{1.3}}, Re > 200 \quad (474\text{-b})$$

In the above relations, d_Π is the diameter of the pores, which is obtained semi-experimentally from

$$d_\Pi = (100\Pi)^{-0.39} \qquad [m] \quad (475)$$

Consider figure (144) to write the heat transfer equation for a single-phase coolant. The plane surface (1) in the element corresponds to the surface of the outer wall, and the surface (2) is spaced from the inner wall as much as the boundary layer. The predominant heat transfer mechanism between the two surfaces (1) and (2) is convection. It is assumed that the exit temperature of the cooling fluid and the wall temperature is the same. Heat transfer right outside the wall through the fluid layer is by conduction, and heat transfer to the outer wall is through radiation. In addition, heat may also flow into the element by conduction in the porous material or by transverse flow of the coolant within the boundary layer. The sum of these flows is designated $(q_{cd}\ dA')$. The heat balance may then be written:

$$k_w\left(\frac{\partial T}{\partial y}\right)_w dA + q_r dA + q_{cd}\, dA' = C_P \rho_a v_a (T_w - T_a) dA$$

(476)

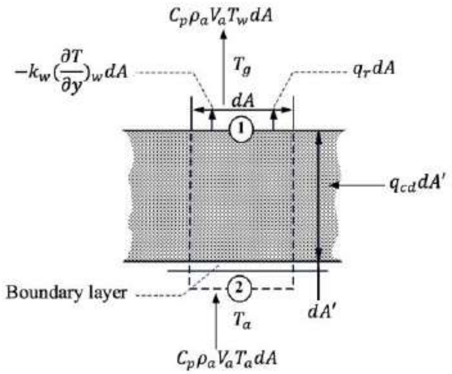

Figure 144- Sketch of element of wall used in setting up Heat balance for transpiration cooling. Adopted from N6638728.

Considering the heat flow along the boundary layer is negligible and assuming the wall temperature is constant (if the heat transfer to the outer wall through conduction and radiation is written based on the heat transfer coefficient), the above relation will be rewritten as follows:

$$\frac{T_w - T_a}{T_g - T_a} = \frac{1}{1 + \frac{C_P \rho_a v_a}{\bar{h}_{g.cv}}\left(\frac{1}{\frac{\bar{h}_{g.t}}{\bar{h}_{g.cv}} + \frac{\bar{h}_r}{\bar{h}_{g.cv}}}\right)} \quad (477)$$

This heat transfer coefficient varies depending on the type of flow regime (slow or turbulent). The average coefficient of heat transfer is obtained by

$$\bar{h}_{g.t} = C_p \rho_a v_a \overline{8 t_{g,t}} \quad (478)$$

Therefore, the final equations for the temperature ratios will be obtained as follows:

Laminar flow without radiation. ($\bar{h}_r = 0$)

$$\frac{T_w - T_a}{T_g - T_a} = \frac{1}{1 + \frac{\rho_a v_a}{\rho_g v_g} \frac{\bar{h}_{g,cv}}{\bar{h}_{g,t}} \frac{\sqrt{Re_g} Pr_g^{2/3}}{0.664}} \tag{479}$$

Laminar flow with radiation.

$$\frac{T_w - T_a}{T_g - T_a} = \frac{1}{1 + \frac{\rho_a v_a}{\rho_g v_g} \frac{\sqrt{Re_g} Pr_g^{2/3}}{0.664} \left(\frac{1}{\frac{\bar{h}_{g,t}}{\bar{h}_{g,cv}} + \frac{\bar{h}_r}{\bar{h}_{g,cv}}} \right)} \tag{480}$$

Turbulent flow without radiation.

$$\frac{T_w - T_a}{T_g - T_a} = \frac{1}{1 + \frac{Re_g^{0.1}}{2.11} (e^{r\varphi} - 1)} \tag{481}$$

$$r\varphi = \frac{2.11}{0.037} Re_g^{0.1} Pr_g^{2/3} \frac{\rho_a v_a}{\rho_g v_g} \tag{482}$$

Turbulent flow with radiation.

$$\frac{T_w - T_a}{T_g - T_a} = \frac{1}{1 + \frac{\rho_a v_a}{\rho_g v_g} \frac{Re_g{}^{0.2} Pr_g^{2/3}}{0.037} \left(\frac{1}{\frac{\bar{h}_r}{\bar{h}_{g,cv}} + \frac{r\varphi}{e^{r\varphi} - 1}} \right)} \tag{483}$$

The following diagrams show transpiration cooling compared to regenerative cooling for both laminar and turbulent flows in a fixed Prandtl (0.7). Smaller temperature difference ratios indicate better cooling.

Two phase transpiration cooling has more advantages than single phase mode, because the phase change of the liquid coolant and the formation of the vapor layer requires a lot of heat, which plays a significant role in cooling.

The self-cooling processing, which has been described before, can also be expressed in general in such a way that after ignition, the temperature of the wall surface increases, and this increase in temperature goes to the melting point of the coolant, and the coolant flows through the pressure forces towards the matrix, and after emerging from the hot surface is vaporized. As a result, it forms a gaseous-liquid interface that recedes with time. The rate of interface recession as well as the coolant flow rate is a function of the temperature distribution within the composite and pressure drop due to the effects of inertia and viscosity effects on the coolant mass flow rate within the porous structure. This recession will continue until the firing ends.

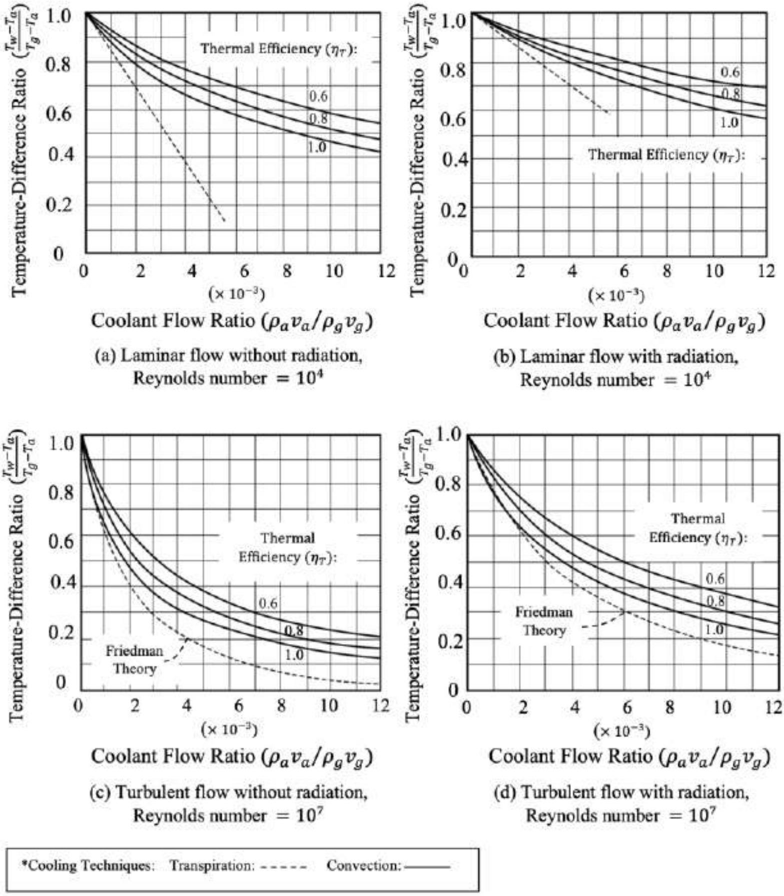

Figure 145- Comparison of transpiration cooling with convection cooling. From N6638728

In addition, the following cooling mechanisms might occur:

1. The evaporating process within the gaseous-liquid interface will cause heat absorption.
2. Coolant flows inside porous structures will cause convection cooling.

3. As the inlet mass to the boundary layer increases, the heat transfer coefficient will decrease, which is the result of increasing the thickness of the boundary layer. (Transpiration cooling effect)
4. Internal dissociation of composite materials causes heat absorption.
5. The occurrence of heat-absorbing due to the endothermic reaction between gaseous coolant and hot gases causes surface cooling.

Of course, it should be noted that the occurrence of exothermic chemical reactions as well as the re-combination of dissociated materials on the surface causes a lot of heat, which is undesirable from the standpoint of heat transfer. A popular model of this method proposed by Gessner is to place a porous refractory matrix filled with infiltrant at the inlet of the nozzle. If the thickness of the insert is small compared to the throat radius of the nozzle, it can be assumed to be an infinite plate of limited thickness. These plates are usually made of fixed porosity tungsten composite with a single infiltrant (here zinc) below the melting point of the refractory matrix to vaporize, and when the plate heats up and the infiltrant reach its boiling point, the liquid/vapor interface It begins to recede and the infiltrant vapor begins to flow through the porous structure. As mentioned, this recession continues as long as the ignition continues or the infiltrant is exhausted.

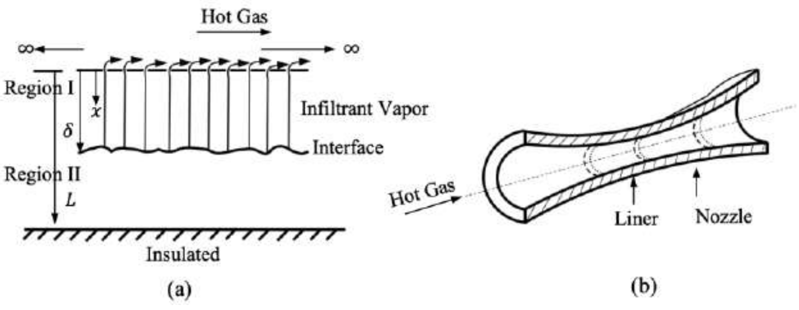

Figure 146- (a): Model after the liquid/vapor interface has formed, (b): Flow of hot gas through a rocket nozzle with a linear at the throat. From N6638728

The assumptions that simplify the analysis are as follows: (from N6638728)

1. One-dimensional, unsteady-state heat transfer.
2. Temperature-constant thermophysical properties.
3. Equal matrix and infiltrant vapor temperature at a given depth in the porous structure.
4. Heat of fusion of infiltrant combined with heat of vaporization.

5. Negligible heat conducted through infiltrant in gaseous phases compared to heat conducted through the porous matrix.
6. Negligible radiation between hot gas and heated surface as compared to convective heat transfer.
7. No diffusion or chemical reaction between infiltrant vapor and hot gas.
8. Negligible radiation within porous structure.

The heat balance equation before the evaporation of infiltrant begins is

$$|K_m(1-P)+K_cP|\frac{\partial^2 T}{\partial x^2}=|\rho_m C_m(1-P)+\rho_c C_c P|\frac{\partial T}{\partial \theta} \quad (484)$$

Where the boundary conditions are as follows:

$$T(x,0)=T_0 \quad (485\text{-a})$$

$$|K_m(1-P)+K_cP|(\frac{\partial T}{\partial x})_{x=0}=h(T_g-T)_{x=0} \quad (485\text{-b})$$

$$0<\theta<\theta_1 \quad (486\text{-a})$$

$$(\frac{\partial T}{\partial x})_{x=0}=0 \quad (486\text{-b})$$

There are two areas in which the heat balance equation must be written when the temperature rises sufficiently and the evaporation process takes place, resulting in a liquid/vapor interface. The first area is the area between the hot surface and the interface, and the second area is the area between the interface and the insulated surface. These equations with their boundary and initial conditions will be as follows:

$$\theta_1 \le \theta \le \theta_{max}$$

Region 1: $(0 \le x \le \delta)$

$$K_m(1-P)\frac{\partial^2 T}{\partial x^2}+(C_c)_g(G_c)_g\frac{\partial T}{\partial x}=\rho_m C_m(1-P)\frac{\partial T}{\partial \theta} \quad (487\text{-a})$$

$$K_m(1-P)(\frac{\partial T}{\partial x})_{x=0}=h(T_g-T) \quad (487\text{-b})$$

Interface:

$$K_m(1-P)(\frac{\partial T}{\partial x})_{\delta}=(G_c)_g\lambda_v-|K_m(1-P)+K_cP|(\frac{\partial T}{\partial x})_{\delta^*}$$

(488)

Region 2: $(\delta \le x \le L)$

$$|K_m(1-P)+K_cP|\frac{\partial^2 T}{\partial x^2}=|\rho_m C_m(1-P)+\rho_c C_c P|\frac{\partial T}{\partial \theta}$$

(489-a)

$$(\frac{\partial T}{\partial x})_{x=L}=0 \quad (489\text{-b})$$

For when the vaporization of the infiltrant has not yet occurred, the expansion of the temperature profile can be obtained from equation (488) using the variable separation technique, and for the case where the infiltrant began to evaporate, the differential equation system with two partial differential equations ((487-a) and (489-a)) which are coupled to the interface equation must be solved.

NUCLEAR PROPULSIONS

The advantage of using nuclear propulsion is due to increasing the specific impulse caused by the nuclear reaction. The generated thermal energy as the result of a nuclear reaction heats the propellant, hence passing this high-temperature propellant via a suitable supersonic nozzle contour the desired thrust will be produced. Compared to chemical rockets, nuclear rockets have vantages that explain further as follows:

- The energy released due to the nuclear reaction is much greater than the energy produced by a chemical reaction. (Million times).
- Because of the segregation of energy sources from the propellants, there is more option for propellant selection. Hydrogen, for instance, could be considered a suitable propellant due to the lowest atomic weight and the highest exit velocity for a given chamber temperature and pressure. In general, given the tendency to increase the specific impulse, it should be noted that the increase in the efficiency of nuclear propulsion depends on the use of propellant with lesser molar mass. The specific impulse on the nuclear fission rocket is almost twice as high as the specific impulse on the best chemical propulsion, (about 800 to 1000 seconds).
- The building block and components inside a nuclear rocket are different from those found in a chemical rocket; because it is necessary for the propellant in nuclear rockets to be heated, whereas the temperature has not to be exceeded from the endurable limits of materials used in the reactor.

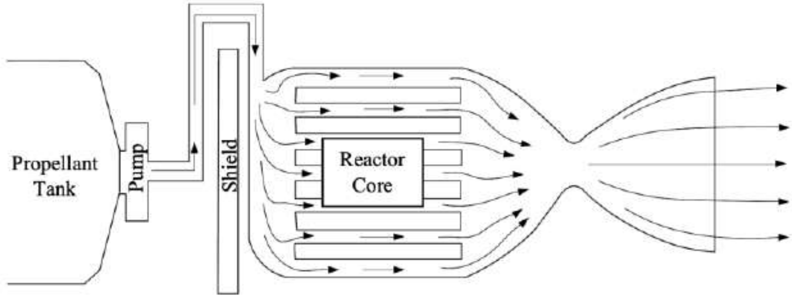

Figure 147- Nuclear Thermal Rocket Schematic. (Adopted from Moon/Mars Prospects May Hinge on Nuclear Propulsion)

ELECTRIC PROPULSIONS

Propulsion systems are generally classified into two basic categories, endogenous and exogenous; in the first case, the energy within the propellant will be used to generate thrust, which involves solid propulsion, liquid propulsion rockets, and cold gas propulsion system. In another type, the energy is supplied from an external power source (electrical energy), which accelerates the propellants and leads to the production of thrust.

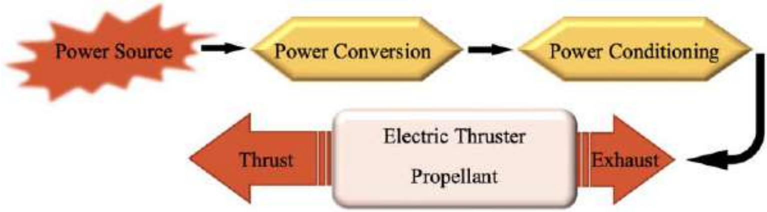

Figure 148- Electric Propulsion Schematic Draft

Higher resulting specific impulses and total impulses are major advantages of exogenous systems over endogenous propulsion due to the existence of an external source for propellant acceleration. For instance, an ion-thruster system, compared to a system consisting of centaur propellant, requires 2,000 kg versus 15,000 kg to produce the same total specific impact of 3,000 seconds, while the dry weight of the two systems is equal. Electric propulsion, which is an inherently low-thrust system, can be used for longer periods of time if clustered. Applications of these propulsion systems include the transition from LEO to GEO for very fragile space structures.

Electric propulsion characteristics can be described as follows: (Ref. 99)

1. High Specific Impulse:
    - Large total impulse for low mass
    - Minimum propellant requirements

2. Low Thrust:
    - Low "g" loading on spacecraft structures
    - precision pointing capability provided

3. High Power Required:
    - Excellent match with high power payloads
4. Orbit Transfer Time/Payload Trade Available
5. Compatible With Long Term Space Storage/Operations

Electric propulsion devices can be divided into three general categories, all of which are capable of producing high impulses, containing

1- Electrothermal 2- Electromagnetic 3- Electrostatics thrusters.

Electrostatic devices, meanwhile, operate particularly well in a wide range of specific impulses.

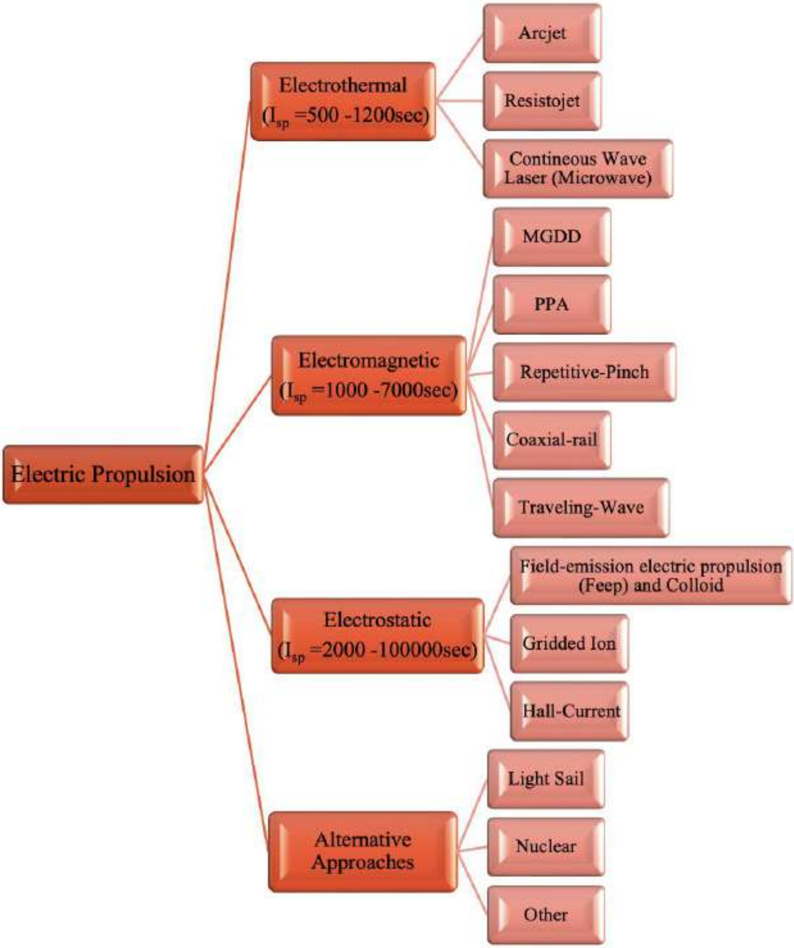

Figure 149- Electric Propulsion Systems

ELECTROTHERMAL PROPULSIONS

In this type of system, electric power exploits to heat the propellant. This heating can be done in two ways: electric discharge through propellant gas (Arc jet) or by flowing propellant gas on the surface heated with electricity (Resistojet). In general, regardless of whether combustion takes place in chemical rockets, electrostatic propellants act in many ways like chemical rockets, meaning that the hot gases from the propellants expand inside the nozzle and produce thrust. However, the velocity of the hot gases will be

higher because the energy added to the gas molecules is greater than the energy from the combustion. But the failure of materials at high temperatures limits the amount of energy added to the propellant. Dissociation breakup of propellant gas molecules, which leads to the absorption of energy without a large increase in gas temperature, also limits the exhaust velocity.
Electrothermal systems can also be used in combination with chemical propulsion. Applications in this category include electrically enhanced catalytic hydrazine to increase the specific impulse of chemical reactions by increasing electrical power, as well as the concept of free radical propulsion, which represents the elimination of hydrogen decomposition and the use of recombinant high temperatures to increase the specific impulse by electrical energy. Due to the fragility of large space structure (LSS), the use of electric propulsion to reduce weight as well as lower acceleration $(< 10^{-3}g)$, which prevents large loads that literally destroy the LSS (due to chemical propulsion) is very practical.

In general, the purpose of advanced chemical and electrical propulsion can be expressed as follows:

ADVANCED CHEMICAL PROPULSION:

- Higher Specific Impulse
- Lower Thrust
- Long life thruster system suitable for taking payload from LEO to GEO orbit.

ADVANCED ELECTRICAL PROPULSION:

- Lowering Specific Impulse
- Increasing thrust per unit of the Ion thruster systems

ELECTROMAGNETIC PROPULSIONS

Electromagnetic or plasma thruster is another type of electric propulsion in which propellant gas is ionized, and a plasma is formed which accelerates rearwards in the presence of an electromagnetic field. It should be noted that plasma consists of ions and electrons that rotate randomly. One of the capabilities of plasma is its high electrical conductivity, which means that when an electric current passes through the plasma in a magnetic field, a force will be applied to the plasma, which will accelerate the plasma rearward. In fact, the system will act like an electric motor that uses plasma instead of a moving rotor.

Electromagnetic rockets could be classified into three common categories:

1. Magneto-Gas- Dynamic Drive (MGDD)
2. Pulsed- Plasma Accelerator (PPA)
3. Traveling Wave (TW)

All these three propulsion systems, which are used as thrusters, use plasma with an electromagnetic field to accelerates the plasma.
As mentioned, one of the characteristics of electric propulsion is high thrust density. Electromagnetic thrusters eliminate the need for a cooling system due to the use of plasma, and since plasma systems are self-neutralizing, reducing the complexity of the power system. Rail gun and mass driver are among the electromagnetic systems that provide it for launching cargo directly from the earth to the orbit or increasing the augmentation of booster capabilities through an electric catapult device.
It should be noted that electrothermal and electromagnetic propulsions have been developed to fill the vacuum between conventional electrostatic ions with chemical propulsion.

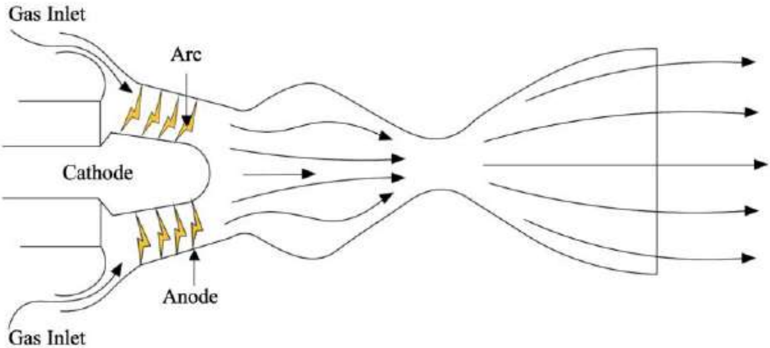

Figure 150-Schematic of Electrothermal Rocket. (Adopted from Moon/Mars Prospects May Hinge on Nuclear Propulsion)

ELECTROSTATICS PROPULSION

The third type of these systems is electrostatic rockets, the most famous of which are (ion thrusters or ion engines). As we know, the ionization phenomenon occurs due to the separation of electrons from propellant atoms. In electrostatic thrusters, electrons leave the ionization region at the same rate as the ions accelerate rearwards.
One of the most versatile and widely used electric propulsions is the electrostatic thruster; Because of the coverage of a wide range of specific impulses and the ability to scale and throttle in a broad range of thrust, become

worthy of auxiliary propulsion for attitude control and station-keeping for the Geostationary spacecraft. Also, another advantage of these systems is the large spectrum of propellants including heavy metals such as mercury, and cesium, as well as gases such as argon, xenon, neon, and nitrogen.

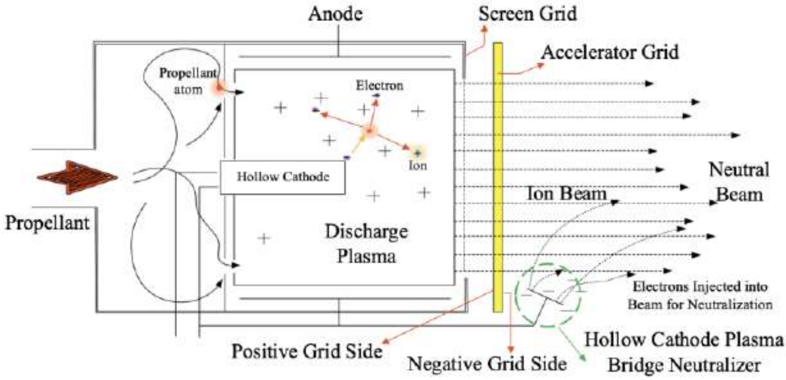

Figure 151- Schematic of Ion Rocket. (Adopted from Moon/Mars Prospects May Hinge on Nuclear Propulsion)

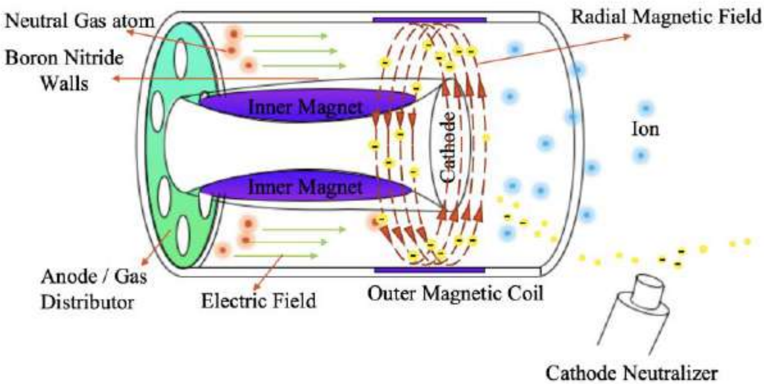

Figure 152- Hall Thruster Schematic Drawing

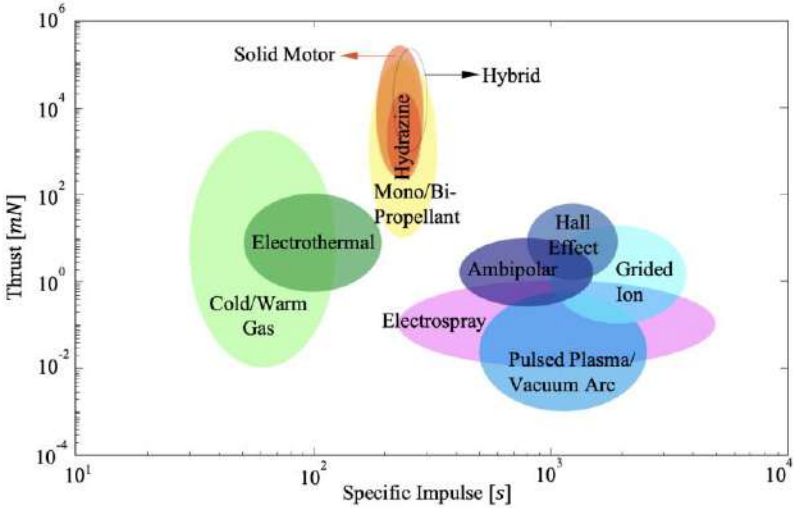

Figure 153- Thrust Ranges Versus Specific Impulse in All Types of Rocket Propulsions.

	Technology	*Thrust Range*	*Specific Impulse Range [s]*
Chemical Propulsion	**Hydrazine monopropellant**	**0.25 – 25 N**	**200 – 285**
	Alternative Mono – and Bi propellants	**10 mN – 120 N**	**160 – 310**
	Hybrids	**1 – 230 N**	**215 – 300**
	Cold/Warm Gas	**10 μN – 3 N**	**30 – 110**
	Solid Motors	**0.3 – 260 N**	**180 – 280**
	Propellant Management Devices	**N/A**	**N/A**
Electric Propulsion	**Electrothermal**	**0.5 – 100 mN**	**50 – 185**
	Electrosprays	**10 μN – 1 mN**	**225 – 5000**
	Gridded Ion	**0.1 – 20 mN**	**1000 – 3500**
	Hall Effect	**1 – 60 mN**	**800 – 1950**
	Pulsed Plasma and Vacuum Arc Thrusters	**1 – 600 μN**	**500 – 2400**
	Ambipolar	**0.25 – 10 mN**	**400 – 1400**

Table 23- Summary of propulsion technologies surveyed. (Adopted from NASA)

REFERENCES

1) ''DESIGN OF LIQUID PROPELLANT ROCKET ENGINES'' by HUZEL and HUANG, Second Edition, NATIONAL AERONAUTICS AND SPACE ADMINISTRATION, NASA SP-125.
2) '' MODERN ENGINEERING FOR DESIGN OF LIQUID-PROPELLANT ROCKET ENGINES'' by D. HUZEL and D. HUANG, PURCHASE FROM AMERICAN INSTITUTE OF AERONAUTICS AND ASTRONAUTICS, A. RICHARD SEEBASS, SERIES EDITOR-IN-CHIEF, VOLUME 147.
3) '' Rocket Propulsion Elements '' by GEORGE P. SUTTON and OSCAR BIBLARZ, Seventh Edition, A Wiley- Interscience Publication JOHN WILEY & SONS, INC.
4) '' Aircraft Propulsion'' by Saeed Farokhi, Second Edition, University of Kansas, WILEY.
5) '' Fundamentals of Aircraft and Rocket Propulsion'' by Ahmed F. El- Sayed, Department of Mechanical Engineering, Zagazive University, Springer.
6) '' Mechanics and Thermodynamics of propulsion'' by Philip G. Hill and Carl R. Peterson, Second Edition, Person.
7) '' Orbital Mechanics for Engineering Students'' by HOWARD D. CURTIES, Embry-Riddle Aeronautical University, Dayton Beach, Florida, ELSEVIER AEROSPACE ENGINEERING SERIES.
8) '' Thermal Protection'' by Polezhayev Yu V & Yurevich F B.
9) '' Modern Compressible Flow with Historical Perspective'' by John D. Anderson Jr., University of Maryland, Consulting editor, Third Edition, McGraw-Hill Series in Aeronautical an Aerospace Engineering.
10) '' ROCKET PROPULSION '' by MARCEL BARRERE, ANDER JAUMOTTE, BAUDOUIN FRAEIJS DE VEUBEKE, AND JEAN VANDENKERCKHOVE, National Office for

Aeronautical Studies and Research (ONERA), Paris, ELSEVIER PUBLISHING COMPANY.
11) ‘’ Spacecraft Chemical Propulsion ‘’ by Robert Lewis Sackheim, NASA Marshall Spaceflight Center.
12) ‘’ HYBRID ROCKET INTERNAL BALLISTICS ‘’ by David W. Netzer, CHEMICAL PROPULSION INFORMATION AGANCY (CPIA) PUBLICATION 222.
13) ‘’ Liquid Rocket Propellants ‘’ by Forrest S. Forbes and Peter A. Van Splinter, Engineering Consultant and General Physics Corporation.
14) ‘’ Rocket Motors, Liquid ‘’ by Bernard R. Bornhorst, Air Force Research Laboratory (Retired).
15) ‘’ Rocket Motors, Hybrid ‘’ by David Altman, Space Propulsion Group, Inc., and Stanford University.
16) ‘’ THRUST CHAMBER COOLING TECHNIQUES FOR SPACECRAFT AND ENGINES’’ NASA-7-103, PROJECT NUMBER 278.
17) ‘’ LIQUID-PROPELLANT ROCKET SYSTEMS’’ N68-18126.
18) ‘’ DESIGN AND COOLING PERFORMANCE OF A DUMP-COOLED ROCKET ENGINE’’, NASA TN D-3532.
19) ‘’REGENERATIVE COOLING OF THE SPACE SHUTTLE IN ENGINE’’ by Henry C. Wieseneck, North American Rockwell, Rocketdyne Division Canoga Park, California.
20) ‘’ PROPELLANT INJECTION SYSTEMS AND PROCESSES’’ by Jackson I. Ito, GenCorp Aerojet Propulsion Segment Sacramento, California U.S.A, NASA-TM-110632.
21) ‘’ Technical Report TR-6 Cluster Techniques’’, Estes Industries 1967.
22) ‘’ TRANSPIRATION AND FILM COOLING OF LIQUID ROCKET NOZZLES’’ by John E. Terry and Gus J. Caras, GEORGE C. MARSHALL SPACE FLIGHT CENTER, US ARMY MISSILE COMMAND, N 66 38728.

23) ‘’ Rocket Propulsion’’ by Prof. Manuel Martinez-Sanchez, Lecture 9: Liquid Cooling.
24) ‘’ LIQUID ROCKET ENGINE INJECTORS’’, NASA SPACE VEHICLE DESIGN CRITERIA (CHEMICAL PROPULSION), NASA SP-8089.
25) ‘’ LIQUID ROCKET ENGINE NOZZLES’’ NASA SPACE VEHICLE DESIGN CRITERIA (CHEMICAL PROPULSION), NASA SP-8120.
26) ‘’ A Simple Equation for Rapid Estimation of Rocket Nozzle Convective Heat Transfer Coefficient’’ by D. R. BARTZ, Jet Propulsion Laboratory, California Institute of Technology, Pasadena, Calif.
27) ‘’ DESIGN AND COOLING PERFORMANCE OF A DUMP-COOLED ROCKET ENGINE’’ by Albert J. Pavli, Jerome K. Curley, Philip A. Masters, and R. M. Scbwartz, Lewis Research Center, Cleveland, Ohio, NASA TN D-3532.
28) ‘’ DESIGN, MANUFACTURING AND TEST OF A PLUG NOZZLE ROCKET ENGINE’’ by Eric Besnard, Hsun Hu Chen, Tom Mueller from Mechanical and Aerospace Engineering Department California State University, Long Beach and John Garvey from Garvey Spacecraft Corporation Huntington Beach CA. AIAA-02-4038.
29) ‘’ LIQUID PROPELLANT GAS GENERATORS’’ NASA SPACE VEHICLE DESIGN CRITERIA (CHEMICAL PROPULSION), NASA SP-8081.
30) ‘’ FABRICATION OF TUBULAR WALL THRUST CHAMBERS FOR ROCKET ENGINES USING LASER POWDER INJECTION’’ Inventors: DALZELL, William, J., Jr.; 18290 Jupiter Landings, Drive, Jupiter, FL 33458 (US). JAHNSEN, Eric; 716 South, Pennock Lane, Jupiter, FL 33458 (US). International Application Number: PCT/US95/05362, International Patent Classification: B23K 26/00, F02K 9/64.
31) ‘’ A Review of the Catalytic Effects of Lead-Based Ballistic Modifiers on the Combustion Chemistry of Double Base

Propellants'' by Lisette R. Warren, Zixuan Wang, Colin R. Pulham, and Carole A. Morrison, Propellants Explos. Pyrotech. 2020, 45, 1-14, Propellants, Explosives, Pyrotechnics.

32) '' METHOD OF FORMING A ROCKET THRUST CHAMBER'' by Robert J. Wright, Charlestown, W. Va., Assignee: United Technologies Corporation, Hartford, Conn., Primary Examiner Irene Cuda, Attorney, Agent, or Firm-Christopher T. Hayes, United States Patent, Patent Number: 6,134,782.
33) ''METHOD OF SIMULTANEOUSLY FORMING ROCKET THRUST CHAMBER COOLING TUBES'' by Daniel A. Bales, Palm City; James R. Joyce, Jupiter, both of Fla., Assignee: United Technologies Corporation, Hartford, Conn. Primary Examiner-Irene Cuda Attorney, Agent, or Firm-Christopher T. Hayes United States Patent, Patent Number: 5,477,613.
34) '' SPACE SHUTTLE MAIN ENGINE ORIENTATION'' Space Transportation System Training Data, BC98-04.
35) '' Space Shuttle System and Flight Mechanics'' by Ulrich Walter, Institute of Astronautics, Technical University, Munich, Germany. Encyclopedia of Aerospace Engineering, Online © 2010 John Wiley & Sons, Ltd., This article is © 2010 John Wiley & Sons, Ltd., This article was published in the Encyclopedia of Aerospace Engineering in 2010 by John Wiley & Sons, Ltd.
36) '' SPACE SHUTTLE ORBITER SUBSYSTEMS'' by Alan Tatourian.
37) https://science.ksc.nasa.gov/shuttle/technology/sts-newsref/sts_coord.html#aft_fuselage
38) http://www.eng.usf.edu/...g%20a%20single, a%20bubble%20of%20empty%20space.&text=However%2C%20there%20is%20always%20one,reason%20about%20the%20scene's%20content
39) https://science.ksc.nasa.gov/shuttle/technology/sts-newsref/srb.

40) ‘’ Rocket Propellants’’ by A. W. SLOAN, Division of Industrial and Engineering Chemistry, ACS, 128th Meeting, Minneapolis, Minn.
41) ‘’ Heat Transfer and Pressure Drop of Liquids in Tubes’’ by E. N. SIEDER AND G. E. TATE, Foster Wheeler Corporation, New York, N. Y.
42) ‘’ THE PLUME PHYSICS BEHIND AEROSPIKE NOZZLE ALTITUDE COMPENSATION AND SLIPSTREAM EFFECT’’ by J. H. Ruf and P.K. McConaughey, NASA Marshall Space Flight Center (MSFC), Huntsville, AL 35806. Branch Chief, Fluid Dynamics Analysis Branch, Member AIAA, Copyright © 1997 by the American Institute of Aeronautics and Astronautics, Inc. No copyright is asserted in the United, States under Title 17, U.S. Code. The U.S. Government has royalty-free license to exercise all rights under the copyright, claimed herein for Governmental Purposes. All other rights are reserved by the copyright owner.
43) ‘’ THERMAL ANALYSIS OF LIQUID ROCKET ENGINES’’ by Mohammad H. Naraghi Department of Mechanical Engineering Manhattan College Riverdale NY 10471. Introduction to Cooling Methods. Combustion gases are 4000 to more than 6000 °F, Updated on Apr 05, 2019.
44) https://www.nakka-rocketry.net/th_grain
45) https://science.ksc.nasa.gov/shuttle/technology/sts-news-ref/sts-rcs
46) ‘’ Recent Developments in Rocket Nozzle Configurations’’ by G. V. R. RAO, National Engineering Science Co., Pasadena, Calif.
47) ‘’ Exhaust Nozzle Contour for Optimum Thrust’’ by by G. V. R. RAO, Marquardt Aircraft Co., Van Nuys, Calif.
48) ‘’ POCKET DATA RI/RD87-142 SPACE SHUTTLE MAIN ENGINE’’ Rockwell International, Rocketdyne Division.
49) ‘’ Parametric Sensitivity Analysis of Convex Star Port Propellant Grain for Solid Rocket Motor’’ by Muhammad Ali

Kamran, University of Engineering and Technology, Peshawar, Article in Journal of Engineering and Applied Sciences • July 2016.

50) ‘’ Combustion of Ammonium Perchlorate-Aluminum Mixtures’’ by V. R. Pai Verneker, DR. Seetharama Charyulu, and R. M. Mallya, Indian Institute of Science, Bangalore, India. Received Feb. 8, 1979; revision received May 9, 1979. Copyright © American Institute of Aeronautics and Astronautics, Inc., 1979. All rights reserved. VOL. 16, NO. 6.

51) https://science.ksc.nasa.gov/shuttle/technology/sts-news-ref/sts-oms

52) https://science.ksc.nasa.gov/shuttle/technology/sts-news-ref/sts-mps

53) ‘’APOLLO OPERATIONS HANDBOOK LUNAR MODULE LM 10 AND SUBSEQUENT’’ Harlow K. Dunton-Ass't Program Director, Support, W. J. Everett, Program Manager, UM Publications Section, VOLUME1, SUBSYSTEMS DATA, LMA790-3-LM 10 and Subsequent, NAS 9-1100, THIS PUBLICATION SUPERSEDES LMA790-3-LM 8 AND SUBSEQUENT DATED 15 JUNE 1970.

54) ‘’ Combustion of Solid Propellants’’ by G. Lengellé, J. Duterque, J.F. Trubert, Research Scientists, Energetic Department, Office national 'études et de recherches aérospatiales (ONERA), 29 avenue de la Division Leclerc, BP 72 92322 Châtillon Cedex, FRANCE. Paper presented at the RTO/VKI Special Course on "Internal Aerodynamics in Solid Rocket Propulsion' held in Rhode-Saint-Genèse, Belgium, 27-3 May 2002, and published in RTO-EN-023.

55) ‘’ CARBON/CARBON EXTENDIBLE NOZZLES’’ M. LACOSTE, A. LACOMBE, and P. JOYEZ, Sociéte Européenne De Propulsion, BP 37, 33165 Saint Medard En Jalles, Cedex, France, and R. A. ELLIS, J. C. LEE, and F. M. PAYNE Pratt & Whitney, Csd, San Jose, CA, USA. Acta Astronautica Vol. 50, No. 6, pp. 357-367, 2002, © 2002 Elsevier Science Ltd. All

rights reserved, Printed in Great Britain, 0094-5765/02/S see front matter.

56) '' Multidisciplinary simulation of a regeneratively cooled thrust chamber of liquid rocket engine: Turbulent combustion and nozzle flow'' by Seong-Ku Kim, Miok Joha, Hwan Seok Choi, Tae Seon Park, Combustion Chamber Department, Korea Aerospace Research Institute, 169-84 Gwahak-ro, Yuseong-gu, Daejeon 305-806, Republic of Korea, School of Mechanical Engineering, Kyungpook National University, 80 Daehak-ro, Buk-gu, Daegu 702-701, Republic of Korea.

57) '' INNOVATIVE AIRBREATHING PROPULSION CONCEPTS FOR ACCESS TO SPACE'' by Woodrow Whitlow, Jr., Richard A. Blech, and Isaiah M. Blankson, Glenn Research Center, Cleveland, Ohio, NASA/TM-2001-210564.

58) '' Various Methods for the Determination of the Burning Rates of Solid Propellants an Overview'' by Garima GUPTA, Lalita JAWALE, MEHILAL, Bikash BHATTACHARYA, Central European Journal of Energetic Materials, 2015, 12(3), 593-620, ISSN 1733-7178, e-ISSN 2353-1843.

59) '' FUNDAMENTALS OF SOLID-PROPELLANT COMBUSTION'' Edited by Kenneth K. Kuo, The Pennsylvania State University, University Park, Pennsylvania, Martin Summerfield, Princeton Combustion Research Laboratories, Inc., Monmouth Junction, New Jersey, Volume 90, Martin Summerfield, Series Editor-in-Chief, Princeton Combustion Research Laboratories, Inc., Monmouth Junction, New Jersey. Published by the American Institute of Aeronautics and Astronautics, Inc., 1633 Broadway, New York, N. Y. 10019.

60) '' Design of a Supersonic Nozzle using Method of Characteristics'' by Md Akhtar Khan, Sanjay Kumar Sardiwal. M.V. Sai Sharath, D. Harika Chowdary, International Journal of Engineering Research & Technology (IJERT), ISSN: 2278-0181, Vol. 2 Issue 11, November 2013.

61) ‘’ Selecting Cooling Techniques for Liquid Rockets for Spacecraft’’ by CLIFFORD D. COULBERT, The Marquardt Corporation, Van Nuys, Calif., Journal of Spacecraft and Rockets, VOLUME 1, MARCH-APRIL 1964, NUMBER 2, Presented as Preprint 63-241 at the AIAA Summer Meeting, Los Angeles, Calif., June 17-20, 1963; revision received January 20, 1964.
62) ‘’ ADVANCED THRUST CHAMBER FOR SPACE MANEUVERING PROPULSION’’ by H. G. Diem, and R. P. Pauckert, Tasks I and INI Thrust Chamber Segment Evaluations, Final Report Materials and Processes, Rocketdyne, A Division of North American Aviation, Inc., Canoga Park, California, TECHNICAL REPORT AFRPL-TR-67-226, AD383260.
63) http://www.braeunig.us/space/propuls
64) ‘’ DESIGN OF DAMPING TREATMENT FOR THE DELTA III RL 10B-2 DEPLOYABLE NOZZLE’’ by Mary Baker and Paul Blelloch, Structural Dynamics Research Corporations, San Diego, California, Tom Burton, Brahe Consulting, San Diego, California, Frederick Mark Payne, Pratt and Whitney, San Jose, California, American Institute of Aeronautics and Astronautics, A98-25024, AIAA 98-1723.
65) ‘’ Advanced Rocket Engines’’ by Oskar J. Haidn, Institute of Space Propulsion, German Aerospace Center (DLR), 74239 Lampoldshausen, Germany, Haidn, O.J. (2008) Advanced Rocket Engines. In Advances on Propulsion Technology for High-Speed Aircraft (pp. 6-1 6-40). Educational, Notes RTO-EN-AVT-150, Paper 6. Neuilly-sur-Seine, France: Available from: http://www.rto.nato.int , RTO-EN-AVT-150.
66) ‘’ INTRODUCTION TO ROCKET PROPULSION’’ by J. Michael Lyon, Propulsion Directorate, Research, Development, and Engineering Center, U.S. ARMY MISSILE COMMAND, Redstone Arsenal, Alabama 35898-5000 TECHNICAL REPORT RD-PR-91-17, AD-A250 424.
67) ‘’ A Preliminary Research on a Two-Stage-To-Orbit Vehicle with Airbreathing Precooling Hypersonic Engines’’ by Jinxing

ZHOU, Hong LU, Haocheng ZHANG, Yazhuo FAN, Lingbo ZHAO, Beijing Aerospace Technology Institute, China and, Jingmin CHEN, Riheng ZHENG, Science and Technology on Scramjet Laboratory, Beijing Power and Machinery Research Institute, China, 21 st AIAA International Space Plane and Hypersonic Systems and Technologies Conference, March 6-9, 2017, Xiamen University, China.

68) Additively Manufactured Rocket Engine Combustion Chamber Structural Analysis'' by Cory Medina, Marshall Space Flight Center, Structural and Dynamics Branch ER41, SLaMS Young Professional Forum, September 1-3, 2015.

69) '' Cryogenic Propellant Storage and Transfer Technology Demonstration for Long Duration In-Space Missions'' by Michael L. Meyer, Susan M. Motil, Trudy F. Kortes, and William J. Taylor, National Aeronautics and Space Administration, Glenn Research Center, Cleveland, Ohio 44135, Patrick S. McRight, National Aeronautics and Space Administration, Marshall Space Flight Center, Huntsville, Alabama 35812, NASA/TM-2012-217642.

70) '' Apollo Guidance, Navigation, and Control (GNC) Hardware Overview''

71) '' Frozen Chemistry Effects on Nozzle Performance Simulations'' by Dennis A. Yoder and Nicholas J. Georgiadis, Glenn Research Center, Cleveland, Ohio, Michael R. O'Gara, Embry Riddle Aeronautical University, Daytona Beach, Florida, NASA/TM-2009-215507, AIAA-2008-3969.

72) ''Scaling of Performance in Liquid Propellant Rocket Engine Combustors'' by James R. Hulka, Jacobs Engineering, ESTS Group, Mail Stop ER32, NASA MSFC, Huntsville, AL, USA, James.R.Hulka@nasa.gov, 20th Memorial Meeting of the Northern Section of the Japan Society for Aeronautical and Space Sciences, Sendai, Japan March 7-9, 2007, Source of Acquisition NASA Marshall Space Flight Center.

73) ‘’ Nucleate Boiling Heat Transfer Studied Under Reduced-Gravity Conditions’’ Glenn contacts: Dr. David F. Chao, (216) 433-8320, David.F.Chao@grc.nasa.gov; and Dr. Mohammad M. Hasan, (216) 977-7494, Mohammad.Hasan@grc.nasa.gov, Headquarters program office: OLMSA, Programs/Projects: Microgravity Science.
74) ‘’ A Study of Nucleate Boiling with Forced Convection in Microgravity, Herman Merte, Jr., The University of Michigan, Department of Mcchanical Engineering and Applied Mechanics, 2148 G.G. Brown, Ann Arbor, Michigan 48109-2125, Study of Nucleate Boiling H. Merte.
75) ‘’ Plug Nozzles-The Ultimate Customer Driven Propulsion System’’ by Carl A. Aukerman, Sverdrup Technology, Inc., Lewis Research Center Group, Brook Park, Ohio, August 1991, Prepared for Lewis Research Center, Under Contract NAS3-25266, NASA Contractor Report 187169, AIAA-91-2208.
76) ‘’ SOLID PROPELLANT GRAIN STRUCTURAL INTEGRITY ANALYSIS’’ NASA SPACE VEHICLE DESIGN CRITERIA (CHEMICAL PROPULSION), NASA SP-8073.
77) ‘’ EXPLORING IN AEROSPACE ROCKETRY - 7. LIQUID-PROPELLANT ROCKET SYSTEMS’’ by E. William Conrad, Lewis Research Center, Cleveland, Ohio, Presented to Lewis Aerospace Explorers, Cleveland, Ohio 1966-67, NASA TM X-52394.
78) ‘’ New Contour Design Method for Rocket Nozzle of Large Area Ratio’’ by Dechuan Sun, Tianyou Luo, and Qiang Feng, Hindawi, International Journal of Aerospace Engineering, Volume 2019, Article ID 4926413, 8 pages, https://doi.org/10.1155/2019/4926413 .
79) ‘’ THE HISTORY OF SOLID-PROPELLANT ROCKETRY: WHAT WE DO AND DO NOT KNOW’’ by J.D. Hunley, NASA Dryden Flight Research Center, Edwards, California, American Institute of Aeronautics and Astronautics.

80) ‘’ Advanced Rocket Nozzles’’ by Gerald Hagemann, DLR, German Aerospace Research Center, Lampoldshausen 74239, Germany, Hans Immicht, DaimlerBenz AG, Munich 81663, Germany, Thong Van Nguyen, Gen Corp Aerojet, Sacramento, California 95813, and Gennady E. Dumnov Keldysh Research Center, Moscow 125438, Russia.
81) ‘’ Application of the Saderholm Erosive Burning Model to Nozzleless Solid Propellant Rocket Motors’’ by Clark D. Mikkelsen, U.S. Army Missile Command, Redstone Arsenal, Alabama, and G. Patrick Royst, Morton-Thiokol, Huntsville, Alabama, VOL. 21, NO. 1, JAN.-FEB. 1984.
82) ‘’ Erosive Burning of Solid Rocket Propellants- A Revisit Ellis M. Landsbaum, The Aerospace Corporation, Los Angeles, California 90009-2957, JOURNAL OF PROPULSION AND POWER, Vol. 21, No. 3, May-June 2005.
83) ‘’ THE METHOD OF CHARACTERISTICS FOR PROBLEMS OF COMPRESSIBLE FLOW INVOLVING TWO INDEPENDENT VARIABLES’’ by R. E. MEYER (Department of Mathematics, The University, Manchester), PART II. INTEGRATION ALONG A MACH LINE. THE RADIAL FOCUSING EFFECT IN AXIALLY SYMMETRICAL FLOW [Received 13 December 1947].
84) ‘’ Conformal cooling channels in injection molding tools – design considerations, Mach’’ by O. Tuteski, A. Kocˇov, Technol. Mater. 12 (2018) 445–448.
85) Feng, S., Kamat, A. M., & Pei, Y. T. (2021). Design and fabrication of conformal cooling channels in molds: Review and progress updates. International Journal of Heat and Mass Transfer, 171, [121082].
86) ‘’ Study of Conical Aerospike Nozzles with Base-Bleed and Freestream Effects Prasanth P. Nair" and Abhilash Suryan, College of Engineering Trivandrum, Kerala 695 016, India, and Heuy Dong Kim, Andong National University, Andong 760749, South Korea.

87) ‘’ SPIKE NOZZLE CONTOUR FOR OPTIMUM THRUST’’ by G. V. R. RAO, Rocketdyne, Canoga Park, California.
88) ‘’ Introduction to Orbital Mechanics and Spacecraft Attitudes for Thermal Engineers’’ Presented by: Steven L. Rickman, NASA Technical Fellow for Passive Thermal, NASA Engineering and Safety Center, 18-20 August 2020.
89) ‘’ PERFORMANCE OF PLUG-TYPE ROCKET EXHAUST’’ by Pires, M., manoloneuzalucas@yahoo.com.br, Fifthvision Technology Research and DevelopmentAv. Brig. Faria Lima, 1699-Jd Flamboyant São José dos CamposSP, Nobres, N. D., Instituto Militar de engenharia-IME Av. Gen. Tibúrcio s/n Praia vermelha-Rio de Janeiro-R.J.
90) ‘’ LIQUID PROPELLANT DENSIFICATION’’, Inventors: Tibor L Lak, Huntington; Steve P., Petrilla, Irvine; Martin E. Lozano, Whittier, all of Calif., Assignee: Rockwell International Corporation, Seal Beach, Calif., United States Patent, Patent Number: 5,644,920, Date of Patent: Jul. 8, 1997.
91) ‘’ HYBRID PROPULSION TECHNOLOGY PROGRAM’’, Final Report, Volume IV, 2 OCTOBER 1989, PREPARED BY S. E. Claflin, A. W. Beckman, APPROVED BY S. A. Evans, G. L. Briley, RI/RD89-261.
92) ‘’ SOLID PROPELLANT GRAIN DESIGN AND INTERNAL BALLISTICS’’, NASA SPACE VEHICLE DESIGN CRITERIA (CHEMICAL PROPULSION), NASA SP-8076.
93) ‘’ Thermomechanical Analysis and Optimization of Cryogenic Liquid Rocket Engines’’ by Detlef Kuhl, Ruhr-University Bochum, D-44780 Bochum, Germany, and, Jörg Riccius, and Oskar J. Haidn, DER, German Aerospace Research Center, D-74239 Hardthausen, Germany, JOURNAL OF PROPULSION AND POWER, Vol. 18, No. 4, July-August 2002.
94) ‘’ Additively Manufactured Rocket Engine Combustion Chamber Structural Analysis’’ by Cory Medina, Marshall Space Flight Center, Structural and Dynamics Branch ER41, SLaMS Young Professional Forum, September 1-3, 2015.

95) ‘’Virtual prototyping of solid propellant rockets’’ by Michael Thomas Heath (University of Illinois, Urbana-Champaign), and William A. Dick (University of Illinois, Urbana-Champaign), Article in Computing in Science and Engineering • April 2000, 1521-9615/00/$ 10.00 © 2000 IEEE, Center for Simulation of Advanced Rockets, UIUC.

96) ‘’ Designing Liquid Rocket Engine Injectors for Performance, Stability, and Cost’’ by Dr. Jeffrey West, NASA Marshall Space Flight Center, Lead, Dr. Doug Westra, NASA Marshall Space Flight Center, Presenting, Brian R. Richardson, Qualis/ESSSA, Paul K. Tucker, NASA Marshall Space Flight Center.

97) ‘’ Thermal Protection Materials: Development, Characterization and Evaluation’’ by Sylvia M. Johnson (Entry Systems and Technology Division), NASA Ames Research Center, Sylvia.m.johnson@nasa.gov, Presented at HiTemp2012, Munich, Germany.

98) ‘’ Moon/Mars Prospects May Hinge on Nuclear Propulsion’’ by Asker, James R., Aviation Week & Space Technology, December 2, 1991.

99) ELECTRIC PROPULSION TECHNOLOGY, Robert C. Finke, NASA Lewis Research Center

Mahdi H. Gholi Nejad is a master's graduate of Mechanical Engineering from the Noshirvani University of Babol. Due to his interest in aerospace, he starts self-studying in Iran in the field of space rockets and propulsion under the supervision of Professor Mofid Gorji-Bandpy. Mahdi H. Gholi Nejad was also a member of the American Society of Mechanical Engineers.

Mofid Gorji-Bandpy obtained his BSc. and MSc. in Mechanical Engineering, Faculty of Engineering, University of Tehran, Iran, in 1976 and 1978 respectively, in advance, Prof. Gorji-Bandpy got his Ph.D. in Hydrodynamics from the School of Engineering, University of Wales College of Cardiff (UWCC), UK. At present he is a Full time Professor in Mechanical Engineering at Babol Noshirvani University of Technology, Iran, and a Visiting Professor in the Department of Mechanical, and Industrial Engineering, University of Toronto, Canada. His major interests are in Advanced Fluid Mechanics, Turbomachinery, Water Distribution Networks and the Solution of both Energy and Environmental problems. He has published more than 300 papers in these fields. He has also published several refereed publications in different fields of mechanical engineering, applied mathematics, and aerodynamics. In addition, Dr. Gorji-Bandpy was recognized as a Highly Cited Researcher by Clarivate Analytics in 2017 and 2018.